



Publicly Accessible Penn Dissertations


1-1-2015

Form and Function: X-Ray Scattering and Spectroscopy of Transition Metal-Based Nanoparticles

Vicky V T Doan-Nguyen

University of Pennsylvania, vdoann@gmail.com

Follow this and additional works at: <http://repository.upenn.edu/edissertations>

 Part of the [Chemistry Commons](#), and the [Mechanics of Materials Commons](#)

Recommended Citation

Doan-Nguyen, Vicky V T, "Form and Function: X-Ray Scattering and Spectroscopy of Transition Metal-Based Nanoparticles" (2015). *Publicly Accessible Penn Dissertations*. 1044.

<http://repository.upenn.edu/edissertations/1044>

This paper is posted at ScholarlyCommons. <http://repository.upenn.edu/edissertations/1044>

For more information, please contact libraryrepository@pobox.upenn.edu.

Form and Function: X-Ray Scattering and Spectroscopy of Transition Metal-Based Nanoparticles

Abstract

In recent decades, nanoparticles have been found to possess unique, tunable properties with an enormous variety of applications. The atomic and nanoscale structures govern these functional properties, and structural deviations from the bulk, in part, are responsible for the vast technological uses of nanoparticles. This dissertation tackles the understanding of structure in a number of metal, metal phosphide, and metal oxide nanoparticle systems. Additionally, the syntheses of monodispersed nanoparticle systems allow for correlating their structure with functional properties. Real space analysis using pair distribution functions of monometallic (Ni, Pd) nanoparticles of less than 5 nm in diameter revealed a deviation from the bulk face-centered cubic structure. Their local atomic packing disorder and lack of long-range order resemble that of bulk metallic glasses, which often consist of complex mixtures of a multitude of elements. Bulk metallic glasses have high mechanical strength and can sustain elastic deformations. The significant connection between these two seemingly disparate systems lie in the short-range ordering of their atomic packing motifs, which consist of icosahedral symmetry as seen in their pair distribution functions. Cobalt phosphide (Co₂P) nanorods are promising as inexpensive, earth abundant catalysts for the oxygen reduction reaction in fuel cells. Additionally, their 1-D structures demonstrated greater stability as compared to conventional Pt catalysts. Their structure was investigated using high-resolution electron microscopy and a suite of X-ray scattering and absorption techniques. The dynamic structural nature of the solid-solid phase transition in vanadium dioxide (VO₂) thin films was investigated using X-ray absorption fine structure spectroscopy. Substitution of transition metal dopants into lattice sites revealed the structurally-driven depression of the metal-to-insulator transition temperature. Bridging form and function, this dissertation reports the colloidal synthesis of monodispersed nanoparticles alongside structural investigations and functional testing.

Degree Type

Dissertation

Degree Name

Doctor of Philosophy (PhD)

Graduate Group

Materials Science & Engineering

First Advisor

Christopher B. Murray

Keywords

bulk metallic glass, exafs, nanoparticles, oxygen reduction reaction, total scattering, vanadium dioxide

Subject Categories

Chemistry | Mechanics of Materials

FORM AND FUNCTION: X-RAY SCATTERING AND SPECTROSCOPY OF TRANSITION

METAL-BASED NANOPARTICLES

Vicky Vi Thuy Doan-Nguyen

A DISSERTATION

in

Materials Science and Engineering

Presented to the Faculties of the University of Pennsylvania

in

Partial Fulfillment of the Requirements for the

Degree of Doctor of Philosophy

2015

Supervisor of Dissertation

Christopher Bruce Murray

Richard Perry University Professor of Materials Science and Engineering, Chemistry

Graduate Group Chairperson

Shu Yang, Professor of Materials Science and Engineering, Chemical and Biomolecular
Engineering

Dissertation Committee

Peter K. Davies, Class of 1942 Term Professor and Chair of Materials Science and Engineering

David P. Pope, Professor of Materials Science and Engineering

Paul A. Heiney, Professor of Physics and Astronomy

FORM AND FUNCTION: X-RAY SCATTERING AND SPECTROSCOPY OF
TRANSITION METAL-BASED NANOPARTICLES

COPYRIGHT

2015

Vicky Vi Thuy Doan-Nguyen

This work is licensed under the
Creative Commons Attribution-
NonCommercial-ShareAlike 3.0
License

To view a copy of this license, visit

<http://creativecommons.org/licenses/by-nc-sa/2.0/>

To my family.

ACKNOWLEDGMENT

I would first like to thank my advisor, Professor Christopher B. Murray. His mentorship has helped me grow immensely as a materials scientist. He has provided his utmost support throughout my time at Penn. I would also like to thank my dissertation committee members—Professor Peter Davies, Professor Paul Heiney, and Professor David Pope—for their guidance and support. Additionally, I would like to thank professors who have served on my qualifying and proposal committees for their guidance and support: Professor Dawn Bonnell, Professor Russell Composto, Professor Cherie Kagan, Professor Ju Li, and Professor Karen Winey.

I owe my parents deep gratitude for their unconditional support and love. I would like to thank my siblings, who on occasion have much more wisdom than their eldest sister. I would like to thank my sister, Nancy H. Nguyen, for keeping it real and reminding me to maintain perspective when I've been stuck on a problem. I would like to thank my sister, Mary T. L. Nguyen, for supporting me with her many emojis and encouraging words. I would like to thank my brother Christopher D. Nguyen who has joined me on many camping adventures into the woods and deserts, and survived. I would like to thank Raleigh L. Martin,

who has not only been a great professional colleague but also a dear friend who has been supportive of most of my ideas for winter camping. I would like to thank E. Ashley Gaulding who has helped me to complete a 5.10 route—something I never imagined I would try, much less accomplish. I would like to thank Edward B. Trigg for the many wonderful discussions about programming data structure as well as crystallographic structure. But more importantly, Ted has been my unwaivering cheerleader and personal Python guru. While we intersected due to our fascination with reciprocal space, I look forward our future adventures together in real space.

I have been enriched by the many fruitful discussions with my collaborators: Dr. Simon A. J. Kimber, Professor Simon J. L. Billinge, Dr. Mahalingam Balasubramanian, Professor Matteo Cargnello, Dr. Thomas R. Gordon, Stan Najmr, and Dr. Sen Zhang. Of note, Dr. Kimber taught me how to set up my first total scattering experiment at the European Synchrotron Radiation Facility, Professor Billinge taught me to think about crystallography beyond Bragg diffraction, Dr. Balasubramanian helped to deepen immensely my understanding of EXAFS, Professor Cargnello and Dr. Gordon are the remainder members of the original CaTeAm, Stan for VO_x synthesis and uniform film prep, and Dr. Zhang for electrocatalysis. Walking up and down the laboratory hallway

these past years have been filled with many thoughtful conversations with my past and current labmates and visiting scholars: Dr. Matteo Cargnello, Jun Chen, Bianca Datta, Benjamin Diroll, Dr. Angang Dong, Dr. Bertrand Donnio, E. Ashley Gaulding, Natalie Gogotsi, Dr. Thomas Gordon, Nicholas Greybush, Dr. Davit Jishkariani, Dr. Yijin Kang, Dr. Dong-Kyun Ko, Dr. Weon-kyu Koh, Jennifer Lee, Dr. Ludivine Malassis, Stan Najmr, Dr. Taejong Paik, Dr. Danielle Reifsnyder Hickey, Dr. Haoran Yang, Dr. Xingchen Ye, Hongseok Yun, Dr. Hyeong Jin Yun, and Dr. Sen Zhang. Through the Penn Graduate Women in Science and Engineering Group, I have had a great chance to meet fellow scientists and engineers, especially my friends. Dr. Jessamyn Fairfield and Dr. Rose Mutiso. Dr. Douglas Yates and Dr. Patrick Carroll have been helpful with fantastic discussions on transmission electron microscopy and single crystal diffraction, respectively. Over my many years at Penn, Candice Adams in the Chemistry Department and Pat Overend, Vicky Lee, and Irene Clements in the Materials Science and Engineering Department have been very helpful with all things administrative.

ABSTRACT

FORM AND FUNCTION: X-RAY SCATTERING AND SPECTROSCOPY OF TRANSITION METAL-BASED NANOPARTICLES

Vicky Vi Thuy Doan-Nguyen

Professor Christopher Bruce Murray

In recent decades, nanoparticles have been found to possess unique, tunable properties with an enormous variety of applications. The atomic and nanoscale structures govern these functional properties, and structural deviations from the bulk, in part, are responsible for the vast technological uses of nanoparticles. This dissertation tackles the understanding of structure in a number of metal, metal phosphide, and metal oxide nanoparticle systems. Additionally, the syntheses of monodispersed nanoparticle systems allow for correlating their structure with functional properties. Real space analysis using pair distribution functions of monometallic (Ni, Pd) nanoparticles of less than 5 nm in diameter revealed a deviation from the bulk face-centered cubic structure. Their local atomic packing disorder and lack of long-range order resemble that of bulk metallic glasses, which often consist of complex mixtures of a multitude of elements. Bulk metallic glasses have high mechanical strength and can sustain elastic

deformations. The significant connection between these two seemingly disparate systems lie in the short-range ordering of their atomic packing motifs, which consist of icosahedral symmetry as seen in their pair distribution functions. Cobalt phosphide (Co_2P) nanorods are promising as inexpensive, earth abundant catalysts for the oxygen reduction reaction in fuel cells. Additionally, their 1-D structures demonstrated greater stability as compared to conventional Pt catalysts. Their structure was investigated using high-resolution electron microscopy and a suite of X-ray scattering and absorption techniques. The dynamic structural nature of the solid-solid phase transition in vanadium dioxide (VO_2) thin films was investigated using X-ray absorption fine structure spectroscopy. Substitution of transition metal dopants into lattice sites revealed the structurally-driven depression of the metal-to-insulator transition temperature. Bridging form and function, this dissertation reports the colloidal synthesis of monodispersed nanoparticles alongside structural investigations and functional testing.

TABLE OF CONTENTS

ABSTRACT	vii
LIST OF TABLES.....	xii
LIST OF ILLUSTRATIONS.....	xiv
1. Introduction: Synthesis and Characterization of Nanoparticles.....	1
1.1 Glossary of Terms	1
1.2 Motivation.....	2
1.3 Synthesis.....	4
1.4 Electron Microscopy	10
1.5 X-ray Scattering: Wide-Angle, Small-Angle, Grazing Incident Small Angle, Total Scattering & Pair Distribution Functions	12
1.6 X-ray Absorption Fine Structure.....	23
1.7 Inductively Coupled Plasma-Optical Emission Spectroscopy	33
2. Bulk Metallic Glass-Like Scattering Signal in Small Metallic Nanoparticles .	34
2.1 Introduction	34
2.2 Methods.....	38
2.3 Results and Discussion.....	41
2.4 Conclusion	49
2.5 Future Directions	49

2.6	Figures	50
3.	Synthesis and X-ray Characterization of Cobalt Phosphide (Co ₂ P) Nanorods for the Oxygen Reduction Reaction	62
3.1	Introduction	62
3.2	Methods.....	72
3.3	Results and Discussion.....	76
3.4	Conclusions.....	84
3.5	Future Directions	85
3.6	Figures	86
4.	Structural Transition of Doped VO ₂ Nanoparticle Thin Films as Probed by Extended X-ray Absorption Fine Structure (EXAFS)	105
4.1	Introduction	105
4.2	Methods.....	118
4.3	Results and Discussion.....	122
4.4	Conclusion	132
4.5	Future Directions	133
4.6	Figures	136
5.	Structure Determination and Modeling of Monoclinic Trioctylphosphine Oxide.....	161
5.1	Introduction	161
5.2	Methods.....	162
5.3	Results and Discussion.....	163
5.4	Figures	165

6. Conclusions.....	170
Appendix A. Bismuth Nanoparticles.....	172
Appendix B. Microwave-Assisted Synthesis	175
Appendix C. Cromer-Mann Coefficients	182
Appendix D. Total Scattering Experimental Set-Up.....	188
Appendix E. Co ₂ P Film Assembly GISAXS.....	189
Appendix F. EXAFS Experimental Set Up	193
Appendix G. Trioctylphosphine Oxide Structural Parameters.....	194
Appendix H. Photocatalysis of CoO Nanoparticles	199
Appendix I. Publications	204
Bibliography	209

LIST OF TABLES

Table 2.1. Surfactant amounts for synthesis of 1 mmol of metal nanoparticles.....	39
Table 2.2. Regression errors and dilution limits for each metal wavelength.	40
Table 2.3. Calculated number of atoms and size of icosahedral clusters ranging from 1-6 shells.....	61
Table 3.1. Types of fuel cells for low and high temperature applications. ¹³⁹	65
Table 3.2. Reflections for cobalt phosphide NRs and Miller indices for the α -Co ₂ P phase.	95
Table 3.3. Atomic positions at the $4c$ site for orthorhombic Co ₂ P in which $a = 5.646$, $b = 3.513$, $c = 6.608$ Å. The $4c$ site occupies the special symmetric positions of $\pm(u, 0.25, v ; 0.5-u, 0.25, v+0.5)$	95
Table 3.4. EXAFS fitting parameters for Co-P and Co-Co nearest neighbors using the Co ₂ P crystal structure. The same amplitude scaling (0.314) and ΔE_0 (-1.178 eV for Co-P, Co-Co and -4.792 eV for Co-O) parameters were used for each type of bond.	98
Table 3.5. Paths for undistorted bulk orthorhombic Co ₂ P.	98
Table 3.6. For orthorhombic Co ₂ P in which $b' = 0.99b$, the single scattering neighboring pathways are summarized below.....	99
Table 4.1. Lattice parameters and volume of VO ₂ monoclinic and tetragonal phases....	112
Table 4.2. V-O and V-V distances for VO ₂ monoclinic and tetragonal phases.....	112
Table 4.3. EXAFS data collection k weighting and time at the V K-edge at 5463.76 eV for a total of 534 points.	121
Table 4.4. EXAFS data collection k weighting and time at the W L _{III} -edge at 10207.00 eV for a total of 415 points.	121
Table 4.5. XANES data collection k weighting and time at the V K-edge at 5463.76 eV for a total of 337 points.	121
Table 4.6. Voigt fitting parameters for (011) peaks in Figure 4.14a.	142
Table 4.7. Gaussian and Lorentzian fitting components for (011) peaks in Figure 4.14a.	142

Table 4.8. Linear regression ($f(x) = a + bx$) for optical transition temperature depression rate of W-doped VO ₂ samples.....	144
Table 4.9. EXAFS fitting parameters for V-O and V-V distances below the transition temperature for W-doped VO ₂	149
Table 4.10. EXAFS fitting parameters for V K-edge above the transition temperature..	150
Table 4.11. Reduced χ^2 and R-factor for EXAFS fitting below and above the transition temperature for k -range of 2.7 to 12 Å ⁻¹	151
Table 4.12. Undoped VO ₂ temperatures for each scan in transmission mode. The “Start” and “End” values are the temperature at the beginning and end of the XANES scan, respectively.	153
Table 4.13. EXAFS fitting parameters for V-O and V-V distances below the transition temperature for Mo-, Cr-, and Fe-doped VO ₂	159
Table 5.1. Refinement parameters for trioctylphosphine oxide.	169

LIST OF ILLUSTRATIONS

Figure 1.1. Cartoons of (left) nucleation and growth plot from LaMer and Dinegar and (right) solution based thermal decomposition synthesis set-up (adapted from Murray <i>et al.</i>). ¹³	6
Figure 1.2. Increasing organic surfactant concentrations (oleylamine and trioctylphosphine) decrease the resulting size of Ni NPs.	8
Figure 1.3. Diagram of the paths of the electron beam before (blue) and after (gray) its interaction with matter (black) in TEM. AES = Auger electron spectroscopy; EDXS = Energy dispersive X-ray spectroscopy; WDS = wavelength dispersive spectroscopy; EPMA = electron probe microanalyzer; EELS = electron energy loss spectroscopy; ESI = energy spectroscopy imaging; STEM = scanning tunneling electron microscopy; SAED = selected area electron diffraction; CBED = convergent beam electron diffraction.	11
Figure 1.4. Bragg diffraction from a periodic crystal with an X-ray source with wavelength λ , incident angle θ , and d_{hkl} is the distance between planes.	13
Figure 1.5. Scattering vector, q , is the difference between the incident wavevector k_i and the exit wavevector k_f	14
Figure 1.6. Cartoon diagram of incident and scattering angles from a sample (adapted from Renaud <i>et al.</i>). ³⁶	17
Figure 1.7. Four possible interaction of incident X-ray beam with particle and substrate (adapted from Zhang Jiang from APS). ³⁷	17
Figure 1.8. (a) Calculated PDFs for nickel (Ni), palladium (Pd), platinum (Pt), iron (Fe), cobalt (Co), and (b) nickel-palladium alloys.	21
Figure 1.9. A map of synchrotron radiation facilities and their names (adapted from www.light2015.org).	22
Figure 1.10. Schematic of an incident X-ray beam (black arrow) scattered by a sample in a capillary tube and detected on a 2D detector.	22
Figure 1.11. Schematic of an atom's energy potential and affiliated absorption energy spectrum. ⁴⁷	25
Figure 1.12. Illustrative denotations of the XANES and EXAFS regions.	26

Figure 1.13. Nomenclature for X-ray absorption transitions. ⁴⁶	27
Figure 1.14 The cartoon depicts an impinging X-ray converting a core-level electron (pink) into a photoelectron without (top) or with (below) its neighbors (blue) at a center-to-center distance R away.	28
Figure 1.15. Schematic X-ray path of a typical EXAFS experiment. ⁴⁷	29
Figure 1.16. Example of the Hanning and Kaiser-Bessel windows used for forward Fourier transform of the EXAFS equation (adapted from S. Calvin, 2013). ⁵⁵ The y-axis is normalized to unity and is representative of any k -weighted $\chi(k)$	30
Figure 1.17. k -weighted EXAFS equations for comparison of different types of neighbors as well as their degeneracies and distances (modified from Russell and Rose). ⁵⁷	32
Figure 2.1. Transmission electron micrograph of superlattice assembly of Ni 17.7 nm nanoparticles at the micrometer length scale. The insets show the electron diffraction pattern (left) and Fourier transform (right) of the superlattice.	50
Figure 2.2. Bilayer superlattice of Ni 5 nm NPs.....	51
Figure 2.3. TEM image of Pd 5 nm.	52
Figure 2.4. TEM image of PdNi NPs.	52
Figure 2.5. (a) Structural characterization of size controlled Ni nanoparticles. Pair distribution functions for the three samples, as determined by Fourier transformation of high energy X-ray scattering data. The blue points represent the data, and the red lines are fits of <i>fcc</i> type models. The residuals of the fits are shown as black lines. (b) TEM images of nickel nanoparticles, note the formation of well-defined superlattices, which indicates uniformity. The scale bars correspond to 20 nm.....	53
Figure 2.6. Small-angle X-ray scattering for three sizes of Ni nanoparticles.....	54
Figure 2.7. Small-angle X-ray patterns of Ni-Pd alloys with fits from IRENA ¹³⁶	55
Figure 2.8. (a) Comparison of pair distribution functions of Pd nanoparticles and a representative bulk metallic glass, Fe ₇₆ MoCuB ₁₅ . Comparison of the pair distribution functions after correction for an overall scale factor. (b) Comparison of the pair distribution functions after scaling for the different metallic radii present in each sample.....	56
Figure 2.9. (a) The ubiquity of the disordered structure in the Ni _{1-x} Pd _x solid solution series shown in pair distribution functions of the solid solutions. The red lines show fits to the high-r region of the PDF of a Gaussian damped single-mode sine function	

as described in the text. (b) Comparison of the pair distribution functions after scaling by the different metallic radii in each sample.	57
Figure 2.10. (a) Scaling of PDFs of synthesized NPs and bulk metallic glasses and evidence for a surface contribution in larger Ni particles. Linear dependence of the density wave fluctuations in NPs and BMGs on the average metallic radii. Data points were extracted using the fits shown in Figure 2.9a and from Ma <i>et al.</i> (B) Residuals from the fits of an <i>fcc</i> model to the data for larger Ni particles compared to the data for the 5 nm particles. Red lines show fits using a damped sine wave function as above.	58
Figure 2.11. (a) PDFs of icosahedral models: Green curves are all PDFs from the 309-atom icosahedral model shown in the inset. In the top curve the PDF was calculated with an unrealistically small ADP of 0.001 Å ² . A more reasonable value for the ADP in the absence of static disorder is 0.01 Å ² , which is shown in the second curve from the top. The bottom green curve is the same model calculated with an ADP of 0.1 Å ² , which implies a considerable non-thermal distribution of atomic positions around the average site. The black curves are fits of a damped single-mode sine wave to the icosahedral PDFs. The underlying blue curve at the bottom is the measured PDF from the 5 nm Ni nanoparticles. In this case, the single-mode sine wave is the best-fit PDF of the same icosahedral model where the only tunable parameters for refinement were a stretching parameter that allows the cluster to increase and decrease uniformly in diameter, a scale factor and a single ADP parameter applied to all the atoms, plus a PDFgui “delta2” parameter that sharpens the PDF peaks in the low-r region. (b) High-resolution TEM images of 5 nm (top) and 17.7 nm (bottom) Ni nanoparticles show lattice fringes indicating existence of twinning and local ordering within the nanostructures.....	59
Figure 2.12. Calculated G(r) for icosahedral increasing in the number of shells, thus increasing in size (blue). The curves of calculated PDFs of icosahedral clusters are overlaid with experimental total scattering data for Ni 5 nm nanoparticles (green).	60
Figure 3.1. Fuel cell stack diagram depicting half-reactions at the anode and cathode with ion pathways. ¹³⁹	66
Figure 3.2. Possible oxygen reduction pathways on platinum. ¹⁴⁰	66
Figure 3.3. Ideal potential for hydrogen-oxygen fuel cells for a range of temperatures. ¹³⁹	68
Figure 3.4. Cobalt-phosphide and cobalt-cobalt bonds (adapted from S. Rundqvist). ¹⁸⁴ .	72

Figure 3.5. Transmission electron microscopy images of synthesized products from increasing millimolar concentrations of oleic acid to trioctylphosphine oxide: (a) 1: 0.25, (b) 3: 0.25, and (c) 9:0.25.....	86
Figure 3.6. TEM images of cobalt phosphide products synthesized with OLAC:TOPO ratios of (a) 0.25:1 and (b) 3:1 molar equivalents of the $\text{Co}(\text{Ac})_2$ precursor.	87
Figure 3.7. Distribution of the dimensions of cobalt phosphide NRs.	87
Figure 3.8. (a), (b) TEM images of aligned cobalt phosphide NRs at different magnifications. (c) High-resolution TEM and (d) electron diffraction of the NRs show growth along $\{020\}$ direction.....	88
Figure 3.9. Closed-packed local ordering of vertically aligned NRs.	89
Figure 3.10. (a) SAXS of NRs, (b) GISAXS of Co_2P film on silicon wafer, and (c) XPS shows the existence of oxidized and zero-valent states of cobalt. The minority metallic peak is denoted The signal for cobalt acetate tetrahydrate precursor (blue) is shown for comparison with the NRs samples (red).....	90
Figure 3.11. Increasing the concentration of the NRs showed a transition from isotropic placement of the particles towards an oriented lamellar alignment.	91
Figure 3.12. (a-e) Assembly of NRs on holey carbon TEM grid at various magnifications show face-to-face alignment of the NRs over a micrometer range.....	92
Figure 3.13. The total X-ray scattering data is shown in black. Simulation of cobalt phosphide NRs (green) confirms particle growth in the $\{020\}$ direction and agrees with the experimental data as compared with a spherical model (pink). Both models were constructed from crystal structures with the contracted b lattice parameter. Dashed black lines have been drawn onto the plot to help guide the eyes in tracing the hkl reflections.....	93
Figure 3.14. Simulated sphere and rod growth along the $\{020\}$ direction with increasing aspect ratio.	94
Figure 3.15. Calculated X-ray diffraction patterns for cobalt phosphide, oxide and metallic phases.....	96
Figure 3.16. (a) Absorption with inset at the Co K-edge and (b) the Fourier transform, $\text{FT}(k^3\chi(k))$, for Co_2P NRs. The data is shown in black, overlaid with the fit in red. ..	97
Figure 3.17. HAADF-STEM image of Co_2P NRs after thermal annealing at 180°C and under ambient pressure. (b) STEM image shows the region selected for electron energy-loss spectrometry mapping. Elemental mapping shows a core of cobalt	

phosphide (c) and (e) surrounded by an amorphous oxide shell (d). The combined elemental map is shown in (f).	100
Figure 3.18. EELS spectrum for Co ₂ P.	101
Figure 3.19. (a) ORR polarization curves of Co ₂ P NRs supported on Ketjan carbon as compared to commercial Pt at 1600 rpm, (b) ORR polarization curves of Co ₂ P NRs over a range of rotation speeds. Polarization measurements were performed in an O ₂ saturated 0.1M KOH solution. (c) Koutecky-Levich plots of Co ₂ P catalysts and (d) chronoamperometric response of Co ₂ P NR catalyst as compared to commercial Pt at -0.3 V.	102
Figure 3.20. Co ₂ P NRs after ligand exchange with isothiocyanate.	103
Figure 3.21. Intensity of reflected beam decreases as the temperature increased from 22°C to 147°C (increasing saturation). The first order reflection region decreases and broadens, reflecting greater disorder.	104
Figure 4.1. Resistivity hysteresis of VO ₂ as reported by F. J. Morin. ²¹⁰	110
Figure 4.2. Vanadium-oxygen phase diagram with VO ₂ highlighted in yellow (adapted from Wriedt). ²²⁰	111
Figure 4.3. Metal oxide materials with metal-insulator transitions (adapted from Yang, Ko, and Ramanathan). ¹⁹⁴	113
Figure 4.4. The three major phases of interest for VO ₂ (tetragonal, M1, and M2) are projected onto the <i>b</i> or <i>b'</i> axes for comparison. The oxygen atoms are depicted in red, fuschia or green, and the vanadium atoms are in blue or light blue. The basis vectors for M1 and M2 can be written in relation to the tetragonal phase as follows. $abcMx = TabcRin$ which $TM1 = 00 - 2 - 102011$ and $TM2 = 020002100$	114
Figure 4.5. The three major phases of interest for VO ₂ (tetragonal, M1, and M2) shown with the oxygen octahedral cages (top) as well as with V-V pairs highlighted in black solid and dashed lines (bottom). In contrast to Figure 4.4 which show the different atomic sites for oxygen atoms, all oxygen atoms here are represented in red.	115
Figure 4.6. Dimerization of V-V bonds along the <i>c</i> axis of the tetragonal phase (adapted from Goodenough). ¹⁹⁸	116
Figure 4.7. Band diagrams of V-O hybridization for the monoclinic (bottom) and tetragonal phases (top). The blue shading schematically represents the band occupancy.	117

Figure 4.8. Density of states for monoclinic and tetragonal phases of VO ₂ (adapted from Tao <i>et al.</i>). ²³⁶	118
Figure 4.9. <i>In-situ</i> powder diffraction of VO _x nanocrystals during annealing under 1 mTorr oxygen atmosphere. There is significant line width narrowing as the particles sinter into VO ₂ starting at 500°C.	136
Figure 4.10. Temperature profile of VO _x annealing cycle under 1 mTorr (black) and under ambient pressure (red) over 80 minutes.	137
Figure 4.11. The powder diffraction patterns of VO ₂ at 500°C (black) is maintained after 20 minutes (dashed blue line). There are minority peaks that may attributed to the V ₂ O ₅ phase as denoted with an asterisk (*) and plus sign (+) corresponding to the (301) and (112) reflections. However, the dominant (002) peak at $q = 1.25 \text{ \AA}^{-1}$ for V ₂ O ₅ is absent.	138
Figure 4.12. <i>In-situ</i> powder diffraction of VO _x nanocrystals during annealing under ambient pressure. There is significant line width narrowing as the particles sinter into VO ₂ starting at 500°C as well formation of V ₂ O ₅ species.....	139
Figure 4.13. Annealing VO _x nanocrystals in an ambient environment reveals a transformation from V ₂ O ₃ to VO ₂ with a coexistence of the two phases 50 minutes at 500°C. The material subsequently transforms to VO ₂ 10 minutes (60 minutes total) still at 500°C. There are minority peaks that may be attributed to V ₂ O ₅ as denoted with an asterisk (*) and plus sign (+).	140
Figure 4.14. (a) X-ray diffraction patterns with Voigt peak fits and (b) the (011) peak centers as a function of doping concentration (0%, 0.2%, 0.3%, 0.7%, and 1.4%) in W-doped VO ₂ thin films.	141
Figure 4.15. The percent transmittance in each VO ₂ thin film on quartz substrate decreases upon heating (solid) and increases upon cooling (dashed).	143
Figure 4.16. First derivative of sigmoid fit as a function of temperature.	143
Figure 4.17. Optical transition temperature for W-doped VO ₂ as a function of W atomic percent, which is dependent upon heating (solid) and cooling (dashed).	144
Figure 4.18. (a) Full absorption and (b) XANES spectra of undoped, 0.2%, 0.3%, 0.7%, and 1.4% W-doped VO ₂ thin films.....	145
Figure 4.19. X-ray normalized absorption, k^3 -weighted $\chi(k)$ and its Fourier transforms for undoped, 0.2%, 0.3%, 0.7%, and 1.4% W-doped VO ₂ thin films.	146

Figure 4.20. Differences in the integrated area in the pre-edge peak for the VO ₂ samples below and above the MIT temperature.	147
Figure 4.21 (a), (b) Fourier transform of the k^3 -weighted EXAFS equation shows threshold of W concentration in monoclinic phase at 0.7%. The splitting of the peak between 1 and 2 Å is lost for the sample with 0.7% W. The collapse of this peak indicates a structural change towards a more symmetric phase. (c), (d) The k^3 -weighted EXAFS equation and its Fourier transform show a tetragonal phase with one V-O bond peak between 1 and 2 Å as well as peaks at 2.36 and 2.98 Å corresponding to V-V interactions.	148
Figure 4.22. (a) W L _{III} -edge absorption peaks and (b) Fourier transforms of the EXAFS equation for 0.2% W and 1.4% W-doped VO ₂	152
Figure 4.23. The VO ₂ pre-edge peak collected at the vanadium K-edge (top) is background subtracted using a spline fitting between 5462 eV and 5472 eV (middle). (Bottom) The zero-crossing of the first derivative of the pre-edge peak shifts to a higher energy as the sample is cooled.	154
Figure 4.24. (a) The first centroid of 0.2% W-doped VO ₂ absorption pre-edge peak as a function of temperature can be determined from (b) the zero-crossing of its first derivative as a function of energy.	155
Figure 4.25. (a) and (b) Deconvolution of the pre-edge peak for undoped VO ₂ at 79.4°C and 62.1°C . (c) The Gaussian fits are summarized with the ratios of the A1 and A2 areas showing a transition at 65°C. The data was collected by Dr. Mahalingam Balasubramanian in transmission mode as the sample cooled from 79.4 °C. The range of temperature for each scan is listed in Table 4.12.	156
Figure 4.26. A1 and A2 fractional areas are plotted as a function of temperature for 0.2% W-doped VO ₂ . The inflection points of the arctangent fits are located at 65°C.....	157
Figure 4.27. Fourier transforms and EXAFS fits of W-, Mo-, Cr-, and Fe-doped VO ₂ k^3 -weighted $\chi(k)$ below the transition temperature (top) and above the transition temperature (bottom).	158
Figure 4.28. X-ray diffraction of first row transition metal-doped VO ₂ . While 4.1% Co-, 6.6% Ni-, and 5.2% Mn have negligible effects on (011) peak of VO ₂ , 1.2% Cr and 9.6% Fe increase the peak center by $> 0.07 \text{ \AA}^{-1}$	160
Figure 4.29. Optical response of Mo-, Cr-, Fe-doped VO ₂	160
Figure 5.1. Refined ORTEP schematic for monoclinic trioctylphosphine oxide with 50% probability thermal ellipsoids.	165

Figure 5.2. In the 2D projection of trioctylphosphine oxide supercell, the carbon atoms are shown in blue, hydrogen atoms in gray, phosphorus atoms in purple, and oxygen atoms in red. The unit cell is outlined in black solid lines for clarity..... 166

Figure 5.3. (a) Total X-ray scattering (black) is simulated as a function of crystallite size from 2 to 8 nm in diameter (green). The bulk crystal wide-angle diffraction calculation shows the most intense peak at 1.45 \AA^{-1} corresponding to the (1 1 -4) set of Miller planes followed by the characteristic peaks at $q = 0.84, 1.61, 1.79, 1.95 \text{ \AA}^{-1}$ corresponding to the set of (2 0 0), (2 0 8), (1 1 7), (2 0 10) planes, respectively. (b) The Gaussian fits of the peaks for the 2 to 8 nm calculated scattering data has a linear dependence with the inverse of the full-width half-maximum values..... 167

Figure 5.4. FTIR spectroscopy of trioctylphosphine oxide show the characteristic vibrational stretching of the P=O bond at 1146 cm^{-1} , P—C bond at 1465 cm^{-1} , and C—H bonds from the alkyl chains at 2850 and 2919 cm^{-1} 168

Figure 5.5. Raman spectroscopy of trioctylphosphine oxide captures the vibrational modes for P=O, P—C, and C—H stretching at $1145, 1138,$ and $2848/2882 \text{ cm}^{-1}$, respectively. 168

1. Introduction: Synthesis and Characterization of Nanoparticles

1.1 Glossary of Terms

Description	Acronym
Alkaline fuel cells	AFCs
Atomic displacement parameter	ADP
Bulk metallic glass	BMG
Electron energy loss	EELS
Extended X-ray absorption fine structure	EXAFS
Grazing incidence small-angle X-ray scattering	GISAXS
High-angle annular dark field	HAADF
High-resolution transmission electron microscopy	HRTEM
Hydrogen evolution reaction	HER
Inductively coupled plasma spectroscopy	ICP
Metal-insulator transition	MIT
Microwave-assisted synthesis	MAS
Nanoparticles, nanorods	NPs, NRs
Oxygen reduction reaction	ORR
Pair distribution functions	PDF
Polymer electrolyte fuel cells	PEMFCs
Rotating disk electrode	RDE
Scanning electron microscopy	SEM
Scanning transmission electron microscopy	STEM
Small-angle X-ray scattering	SAXS
Transmission electron microscopy	TEM
Wide-angle X-ray scattering	WAXS
X-ray absorption near-edge spectroscopy	XANES
X-ray diffraction	XRD
X-ray photoelectron spectroscopy	XPS

Facilities	Acronym
Advanced Photon Source	APS
Brookhaven National Laboratory	BNL
Center for Functional Nanomaterials	CFN
European Synchrotron Radiation Facility	ESRF
National Center for Electron Microscopy	NCEM

Chemicals	Acronym
1-Octadecene	ODE
Benzyl ether	BE
Cobalt acetate tetrahydrate	Co(Ac) ₂
Nickel acetylacetonate	Ni(acac) ₂
Oleic acid	OLAC
Oleylamine	OLAM
Palladium acetylacetonate	Pd(acac) ₂
Tributylphosphine	TBP
Trioctylphosphine	TOP
Trioctylphosphine oxide	TOPO

1.2 Motivation

Investigations of structure-property relations encompass the study of correlating inherent and emergent properties to both crystallographic and disordered structures. The body of this dissertation will focus on the synthesis, structural characterization, and functional testing of monodispersed nanoparticles (NPs). As a central theme, structural deviations from the bulk in metal, metal phosphide, and metal oxide NPs will be discussed. As systems tend towards

greater entropy, disorder and crystallographic distortions in these systems provide for a lifetime's worth of exploration.

In this introductory section, I will discuss the theory of nucleation and growth of NPs, electron microscopy, Bragg diffraction, grazing incidence and transmission small-angle X-ray scattering (GISAXS, SAXS), total X-ray scattering, pair distribution functions (PDF), Debye function calculations, X-ray absorption fine structure (XAFS), and inductively coupled plasma spectroscopy (ICP).

Chapter 2 is a discussion on long-range atomic packing disorder within Ni, Pd, and Ni_{1-x}Pd_x NPs. As efficient catalysts for numerous reactions, including hydrogenation,¹ cross-coupling,² and CO oxidation,³ these materials are of significant interest to both the homogeneous and heterogeneous catalysis communities. Atomic structure plays an important role in catalytic properties. The elucidation of the NPs icosahedral local atomic packing within a certain size involved the combination of aberration-corrected transmission electron microscopy (TEM), total X-ray scattering, and pair distribution analysis.

Chapter 3 is a discussion on synthesis, characterization, and electrocatalytic testing of cobalt phosphide (Co₂P) nanorods as a less expensive alternative to commercial Pt/C catalysts for the electroreduction of oxygen. This reaction is of

particular interest because it is used in low temperature fuel cells, which convert chemical energy into electrical energy.

Chapter 4 is a discussion on the synthesis, characterization, and optical spectroscopy of doped vanadium dioxide (VO₂) thin films. The solid-state transition of this fascinating correlated material from a monoclinic to tetragonal phase is probed by *in-situ* powder X-ray diffraction, optical spectroscopy, and *in-situ* X-ray absorption fine structure.

Chapter 5 is a discussion on single crystal diffraction of trioctylphosphine oxide, a compound often used for heavy metals removal and particularly as a particle stabilizer in nanomaterials synthesis.

1.3 Synthesis

Michael Faraday's pioneering work on "gold leafs", published in his 1857 "*Bakerian Lecture*", marks an early success in controlled colloidal synthesis.⁴ Since then, at least 8,376¹ publications have been produced reporting colloidal synthesis via thermal decomposition (heat-up and hot injection), polyol sol-gel, solvothermal, hydrothermal, microwave-assisted, and seed-mediated techniques to generate a diverse library of NPs. Synthesis of monodispersed quantum dots

¹ Since 1945 from ISI Web of Science

received wide attention with the work of Murray *et al.* for the hot injection of sulfur, selenium, and tellurium precursors into a solution of cadmium precursor, organic ligands and solvent.⁵ Monodispersed NPs of metal oxides such as Fe₃O₄ have allowed for insight into magnetic assemblies as well as bioimaging and cell ablation treatments against certain types of cancer.⁶ Control over size and shape of metal NPs allow for higher activity and selectivity of heterogeneous catalysis.^{7,8} Recent developments include the scaling up of synthetic techniques for gram-scale production as well as work towards green synthesis.⁹⁻¹¹

LaMer and Dinegar proposed in 1950 that a thermodynamically favorable period of nucleation of precursors precede periods of subsequent growth, ripening, and saturation of colloids.¹² The concentration of precursor as a function of time is shown in Figure 1.1, accompanied by a cartoon of the experimental set-up for production of monodispersed NPs. The adjustable parameters of reaction temperature, heating rate, chemical precursors, organic surfactant concentrations, and solvent volume direct the products' supersaturation concentration, free energy and eventual nanoparticle size. After monomer nucleation reaches a critical concentration at the supersaturation point, the nucleation process digests remaining monomeric species until a critical size is achieved. As demonstrated by Murray *et al.* with the hot injection method for

combining reactants at an elevated temperature (typically 200-300°C), supersaturation is achieved then quickly cooled to quench growth for monodispersed CdSe NPs.¹³ Ostwald ripening may result in a dispersion of sizes, thus control of nucleation and growth processes is key for producing monodispersed NPs. Despite the inherent high surface energy within NPs, the Kirkendall Effect has been reported for spherical metal NPs transforming to hollow shell metal oxides.¹⁴

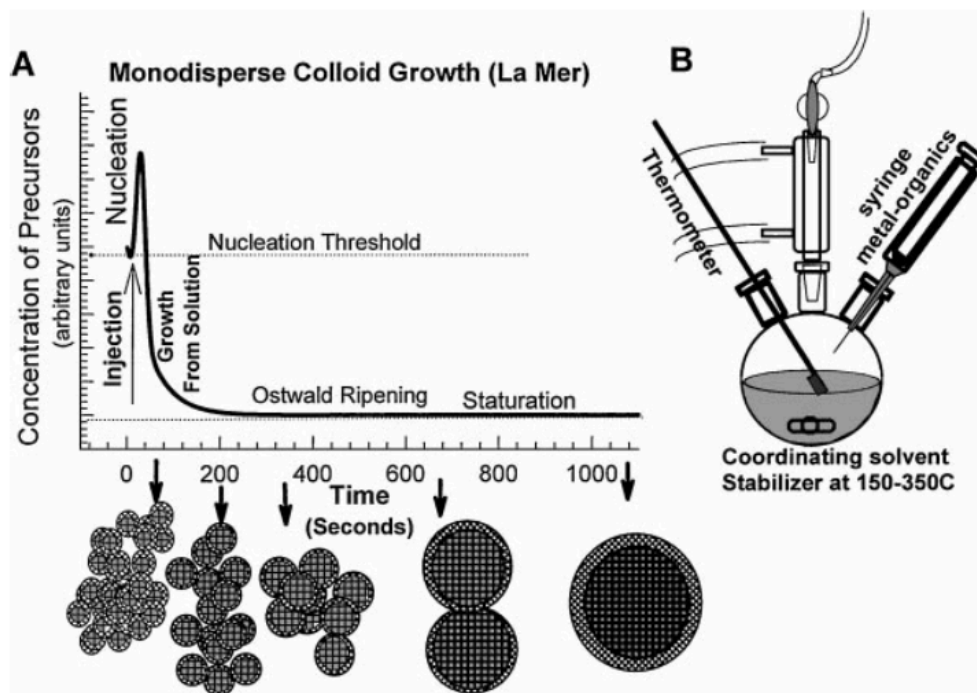


Figure 1.1. Cartoons of (left) nucleation and growth plot from LaMer and Dinegar and (right) solution based thermal decomposition synthesis set-up (adapted from Murray *et al.*).¹³

The synthetic procedure most often used in this dissertation is that of a surfactant-assisted heat-up chemical decomposition of metal salt precursors in high boiling point organic solvent. Additionally, there is a multitude of techniques that involve gaseous precursors in ultra-high vacuum such as atomic layer deposition (ALD) and vapor liquid solid (VLS)—both forms of chemical vapor deposition (CVD)—as well as aqueous chemistry.

The nucleation and growth of the NPs will be discussed to provide insight into factors that influence their resulting atomic and superlattice structure. At the nanoscale, the surface energy is an important factor in the precipitation reaction via both homogeneous nucleation in the solution as well as heterogeneous nucleation from cracks within the glassware surfaces. The surface energy, γ , as it relates to the critical radius, r , is shown in Equation 1.1 in which R is the gas constant, T is the temperature, S is the ratio of free monomers to monomer concentration in equilibrium on a flat surface, and V is the volume of the monomer^{1.11.1}. A complete derivation can be found in *Phase Transformation of Metals and Alloys* by Porter and Easterling covering nucleation and growth theory.¹⁵ While the NPs reported in this work were synthesized at temperatures > 200°C, lower melting point metals such as lead, indium, and bismuth have

interesting chemistry that produce monodispersed NPs up to 500 nm in diameter. An example for Bi is provided in Appendix A.

$$r = \frac{2\gamma V}{RT \ln(S)} \quad (1.1)$$

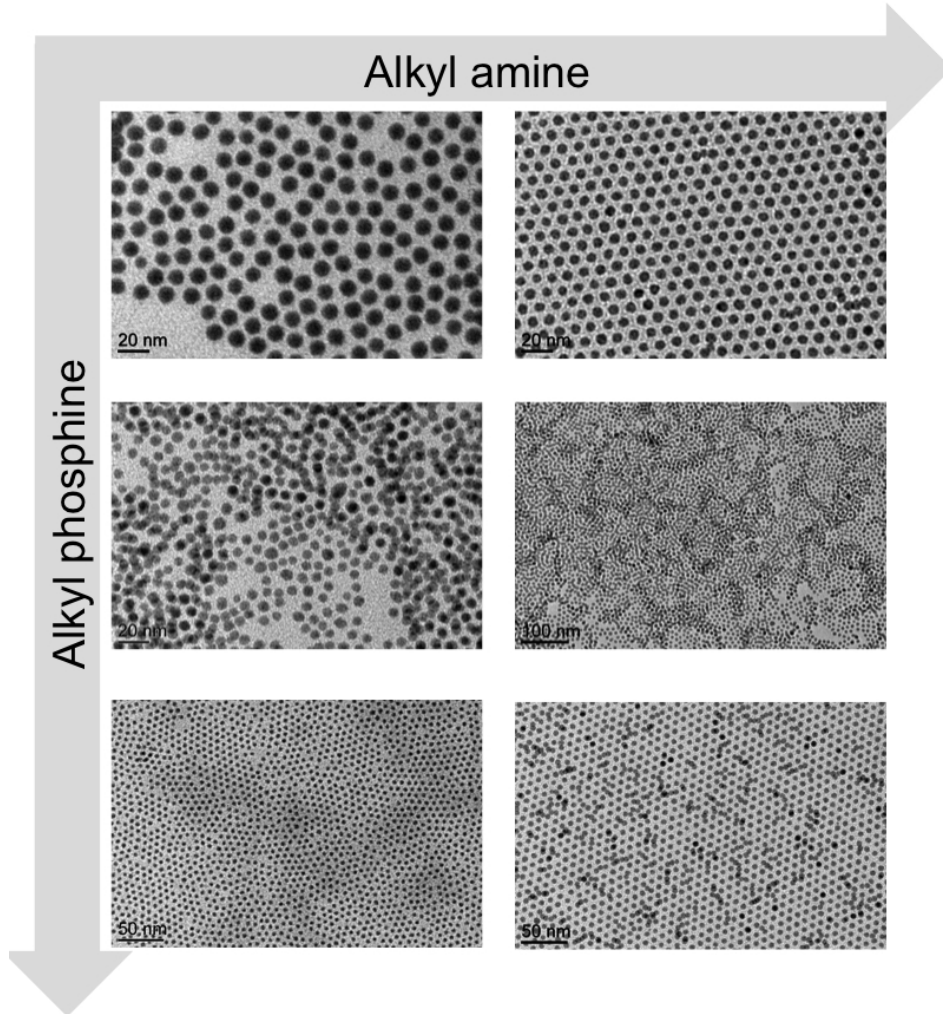


Figure 1.2. Increasing organic surfactant concentrations (oleylamine and trioctylphosphine) decrease the resulting size of Ni NPs.

Microwave-assisted synthesis has been reported to be successful for high-yield production of organic compounds.¹⁶⁻¹⁸ Recently, this method has been translated to produce transition metal,¹⁹⁻²² transition metal oxide,²³ transition metal phosphide,²⁴ and semiconductor metal chalcogenide NPs.²⁵⁻²⁷ The appeal of using microwave irradiation as the dielectric heat source is the potential reduction of reaction time, increase in product yield, and increase in selectivity of morphology.²⁸ A typical surfactant-assisted microwave reaction consists of loading precursors into a vessel with polar solvents. The choice of solvent is determined by its loss tangent ($\tan \delta = \epsilon''/\epsilon'$) in which ϵ'' is the dielectric loss (efficiency of electromagnetic radiation conversion into heat) and ϵ' is the dielectric constant. A loss tangent of 0.1 to 1.3 at reaction temperature is high-absorbing, and thus efficient for converting microwave energy to heat.

Simply changing the heating source from traditional convective heating to microwave irradiation is less successful in terms of yield and monodispersity of products due to heat conduction in the solvent bath. However, this method has scale-up potential with small volume, high throughput batch synthesis for nanoparticle production. An example of direct translation of EuS synthesis is provided in Appendix B. A decrease in reaction time by a factor of 5 is reported

relative to convective heating with a heating mantle, while maintaining nanoparticle monodispersity.

1.4 Electron Microscopy

Probing the size, shape, elemental composition, and crystal structure can be done with electron microscopy using transmission electron microscopy (TEM) and scanning electron microscopy (SEM). With TEM, the de Broglie wavelength of electrons allows for measurement at the atomic length scale where optical microscopy fails due to physical limitations. Equation 1.2 relates the wavelength of an electron to its momentum p and Planck's constant. For an electron traveling at the speed of light, its wavelength is 2.4×10^{-12} m. Current technologies such as the FEI Titan 80-300 provide for access to sub-Ångstrom resolution. The detection of electrons transmitted or scattered by a sample provides a wealth of structural information. The types of interactions are summarized in Figure 1.3.

$$\lambda = \frac{h}{p} = \frac{h}{mv} \quad (1.2)$$

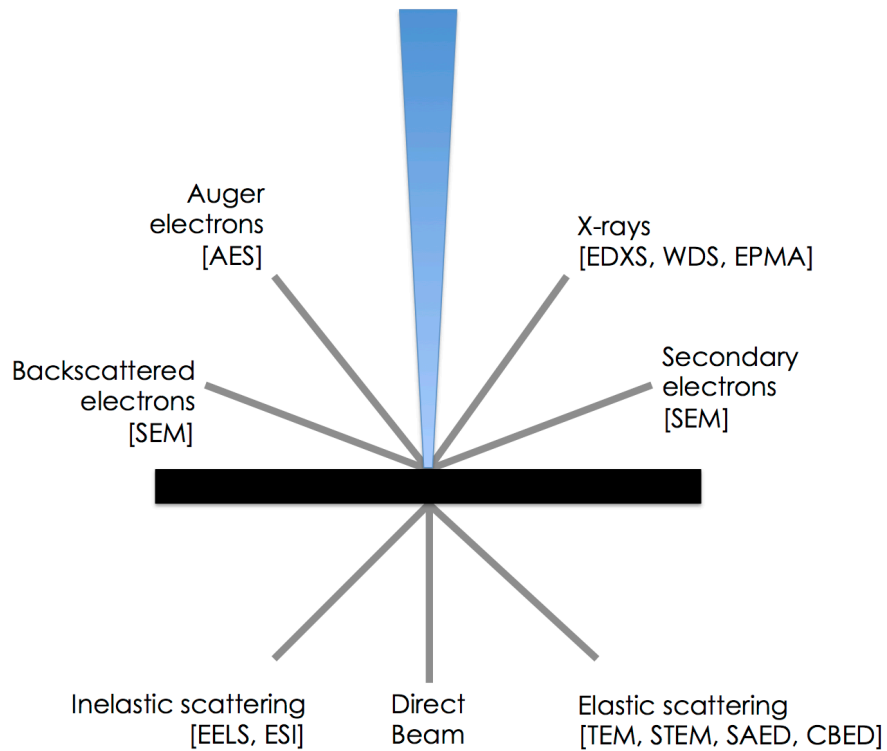


Figure 1.3. Diagram of the paths of the electron beam before (blue) and after (gray) its interaction with matter (black) in TEM. AES = Auger electron spectroscopy; EDXS = Energy dispersive X-ray spectroscopy; WDS = wavelength dispersive spectroscopy; EPMA = electron probe microanalyzer; EELS = electron energy loss spectroscopy; ESI = energy spectroscopy imaging; STEM = scanning tunneling electron microscopy; SAED = selected area electron diffraction; CBED = convergent beam electron diffraction.

Scanning electron microscopy (SEM) utilizes emitted secondary and backscattered electrons from the sample for imaging and elemental analysis. Secondary electrons are generated from inelastic collision and scattering of electrons from the beam with electrons in the sample. Backscattered electrons are generated from elastic collision and scattering of electrons from the beam with electrons or the nuclei from the sample. For in-depth discussion of the theory, capabilities, and limitations of TEM as well as SEM, please refer to the electron microscopy tome by William and Carter.²⁹

1.5 X-ray Scattering: Wide-Angle, Small-Angle, Grazing Incident Small Angle, Total Scattering & Pair Distribution Functions

1.5.1 Wide-Angle X-ray Scattering (WAXS)

The diffraction of X-ray light with matter is elegantly and succinctly summarized by Bragg's Law in Equation 1.3. The wide-angle range in X-ray diffraction is illustrated in Figure 1.4. The periodicity (or lack thereof) of a crystal's planes in real space can be represented in reciprocal space. More broadly, the scattering wavevector q (Equation 1.4), which is independent of the type of X-ray radiation and wavelength, is the difference between the exit and incident wavevectors.

$$n\lambda = 2d \sin(\theta) \quad (1.3)$$

$$q = |\vec{q}| = \frac{2\pi}{d} = \frac{4\pi \sin(\theta)}{\lambda} = |\vec{k}_f - \vec{k}_i| \quad (1.4)$$

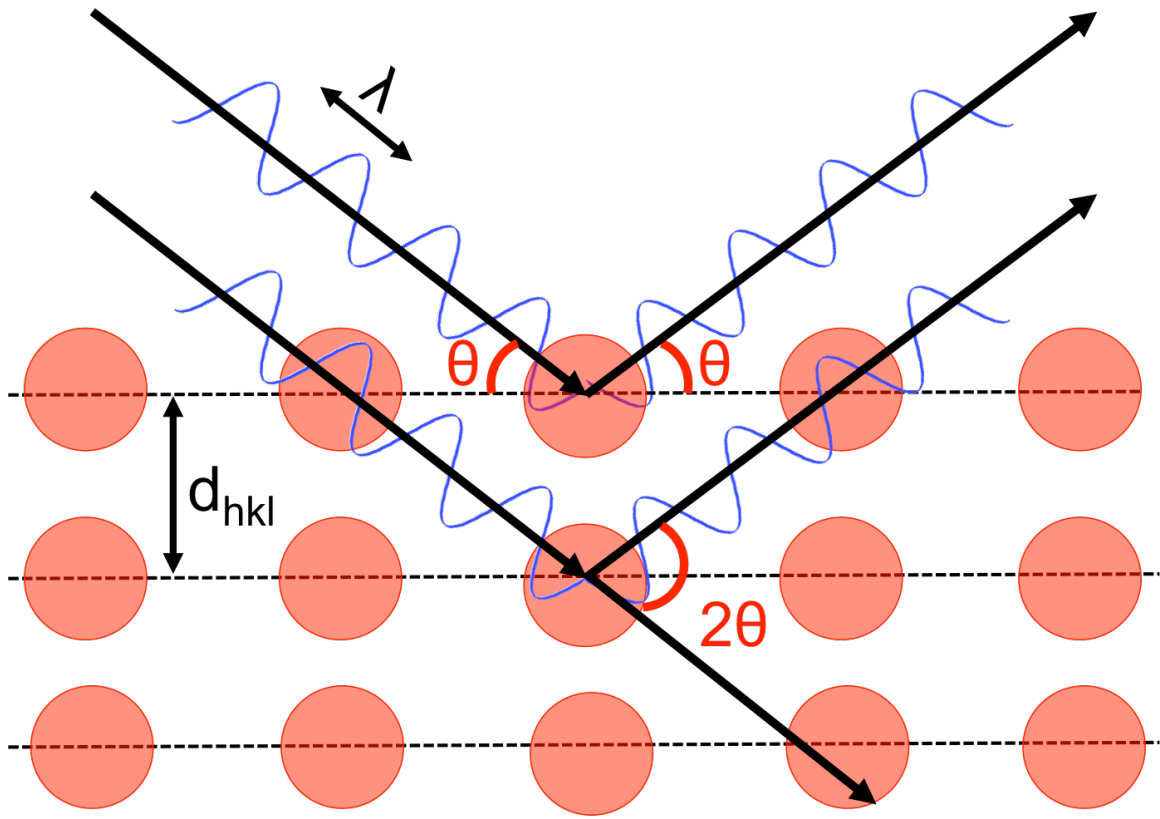


Figure 1.4. Bragg diffraction from a periodic crystal with an X-ray source with wavelength λ , incident angle θ , and d_{hkl} is the distance between planes.

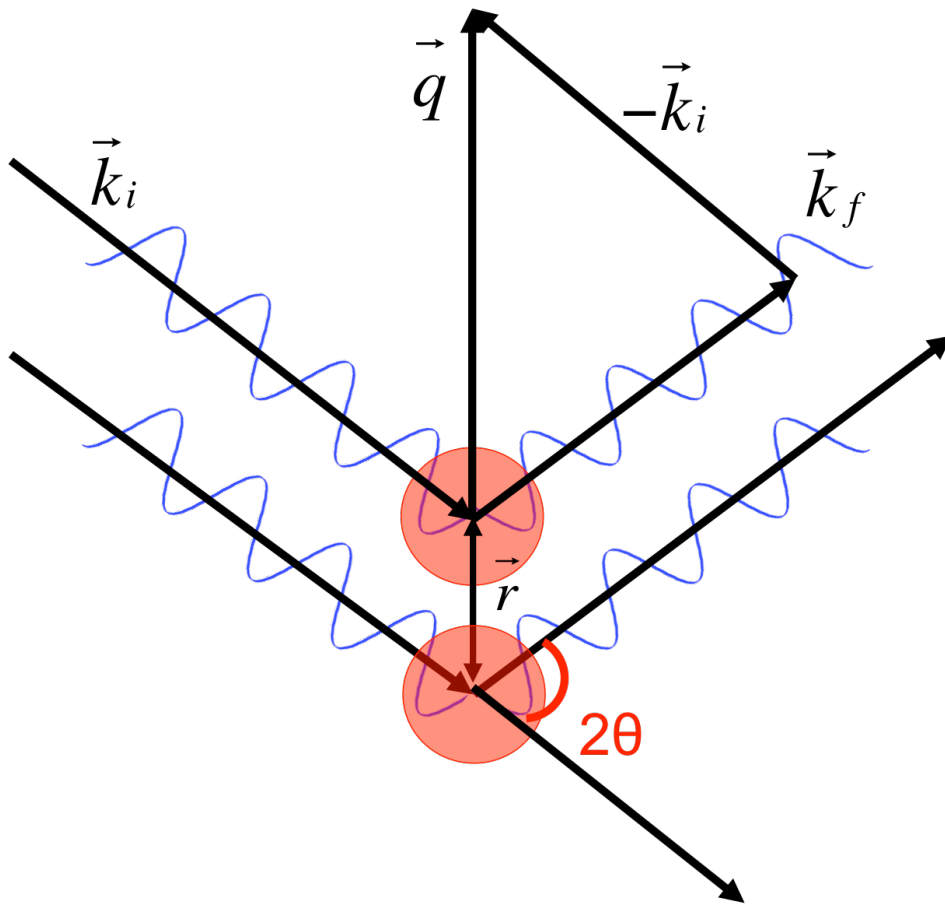


Figure 1.5. Scattering vector, q , is the difference between the incident wavevector k_i and the exit wavevector k_f .

Beyond TEM, average particle size can be determined with data from X-ray diffraction (XRD). Nanoparticles on the order of 1 to 10 nm size do not have as many parallel planes available for sharp diffraction peaks. Therefore, the peaks become broadened. The Scherrer Equation as given in Equation 1.5 relates the

diffraction peak broadening from XRD³⁰ in which β is the diffraction peak width at full-width half-maximum, θ is the angle of diffraction in degrees, λ is the X-ray wavelength in Å, and t is the crystallite size in Å. The 0.9 shape factor has a typical range of 0.9-1.36.³¹ For bimetallic species, lattice constants can be determined using Vegard's Law,³² which states that the relationship between lattice parameter a is directly proportional to the atomic percent of the solute present in the solid solution (Equation 1.6) in which a_1 and a_2 are lattice constants of the pure species and f_1 and f_2 are the fractional weights.

$$t = \frac{0.9\lambda}{\beta \sin \theta} \quad (1.5)$$

$$a = f_1 a_1 + f_2 a_2 \quad (1.6)$$

1.5.2 Transmission and Grazing Incidence Small-Angle X-ray Scattering

The theory of small-angle X-ray scattering (SAXS) is used to measure properties such as particle morphology (size, shape, defects, pore size), interactions, superlattice assembly, microstructure orientation, or macromolecular conformations for hard and soft matter.³³ Transmission SAXS can be used as a tool for determining size distribution of NPs. In contrast to WAXS experimental

set-up, SAXS 2θ range is typically $< 10^\circ$ for a laboratory Cu $K\alpha$ source. For detailed theory of SAXS, please refer to excellent publications by Guinier and Fournet³⁴ and Glatter and Kratky.³³

Grazing incident small-angle X-ray scattering (GISAXS) measures the (dis)ordered assemblies of samples such as nanoparticle assemblies.³⁵ The wavevector, q , can be written as components of incoming and exit angles as defined in Equation (1.9). A cartoon schematic of GISAXS geometry is shown in Figure 1.6. The q range probes structural parameters beyond 1 nm, which is useful for studying interparticle interactions. Additionally, surface thickness and roughness can be ascertained given the grazing incident wavevector. The exiting wavevector can be reflected and/or refracted from the sample and/or substrate. The four combinations shown in Figure 1.7 are summarized in Equation 1.8 in which the components of q are defined in Equation 1.7. The q_\perp and q_\parallel are the perpendicular and parallel components of the wavevector.

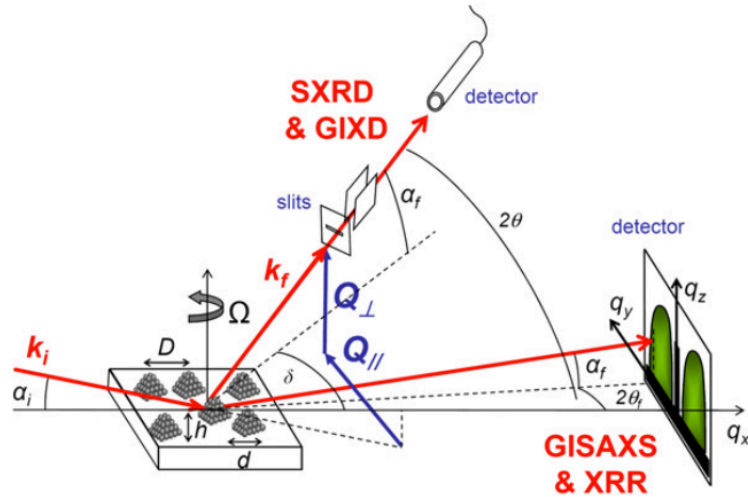


Figure 1.6. Cartoon diagram of incident and scattering angles from a sample (adapted from Renaud *et al.*).³⁶

$$q = \begin{pmatrix} q_x \\ q_x \\ q_z \end{pmatrix} = \frac{2\pi}{\lambda} \begin{pmatrix} \cos \alpha_f \cos 2\theta \cos \alpha_i \\ \cos \alpha_f \sin 2\theta \\ \sin \alpha_f + \sin \alpha_i \end{pmatrix} \quad (1.7)$$

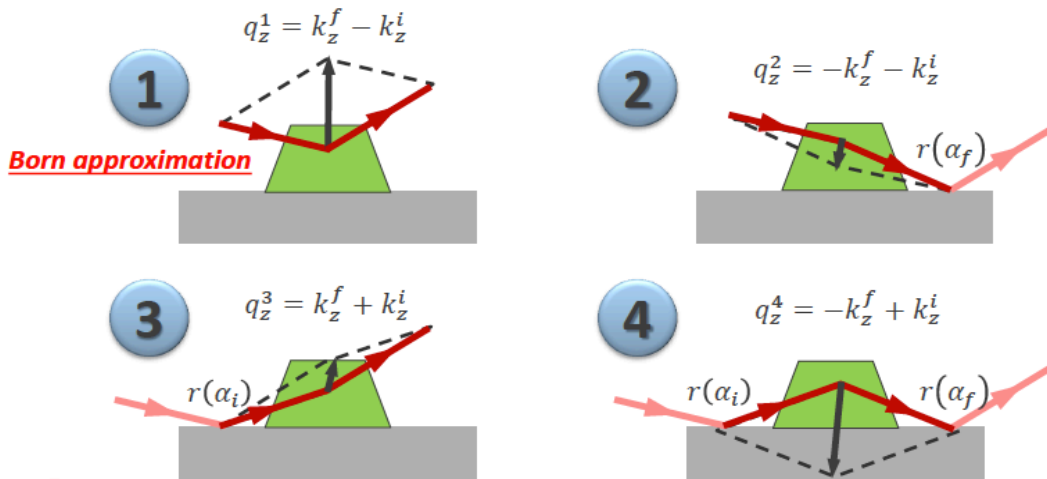


Figure 1.7. Four possible interaction of incident X-ray beam with particle and substrate (adapted from Zhang Jiang from APS).³⁷

$$F(q_{\parallel}, k_z^i k_z^f) = F(q_{\parallel}, q_z^1) + r(\alpha_f)F(q_{\parallel}, q_z^2) + r(\alpha_i)F(q_{\parallel}, q_z^3) + r(\alpha_i)r(\alpha_f)F(q_{\parallel}, q_z^4) \quad (1.8)$$

For theory and experimental development of GISAXS using the distorted wave Born approximation (DWBA), please refer to excellent publications by Renaud *et al.*³⁶ and Lazzari³⁸ as well as helpful resources such as www.gisaxs.de, www.gisaxs.com, and www.bornagainproject.org.

1.5.3 Debye Equation

X-ray scattering simulation can be done using the Debye Equation as noted in Equation 1.9. The calculation equates the observed intensity to the weighted sum of the sinc of pair-wise distances of atom i and j . The Debye Equation also captures exponentially damped intensity as a function of q due to static and dynamic thermal parameters similar to the Scherrer Equation in Equation 1.5. Computationally, execution can be on the order of seconds to minutes on current systems depending on the binning of the pair-wise distances. The atomic form factors f_i and f_j are computed from Equation 1.10 in which a_i , b_i , and c are experimentally determined Cromer-Mann coefficients as tabulated in the Appendix C. Scattering intensity can also be damped by thermal atomic

displacements. The Debye-Waller factor, B , is explicitly expressed in the exponential damping term in which u is the atomic displacement in Å.

$$I = \sum_k w_k \left(\exp \left(- \left(\frac{q}{4\pi} \right)^2 B \right) \sum_{i,j} f_i f_j \frac{\sin(qr_{ij})}{qr_{ij}} \right) \quad (1.9)$$

$$f \left(\frac{q}{4\pi} \right) = \sum_{i=1}^4 \left[a_i \exp \left(-b_i \left(\frac{q}{4\pi} \right)^2 \right) \right] + c \quad (1.10)$$

$$B = 8\pi^2 \langle u^2 \rangle \quad (1.11)$$

1.5.4 Total Scattering and the Pair Distribution Function

The atomic pair distribution function (PDF) analysis method performs a Fourier transform of X-Ray scattering data into real space to solve for the crystal structure of a material. In ordered bulk material, the crystal structure can be determined by analyzing the peaks at specific 2θ values. In the case of NPs, there is greater disorder and disregistry in the crystal structure due to the greater percentage of surface atoms in the sample. The PDF can solve for local ordering of atoms in NPs from the diffuse scattering and Bragg peaks of the Fourier transformed X-Ray diffraction pattern. The PDF, noted as $G(r)$ in Equation 1.12, is the Fourier transform of the total scattering structure factor function, $S(q)$ in Equation 1.13.

$$G(r) = \frac{2}{\pi} \int_0^{\infty} q(S(q) - 1) \sin(qr) dq \quad (1.12)$$

$$S(q) = 1 + \frac{1}{q} \int_0^{\infty} G(r) \sin(qr) dr \quad (1.13)$$

Bragg diffraction gives information regarding the average structure of the material. The PDF extracts data from the diffuse scattering to give information regarding the local structure in addition to the overall structure from the Bragg diffraction. This is especially useful for nanostructured materials in which the Bragg diffraction pattern is broadened by the small particle size. The Fourier transform of a finite q range introduces termination defects.³⁹ The nearest neighbor peak in $G(r)$ vs. r plots gives information on the local structure. Its peak width and area give information regarding the atomic thermal motions as well as the coordination number, respectively.

Illustrative examples are provided in simulated PDF patterns in Figure 1.8a for bulk *fcc* (Ni, Pd, Pt), *hcp* (Co), and *bcc* (Fe). For the alloy mixtures of Ni and Pd, the PDFs are calculated in Figure 1.8b in which occupancy of Ni or Pd at an atomic site is weighted by the stoichiometry. The nearest neighbor peaks of Ni and Pd have become one broad peak in which either the Ni-Ni or Pd-Pd shoulders are apparent depending on the stoichiometry.

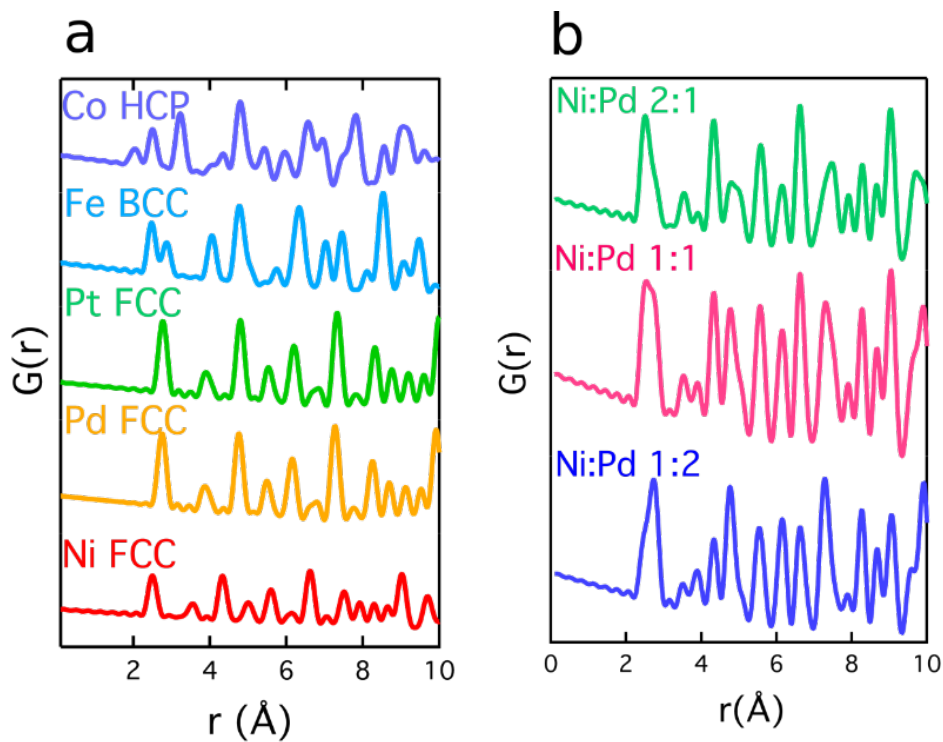


Figure 1.8. (a) Calculated PDFs for nickel (Ni), palladium (Pd), platinum (Pt), iron (Fe), cobalt (Co), and (b) nickel-palladium alloys.

Synchrotron facilities around the world (Figure 1.9) provide access to greater brilliance light source, large q range, and rapid acquisition which allow for total X-ray scattering data collection for PDF analysis. Rapid acquisition can be done using 2D detectors.⁴⁰ A cartoon of a typical scattering experimental set up is shown in Figure 1.10. Photographs of an experimental set-up are provided in Appendix D. Software used for processing collected data from the Advanced Photon Source at Argonne National Laboratory and the European Synchrotron Radiation Facility includes iPDF, PDFgetX2,⁴¹ PDFgetX3,⁴² PDFgui,⁴³ and SrFit.⁴⁴

(in DiffPy-CMI)⁴⁴. Both PDFgui and SrFit are robust for PDF calculations. PDFgui has a user-friendly interface while SrFit is suited for batch processing of large data sets in a Python environment. Recent developments of xPDFsuite improves upon current packages to provide a GUI interface with high throughput of multiple data sets.



Figure 1.9. A map of synchrotron radiation facilities and their names (adapted from www.light2015.org).

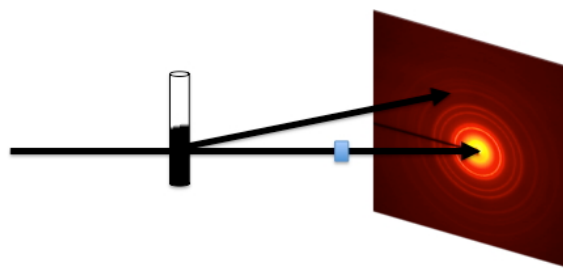


Figure 1.10. Schematic of an incident X-ray beam (black arrow) scattered by a sample in a capillary tube and detected on a 2D detector.

1.6 X-ray Absorption Fine Structure

X-Ray absorption spectroscopy (XAFS) involves the use of synchrotron radiation to excite a core electron from the K, L, or M shell. Analysis of absorption (near-edge and extended fine structure) by the ejected photoelectron and the backscattering signal caused by interactions with neighboring atoms can reveal important information regarding the identity of its neighbors as well as the interatomic distances. The momentum of the photoelectron is related to its kinetic energy (Equations 1.14 and 1.15) to give the relationship in Equation 1.16 in which \hbar is Planck's constant divided by 2π and E_0 is the amount of energy required to remove the photoelectron from the absorbing atom. The wavevector k is related to its momentum. The intensity of the Extended X-Ray Absorption Fine Structure (EXAFS) is dependent on a number of factors such as the phase ($\phi(k)$) and amplitude ($F_j(k)$) of the spherical wave function, dampening due to amplification reduction effects, S_0 , change in half-path length, ΔR (Equation 1.17), finite lifetime of the excited state ($e^{-\frac{2R_j}{\lambda(k)}}$), and disorder due to thermal and static motions ($e^{-2k^2\sigma_j^2}$) (Equation 1.18). The extended X-ray absorption fine structure is defined for each type of scatterer in Equation 1.19 and their sum is the overall EXAFS equation is in Equation 1.20. The incoming X-ray and its

conversion to photoelectrons are depicted in Figure 1.14 with defined the half-path lengths.

$$p = \hbar k \quad (1.14)$$

$$KE = \frac{p^2}{2m_e} = E - E_0 \quad (1.15)$$

$$k = \sqrt{\frac{2m_e}{\hbar^2} (E - E_0)} \quad (1.16)$$

$$R_j = R_0 + \Delta R \quad (1.17)$$

$$A_j(k) = e^{-2k^2\sigma_j^2} e^{-\frac{2R_j}{\lambda(k)}} \quad (1.18)$$

$$\chi_j(k) = A_j(k) \frac{N_j F_j(k) S_0^2}{k R_j^2} \sin(2kR_j + \phi_j(k)) \quad (1.19)$$

$$\chi(k) = \sum_{j=1}^n \chi_j(k) \quad (1.20)$$

There are two areas of interest in an absorption spectrum obtained for fine structure analysis: the near-edge (XANES) and extended (EXAFS) regions. These regions are shown schematically in Figure 1.11. The absorption edge (E_0) in a spectrum is defined as “the energy at which there is a sharp rise (discontinuity) in the (linear) absorption coefficient of X-rays by an element.”⁴⁵ Up to 50 eV beyond the edge is the XANES region. Beyond the XANES range is the EXAFS

region (Figure 1.12). The absorption nomenclature is shown in Figure 1.13 (adapted from Feidman and Mayer).⁴⁶

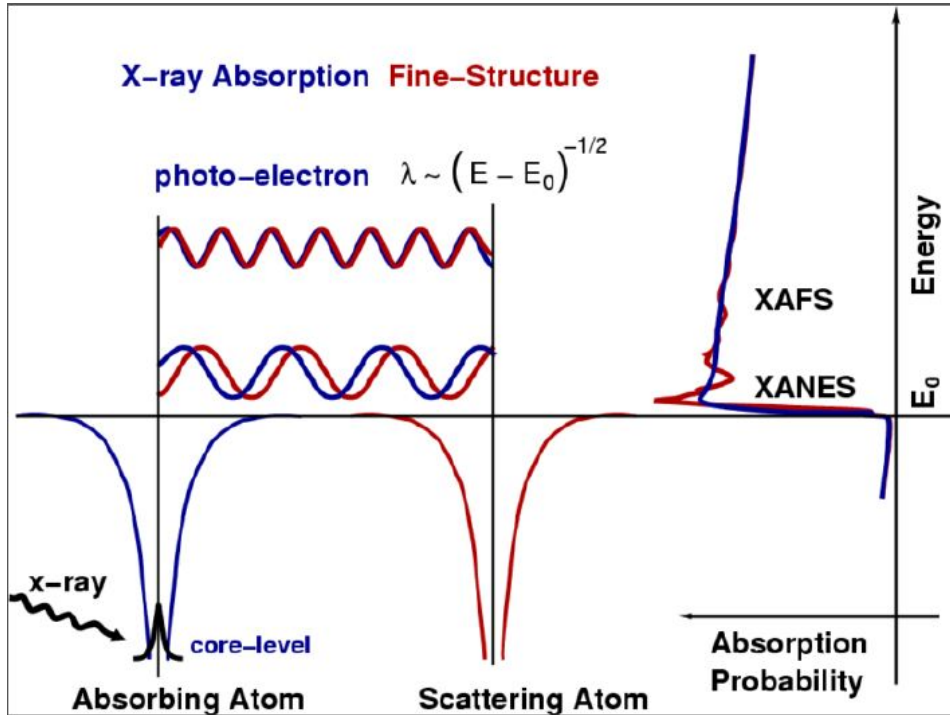


Figure 1.11. Schematic of an atom's energy potential and affiliated absorption energy spectrum.⁴⁷

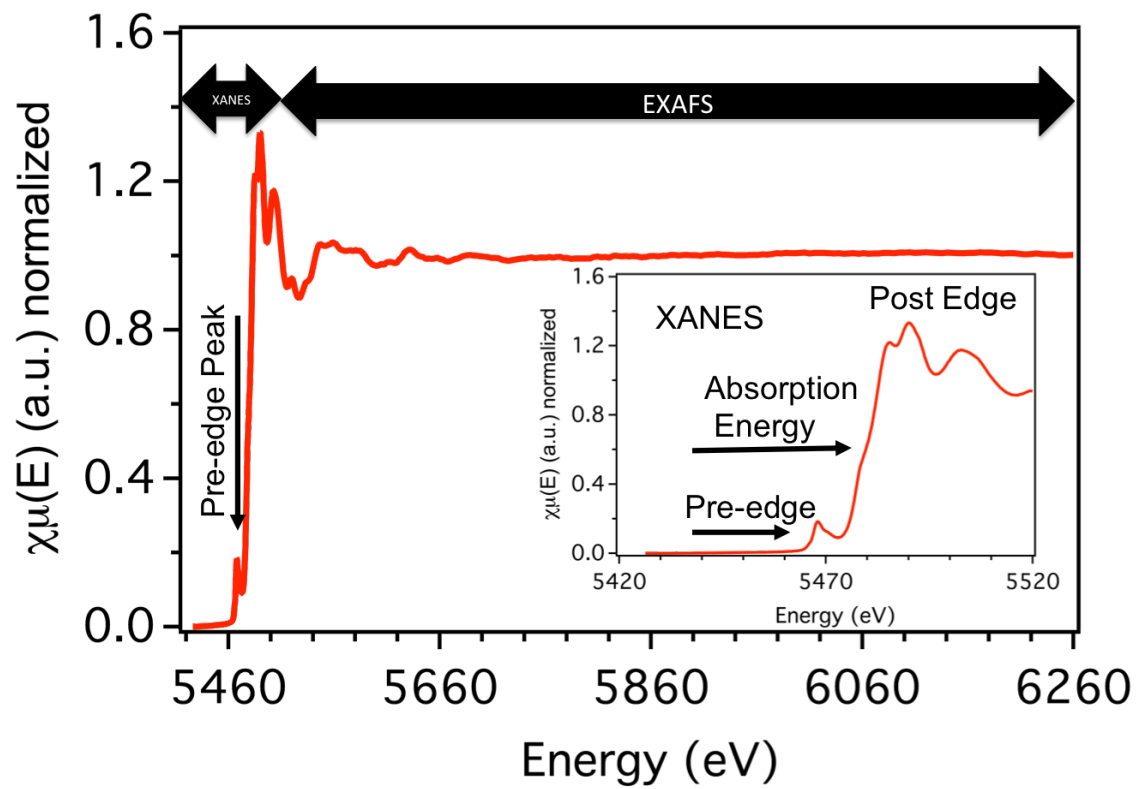


Figure 1.12. Illustrative denotations of the XANES and EXAFS regions.

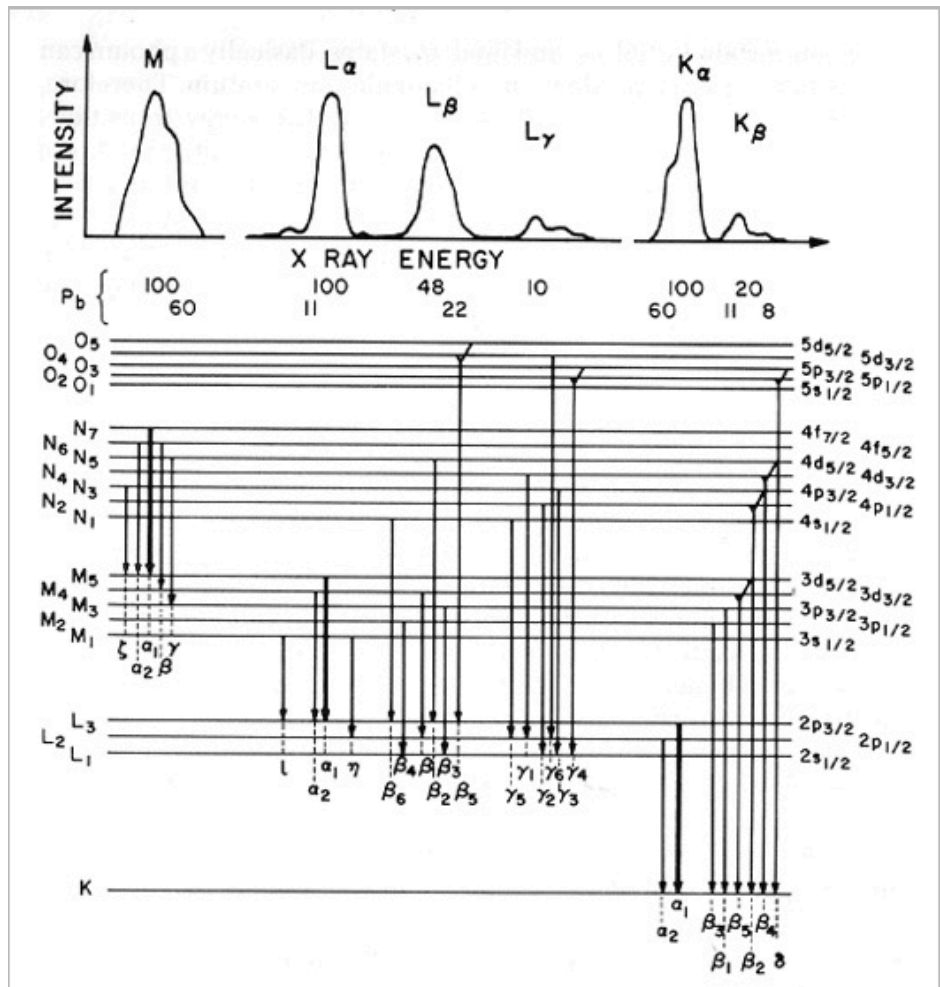


Figure 1.13. Nomenclature for X-ray absorption transitions.⁴⁶

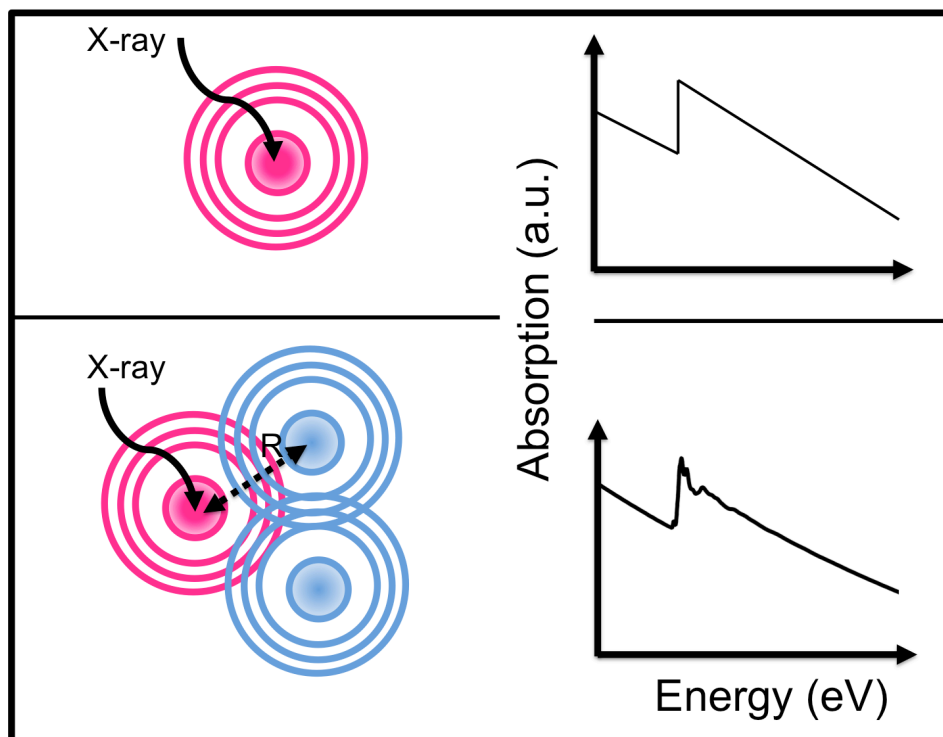


Figure 1.14 The cartoon depicts an impinging X-ray converting a core-level electron (pink) into a photoelectron without (top) or with (below) its neighbors (blue) at a center-to-center distance R away.

The EXAFS measurements may be performed in transmission or fluorescence mode using a typical set up as shown in Figure 1.15. An incoming X-ray synchrotron source is tuned to the desired energy using a variety of Si crystal hkl planes with high-order harmonic rejection. The monochromatic X-rays excite K, L, and M-level electrons and the absorption is detected in fluorescence mode at 45° or in transmission. The intensity values are I_f/I_0 or $I_t=I_0e^{(-\mu t)}$ (Beer-Lambert

Law)⁴⁸⁻⁵⁰ in which I_f is the fluorescence signal, I_t is the transmission signal, I_0 is the corrected incident photon intensity, μ is the product of the material's density (g/cm^3) and its mass absorption coefficient $\mu/\rho(E)$ (cm^2/g) cross-section, and t is the thickness of the sample in cm^{-1} . The absorption intensity will be subsequently normalized so that the step size is unity.

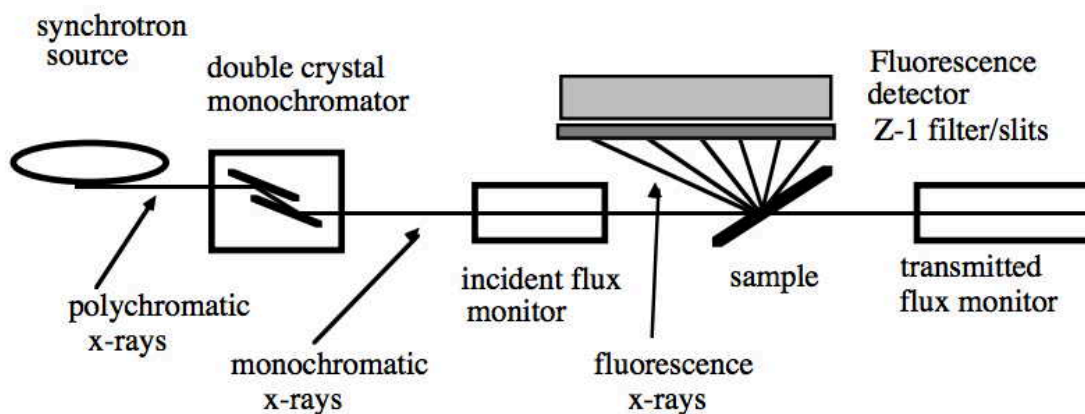


Figure 1.15. Schematic X-ray path of a typical EXAFS experiment.⁴⁷

The Fourier transform of the normalized absorption data from ATHENA⁵¹ was input into ARTEMIS⁵¹ for fitting in which path lengths were built starting from ATOMS.⁵² The modeling procedure involves iterative cycles of simultaneous fitting of correlated key parameters such as the half-path length, reduction amplitude, degeneracy, Debye-Waller factor, and E_0 . To calculate the Fourier transform of the EXAFS equation, a Hann/Hanning window was used with a sill (dk) of 1 \AA^{-1} . Another window option is the Kaiser-Bessel, which is schematically

shown in Figure 1.16. These windows are important for smoothly reducing all paths to zero by being small in intensity at the endpoints of the k range and smooth within the range. For more in-depth discussions of Fourier transform windows, please refer to texts by Robert Ramirez⁵³ and William Hartmann.⁵⁴

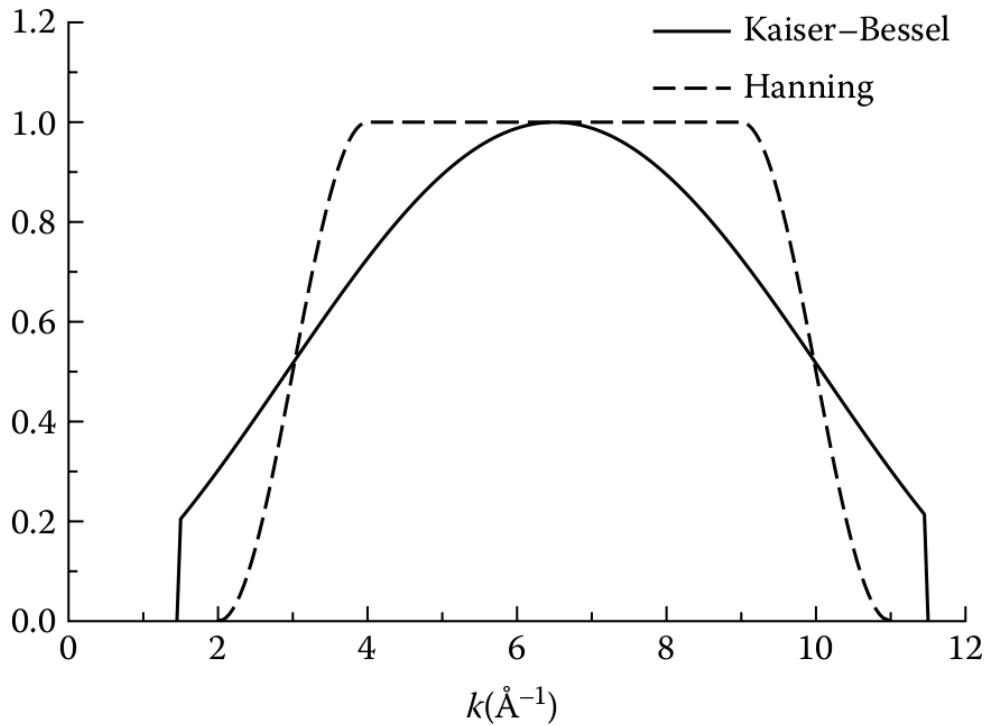


Figure 1.16. Example of the Hanning and Kaiser-Bessel windows used for forward Fourier transform of the EXAFS equation (adapted from S. Calvin, 2013).⁵⁵ The y-axis is normalized to unity and is representative of any k -weighted $\chi(k)$.

Metrics used for determining “goodness of fit” or quantity of mismatch include the reduced χ^2 (Equation 1.21) and the Hamilton R factor⁵⁶ (Equation 1.22). For the reduced χ^2 , the average squared difference between data and fit is weighed by the ratio of independent points ($N_{independent}$) to the degrees of freedom (ν) and the number of measured points (N). The R factor is the sum of the squared differences between data and fit over all measured points normalized by the sum of the square of the measured points over all measured points.

$$\chi^2 = \frac{N_{independent}}{\nu N} \sum_{i=1}^N \frac{(data_i - fit_i)^2}{\varepsilon_i^2} \quad (1.21)$$

$$R = \frac{\sum_{i=1}^N (data_i - fit_i)^2}{\sum_{i=1}^N (data_i)^2} \quad (1.22)$$

Figure 1.17 is adapted from Russell and Rose to provide illustrative examples for comparing photoelectron interaction with different types of neighbors as well as their degeneracies and distances. According to definition of k (Equation 1.16), a lighter element will have a smaller wavevector due to its smaller absorption edge energy. Therefore, the backscattering, $F_j(k)$, from an atom with lower Z will decrease in amplitude more quickly than from that of a heavier atom. The number of neighbors of a certain type of element would factor into the EXAFS equation via the N_j term. The decreasing the amplitude decays more rapidly with

fewer neighbors. Different bond lengths would lead to a phase difference— $\sin(2kR_j + \varphi_j(k))$. Shorter half-path lengths would result in decreased frequency.

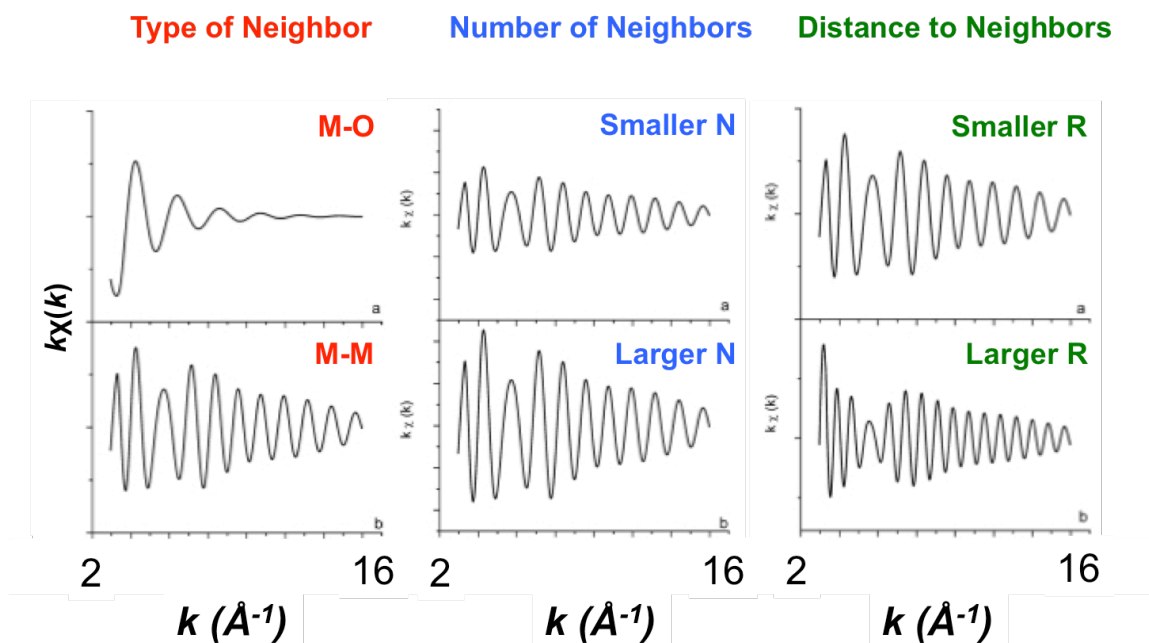


Figure 1.17. k -weighted EXAFS equations for comparison of different types of neighbors as well as their degeneracies and distances (modified from Russell and Rose).⁵⁷

For more information on X-ray absorption fine structure, please refer to excellent publications by Grant Bunker,⁵⁸ Scott Calvin,⁵⁵ Shelly Kelly,⁵⁹ Matt Newville,⁴⁷ Bruce Ravel,⁶⁰ and John Rehr.⁶¹

1.7 Inductively Coupled Plasma-Optical Emission Spectroscopy

Inductively coupled plasma (ICP) spectroscopy is a technique used for quantitative elemental analysis of samples. Coupled with optical emission spectroscopy or mass spectrometry, the quantitative measurements are accurate to parts per billion amounts. ICP is heavily used in agricultural, biological, geological, and chemical fields for accurate measurements and identification of samples.^{62,63} Typically, powders or dried NPs are digested in caustic media such as nitric acid, hydrochloric acid, sulfuric acid, hydrofluoric acid, or various combinations such as aqua regia or piranha solution. The digested parts per million quantities of samples are nebulized and their optical emissions are analyzed. The elementally characteristic emissions are results of relaxation from excited states of the atoms in collision with the radio frequency-induced plasma as well as from excited ions. Concentrations are determined against a regression of calibrated standards containing the same elements of interest. For more in-depth discussions of ICP theory and operations, please refer to the excellent text by Boss and Fredeen.⁶⁴

2. Bulk Metallic Glass-Like Scattering Signal in Small Metallic Nanoparticles

Chapter 2—in part—has been published in *ACS Nano*. V.V.T. Doan-Nguyen, S.A.J. Kimber, D. Pontoni, D. Reifsnnyder Hickey, B.T. Diroll, X. Yang, M. Miglierini, C.B. Murray, S.J.L. Billinge. *ACS Nano* 8 (6), 6163-6170 (2014).

2.1 Introduction

The structure of small metallic nanoparticles has been the subject of extensive research for many years.⁶⁵⁻⁶⁹ Although the boundary is somewhat blurred, such nanostructures have often been separated into clusters on the one hand and colloidal nanoparticles (NPs) on the other. The former tend to be smaller and are often formed in atomic beam experiments^{70,71} whereas the latter are made using approaches such as arrested precipitation from a solvent, and are capped with organic ligands that stabilize them.^{5,10,72-74} Clusters may be separated into perfectly monodisperse samples, and it is meaningful to discuss the solution of their structure on the assumption that it is unique and well-defined. The structures of small metallic clusters have been extensively studied using transmission electron microscopy (TEM) with a prevalence of decahedral and

icosahedral packing motifs.⁷⁵⁻⁷⁷ Furthermore, through seeded or ripening growth mechanisms, larger NPs with the same platonic morphology have also been synthesized and characterized via electron microscopy.⁷⁸⁻⁸⁶

On the other hand colloidal nanoparticles are made in bulk quantities and samples have a range of structures and sizes for a library of technological applications.^{3,87-92} Larger NPs take the structure of the parent material and resemble small chunks of the bulk parent, albeit with different defects.⁹³⁻⁹⁶ However, at very small sizes, their structures may modify qualitatively from the bulk,^{97,98} with a tendency towards structural disorder. Some very stable small NPs form crystals of identical particles and the structure may be refined by crystallographic methods. These are characterized by lower symmetry—even chiral—structures built around decahedral or icosahedral cores similar to those seen in the metallic clusters.⁹⁹⁻¹⁰⁴ Nanoparticles that crystallize are the exception rather than the rule, and it is important to develop methods to study structure of small metallic NPs in general.¹⁰⁵

Improvements in colloidal synthesis methods of metallic nanoparticles have resulted in bulk samples of very small particles that are highly monodisperse.⁵ Concurrently, powerful new methods are emerging, such as the atomic pair distribution function (PDF) approach,¹⁰⁶ for characterizing the structure of small

clusters and nanoparticles. Here we combine these developments in a study with synchrotron based total X-ray scattering PDF methods applied to highly monodisperse Ni, Pd, and Ni_xPd_{1-x} NPs.

We find that, below a certain NP size, the scattering signal and the resulting PDF from these systems changes from that of the bulk close-packed *fcc* structure to an amorphous scattering signal. Interestingly, the amorphous signal is nearly identical to that observed in bulk metallic glasses (BMGs) formed from highly tuned mixes of particular elements.^{107,108} The PDFs of BMGs are very characteristic with broad sinusoidal oscillations extending a significant range up to $r \approx 20 \text{ \AA}$,¹⁰⁹⁻¹¹¹ and quite different from network glass PDFs where the features disappear by $r = 10 \text{ \AA}$ in general.^{112,113} Given the isotropic, non-specific, nature of the metallic bonding, and the extensive disorder coming from the BMG materials, the extent of the range of structural correlations is somewhat surprising. Furthermore, the presence of icosahedral-like packing in the BMGs has been studied using a combination of electron diffraction and X-ray scattering techniques.^{114,115} It is striking that the ultra-small nanoparticles studied here have a signal that can be mapped onto BMG signals with only a rescaling of the frequency and the phase of the sinusoidal signal. Additionally, the range of the oscillations and their damping envelope do not have to be rescaled. The

frequency of the oscillations is re-scaled by the mean metallic radius of the sample to bring the curves into agreement.

Quantitative nanoscale structure determination requires bulk probes that yield structural information on length scales below 10 nm. Recent developments of hard X-ray total scattering and atomic pair distribution function analysis have proven ideal for examining the structure of such nanoparticles.^{116,117} PDF studies complement high-resolution transmission electron microscopy (HRTEM) experiments, which yield atomically resolved images of individual nanoparticles, by providing high precision measurements of bond-length distributions and atomic arrangements averaged over the whole sample. Since the PDF is a sample average, the most precise structural information about individual nanoparticles requires samples that have great structure, size and shape uniformity, otherwise sample polydispersity may limit the information available in the PDF. In cases where X-ray methods do not yield sufficient information to constrain a unique structural solution,¹¹⁶ combining PDF data with complementary measurements such as HRTEM should be pursued.

In the current study, we use nanoparticle samples prepared with precise control over size and shape uniformity, taking advantage of recent developments in metallic nanoparticle synthesis control.¹¹⁸ We characterize the particles by

acquiring both high quality PDF and HRTEM data. The uniformity of our samples is demonstrated by TEM images of Ni particles in Figure 2.1 and bilayer superlattice in Figure 2.2. TEM images of the Pd (Figure 2.3) and alloy samples (Figure 2.4) exhibit similar uniformity. The PDF analysis was carried out on high-energy synchrotron X-ray data from size selected Ni, Pd, and $\text{Ni}_x\text{Pd}_{1-x}$ alloy nanoparticles as a function of size and composition. HRTEM images were also collected for the smallest nanoparticles.

2.2 Methods

Nickel (II) acetylacetonate, palladium (II) acetylacetonate, oleylamine (70%), trioctylphosphine (97%), and 1-octadecene were purchased from Sigma Aldrich. Synthesis of nanoparticles involves Schlenk line techniques that utilized thermal decomposition of a metal-salt precursor in a flask with surfactants and a high-boiling solvent. The reactant amounts and reaction and purification conditions are detailed in Table 2.1. Before heating, the reaction was evacuated at 100°C for 30 minutes. After degassing, the reactants were quickly heated to the reaction temperature as indicated in and maintained for 30 minutes with constant magnetic stirring then cooled to 25°C. The nanoparticles were obtained by a washing process that involved addition of excess acetone and centrifugation at

8000 RPM for 10 minutes. The supernatant was discarded, and the nanoparticles were redispersed in toluene.

Table 2.1. Surfactant amounts for synthesis of 1 mmol of metal nanoparticles.

Sample	Oleylamine (Molar Equivalents)	Trioctylphosphine (Molar Equivalents)	Reaction Temperature (°C)
Ni 17.7 nm	2.5	1	220
Ni 9.0 nm	10	1	220
Ni 5 nm	2.5	5	220
Pd 2 nm	10	2.5	290
Pd 3 nm	10	2.5	290
Pd 4 nm	20	2.5	290
NiPd	20	10	290
Ni ₉ Pd	20	10	290

The nanoparticles were deposited on 300-mesh carbon-coated copper grids purchased from Electron Microscopy Sciences. TEM was done on a JEOL 1400 TEM with a LaB₆ filament, operating at 120 kV and equipped with an SC1000 ORIUS CCD camera and Digital Micrograph software. HRTEM was done on a JEOL 2010F TEM/STEM, equipped with a field emission gun (FEG), operating at 200 kV as well as the National Center for Electron Microscopy's Philips CM300FEG/UT TEM with an FEG and low spherical aberration ($C_s = 0.60$ mm), operating at 300 kV. For ICP-OES, the nanoparticle samples were digested in 69.4% HNO₃ for 24 hours. The solutions were diluted to 0.7-7 ppm. The nickel and palladium calibration standards (0.1-500 ppm) were prepared by diluting

from Sigma Aldrich TraceCERT-grade stock solutions of nickel 1000 ppm and palladium 970 ppm. The measurements were done using a Spectro Genesis spectrometer. The operating conditions are as follows: RF power: 1350 W; plasma Ar flow rate: 13.50 L/min; auxiliary Ar flow rate: 1.00 L/min; nebulizer flow rate: 0.9 L/min. For each metal, calibration standards were made ranging in concentration from 0.1-50 ppm. The dilutions were used to make a regression curve for intensity vs. concentration. The unknown sample concentrations were calculated using this regression. The errors and dilution limits in ppm are listed in Table 2 for each wavelength. The maximum error is 0.0693 ppm (0.001 mmol) for Ni and 0.0622 ppm (0.0005 mmol) for Pd.

Table 2.2. Regression errors and dilution limits for each metal wavelength.

Metal	Wavelength	Dilution Limit	Std. Error	R ²
Ni	231.604	0.00363	0.0318	1
Ni	300.249	0.00779	0.0105	1
Ni	341.476	0.00374	0.0693	0.99999
Pd	340.458	0.00324	0.0168	0.99998
Pd	360.955	0.00144	0.0622	0.99999

Small-angle X-ray scattering data was collected at Penn using a Multi-Angle X-ray Scattering system with 1.54 Å X-ray wavelength with detector distances at 11 and 54 cm as well as at the ESRF at ID02 using 12.5 keV X-rays with detector distances at 1.5 and 10 m covering a q range of 0.5-0.001 Å⁻¹. Collection of the X-

ray scattering data was done at the ESRF at ID15B using 87.8 keV X-rays (0.1412 Å) and a Mar345 detector. The raw images were integrated using Fit2D¹¹⁹. Background contributions from the 2 mm Kapton capillary tubes as well as Compton and fluorescence contributions were subtracted from the data. An in-house Igor Pro code 'iPDF' written by Dr. Simon Kimber was used to correct and Fourier transform the data into real space pair distribution functions. PDFgui was used to model the PDFs in the small-box approximation.⁴³ The PDFs of icosahedral clusters were calculated using SrFit—a program framework for not only calculating functions but also co-refining structures with multiple sets of characterization data and model inputs.⁴⁴

2.3 Results and Discussion

The PDF is the Fourier transform of the properly corrected and normalized total scattering powder diffraction intensity, and may be understood as a histogram of the atomic distances in the material¹⁰⁶. For example, the nearest neighbor distance in *fcc* nickel is 2.5 Å corresponding to the first peak in the PDF. The PDFs of the larger particles show sharp peaks across a wide range of r as shown in Figure 2.5a. These could be modeled⁴³ using the *fcc* structure of bulk nickel modified by a spherical envelope function responsible for the fall-off in PDF peak intensity with increasing r due to the finite particle size. However, this model fails to

reproduce our data for the 5 nm particles. For the smallest particles (5 nm), the PDF peaks are extremely broad, reflecting significant disorder. Even with extensive peak broadening, the model peaks from the best-fit *fcc* model (continuous lines Figure 2.5) are completely out-of-phase in the high-*r* region and clearly do not reproduce the measured PDF, which therefore is not simply describing disordered *fcc* local order: it is not possible to fit self-consistently with an *fcc* model both the low-*r* and high-*r* peaks in the PDF. Similar results were found in all small-sized (< 5nm) nanoparticles throughout the entire solid solution of Ni_xPd_{1-x} nanoparticles. The SAXS patterns for the Ni-Pd NPs are shown in Figure 2.6 and Figure 2.7.

There is a striking resemblance between the PDFs of the small nanoparticles and those of bulk metallic glasses.¹²⁰⁻¹²² This is illustrated in Figure 2.8, which shows the PDF of a macroscopic ribbon of Fe₇₆MoCuB₁₅, plotted with the scattering from the small nanoparticles. The PDF of the ribbon is representative of a wide range of BMG samples and is used as a convenient reference for this class of materials.¹²³⁻¹²⁹ In Figure 2.8a, the BMG PDF is over plotted by the PDF of 5 nm Pd nanoparticles with only a scale factor applied. The overall similarity of the curves is immediately apparent with broad sinusoidal features in both cases, although the phase and wavelength of the oscillations differ. However, a simple

re-scaling of the distance axis brings the two curves into correspondence. In Figure 2.8b we show the two curves plotted on top of each other after rescaling by the average metallic radius $\langle r_{\text{metallic}} \rangle$ of each sample. This simple scaling yields an agreement between the two data sets that is remarkable and superior to the best-fit *fcc* model. This is a strong indication that the nanoparticles, despite being made from elemental Ni, are mainly characterized by BMG-like disorder rather than a cubic-close-packed structure. While “disorder” has been observed in some small metallic nanoparticles, this close, quantitative, relationship to the BMG structure is heretofore unnoted.

The similarity between the nanoparticle and the rescaled BMG PDFs extends beyond peak positions and widths to the damping envelope, which is a measure of the range of structural coherence of the local order. The BMGs obtained from a wide range of compounds exhibit universal PDF features.^{123,130} Our results extend such universality to simple-metal nanoparticles.

We now explore the ubiquity of this type of disordered structure for a range of small Ni, Pd and Ni_{1-x}Pd_x alloy nanoparticles. As shown in Figure 2.9a, the similarity of the intermediate range structure in all the samples is clearly apparent, with a broadened and non-*fcc*-like PDF above ≈ 5 Å. This PDF can be well fit with a damped single-mode sine wave as shown in Figure 2.9a. This fact

suggests that in this intermediate range the structure is isotropic, distinct from close-packed structures such as *fcc* and *hcp* that have different periodicities in the different crystallographic directions. In order to test whether all our samples show the same $\langle r_{\text{metallic}} \rangle$ scaling that we reported above, in Figure 2.9b we show all the rescaled curves plotted on top of each other. This simple scaling works remarkably well for all the Ni and alloy samples showing that the isotropic atomic packing is robust to a large variation in mean metallic radius. The agreement is still good, but less perfect, for the pure Pd nanoparticles.

The simple $\langle r_{\text{metallic}} \rangle$ -scaling is different from the fractal scaling reported in Ma *et al.*,¹³¹ and has a simpler explanation: that the packing is isotropic and depends only on the mean metallic radius for a wide range of BMGs.¹³¹ Figure 2.10 shows that the new data from these nanoparticle experiments significantly extends the range of $\langle r_{\text{metallic}} \rangle$ over which the scaling analysis can be carried out, giving a more accurate determination of the exponent, if indeed it is valid to combine the NP and BMG signals.

Ultra-small metallic clusters often form in cuboctahedral, decahedral or icosahedral morphologies, as suggested by HRTEM measurements.⁷⁶ HRTEM images of the 5 nm Ni clusters are shown in Figure 2.11b, top, where it is immediately clear that, despite the “glassy” PDF signal, lattice fringes are

evident in the images, suggesting a well-defined short-range structure. By tilting the microscope stage appropriately it is possible to see lattice fringes in virtually all the particles suggesting that this is not a minority effect affecting only a few particles. To reconcile these apparently contradictory HRTEM and PDF results we calculated the PDFs of icosahedral clusters, which have well defined order but are highly isotropic. The calculated PDFs for 309-atom icosahedra, which consist of a core atom surrounded by four additional atomic shells, are shown in Figure 2.11a with the icosahedral structure shown in the upper inset. The green curves are all PDFs calculated from this icosahedral model with different atomic displacement parameters (ADPs), which are a measure of the static and dynamic atomic disorder. The top curve has an unrealistically small ADP of 0.001 \AA^2 but it serves to illustrate the large number of distinct atomic distances present in the perfect icosahedral cluster. The second green curve was calculated with an ADP of 0.01 \AA^2 , which is a reasonable value if there was just thermal motion but no static disorder in the material. The bottom green curve—overlaid on top of the 5 nm Ni PDF—was calculated with a large value of 0.1 \AA^2 . This is appropriate if there is a broad atomic positional distribution around the average sites in the icosahedral cluster. In the latter two cases a damped sine wave is shown overlaid in black. The good agreement shows that the PDF of a broadened icosahedral

model is well represented by a damped single-mode sine wave, consistent with the measured PDF of the icosahedral clusters. Moreover, we have attempted fits of the icosahedral model to the nanoparticle PDFs where the only tunable structural parameters are an isotropic breathing parameter that allows the cluster to uniformly shrink or expand, and a single global ADP. Additionally, the fits include a tunable scale factor and a correlation parameter that allows lower- r PDF peaks to be sharper, thus bringing to 5 the total number of fitting parameters. The results of the fit are shown as the bottom curve in Figure 2.11a. The agreement between the fit and experimental data shows that a well-defined local icosahedral atomic geometry, albeit with a large atomic density distribution around each average atomic position, is consistent with the PDF data. We note that the PDF peaks are too broad and the nanoparticles too disordered to claim that the icosahedral model gives the “correct” packing arrangement. Other isotropic models such as decahedral might also be expected to give good agreement with the data after broadening. However, models such as cubic close packing that have different frequencies in different directions, are not consistent with the data.

The fringes in the TEM survive presumably because the intermediate range order is well defined. Even though the positional order of the atoms around each

average atomic position is loose, the average position itself is well enough defined to yield interference and fringes in the HRTEM image. Furthermore, the disorder within the nanoparticle can be compared with calculated PDFs of bare icosahedral clusters ranging in size from 0.4 to 2.5 nm as seen in Figure 2.12. The corresponding number of shells for the icosahedral clusters has been tabulated in Table 2.3. The broadened $G(r)$ curves for the clusters are overlaid with experimental Ni 5 nm data to demonstrate the consistency of the model.

The appearance of isotropic glassy packing consistent with non-space filling packing of atoms below a critical diameter in Ni suggests that the vicinity of a surface may be important to stabilize it. Atomic arrangements routinely reconstruct at surfaces and highly curved surfaces may result in reconstructions that appear quite disordered.^{132,133} However, in these nanoparticles the structure of the core and the surface modifies below a critical diameter, which is much larger than the first one or two atomic layers, but comparable to twice the range of coherence of the intermediate order. This means that the icosahedral cluster around any origin atom will not span the diameter of the particle, but is likely to impinge on a surface in some direction. We speculate that the large ADP values may arise from the need to create interpenetrating icosahedra, centered on different atoms and randomly oriented. In this picture the nanoparticles

apparently prefer defective icosahedral packing to *fcc* order at these small sizes. We speculate that the alloying of elements with a large size distribution in BMGs may achieve a similar effect by packing mismatches that create voids and free volume in the system. This allows for the non-space filling, such as icosahedral, packing to form, with small interstitial atoms filling the voids to lower the energy further. Such ideas are not new^{110,134} but this work gives direct experimental support to their validity.

The idea that the presence of a surface might stabilize the icosahedral state led us to explore the possibility that there is a thin layer of icosahedrally-packed structure at the surface of the larger Ni nanoparticles. Close examination of the difference curves in Figure 2.10 indicates that after fitting the *fcc* model there is considerable signal left in the residual which, although noisy, appears to have an oscillatory nature. The difference curves are plotted in Figure 2.10b and compared to the PDF of the 5 nm Ni nanoparticles. The similarity is again striking, and the same Gaussian damped single-mode sine wave fits the data well. These observations are highly suggestive of the existence of glassy isotropic packing also in the larger particles, which we speculate are at the surface.

2.4 Conclusion

In summary, we have shown that an isotropic, non-space filling, structure such as icosahedral clusters, highly analogous to the structure of bulk metallic glasses, emerges in very small Ni and Pd nanoparticles. We show that this structure is consistent with the presence of an average geometry of four shell icosahedral clusters with significant atomic smearing. The stabilization of this non-space-filling cluster in very small nanoparticles, in the presence of a nearby surface, suggests the importance of the presence of free volume in stabilizing the structure in the bulk. The likelihood of this type of layer on the surface of larger Ni particles has profound implications for catalysis employing supported nanoparticles, since heterogeneous catalysis is mediated by the surface.

2.5 Future Directions

This work has focused on *fcc* monometallic and bimetallic transition metals. An extension of the study can be done to include *bcc* metals such as Fe, Cr, and V. Precious metals such as Pt and Au are also of interest given their use in homogeneous and heterogeneous catalysis such as CO oxidation.^{3,135} The pair distribution functions can also benefit from additional modeling using Reverse Monte Carlo coupled with SAXS and EXAFS data. Going forward, packages such as xPDFsuite can simultaneously fit complementary sets of data for a given

system. An advantage of using this Python-based package is its ability to batch process large data sets collected from *en operando* measurements.

2.6 Figures

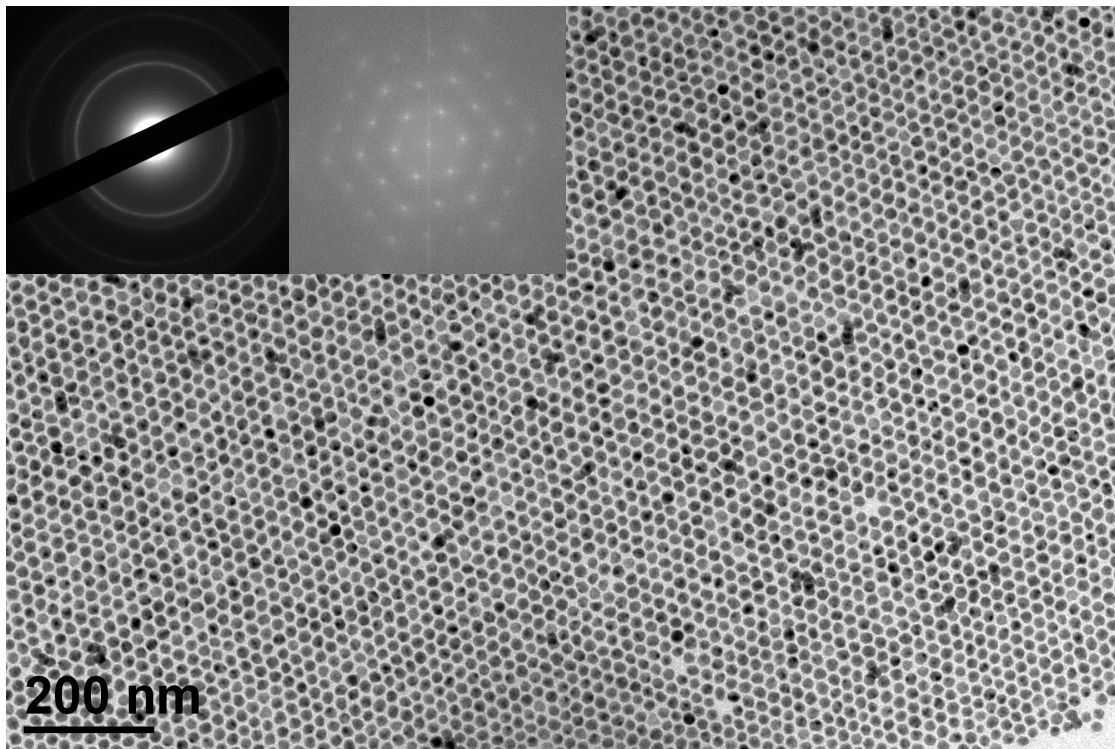


Figure 2.1. Transmission electron micrograph of superlattice assembly of Ni 17.7 nm nanoparticles at the micrometer length scale. The insets show the electron diffraction pattern (left) and Fourier transform (right) of the superlattice.

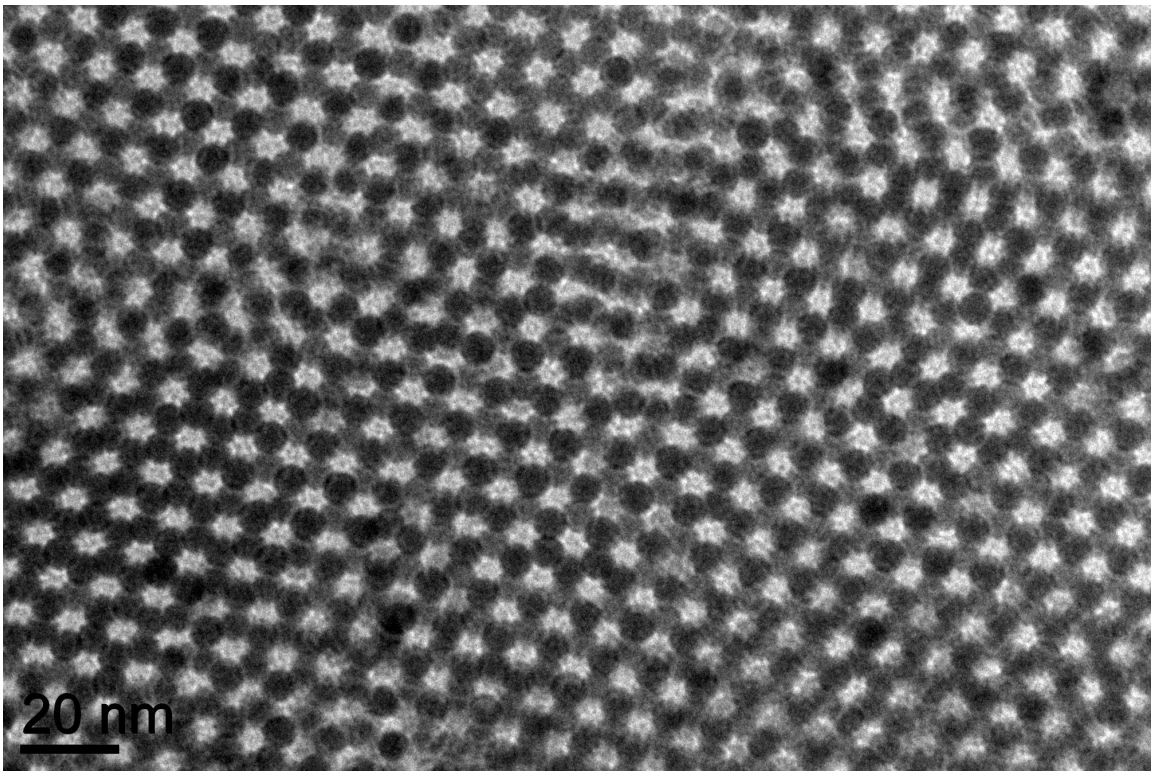
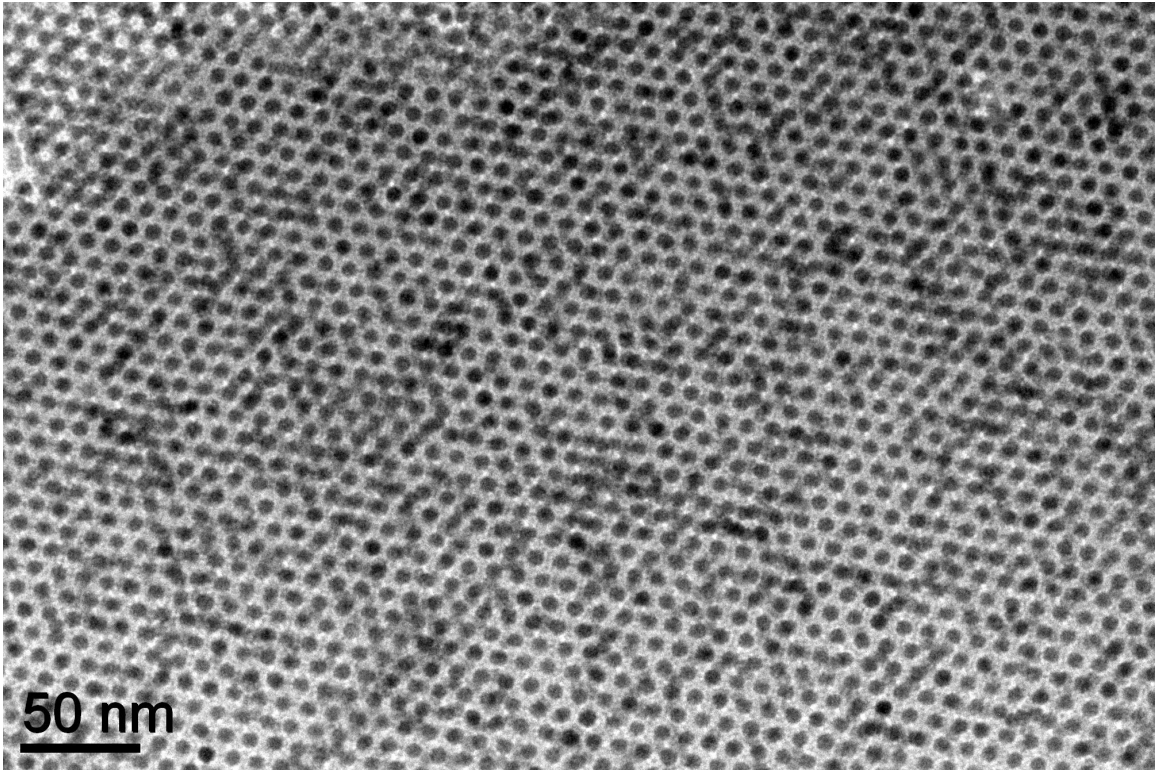


Figure 2.2. Bilayer superlattice of Ni 5 nm NPs.

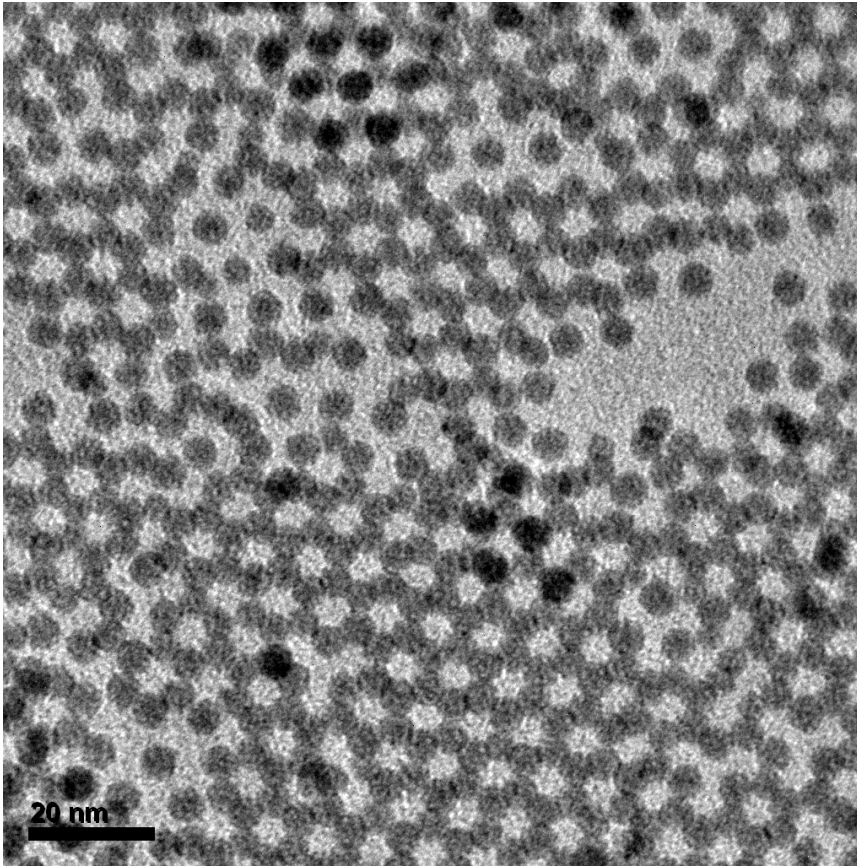


Figure 2.3. TEM image of Pd 5 nm.

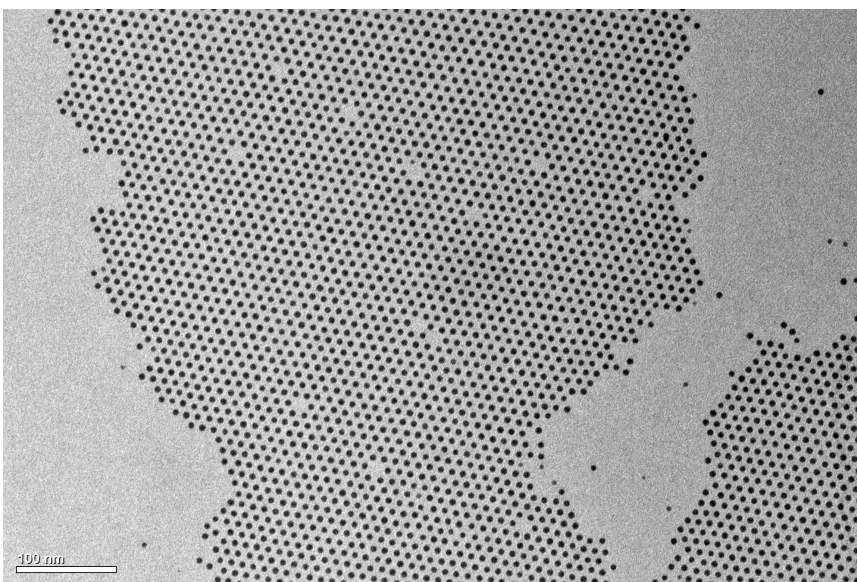


Figure 2.4. TEM image of PdNi NPs.

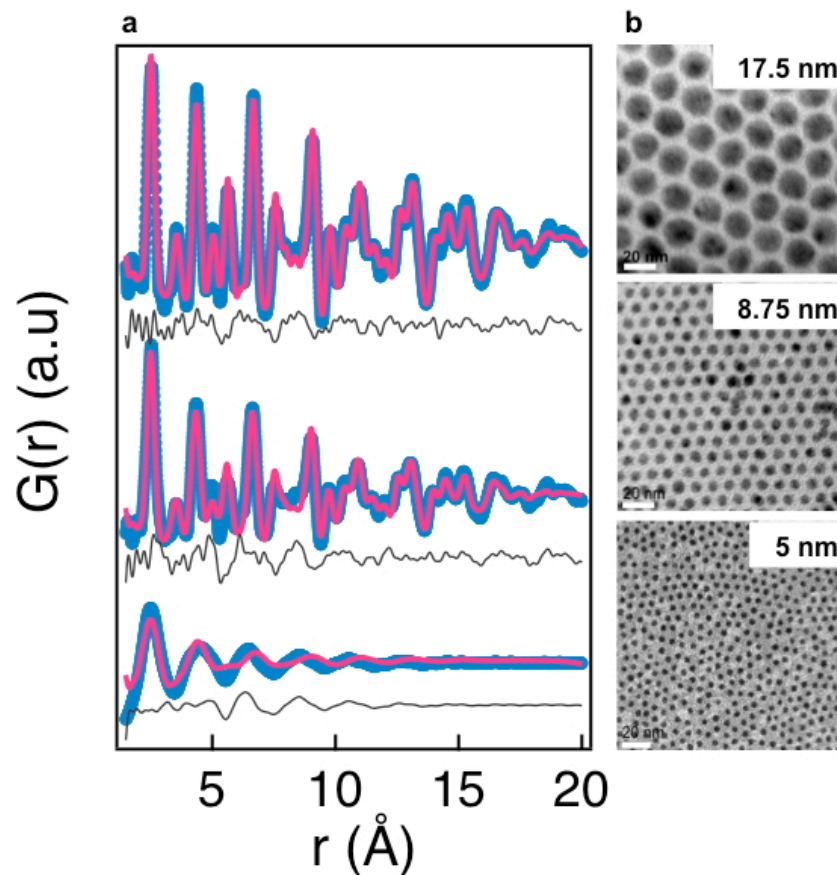


Figure 2.5. (a) Structural characterization of size controlled Ni nanoparticles. Pair distribution functions for the three samples, as determined by Fourier transformation of high energy X-ray scattering data. The blue points represent the data, and the red lines are fits of *fcc* type models. The residuals of the fits are shown as black lines. (b) TEM images of nickel nanoparticles, note the formation of well-defined superlattices, which indicates uniformity. The scale bars correspond to 20 nm.

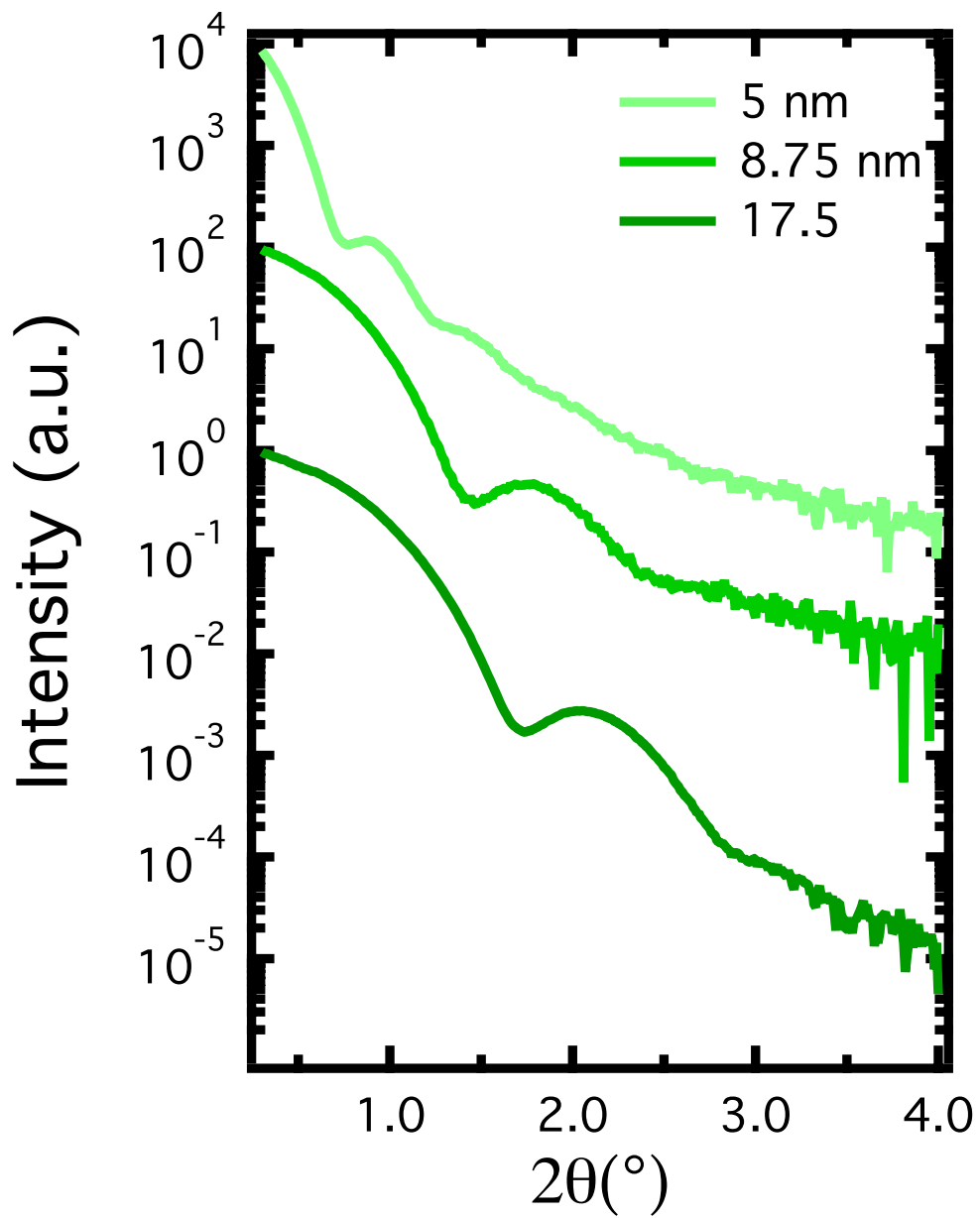


Figure 2.6. Small-angle X-ray scattering for three sizes of Ni nanoparticles.

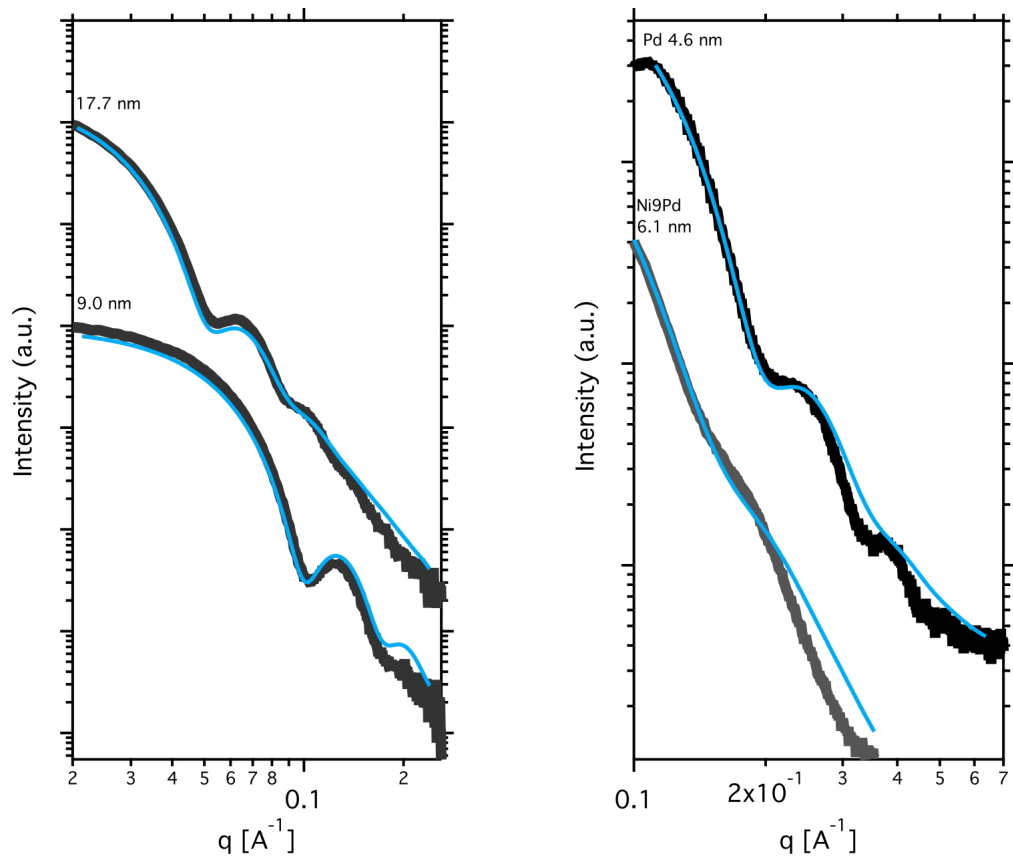


Figure 2.7. Small-angle X-ray patterns of Ni-Pd alloys with fits from IRENA¹³⁶.

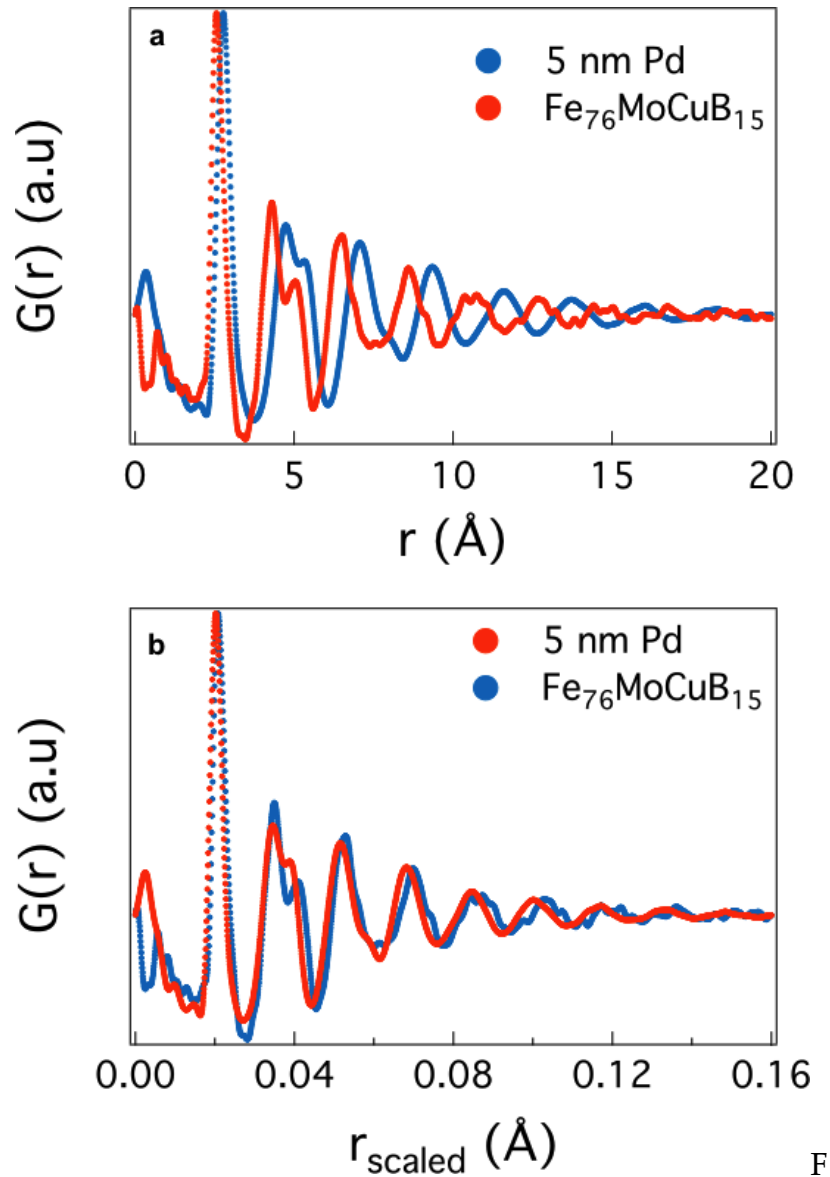


Figure 2.8. (a) Comparison of pair distribution functions of Pd nanoparticles and a representative bulk metallic glass, $\text{Fe}_{76}\text{MoCuB}_{15}$. Comparison of the pair distribution functions after correction for an overall scale factor. (b) Comparison of the pair distribution functions after scaling for the different metallic radii present in each sample.

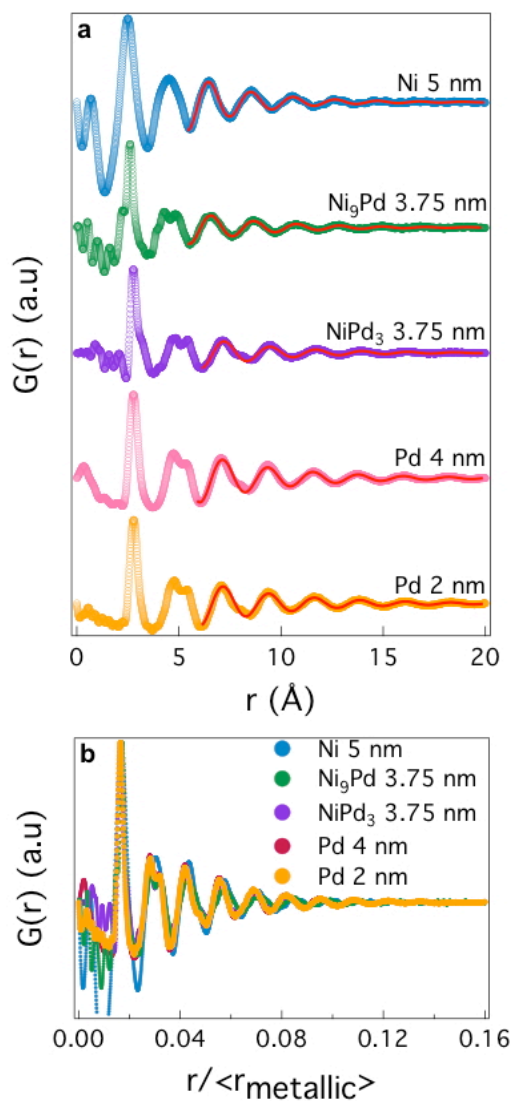


Figure 2.9. (a) The ubiquity of the disordered structure in the Ni_{1-x}Pd_x solid solution series shown in pair distribution functions of the solid solutions. The red lines show fits to the high- r region of the PDF of a Gaussian damped single-mode sine function as described in the text. (b) Comparison of the pair distribution functions after scaling by the different metallic radii in each sample.

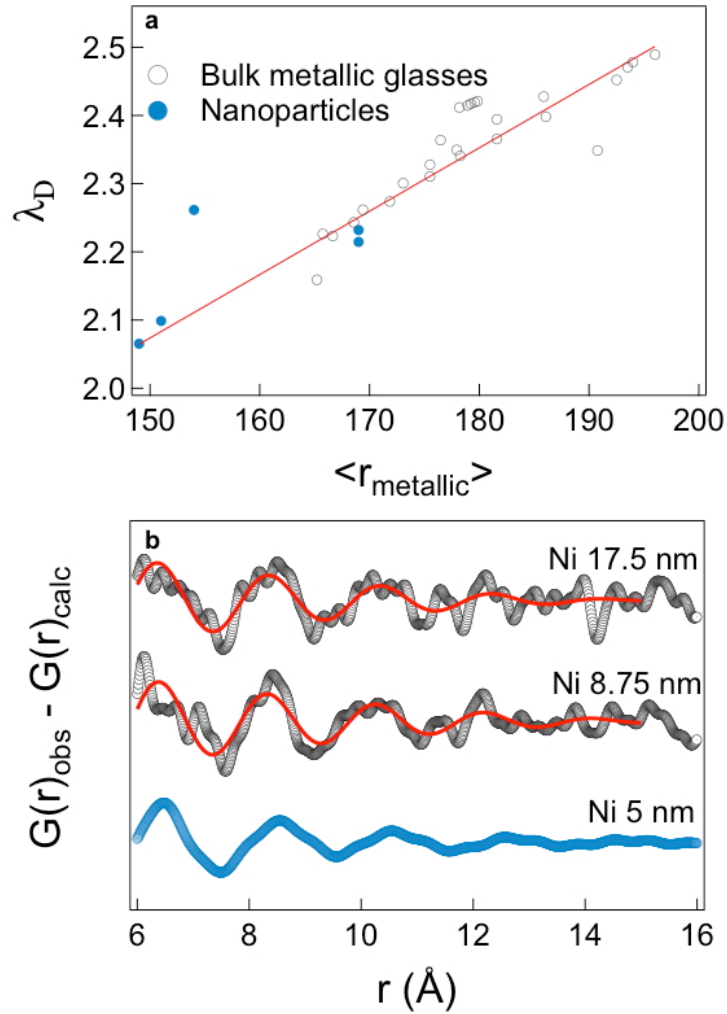


Figure 2.10. (a) Scaling of PDFs of synthesized NPs and bulk metallic glasses and evidence for a surface contribution in larger Ni particles. Linear dependence of the density wave fluctuations in NPs and BMGs on the average metallic radii. Data points were extracted using the fits shown in Figure 2.9a and from Ma *et al.* (B) Residuals from the fits of an *fcc* model to the data for larger Ni particles compared to the data for the 5 nm particles. Red lines show fits using a damped sine wave function as above.

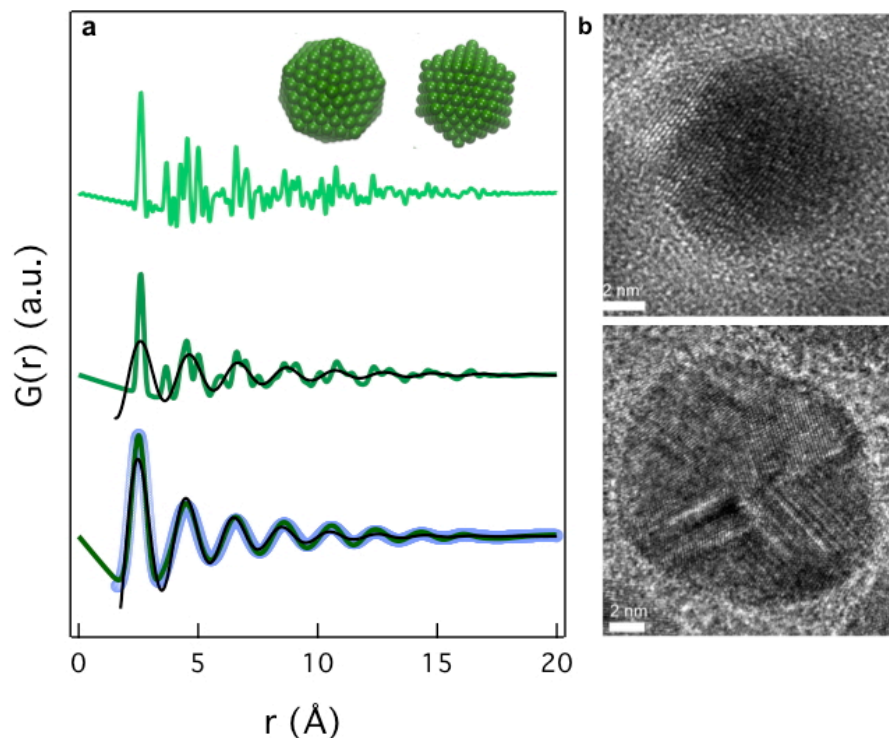


Figure 2.11. (a) PDFs of icosahedral models: Green curves are all PDFs from the 309-atom icosahedral model shown in the inset. In the top curve the PDF was calculated with an unrealistically small ADP of 0.001 \AA^2 . A more reasonable value for the ADP in the absence of static disorder is 0.01 \AA^2 , which is shown in the second curve from the top. The bottom green curve is the same model calculated with an ADP of 0.1 \AA^2 , which implies a considerable non-thermal distribution of atomic positions around the average site. The black curves are fits of a damped single-mode sine wave to the icosahedral PDFs. The underlying blue curve at the bottom is the measured PDF from the 5 nm Ni nanoparticles. In this case, the single-mode sine wave is the best-fit PDF of the same icosahedral model where the only tunable parameters for refinement were a stretching parameter that allows the cluster to increase and decrease uniformly in diameter, a scale factor and a single ADP parameter applied to all the atoms, plus a PDFgui “delta2” parameter that sharpens the PDF peaks in the low- r region. (b) High-resolution TEM images of 5 nm (top) and 17.7 nm (bottom) Ni nanoparticles show lattice fringes indicating existence of twinning and local ordering within the nanostructures.

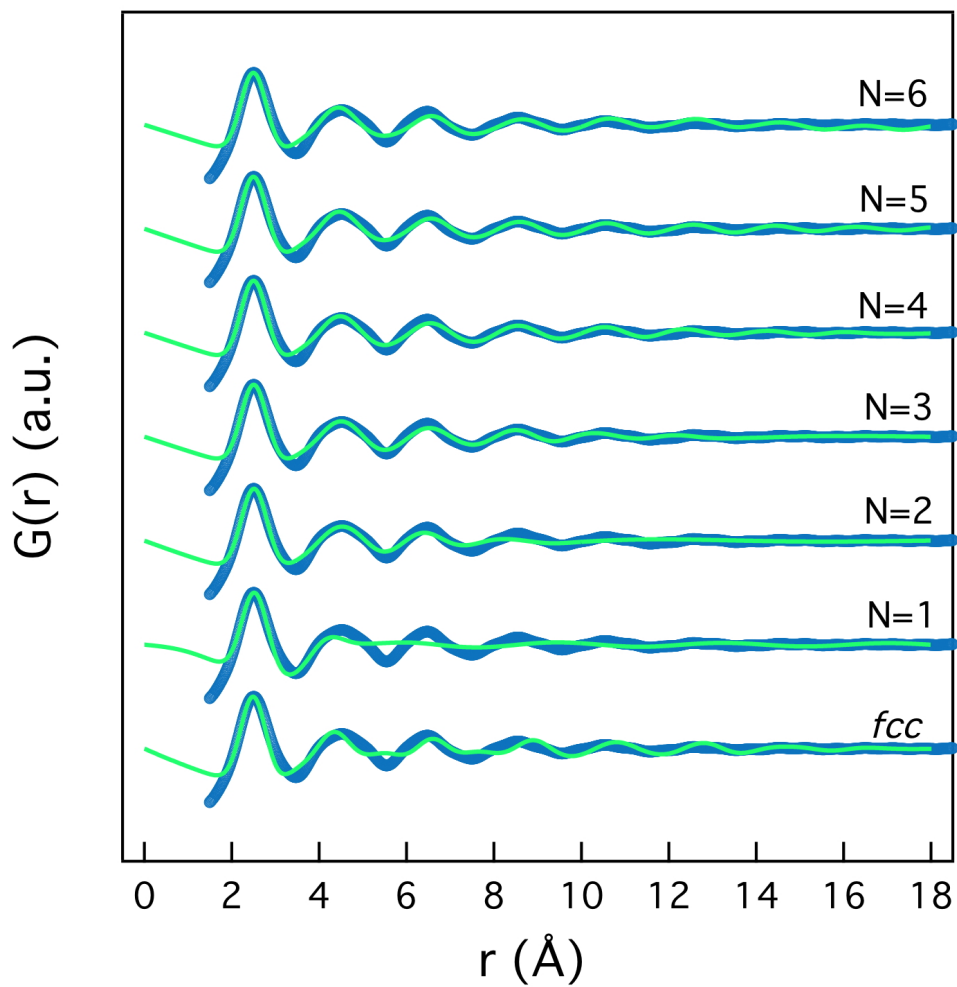


Figure 2.12. Calculated $G(r)$ for icosahedral increasing in the number of shells, thus increasing in size (blue). The curves of calculated PDFs of icosahedral clusters are overlaid with experimental total scattering data for Ni 5 nm nanoparticles (green).

Table 2.3. Calculated number of atoms and size of icosahedral clusters ranging from 1-6 shells.

Number of Shells	Number of Atoms
1	13
2	55
3	147
4	309
5	561
6	923

3. Synthesis and X-ray Characterization of Cobalt Phosphide (Co₂P) Nanorods for the Oxygen Reduction Reaction

Chapter 3—in part—has been submitted as a manuscript. V. V. T. Doan-Nguyen, S. Zhang, E. B. Trigg, R. Agarwal, J. Li, D. Su, K. I. Winey, C. B. Murray. Synthesis and X-ray Characterization of Cobalt Phosphide (Co₂P) Nanorods for the Oxygen Reduction Reaction.

3.1 Introduction

This chapter will discuss the synthesis, characterization, and electrocatalysis of cobalt phosphide (Co₂P) nanorods. The motivation of the development of a relatively inexpensive, earth abundant electrocatalyst to replace Pt for oxygen reduction reaction (ORR) is first summarized. This is proceeded by a discussion of fuel cell applications and experimental testing conditions using a rotating disk electrode. High-resolution transmission electron microscopy (HRTEM) and high-angle annular dark field scanning transmission electron microscopy (HAADF-STEM) combined with X-ray total scattering and extended X-ray absorption fine structure (EXAFS) and modeling lead to greater understanding of the active catalyst structure, morphology, and architecture for electroreduction of oxygen.

Electrocatalytic tests show durable cobalt phosphide nanorods that are highly efficient and selective for the ORR four-electron pathway.

3.1.1 Oxygen Reduction Reaction

Global needs for energy are rising rapidly so the search for alternative energy production methods is important for not only meeting those demands but also minimizing greenhouse emissions from the combustion of fossil fuels. The hydrogen economy encompasses technologies that improve hydrogen production efficiency, storage, and use in applications such as fuel cells.¹³⁷ The attractive features of fuel cell technology include their zero pollution emissions and their electrical output can be tailored to the specific needs such as portability for small electronics or large-scale industrial plants.¹³⁸ The various input and output parameters of polymer electrolyte membrane (PEMFCs), alkaline (AFCs), phosphoric acid (PAFCs), molten carbon (MCFCs), and solid oxide (SOFCs) fuel cells are listed in Table 3.1.

In this chapter, I will focus on the anode catalyst for oxygen reduction reaction (ORR), which is one of the half-reactions in PEMFCs, AFCs, and PAFCs (Equations 3.1 and 3.2). The FCs target applications with low operating temperatures (approximately $< 250^{\circ}\text{C}$) and portability requirements. PEMFCs

and PAFCs are efficient proton conductors and produce water as a byproduct. In contrast, AFCs conduct hydroxides through the electrolyte.



For ORR specifically, the 4 electron and 2 electron pathways are summarized below for acidic environments (Equations 3.3-3.5) and in alkaline environments (Equations 3.6-3.8).



Table 3.1. Types of fuel cells for low and high temperature applications.¹³⁹

	PEFC	AFC	PAFC	MCFC	SOFC
Electrolyte	Hydrated Polymeric Ion Exchange Membranes	Mobilized or Immobilized Potassium Hydroxide in asbestos matrix	Immobilized Liquid Phosphoric Acid in SiC	Immobilized Liquid Molten Carbonate in LiAlO ₂	Perovskites (Ceramics)
Electrodes	Carbon	Transition metals	Carbon	Nickel and Nickel Oxide	Perovskite and perovskite / metal cermet
Catalyst	Platinum	Platinum	Platinum	Electrode material	Electrode material
Interconnect	Carbon or metal	Metal	Graphite	Stainless steel or Nickel	Nickel, ceramic, or steel
Operating Temperature	40 – 80 °C	65°C – 220 °C	205 °C	650 °C	600-1000 °C
Charge Carrier	H ⁺	OH ⁻	H ⁺	CO ₃ ⁼	O ⁼
External Reformer for hydrocarbon fuels	Yes	Yes	Yes	No, for some fuels	No, for some fuels and cell designs
External shift conversion of CO to hydrogen	Yes, plus purification to remove trace CO	Yes, plus purification to remove CO and CO ₂	Yes	No	No
Prime Cell Components	Carbon-based	Carbon-based	Graphite-based	Stainless-based	Ceramic
Product Water Management	Evaporative	Evaporative	Evaporative	Gaseous Product	Gaseous Product
Product Heat Management	Process Gas + Liquid Cooling Medium	Process Gas + Electrolyte Circulation	Process Gas + Liquid cooling medium or steam generation	Internal Reforming + Process Gas	Internal Reforming + Process Gas

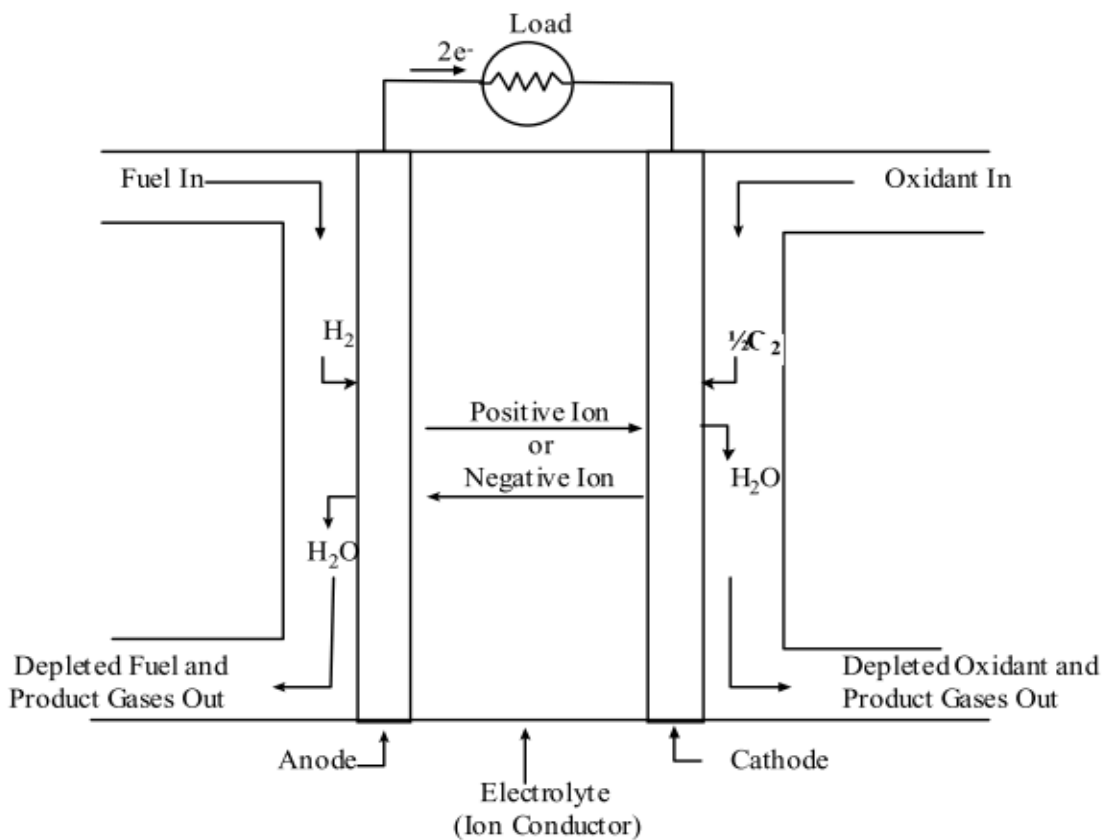


Figure 3.1. Fuel cell stack diagram depicting half-reactions at the anode and cathode with ion pathways.¹³⁹

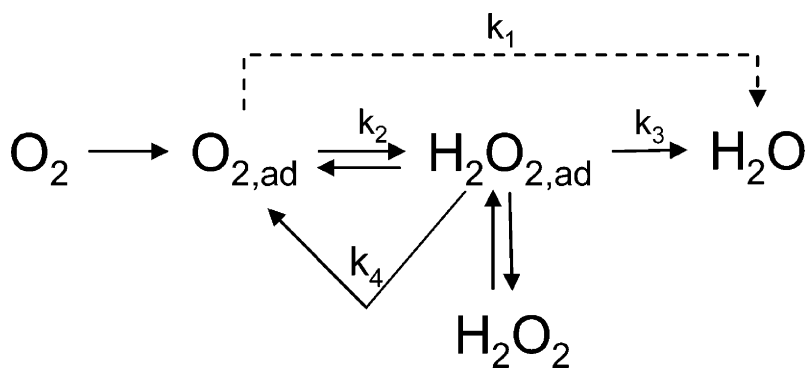


Figure 3.2. Possible oxygen reduction pathways on platinum.¹⁴⁰

Electrode materials for fuel cells have been actively investigated for decades with high activity achieved for Pt-based systems.^{141,142} Platinum nanoparticles (NPs) with high surface area have proven to be robust as electrocatalyst for both hydrogen oxidation and ORR.^{139,141–143} However, the high cost of Pt, approximately 50% of a fuel cell stack, has motivated many investigations, including this study, to find less expensive, more earth abundant materials alternatives for catalyzing either of the two half-reactions.^{142,144–148} We focus on the cathode material because ORR still presents many serious commercialization challenges such as efficiency, materials cost, and stability. Even though many recent reports on non-precious metals,¹⁴⁹ metal-polymer composites,^{150,151} and graphene-based systems^{152–154} have shown promise in fabricating a catalyst beyond the Pt for ORR, it is still a challenge to provide a non-Pt-based catalyst with comparable or better activity, durability or selectivity to Pt catalysts. In this chapter, I will present a non-precious metal alternative from colloidal synthesis for enhanced stability in ORR in fuel cell applications.

The electrochemical potential for ORR of 1.23 V versus a normal hydrogen electrode (NHE) is quite high even for relatively stable materials such as Pt-based systems. Platinum can oxidize at $E^0 = 0.88$ V. The ideal standard potential (E°) for the cell reaction and the ideal equilibrium potential (E) at other partial pressures

of reactants and products is given by the Nernst Equation (Equation 3.9) for the overall fuel cell reaction in which R is the gas constant ($8.3145 \text{ VC K}^{-1} \text{ mol}^{-1}$), T is the temperature (K), F is the Faraday constant ($9.64853 \times 10^4 \text{ C mol}^{-1}$), P are partial pressures of the denoted species.

$$E = E^0 + \frac{RT}{2F} \left[\ln \left(\frac{P_{H_2}}{P_{H_2O}} \right) + \ln P_{O_2}^{1/2} \right] \quad (3.9)$$

The ideal operating potential as a function of temperature for FCs, according to the Nernst equation, is plotted in Figure 3.3. At 25°C the ideal operating voltage is 1.18 V; for AFCs, the ideal voltage would be 1.16 V at 80°C .

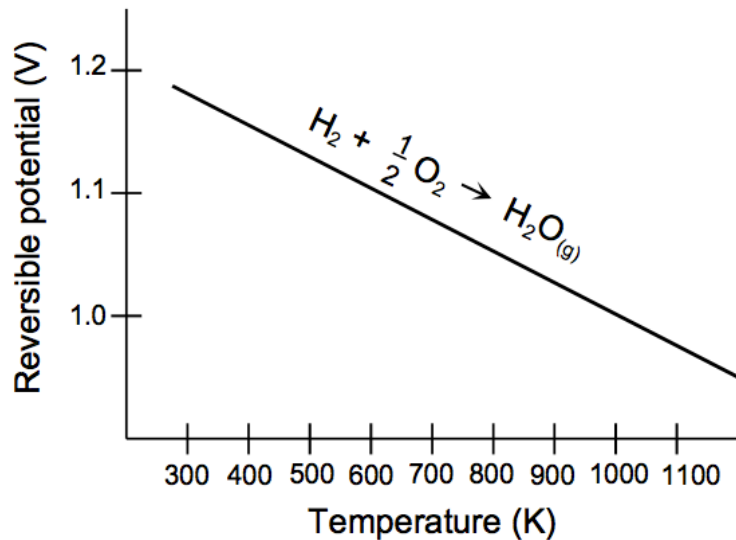


Figure 3.3. Ideal potential for hydrogen-oxygen fuel cells for a range of temperatures.¹³⁹

3.1.2 Rotating Disk Electrode

Electrocatalytic studies can be carried out in a variety of configurations such as steady-state polarization, cyclic voltammetry (CV), rotating ring-disk electrodes, and rotating disk electrode. Here, I will focus on the rotating disk electrode and the governing equations for current. One of these is the Koutecky-Levich Equation, provided in Equation 3.10, in which j is the disk current density, j_L is the Levich current density, and j_K is the kinetic current density. The values j_L and j_K can be expanded as shown in Equation 3.11 and 3.12 in which n is the number of electrons, A is the area of the electrode, F is Faraday's constant, C_{O_2} is the concentration of dissolved molecular oxygen, D_{O_2} is the diffusion coefficient of molecular oxygen, ν is the kinematic viscosity of the electrolyte solution (ratio of solution viscosity to density), Γ is the surface concentration of the catalyst, and ω is the experimental rotation velocity in radians/second. From the current-potential polarization curves, the j_{lim} (for $\omega \rightarrow \infty$) can be determined as a function of rotation rate. The inverse of j_{lim} has a linear relationship with ω^{-2} , and the slope of such a Koutecky-Levich plot is the number of electrons transferred in the reaction.

$$\frac{1}{j} = \frac{1}{j_L} + \frac{1}{j_K} = \frac{1}{B\omega^2} + \frac{1}{j_K} \quad (3.10)$$

$$B = 0.62nAF C_{O_2} D_{O_2}^{2/3} \nu^{-1/6} \quad (3.11)$$

$$j_K = nFAK_{O_2} C_{O_2} \Gamma \quad (3.12)$$

3.1.3 Cobalt Phosphide (Co₂P) Nanoparticles

Herein, we report a solution colloidal synthesis for cobalt phosphide (Co₂P) nanorods (NRs), which show promise as efficient catalysts for ORR in the alkaline solution. Controlled synthesis of 1D structured materials such as NRs is of great interest for many applications including optics,¹⁵⁵ electronics,¹⁵⁶ magnetism,^{157,158} and catalysis.^{159,160} In the colloidal solution chemistry, rod-like nanoparticles (NPs) can be produced by controlling surfactant choice/concentration,¹⁶¹ time of growth,¹⁶² and seeded precursors.^{163–165} Previous studies have shown that, using trioctylphosphine and/or trioctylphosphine oxide as the phosphorus sources, metal nanoparticles (i.e. magnesium, nickel, iron, copper, molybdenum, palladium) can be translated to metal phosphides through the diffusion process.^{158,166–170} Co₂P NPs have been synthesized to support their applications in magnetics,¹⁷¹ heterogeneous catalysis,^{163,172–174} energy storage,^{175,176} and heavy-metal capture and recycling.¹⁷⁷ Recently, cobalt phosphide (CoP) and other base-metal phosphides have also been reported to be active electrocatalysts for hydrogen evolution reaction (HER),^{178,179} which provides motivation for the study of ORR electrocatalysis by on metal phosphide NPs.^{164,178} By using the co-

surfactants of oleic acid (OLAC) and trioctylphosphine oxide (TOPO), we have synthesized the monodisperse Co₂P NRs. The structure of the Co₂P NRs are systematically characterized by high-resolution transmission electron microscopy (HRTEM), high-angle annular dark field scanning transmission electron microscopy (HAADF-STEM), extended X-ray absorption fine structure spectroscopy (EXAFS), total X-ray scattering, and modeling. These techniques have been robust for not only distinguishing bimetallic core-shell vs. alloy architectures but also formation of metal-oxide shells that emerge from cleaning pre-treatments in preparation for functional testing.¹⁸⁰⁻¹⁸³ Such careful study of the average and local crystallographic structures of our NRs provides valuable insights into the structure-property relations in shape-dependent electrocatalysis. Besides the unique 1-D structure, Co₂P NRs supported on carbon exhibit intriguing catalytic performance for catalyzing ORR in an alkaline medium. The Co₂P catalyst shows comparable activity and remarkable enhanced durability as compared to commercial Pt catalysts. This presents a new type of non-Pt containing electrocatalyst for ORR for alkaline fuel cells application.

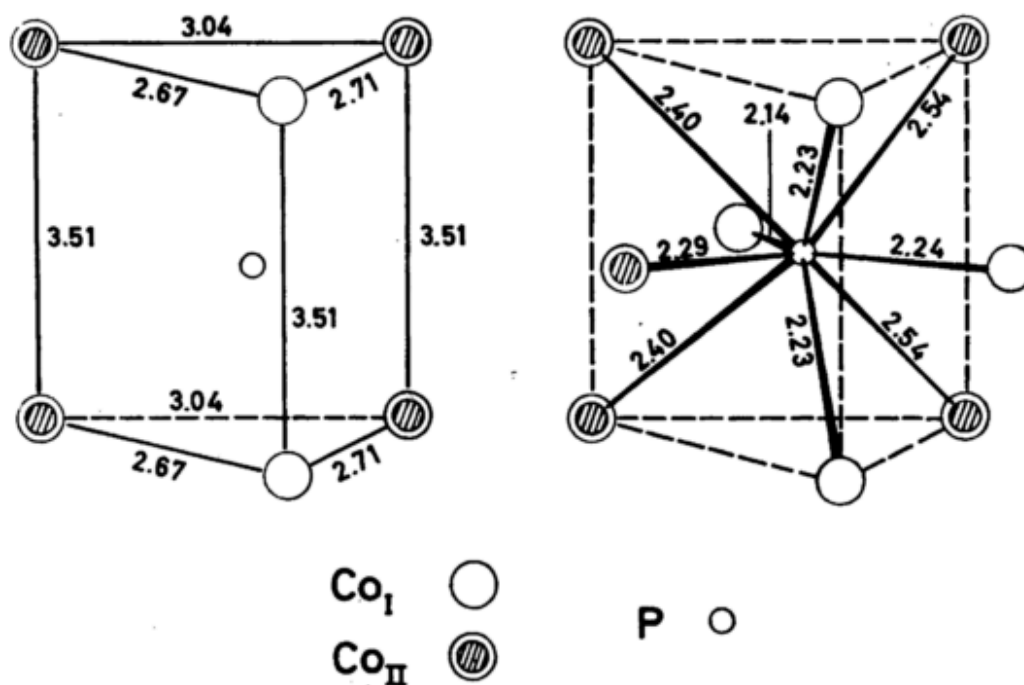


Figure 3.4. Cobalt-phosphide and cobalt-cobalt bonds (adapted from S. Rundqvist).¹⁸⁴

3.2 Methods

Chemicals. Cobalt (II) acetate tetrahydrate ($\text{Co}(\text{Ac})_2$), trioctylphosphine oxide (TOPO), tributylphosphine (97%) (TBP), oleic acid (OLAC), benzyl ether were purchased from Sigma Aldrich.

Synthesis and Purification. Synthesis of NPs involved a Schlenk line technique that utilized thermal decomposition of a metal-salt precursor in a flask with surfactants and a high-boiling solvent. In a typical reaction, 1 mmol $\text{Co}(\text{Ac})_2$, 1

mmol TOPO, and 3 mmol OLAC were loaded into a three-neck 50 mL flask containing 20 mL benzyl ether. The flask was degassed at 100°C for 30 minutes. The flask was refilled with nitrogen. The solution temperature was increased to 200°C at which point 3 mmol TBP was injected. Then, the reaction was carried out at 260°C for 60 minutes. The reaction was cooled to room temperature and washed with acetone and toluene. After centrifugation at 7000 RPM, the NPs were re-dispersed in hexane.

Characterization. For electron microscopy, the NPs were deposited on 300-mesh carbon-coated copper grids purchased from Electron Microscopy Sciences as well as holey carbon 400-mesh copper grids purchased from Ted Pella, Inc. TEM was done on a JEOL 1400 TEM with a LaB₆ filament, operating at 120 kV and equipped with an SC1000 ORIUS CCD camera and Digital Micrograph software. High-resolution TEM was done on a JEOL 2100 with a LaB₆ filament at 200 kV. Aberration-corrected HAADF-STEM imaging and STEM-EELS were performed at Brookhaven National Laboratory Center for Functional Nanomaterials on a Hitachi HD2700C at 200 kV with a Gatan Enfina-ER spectrometer.

X-ray photoelectron spectroscopy (XPS) was done on a Physical Electronics VersaProbe 5000. Analysis was made with High Power X-ray setting of 100 μm 25W electron beam. Photoelectrons were collected using hemispherical analyzer.

Survey data collection was performed at 117 V. The powder samples were mounted onto the holder using double-sided tape. High-resolution X-ray diffraction was done at Advanced Photon Source (APS) 11-ID-B at Argonne National Laboratory with a 58.6 keV beam corresponding to a wavelength of 0.2114 Å. Background contributions from the Kapton capillary tape and poly(vinyl) butyral matrix were subtracted from the data. Simulation of the wide-angle X-ray diffraction pattern was done using an in-house Python script, which is available on Github.¹⁸⁵ GISAXS was done at APS 12-ID-B with a 14 keV beam corresponding to a wavelength of 0.886 Å. The incident angles ranged from 0.02 to 0.15° where the critical angle of the Si substrate is about 0.127°. The standard used for q calibration was silver behenate. The scattered beam was collected with a Pilatus 2M area detector at 2 m from the sample. Data processing was done using GISAXShop available at the beamline.

EXAFS was done at Advanced Photon Source 12-BM-B. The nanoparticle samples were loaded into a 1.5 mm Kapton tube for measurement. The absorption was measured from the cobalt K -edge (7.7 keV) and calibrated by normalization of the pre-edge and post-edge from cobalt foil. The E_0 value from cobalt foil reference was used for all samples. The edge was set to 7.708 keV in accordance with Kraft *et al.*¹⁸⁶ Three fluorescence scans were averaged for the

reported absorption intensity using ATHENA, an open source package for spectroscopy analysis.⁵¹ Analysis was done during the *ab-initio* package ARTEMIS⁵¹ between 1 and 3 Å, and structure models were created using ATOMS⁵². The *k* range was analyzed from 1.9 to 10 Å⁻¹ with Hanning windows and sills of 1 Å⁻¹.

Oxygen reduction reaction electrocatalysis testing was done using a glassy carbon rotating disk electrode on the Bioanalytical Systems, Inc. Epsilon potentiostat. Voltage values for commercial Pt purchased from the Fuel Cells Store and Co₂P NRs were normalized against a Ag/AgCl reference electrode (3M NaCl) and Pt coil as the counter electrode. NRs/C catalyst was dispersed in the mixture of deionized water with isopropanol (IPA) in a volume ratio of 4:1 H₂O:IPA and 5% Nafion, which was then transferred onto the glassy carbon RDE of 6 mm diameter. Similar sample preparation was done for commercial 2.5-3.5 nm Pt on carbon. ORR polarization measurements were collected using linear scan voltammetry with rotation speeds of 400, 900, 1200, 1600, and 2500 RPM. Both polarization measurements and stability testing was done in an O₂-saturated 0.1 M KOH solution. Stability tests were performed at 0.2 V and with a rotation speed of 200 RPM for total of 25,000 seconds.

3.3 Results and Discussion

The morphology of the cobalt phosphide (Co_2P) NRs is dependent on the ligand concentration ratios of oleic acid to trioctylphosphine oxide as shown in the transmission electron microscopy (TEM) images of Figure 3.5. Relative to the metal salt precursor quantity, 0.25 molar equivalent of TOPO and 1 molar equivalence of OLAC produced a mixture of spheres and rods. The reaction produced solely rods when the concentration of OLAC was increased to 3 molar equivalence. Increasing further the amount OLAC to 9 molar equivalence dramatically changes the growth kinetics and impedes nanorod formation. In addition, the evolution of nanoparticle morphology is dependent on the amount of TOPO present in the reaction since TOPO acts as the phosphorus source. Maintaining same molar equivalence of OLAC but increasing TOPO from 0.25 to 1 molar equivalence produced similar mixture of rods and spheres (Figure 3.6). The co-stabilization of two surfactants for selective binding to preferred Miller planes have been implemented for a variety of anisotropic morphologies amongst first-row transition metals and metal phosphides.^{158,187} The morphology and dimensions were maintained when the reaction temperature was increased to 300°C or when the time was increased from 60 to 120 minutes.

Nanorods have an average diameter of $2.8 \text{ nm} \pm 0.9 \text{ nm}$ and an average length of $12.4 \text{ nm} \pm 3.5 \text{ nm}$ based on TEM (Figure 3.7). The cooperative interplay between OLAC and TOPO resulted in anisotropic growth along the {020} direction of orthorhombic cobalt phosphide. The high-resolution (HRTEM) images shows a lattice spacing of 0.27 nm for the {111} direction and an interplanar angle of 39.2° between {020} and the {111} direction (Figure 3.8c). The small X-ray scattering (SAXS) pattern in Figure 3.10a confirms the nanorod self-assembly seen in Figure 3.8a,b with a peak at $q = 0.117 \text{ \AA}^{-1}$, corresponding to the expected average center-to-center distance of $2.8 \pm 0.9 \text{ nm}$ for the hard core surrounded by two layers of OLAC in the soft ligand shell. Transmission SAXS was obtained for a powder in which the NRs are expected to be randomly oriented, thus increasing the expected width center-to-center distance. Grazing incidence small-angle X-ray scattering of Co_2P showed that there is local hexagonal packing of the NRs in the films (Figure 3.9). This based on higher scattering intensities at azimuthal angles of integer multiples of $\pi/3$ seen in Figure 3.10b. Out of the plane, nanorod films are oriented randomly as concluded by the constant intensities at a fixed scattering angle. This confirms the observed superlattice formation from electron microscopy, which are also provided in Figure 3.11 and Figure 3.12.

The wide-angle X-ray scattering pattern was also simulated using the Debye Equation (Equation 1.9) to confirm the growth direction, calculate the size polydispersity, and quantify peak broadening from static and dynamic thermal motion. The intensity in the Debye Equation is the summation of the pairwise interactions at r_{ij} of atoms at each q (in which $q = 4\pi \sin \theta/\lambda$ for a scattering angle θ and at a wavelength of λ) and scaled by the atomic scattering factors of the i^{th} and j^{th} atoms (f_i and f_j if $i \neq j$).¹⁸⁸ This intensity is then damped by the Debye-Waller factor, B , representing the thermal motion of atoms at a given temperature, which was 25°C. Here, B is equal to $8\pi^2\langle u^2 \rangle$ in which u is the atomic displacement in Å. Size polydispersity was simulated as a Gaussian weighted average of the scattering from perfect crystals in which w_k is the normalized weighting factor.

$$I = \sum_k w_k \left(\exp \left(- \left(\frac{q}{4\pi} \right)^2 B \right) \sum_{i,j} f_i f_j \frac{\sin(qr_{ij})}{qr_{ij}} \right) \quad (3.13)$$

The q values for the NRs X-ray scattering pattern indexed for the Co₂P $Pnma$ are summarized in Table 3.2. These ratios of the q values are in good agreement with the ratios of the lattice spacing as calculated from the selected area electron diffraction pattern (Figure 3.8d). When the lattice spacing from HRTEM is converted to q , the ratios are 1 : 1.28 : 1.86 as compared to the q values from

electron diffraction, which are 1 : 1.27 : 1.85 for the (112), (020), and (322) peaks, respectively. Similar to structure refinement of bulk compounds of Co₂P (ICDD PDF No. 01-089-3030),¹⁸⁴ the scattering of nanocrystalline α -Co₂P captures the dominant (112) reflection at 2.85 Å⁻¹ followed by the (103) reflection at 3.07 Å⁻¹. Additional reflections at $q = 3.63, 3.86, 4.81, 2.96, 5.27,$ and 5.87 Å⁻¹ have been assigned to the (020), (302), (402), (321), (322) and (230) planes, respectively. These prominent reflections are only partially reproduced in a simulated Co₂P sphere with a radius of 2.8 nm using the Debye Equation, Figure 3.13. The finite size effect broadening of the first peak results in indiscernible peak centers of the (112) and (201) reflections. The spherical model does not capture the high intensity for the (020) reflection. Overall, the scattering peaks from the spherical model are uniformly broadened as compared to peaks from NRs with with a range of aspect ratios (Figure 3.14). Notably, the anisotropy of the NRs is evident in the high intensity and small width of the (020) peak at $q = 3.63$ Å⁻¹. The 0.1 Å⁻¹ shift in the nanorod model (Figure 4 green line) peak $q = 3.63$ Å⁻¹ from the experimental data can be reasoned to originate from a 1% contraction in the b lattice parameter of the bulk orthorhombic crystal structure. The shift is not purely from the difference in shape factor between a sphere and rod with aspect

ratio of 4.3. Bulk lattice parameters for Co₂P has been reported to be $a = 5.646$, $b = 3.513$, and $c = 6.608$ Å by S. Rundqvist with the atomic positions listed in

Table 3.3.¹⁸⁴ Under anisotropic strain, the (020) reflection shift in q is accounted for while the dominant (112), (201) and (230) peak centers are maintained.

XPS (Figure 3.10) confirmed the oxidized state of the cobalt species, with the detection of a binding energy of 781.7 eV. In addition to the expected Co(II) state, zero-valent cobalt was also detected at 778.3 eV in sparse amounts. The Co 2p_{1/2} peak for the Co(II) species is seen at 797.9 eV with its shake-up satellite at 803.1 eV. In contrast to the NRs sample, only the Co(II) species was observed in the precursor for the Co 2p_{3/2} peak at 782.7 eV. The peak shoulder occurring at 787.6 eV is a shake-up satellite peak arising from multiplet splitting of Co 2p_{3/2}. Additional peaks from the precursor sample for the Co(II) species can be seen in the Co 2p_{1/2} peak at 797.8 eV and its satellite at 802.9 eV.

EXAFS captured the Co-P and Co-Co local environments of the cobalt phosphide phases. In the Co₂P first shell, the cobalt K-edge probes the photoelectron interaction from two types of cobalt atoms. To distinguish between the two sites, the atoms will be denoted as Co_I and Co_{II}. Shown in Figure 3.16, the fit shows good agreement with the $\chi(R)$ with an R-factor of 9.648×10^{-3} and reduced χ^2

value of 25.057. Additional fitting parameters are summarized in Table 3.4. The undistorted path lengths for bulk Co₂P in Table 3.5 with the R_{eff} values and degeneracy for the path lengths are provided in Table 3.6. In fitting the first shell in the Fourier transform of the k^3 -weighted $\chi(k)$, the nearest neighbor phosphorus and cobalt scattering paths in the Co₂P were used. To satisfy the Nyquist criteria for fitting with fitting with k from 1.9 to 10 Å⁻¹ with $dk = 1$ Å⁻¹ and R from 1 to 3.4 Å, the amplitude and ΔE_0 were constrained for all Co-P and Co-Co scattering paths. The Co-O bond (with $Fm\bar{3}m$ symmetry) was constrained to the same S_0 with a separate ΔE_0 . While the X-ray scattering did not detect Bragg diffraction from cobalt oxide phases as shown in Figure 3.13, the Co-O bonds were considered for the EXAFS fitting due to amorphous oxygen species on the surface of the cobalt NRs. The two Co_I-P and three Co_{II}-P paths were subsumed into one of each type for the EXAFS fitting due to number of independent variable constraints as well as resolution from $\Delta k = 8.9$ Å⁻¹. Similar treatment was done for Co_I-Co and three Co_{II}-Co paths.

To study NRs electrocatalysis in ORR, we loaded the NRs on Ketjan carbon (C) with a weight ratio of 1:1 (NR: C) through sonication and activated the catalysts via thermal annealing at 180°C and under the ambient pressure. We further characterized the activated electrocatalyst with aberration-corrected STEM.

Figure 3.17a is a HAADF-STEM image of the activated NRs on C, which shows the NRs are uniformly deposited on C and preserved their 1-D morphology after thermal treatment. After annealing in air, the NRs surface is oxidized, forming a core/shell structure with a shell of oxides, which is likely to be CoO. STEM electron energy-loss (EELS) elemental mapping Figure 3.17b-f. The spectrum is shown in Figure 3.18. ORR polarization curves in Figure 3.19a indicate that Co₂P/C has a steeper polarization curve and with a similar limit current density as compared to commercial Pt/C catalysts. Moreover, the Co₂P catalyst has a half-wave potential at -0.196 V, which is only 49 mV below that of commercial Pt catalyst. This suggests that the Co₂P's ORR catalytic activity performance is close to commercial Pt. It is noteworthy to report that the Co₂P NRs are supported on commercial carbon. Unlike systems using nanotubes, reduced graphene oxide, or highly ordered porous carbon matrices,¹⁸⁹ these NRs do not rely on the electrocatalytic activity enhancement from the carbon support.^{190,191} Additionally, amorphous commercial carbon has the benefit of being less expensive than the aforementioned support alternatives. The ORR kinetics on Co₂P NRs were also evaluated using a range of controlled rotation speeds (Figure 3.19b) and the Koutecky-Levich Equation. As shown in Figure 3.19c, the linearity of the Koutecky-Levich plots and the parallelism of the fitting line suggest the first

order reaction kinetics towards the concentration of O₂ on Co₂P NRs from -0.3 V to -0.75 V. The electron transfer number (n) was also calculated from the slopes of Koutecky-Levich plots where where j , j_K and j_L are measured current, kinetic current and diffusion-limiting current, respectively, ω is the angular velocity in radians/s, F is the Faraday constant (9.64853×10^4 C/mol), A is the electrode surface area in cm², C_{O_2} is the concentration of dissolved O₂ (1.26×10^{-6} mol/cm³), D_{O_2} is the diffusion coefficient of O₂ (1.9×10^{-5} cm²/s) and ν is the kinetic viscosity of the electrolyte (0.01 cm²/s). Reconfiguring Equation 3.11, n for Co₂P NRs is calculated to be 3.98-4.18. This was indicative of a complete four electron oxygen reduction process confirming the NRs' favorable kinetics for ORR.

The catalyst's durability was performed using chronoamperometric testing at a voltage of -0.3 V. As shown in Figure 3.19d, our Co₂P NRs catalyst showed a much slower current decay than commercial Pt catalyst. After a 25000-second test, Co₂P NRs catalyst retained a 75% of the original current density, while commercial Pt catalyst only preserved only 49% of initial current density. This suggests enhanced long-term stability of Co₂P NRs over the commercial Pt catalysts. As reported from previous work on FePt-based nanowires and nanorods, 1-D structures showed stronger interaction with carbon support, thus allowing for higher stability than 0-D NPs in the catalysis.^{192,193} Our Co₂P NRs

catalyst also takes advantage of this strong interaction induced by 1-D shape to enhance its durability in catalyzing ORR.

3.3.1 Assembly of Nanorods

As seen in the TEM images, the NRs preferentially align face-to-face for micrometers when deposited on a substrate. *In-situ* GISAXS confirms the stability of these films up to 300°C. The GISAXS patterns for the series from 22 to 300°C are provided in Appendix E. The first peak in the set of line cuts along q_z shown in Figure 3.21 shifts to larger q indicating a decrease in center-to-center distances between the NRs as the temperature is increased. This is due to a collapse in the film as the organic ligand shells are removed. The stability of the nanorod films makes them attractive for study of assembly effects on electrocatalysis.

3.4 Conclusions

A one-pot synthesis of cobalt phosphide nanorods has been characterized and modeled to understand the structure-property relations for enhanced stability during electroreduction of oxygen. The monodispersity in size and shape of the NRs was controlled by varying co-surfactant concentrations of oleic acid and trioctylphosphine oxide. Structural characterization involving electron

microscopy, electron diffraction, total X-ray scattering, and EXAFS have confirmed the anisotropic growth of Co₂P particles in the {020} direction with thin amorphous CoO shell. Modeling demonstrated that there is a 1% contraction in the *b* lattice parameter of the orthorhombic crystal structure. Electrocatalysis indicated that a four-electron mechanism was carried out by the Co₂P catalyst with remarkable durability in an alkaline environment as compared to commercial Pt catalysts. Additionally, the carbon support for the Co₂P NRs is commercially available. This is encouraging for use of Co₂P catalysts as alternative to Pt ORR catalysts.

3.5 Future Directions

Co₂P NRs have been demonstrated to be robust and efficient for electroreduction of oxygen. Future studies include controlling the morphology of these materials to investigate its effects on electrocatalytic activity. For instance, the exposed facets on a sphere vs. a cube can dramatically affect ORR activity as demonstrated by Kang *et al.*⁷³ In the vein of stability enhancement of 1-D structures for ORR, Co₂P nanowires can be investigated as electrocatalysts for even greater stability and activity. Architecture can also be varied to take advantage of the activity of Pt while reducing the amount of Pt used. For

instance, a core-shell type of Co₂P core and thin Pt shell can be synergistically active for ORR.

3.6 Figures

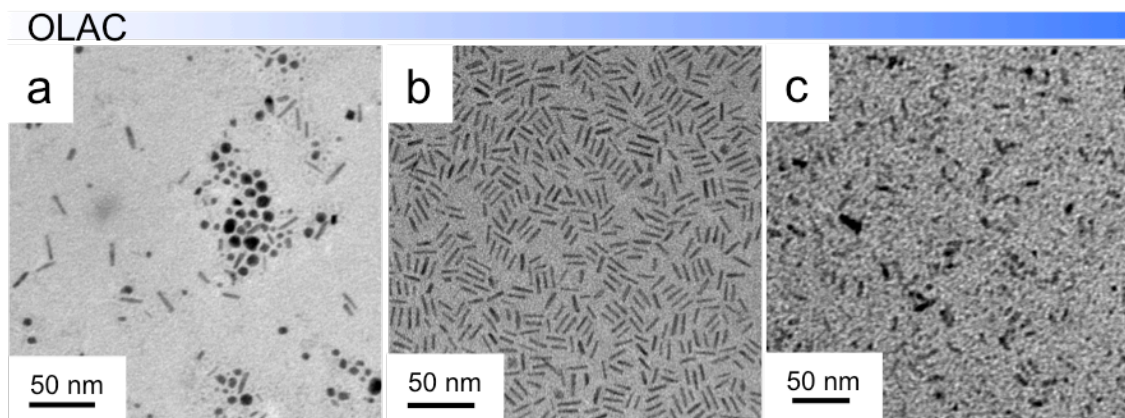


Figure 3.5. Transmission electron microscopy images of synthesized products from increasing millimolar concentrations of oleic acid to trioctylphosphine oxide: (a) 1: 0.25, (b) 3: 0.25, and (c) 9:0.25.

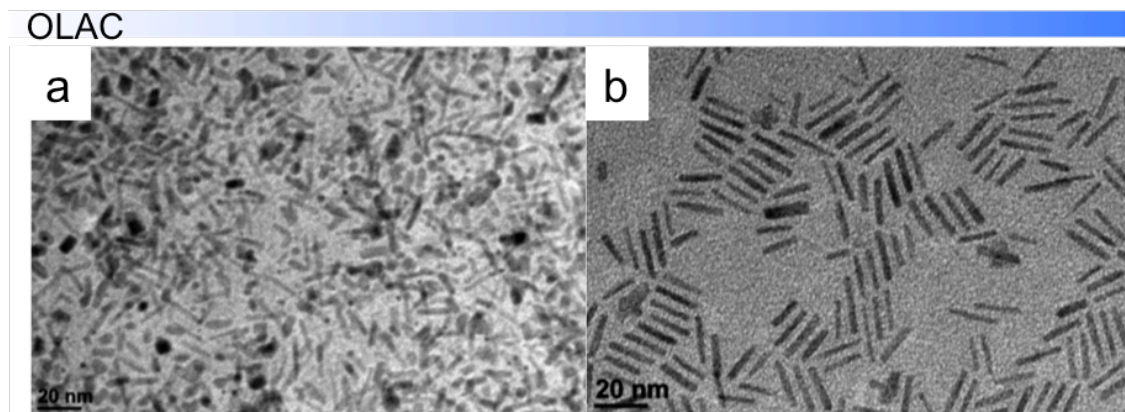


Figure 3.6. TEM images of cobalt phosphide products synthesized with OLAC:TOPO ratios of (a) 0.25:1 and (b) 3:1 molar equivalents of the $\text{Co}(\text{Ac})_2$ precursor.

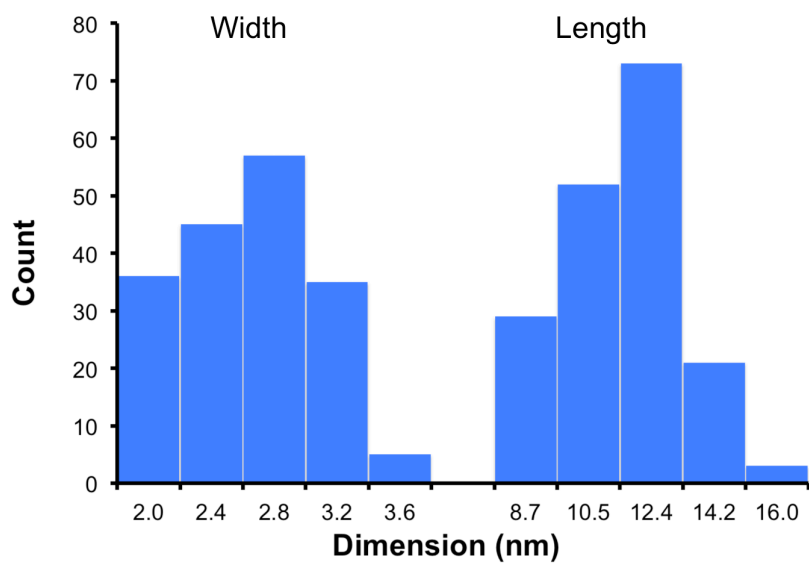


Figure 3.7. Distribution of the dimensions of cobalt phosphide NRs.

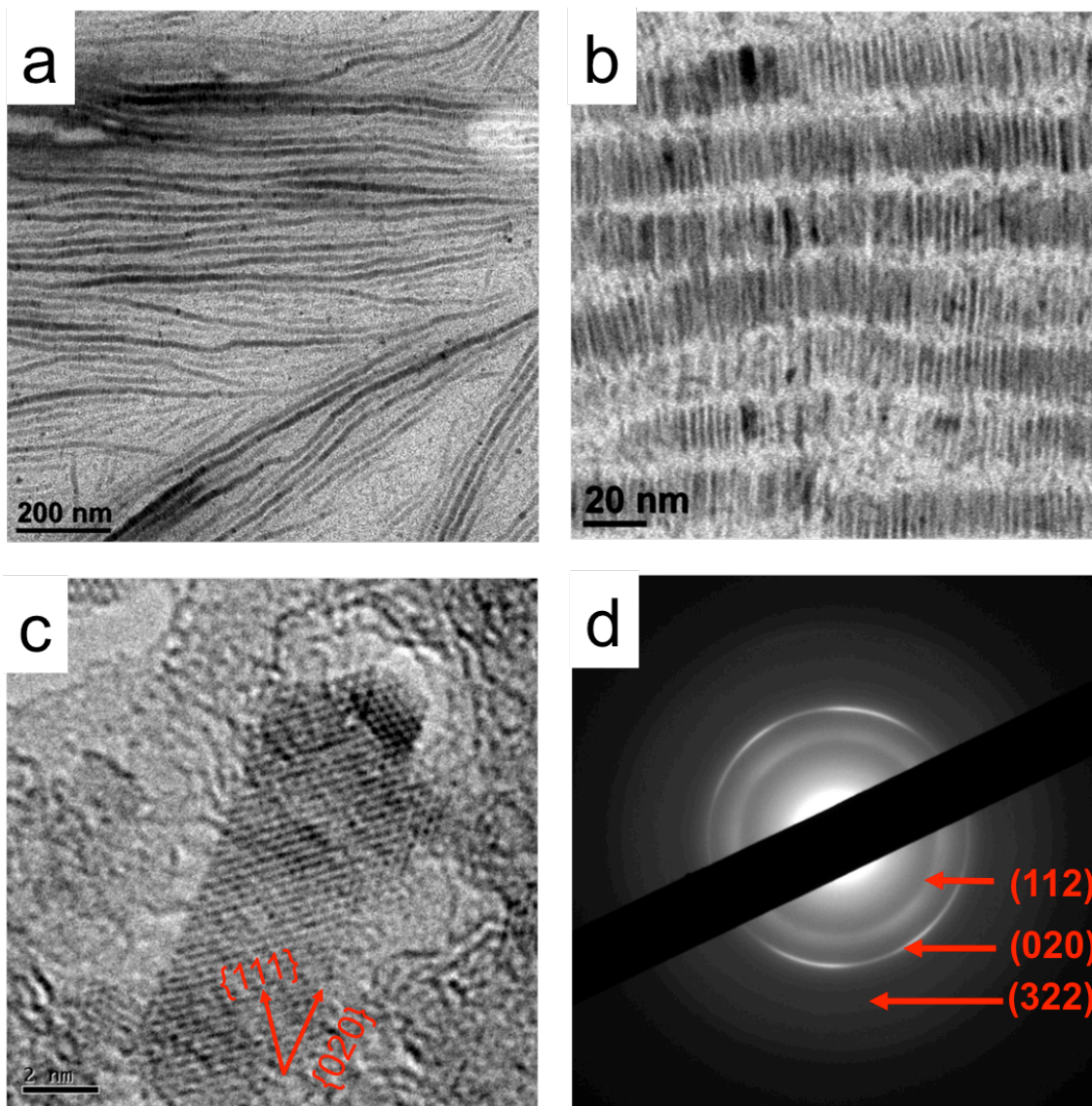


Figure 3.8. (a), (b) TEM images of aligned cobalt phosphide NRs at different magnifications. (c) High-resolution TEM and (d) electron diffraction of the NRs show growth along {020} direction.

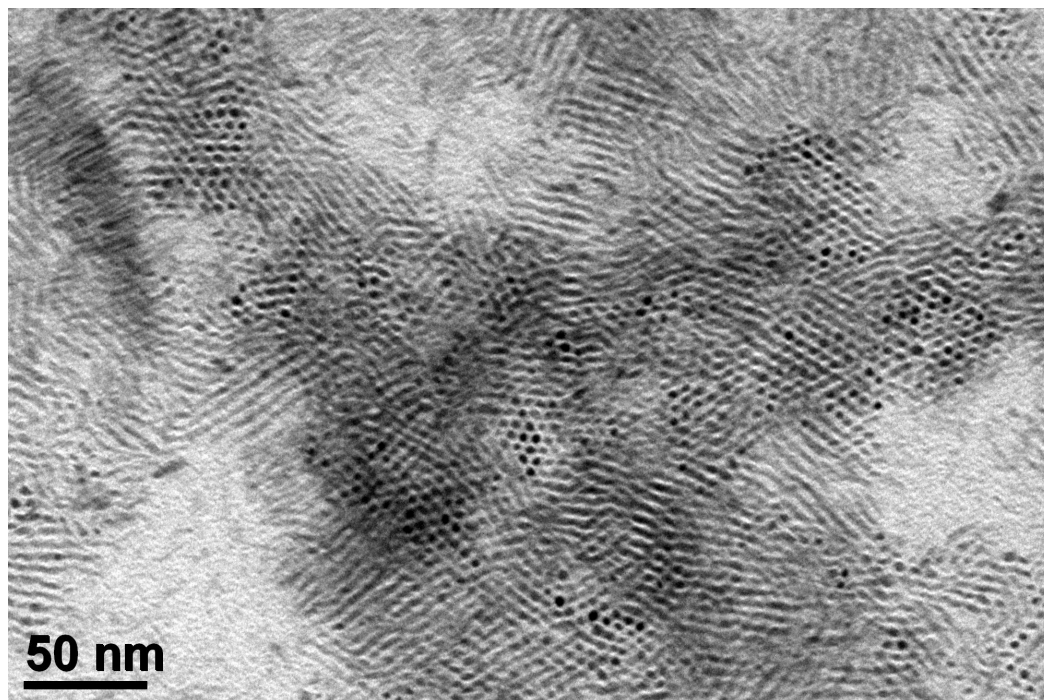


Figure 3.9. Closed-packed local ordering of vertically aligned NRs.

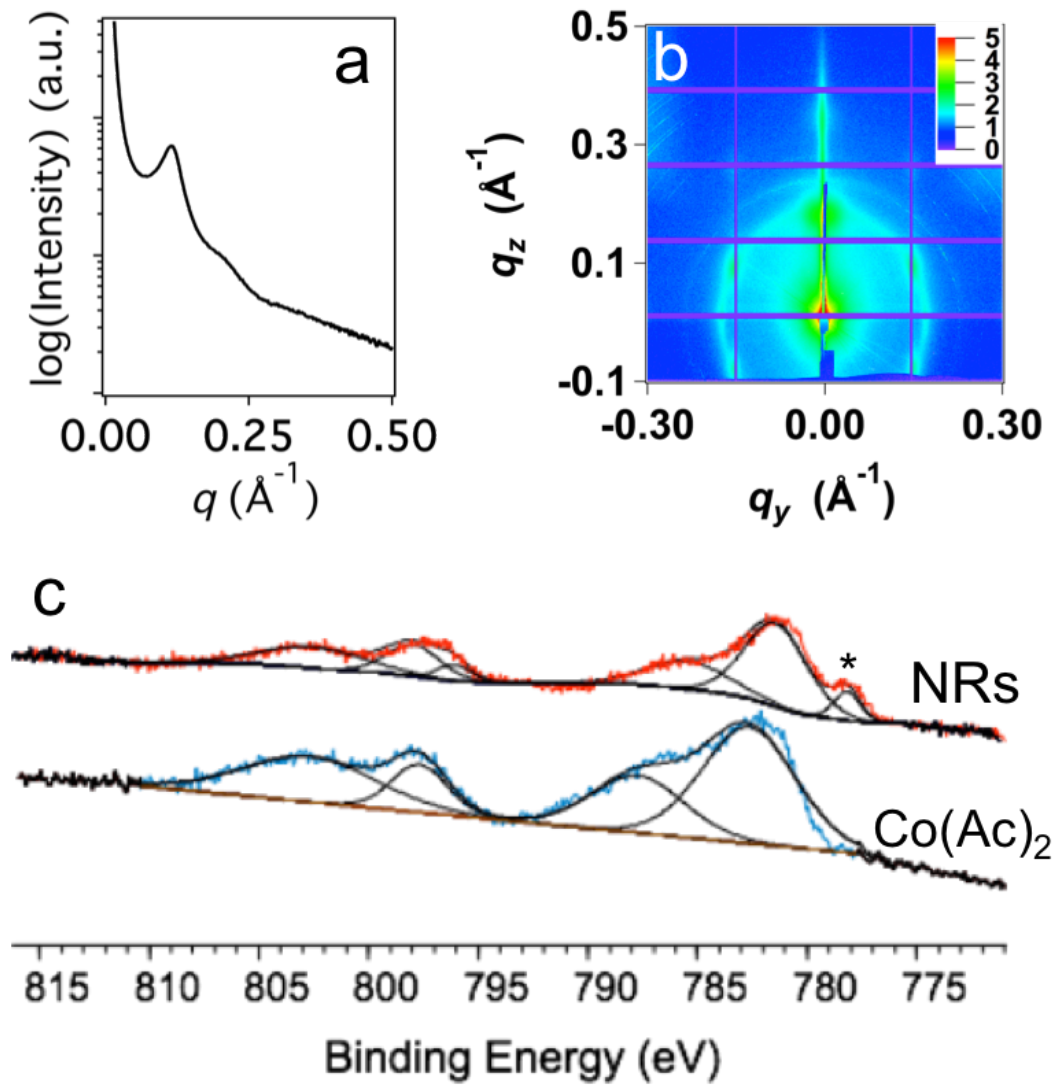


Figure 3.10. (a) SAXS of NRs, (b) GISAXS of Co_2P film on silicon wafer, and (c) XPS shows the existence of oxidized and zero-valent states of cobalt. The minority metallic peak is denoted. The signal for cobalt acetate tetrahydrate precursor (blue) is shown for comparison with the NRs samples (red).

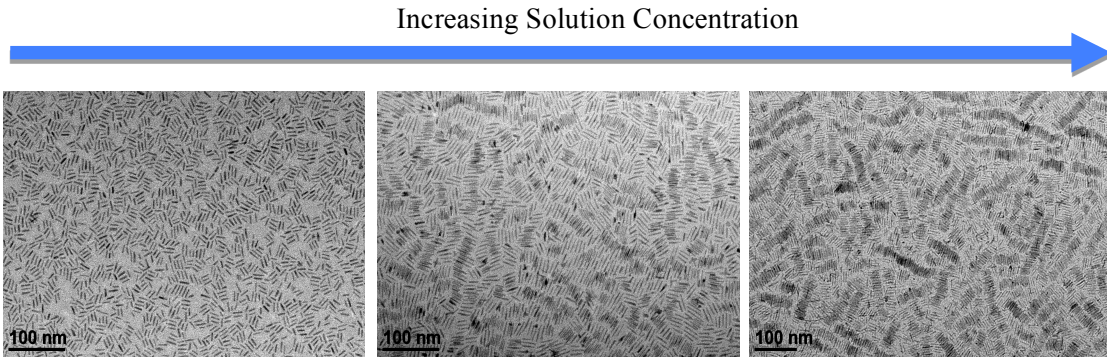


Figure 3.11. Increasing the concentration of the NRs showed a transition from isotropic placement of the particles towards an oriented lamellar alignment.

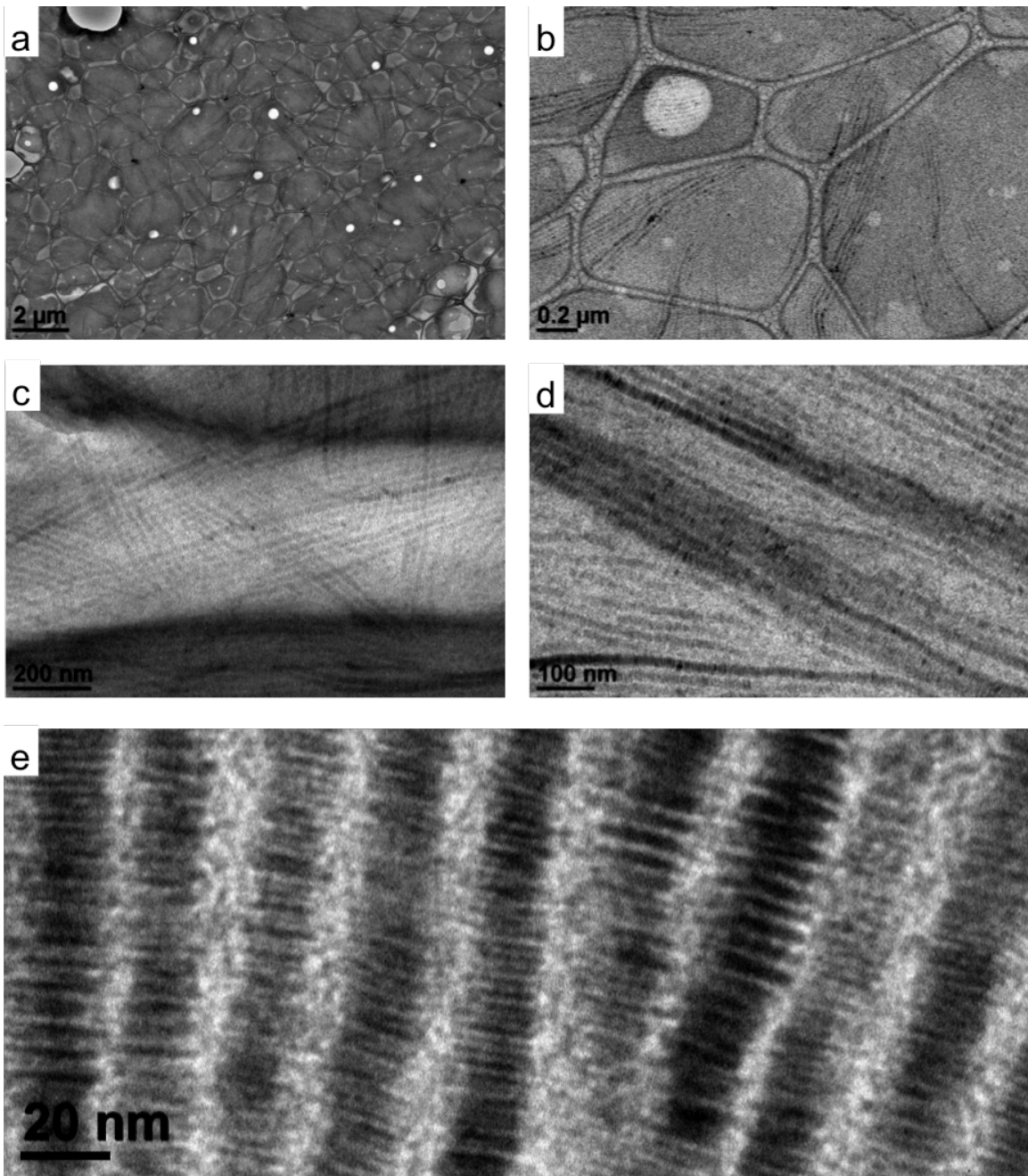


Figure 3.12. (a-e) Assembly of NRs on holey carbon TEM grid at various magnifications show face-to-face alignment of the NRs over a micrometer range.

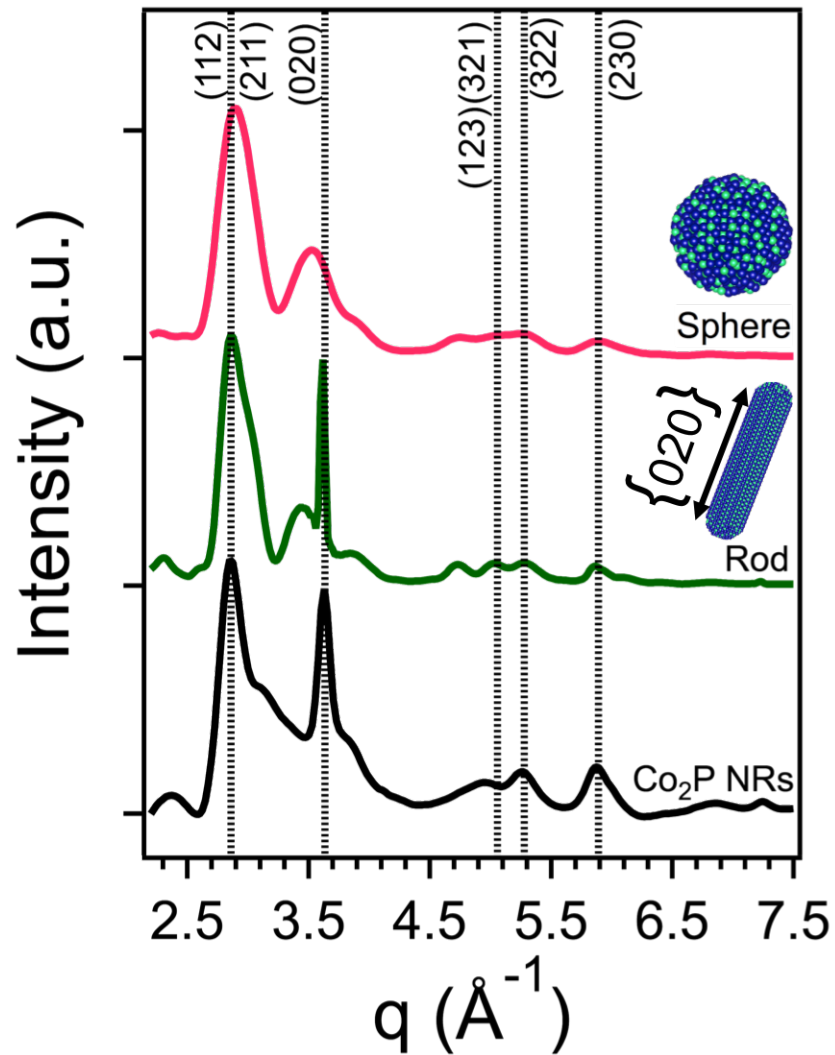


Figure 3.13. The total X-ray scattering data is shown in black. Simulation of cobalt phosphide NRs (green) confirms particle growth in the $\{020\}$ direction and agrees with the experimental data as compared with a spherical model (pink). Both models were constructed from crystal structures with the contracted b lattice parameter. Dashed black lines have been drawn onto the plot to help guide the eyes in tracing the hkl reflections.

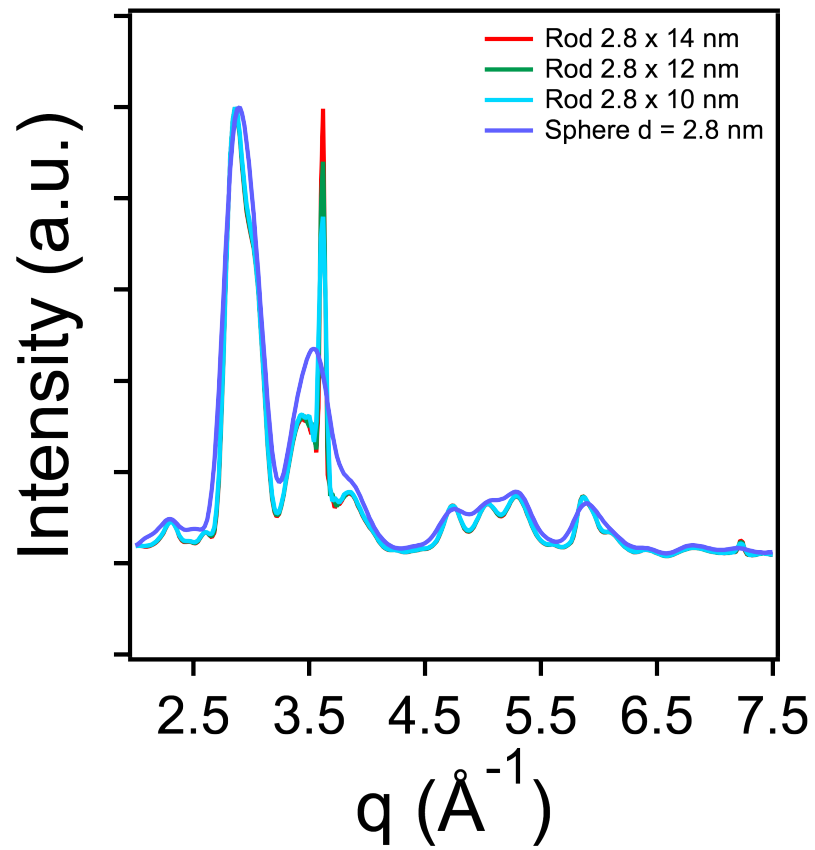


Figure 3.14. Simulated sphere and rod growth along the {020} direction with increasing aspect ratio.

Table 3.2. Reflections for cobalt phosphide NRs and Miller indices for the α -Co₂P phase.

q (\AA^{-1})	hkl
2.85	112, 210
3.07	103
3.63	020
3.86	302
4.81	402
4.96	321
5.27	322
5.87	230

Table 3.3. Atomic positions at the $4c$ site for orthorhombic Co₂P in which $a = 5.646$, $b = 3.513$, $c = 6.608$ \AA . The $4c$ site occupies the special symmetric positions of $\pm(u, 0.25, v ; 0.5-u, 0.25, v+0.5)$.

Element	u	v
Co	0.8560	0.0647
Co	0.9685	0.6657
P	0.2461	0.1249

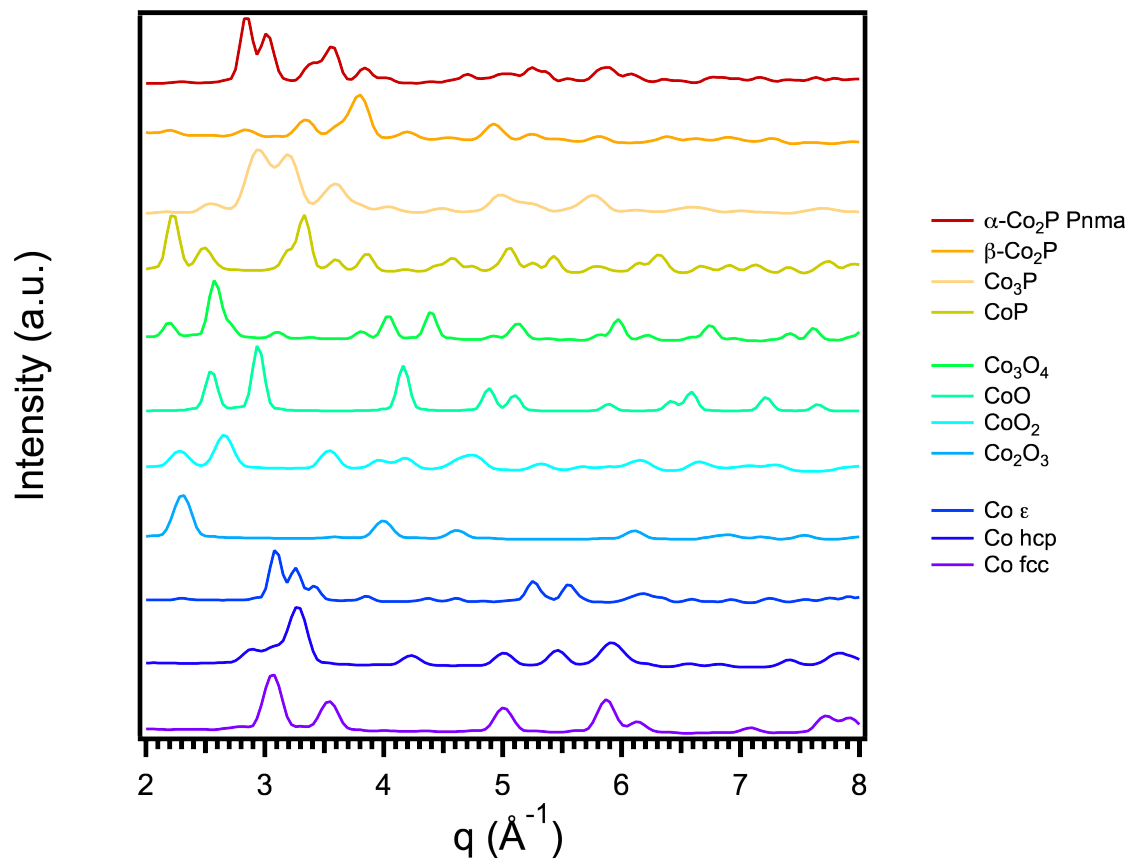


Figure 3.15. Calculated X-ray diffraction patterns for cobalt phosphide, oxide and metallic phases.

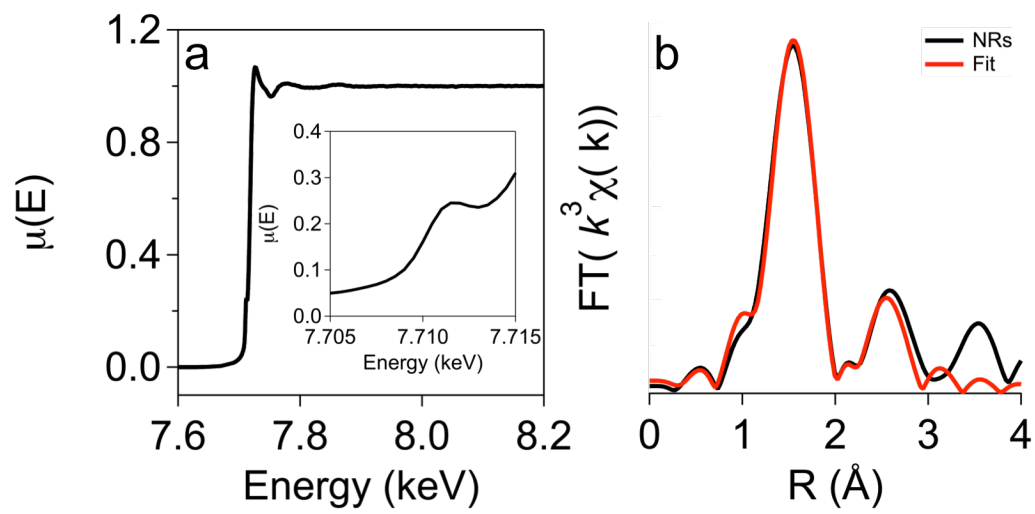


Figure 3.16. (a) Absorption with inset at the Co K-edge and (b) the Fourier transform, $FT(k^3\chi(k))$, for Co_2P NRs. The data is shown in black, overlaid with the fit in red.

Table 3.4. EXAFS fitting parameters for Co-P and Co-Co nearest neighbors using the Co₂P crystal structure. The same amplitude scaling (0.314) and ΔE_0 (-1.178 eV for Co-P, Co-Co and -4.792 eV for Co-O) parameters were used for each type of bond.

Path	N	R	σ^2	ΔR	R _{eff}
CoI-P	4	2.21673	0.00979	0.07383	2.1429
CoI-Co	4	2.47626	0.02287	-0.05334	2.5296
CoII-P	5	2.45983	0.00979	0.07383	2.3860
CoII-Co	5	2.55936	0.02287	-0.05334	2.6127
Co-O	6	2.06172	0.01291	-0.07168	2.1334

Table 3.5. Paths for undistorted bulk orthorhombic Co₂P.

Cobalt Type	Path	N	R _{eff} (Å)
I	Co-P	1	2.1429
	Co-P	3	2.2349
	Co-Co	2	2.5418
	Co-Co	2	2.6244
	Co-Co	3	2.6824
	Co-Co	1	2.7120
II	Co-P	1	2.2944
	Co-P	2	2.3988
	Co-P	2	2.5432
	Co-Co	2	2.6244
	Co-Co	3	2.6824

Table 3.6. For orthorhombic Co_2P in which $b' = 0.99b$, the single scattering neighboring pathways are summarized below.

Cobalt Type	Path	N	R_{eff} (Å)
I	Co-P	1	2.1429
	Co-P	3	2.2257
	Co-Co	2	2.5296
	Co-Co	2	2.6127
II	Co-P	1	2.2944
	Co-P	2	2.3860
	Co-P	2	2.5311
	Co-Co	2	2.6127
	Co-Co	3	2.6748

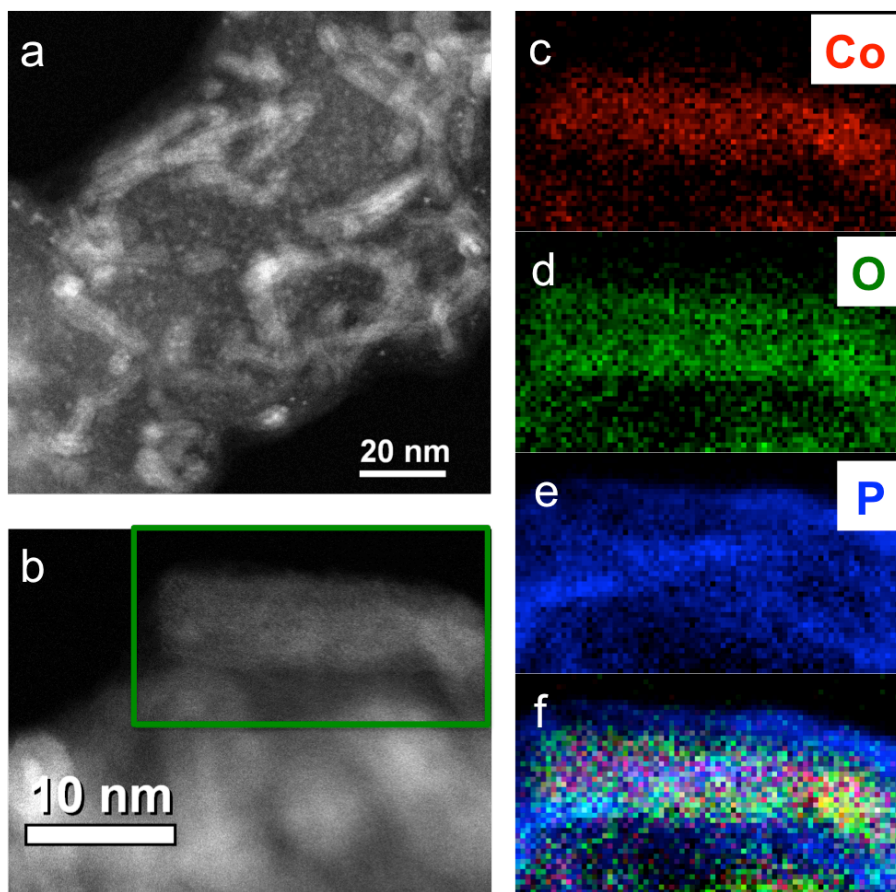


Figure 3.17. HAADF-STEM image of Co_2P NRs after thermal annealing at 180°C and under ambient pressure. (b) STEM image shows the region selected for electron energy-loss spectrometry mapping. Elemental mapping shows a core of cobalt phosphide (c) and (e) surrounded by an amorphous oxide shell (d). The combined elemental map is shown in (f).

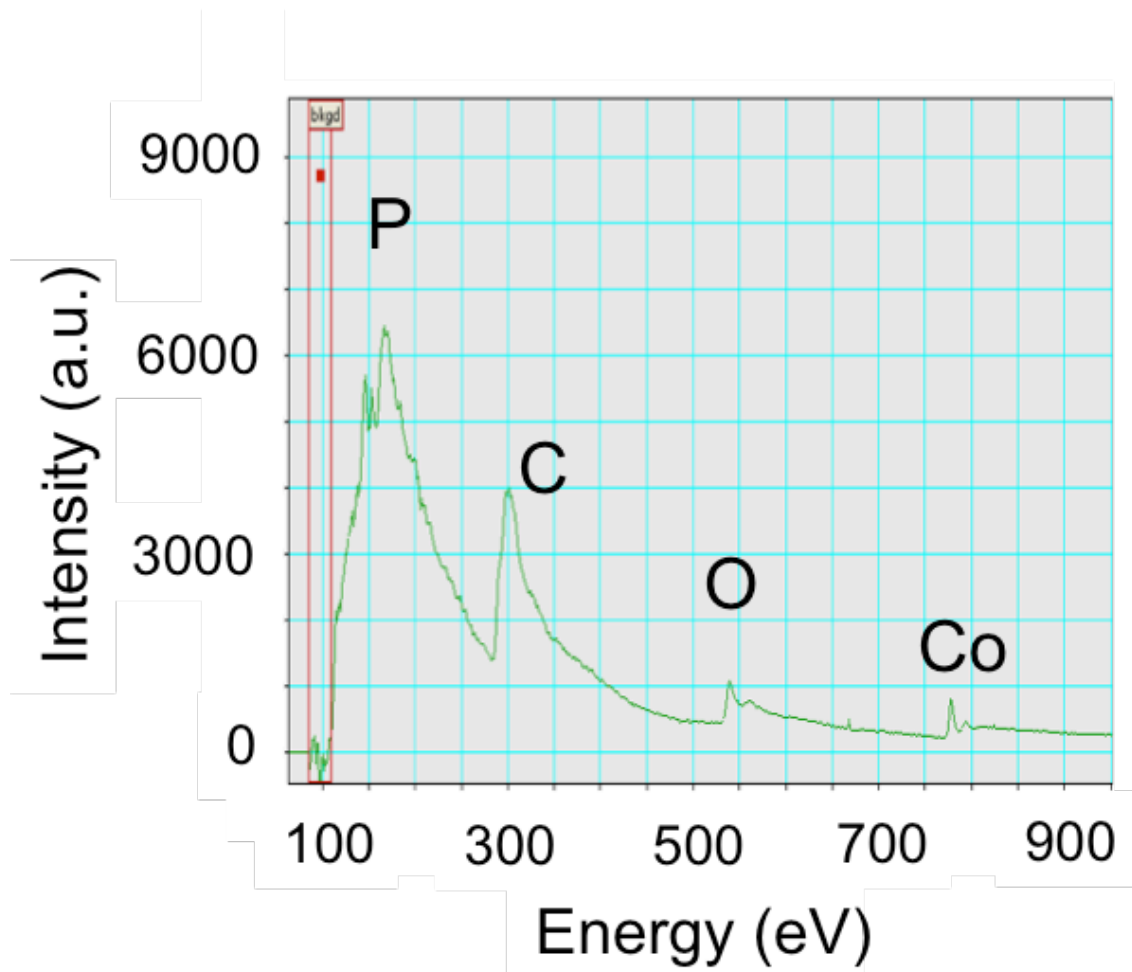


Figure 3.18. EELS spectrum for Co_2P .

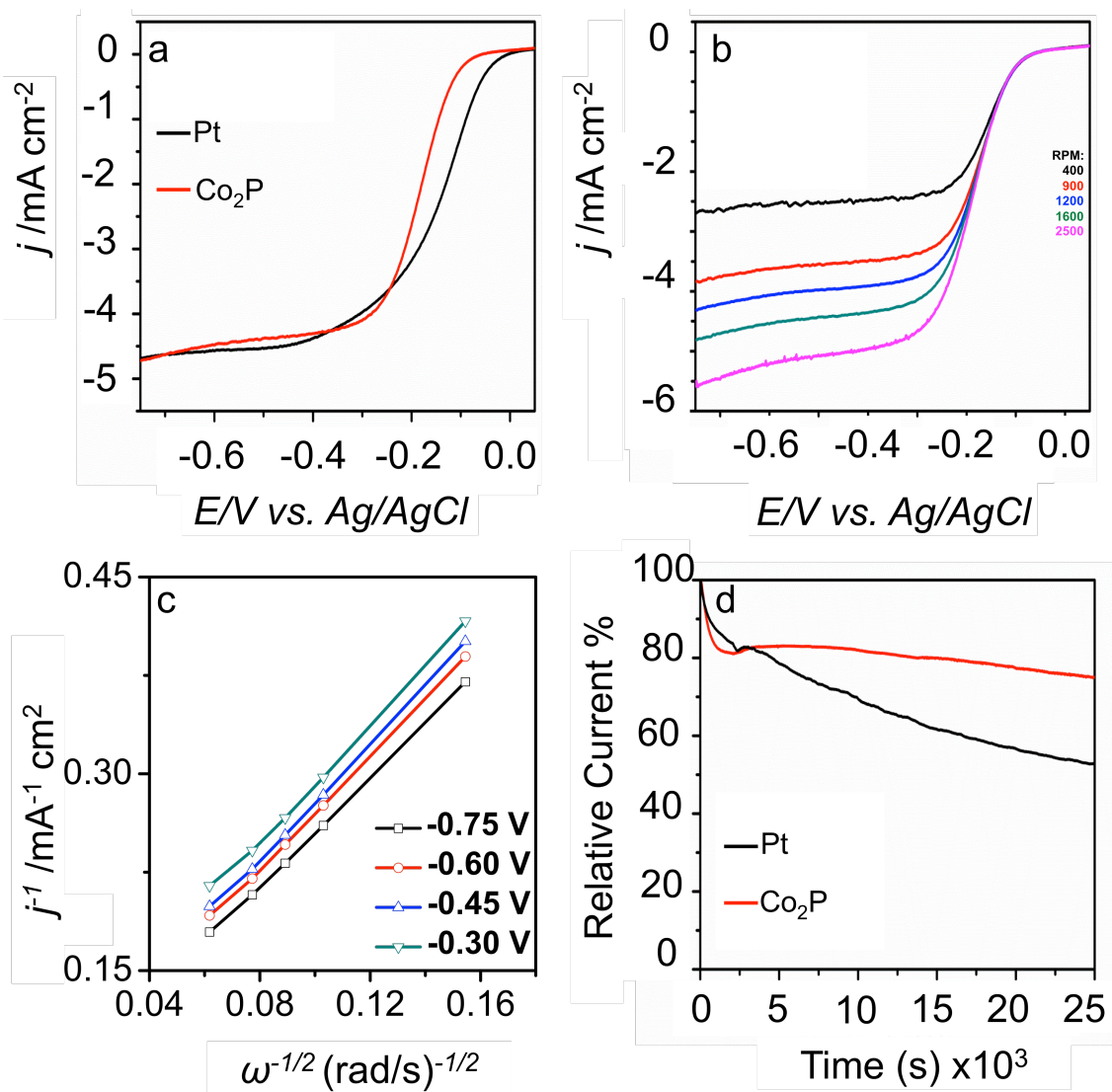


Figure 3.19. (a) ORR polarization curves of Co₂P NRs supported on Ketjan carbon as compared to commercial Pt at 1600 rpm, (b) ORR polarization curves of Co₂P NRs over a range of rotation speeds. Polarization measurements were performed in an O₂ saturated 0.1M KOH solution. (c) Koutecky-Levich plots of Co₂P catalysts and (d) chronoamperometric response of Co₂P NR catalyst as compared to commercial Pt at -0.3 V.

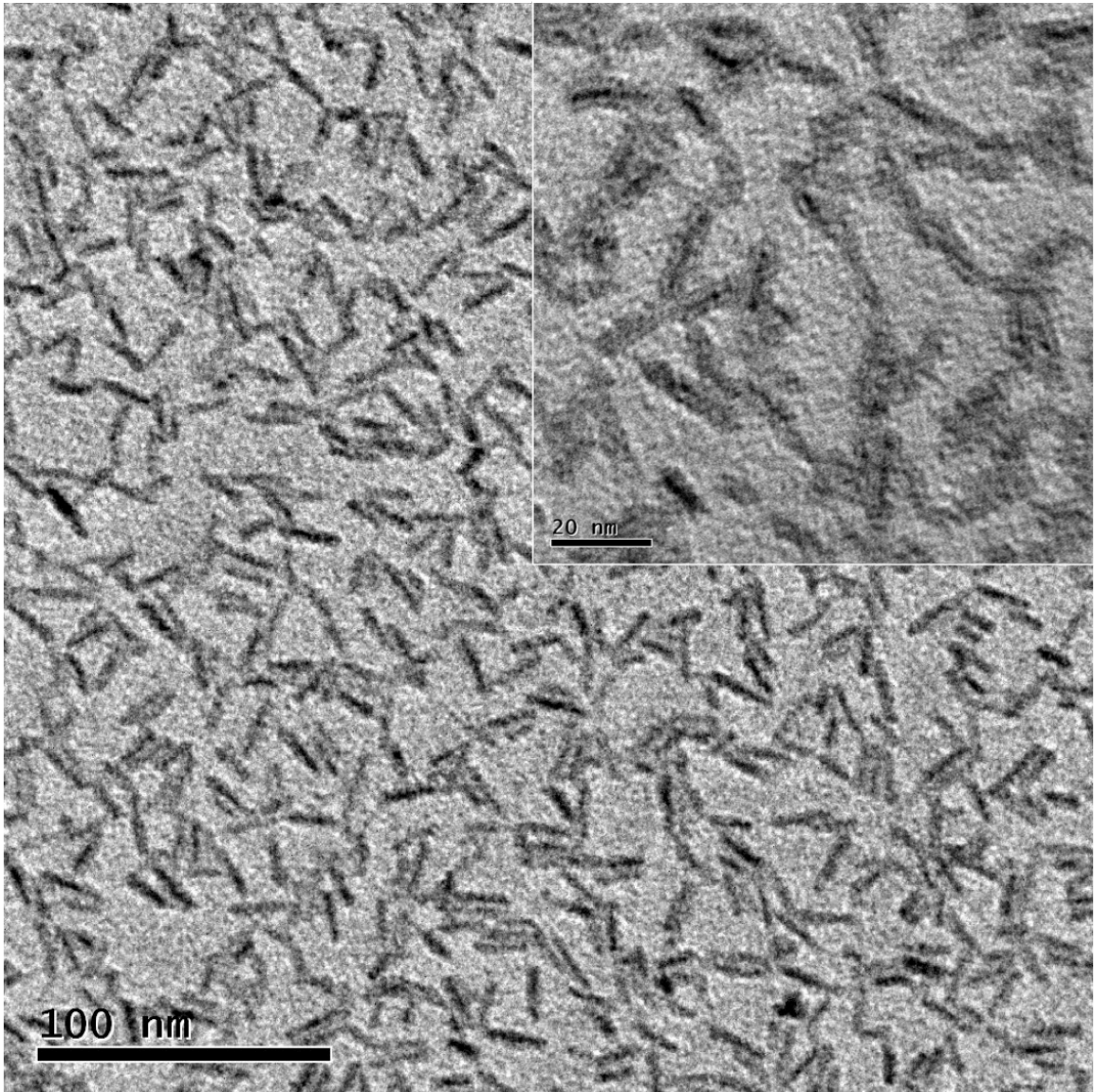


Figure 3.20. Co₂P NRs after ligand exchange with isothiocyanate.

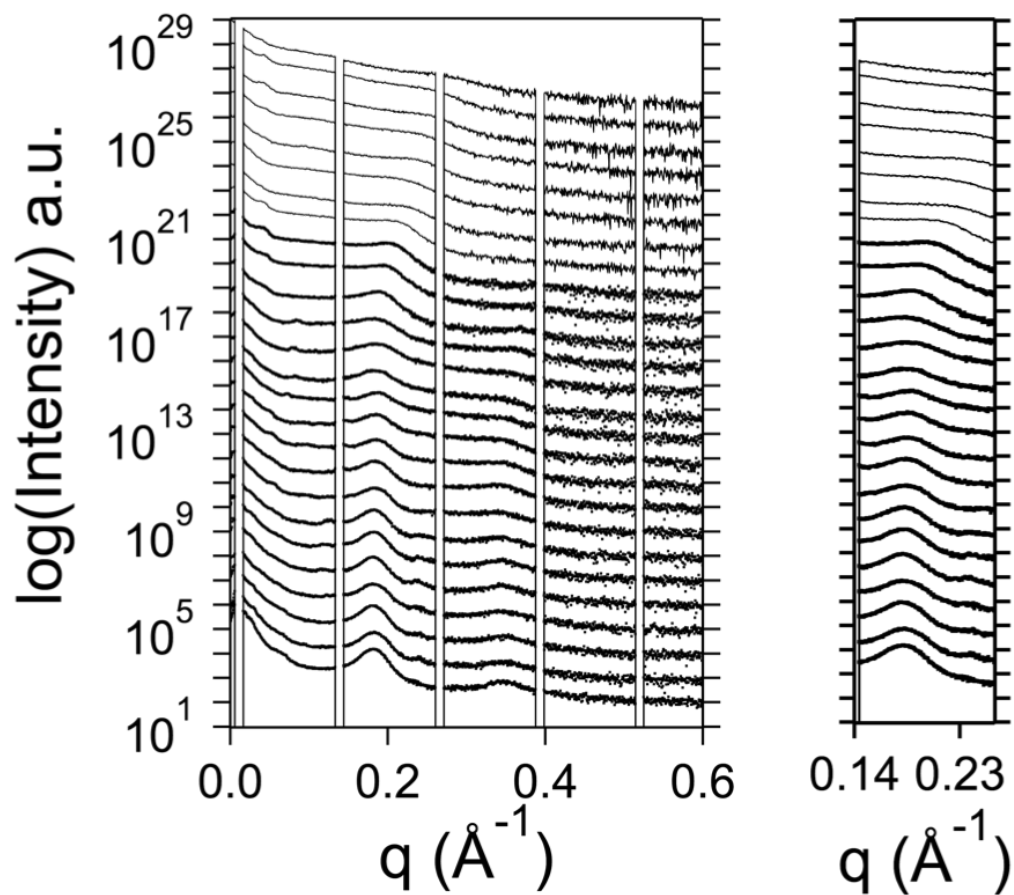


Figure 3.21. Intensity of reflected beam decreases as the temperature increased from 22°C to 147°C (increasing saturation). The first order reflection region decreases and broadens, reflecting greater disorder.

4. Structural Transition of Doped VO₂ Nanoparticle Thin Films as Probed by Extended X-ray Absorption Fine Structure (EXAFS)

Chapter 4—in part—is in preparation for submission. Structural Transition of Doped VO₂ Nanoparticle Thin Films as Probed by Extended X-ray Absorption Fine Structure.

4.1 Introduction

The thermochromic response of vanadium dioxide (VO₂) has been widely studied for its potential in optical and electronic applications.^{194–196} For smart windows applications, VO₂ is attractive due to its near room temperature semiconducting to metallic phase transition. Below the transition temperature, it is transparent in the near-infrared, and above the transition temperature, it is translucent to near-infrared. Since its monoclinic *P2₁/c* and rutile *P4₂/mmm* structures were reported in 1956 for the pure compound, additional monoclinic structures have been reported.^{197,198} The additional “M2” and “M3” phases are results of strain effects^{199–201} and/or transition metal, chalcogenide, and alkali dopants.^{202–208} Depending on the synthetic technique, the reversible metal-insulator transition (MIT) temperature of the undoped VO₂ system can vary from

63 to 78°C.^{209,210} Bulk transition temperature for VO₂ was first reported to be 68°C in 1959 by Morin (Figure 4.1).²¹⁰ The transformations are reasoned to be induced from electron-electron or electron-phonon interactions.²¹¹⁻²¹³ The dramatic transition in the optical and electronic response of doped VO₂ makes it a promising for use in metamaterial applications in which the artificial system is engineered for its emergent optical properties. In this chapter, I will discuss the local structure change in doped VO₂ thin films. The dopants were incorporated during the colloidal synthesis to ensure homogeneous distribution. X-ray absorption spectroscopy (XAFS) was carried out to understand (1) local structure of W dopant sites as well as V site from extended X-ray absorption fine structure (EXAFS), (2) orbital filling evolution as a function of W quantities from X-ray absorption near edge (XANES), (3) and deconvolution of orbital filling going through the transition temperature.

4.1.1 Synthesis and Solution Processable Thin Film Deposition

Vanadium dioxide's phase change tunability can be used as windows coatings to block absorption of infrared light for temperature control. Solution processability of vanadium dioxide thin films from VO_x nanocrystals allows for uniform coatings.²⁰⁹ The path to VO₂ production typically consists of reduction from V₂O₅ powders or high-temperature (700-1077°C) oxidation from V₂O₃ or VO.²¹⁴⁻²¹⁸ We

take advantage of colloidal synthesis to uniformly incorporate dopants into VO_x nanocrystals followed by annealing in a reduced oxygen pressure as previously reported.²⁰⁹ The controlled oxygen pressure is key to avoid a myriad of side products readily accessible given vanadium-oxygen line phase diagram (Figure 4.2).^{219,220}

4.1.2 Correlated Materials

Vanadium dioxide is the archetype for the class of correlated materials with metal-insulator transitions, some of which are highlighted in Figure 4.3. This material's thermochromic properties exhibit drastic changes optically, magnetically, structurally, and electronically. The time scale on which these transitions occur could be picoseconds.^{221–223} The focus of this chapter will be on a thermally activated correlated material—VO₂—and its transition-metal doped species. Other metal-insulator transition materials include classes of cuprates, manganites, ruthenates, iridates, and multiferroics that can be controlled via non-thermal electronic band-filling mechanisms.²²⁴ Within the electronic band model, the energy levels of insulators can be classically represented by localized electron density. Electronic structure for metals can be classically represented by broad bands with extended overlapping waves. Metals exist in between these two states with some overlap of the extended waves between atoms. The

classifications of insulators depend on the theory of the underlying cause for the metal-insulator transition: Mott-Hubbard (electron-electron interactions),²²⁵ Peierls (electron-phonon), Anderson (disorder-induced electron localization), and Bloch-Wilson (classical band theory). With the same material, the insulator classification may change depending on the probe used for inducing the transition: temperature, bandwidth, and band-filling. As Marini *et al.* have demonstrated, pressure-induced bandwidth control of VO₂ may have an electronically induced transition, which is different than the transition that occurs via temperature control.^{208,226} For more detailed discussions of metal-insulator transitions, please refer to excellent publications by N. Mott,²²⁵ D. Adler,²²⁷ and M. Imada *et al.*²²⁸

4.1.3 Physical Structure of a VO₂

The structure-driven metal-insulator transition in VO₂ relies on understanding of local structure around the V sites as well as the average crystal structure of each phase.²²¹ Vanadium dioxide's optical switchability has been modeled and studied by a library of techniques involving spectroscopy, microscopy, and electronic measurements to elucidate the structural transformation concomitant with electron localization.^{229–232} EXAFS is useful technique for probing the local structure, especially for this particular system in which a low concentration of

dopants has a significant effect on the MIT transition temperature. This structural probe has been implemented to study the anti-ferroelectric distortions of a variety of dopants in VO₂.^{208,233–235} As summarized in Table 4.1 and Table 4.2, the V-V distance dimerize into 2.65 Å and 3.12 Å in the undoped, VO₂ M1 phase from 2.88 Å in the undoped, VO₂ tetragonal phase. For the V-O distances, the more symmetric apical and equatorial bonds of 1.91 and 1.96 Å distort into distances between 1.76 Å and 2.05 Å. The unit cells for the monoclinic and tetragonal phases are shown in Figure 4.4. The V-V bonds are highlighted in Figure 4.5. In this study, we report a systematic study of using X-ray spectroscopy of the *d⁴* family of dopants and their effects on transition temperature depression as well as local structure Jahn-Teller (Peierls) distortions.

4.1.4 Electronic Structure of VO₂

The electronic structure of VO₂ can be understood by examining its V-O hybridized orbitals with crystal field theory. Goodenough in 1971¹⁹⁸ proposed the transformation from monoclinic to tetragonal phase (Figure 4.6) and electronic band structures of tetragonal and M1 VO₂ summarized pictorially in Figure 4.7. For the tetragonal phase, the hybridized *d_{||}* and *π** orbitals are split from the lower energy V 3d *t_{2g}* state. For the monoclinic M1 phase, the 2.88 Å V-V linear chains are separated into a zig-zag pattern coupled with a tilt. This results in the

splitting of the $d_{||}$ state into bonding and anti-bonding energy states. Additionally, the π^* orbital is slightly higher in energy than in the tetragonal phase.

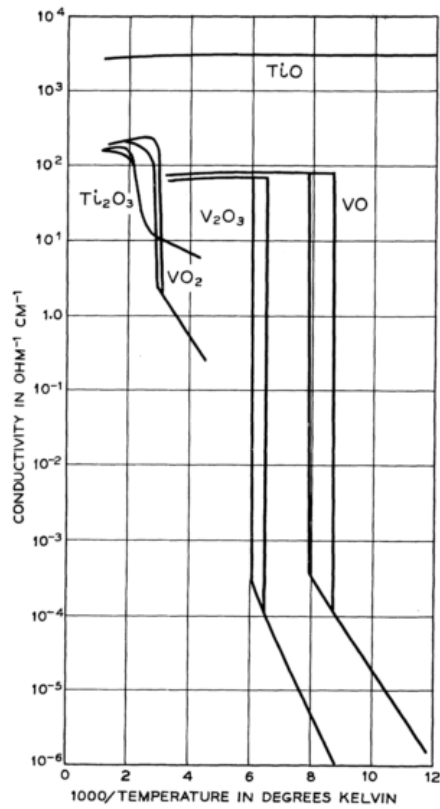


Figure 4.1. Resistivity hysteresis of VO₂ as reported by F. J. Morin.²¹⁰

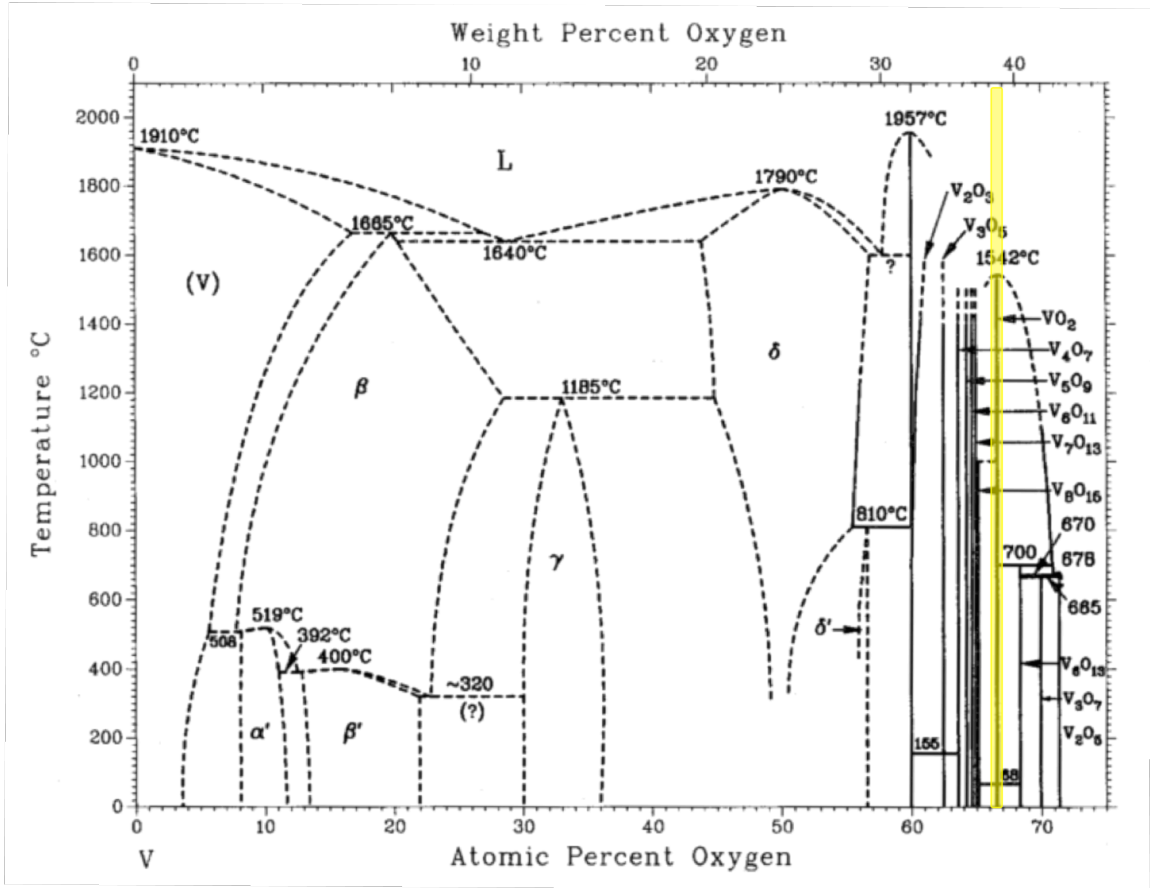


Figure 4.2. Vanadium-oxygen phase diagram with VO₂ highlighted in yellow (adapted from Wriedt).²²⁰

Table 4.1. Lattice parameters and volume of VO₂ monoclinic and tetragonal phases.

Phase	Monoclinic M1	Monoclinic M2	Monoclinic M3	Monoclinic B	Tetragonal
Space Group	P2 ₁ /c (14)	C2/m (12)	C2/m (12)	C2/m (12)	P4 ₂ /mmm (136)
a (Å)	5.743	9.0664	9.0664	12.03	4.55
b (Å)	4.517	5.797	5.797	3.693	4.55
c (Å)	5.375	4.5255	4.5255	6.42	2.88
β (°)	122.61	91.88	91.88	106.6	90
Vol. (Å ³)	117.45	237.72	237.72	285.22	59.62

Table 4.2. V-O and V-V distances for VO₂ monoclinic and tetragonal phases.

	Monoclinic M1		Monoclinic M2		Monoclinic M3		Monoclinic B		Tetragonal	
	Distance	N	Distance	N	Distance	N	Distance	N	Distance	N
V-O	1.76	1	1.86	4	1.86	4	1.65	1	1.91	4
	1.86	2	2.09	2	2.08	2	1.96	3	1.96	2
	2.02	2					1.98	1	3.45	4
	2.05	1					2.17	1	3.49	4
	3.44	4					3.52	2		
							3.58	2		
V-V							1.82	1		
	2.65	1	2.54	1	2.55	1	3.05	2	2.88	2
	3.12	1	3.43	1	3.24	1	3.36	2	3.53	8
	3.37	2					2.95	2		
	3.47	2					3.27	1		
	3.57	2					3.54	1		

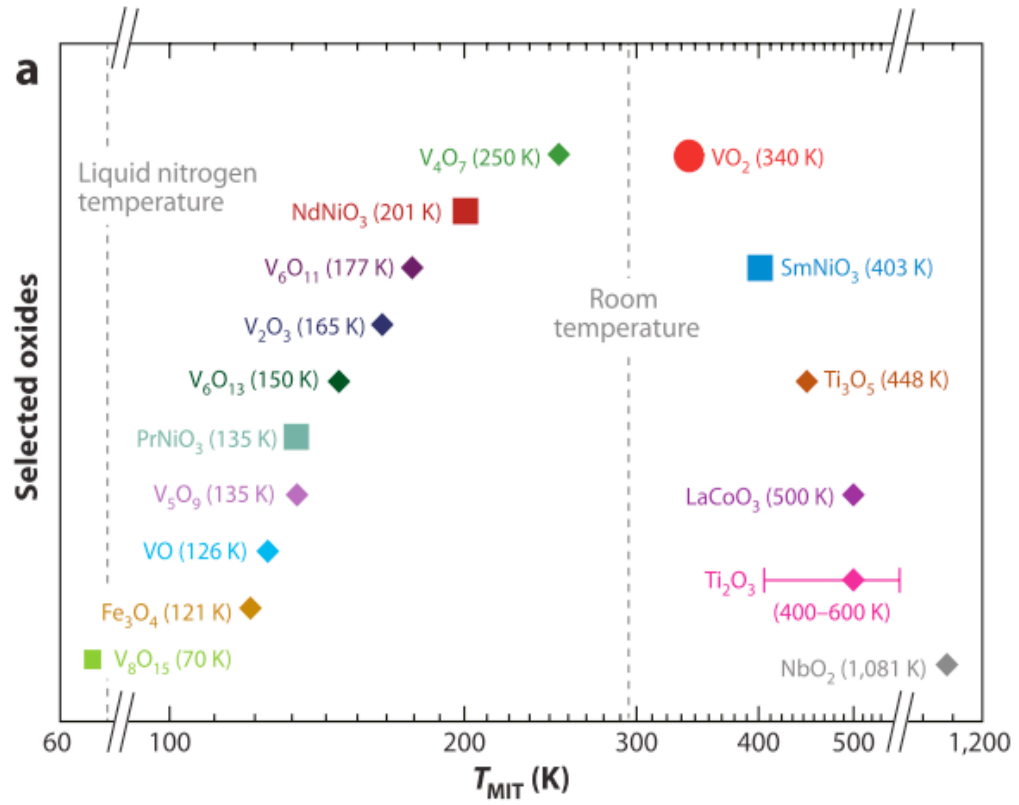


Figure 4.3. Metal oxide materials with metal-insulator transitions (adapted from Yang, Ko, and Ramanathan).¹⁹⁴

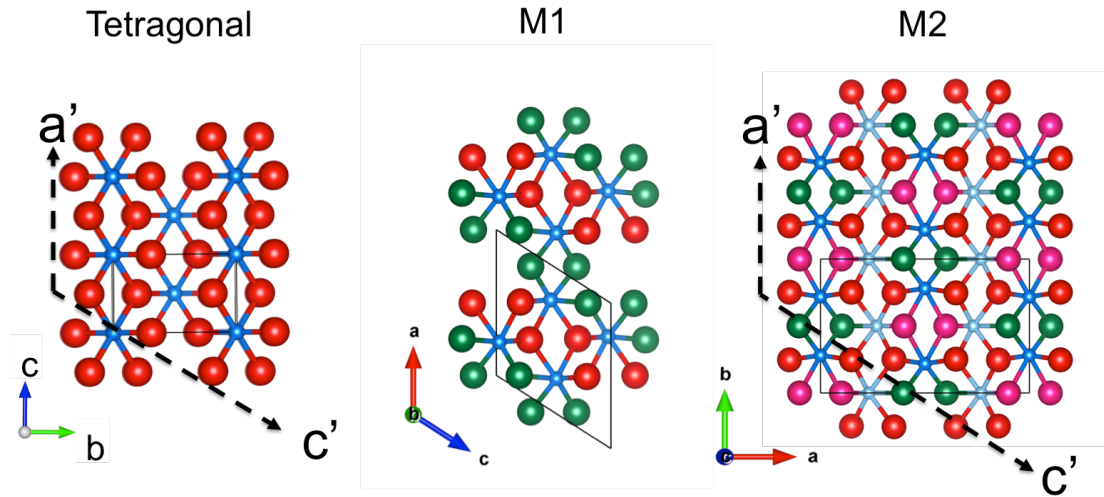


Figure 4.4. The three major phases of interest for VO_2 (tetragonal, M1, and M2) are projected onto the b or b' axes for comparison. The oxygen atoms are depicted in red, fuschia or green, and the vanadium atoms are in blue or light blue. The basis vectors for M1 and M2 can be written in relation to the tetragonal phase as

$$\text{follows. } \begin{pmatrix} a \\ b \\ c \end{pmatrix}_{Mx} = T \begin{pmatrix} a \\ b \\ c \end{pmatrix}_R \text{ in which } T_{M1} = \begin{pmatrix} 0 & 0 & -2 \\ -1 & 0 & 2 \\ 0 & 1 & 1 \end{pmatrix} \text{ and } T_{M2} = \begin{pmatrix} 0 & 2 & 0 \\ 0 & 0 & 2 \\ 1 & 0 & 0 \end{pmatrix}$$

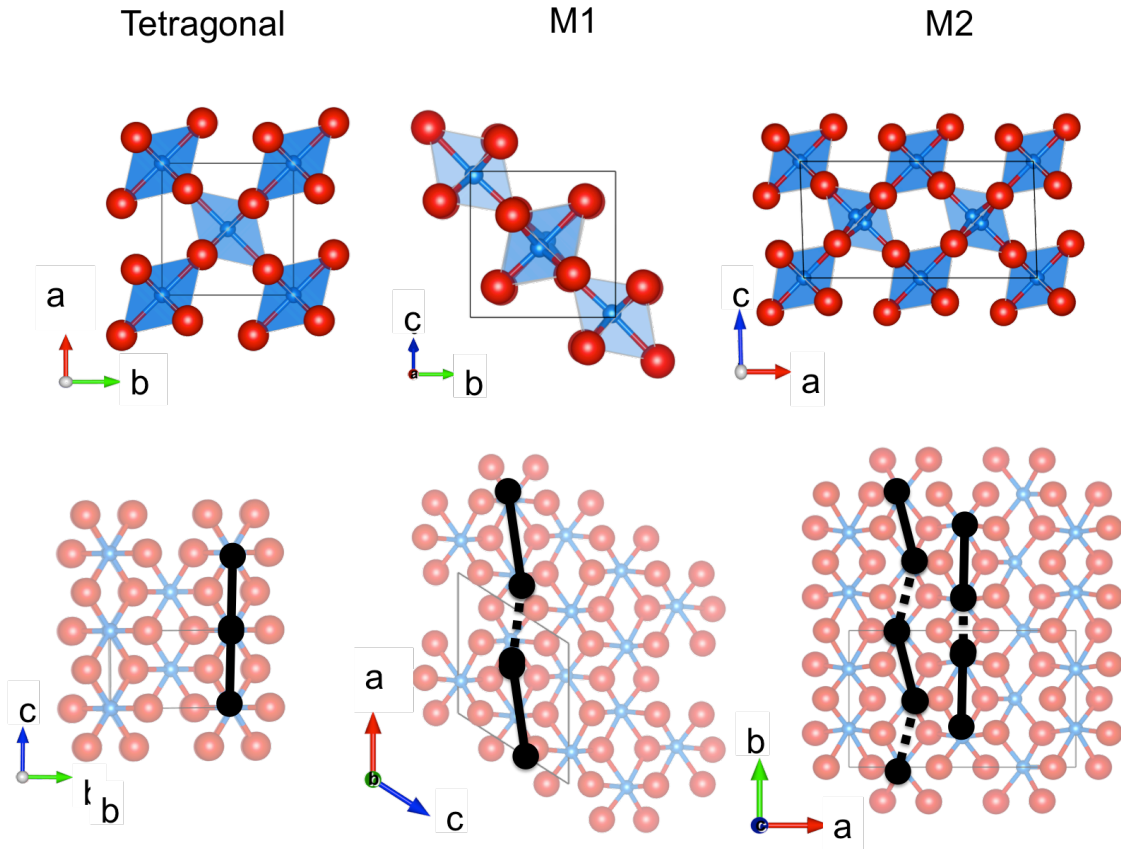


Figure 4.5. The three major phases of interest for VO₂ (tetragonal, M1, and M2) shown with the oxygen octahedral cages (top) as well as with V-V pairs highlighted in black solid and dashed lines (bottom). In contrast to Figure 4.4 which show the different atomic sites for oxygen atoms, all oxygen atoms here are represented in red.

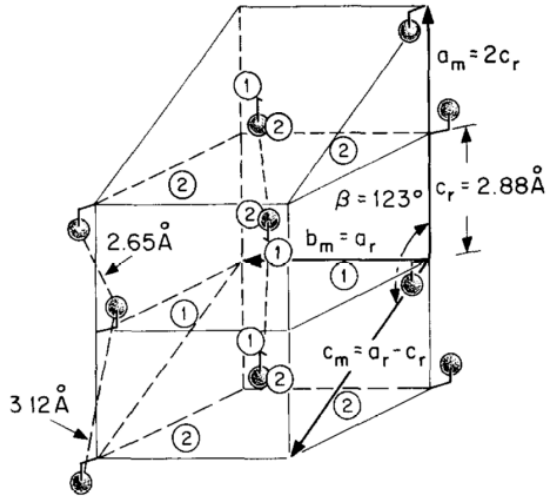


Figure 4.6. Dimerization of V-V bonds along the c axis of the tetragonal phase (adapted from Goodenough).¹⁹⁸

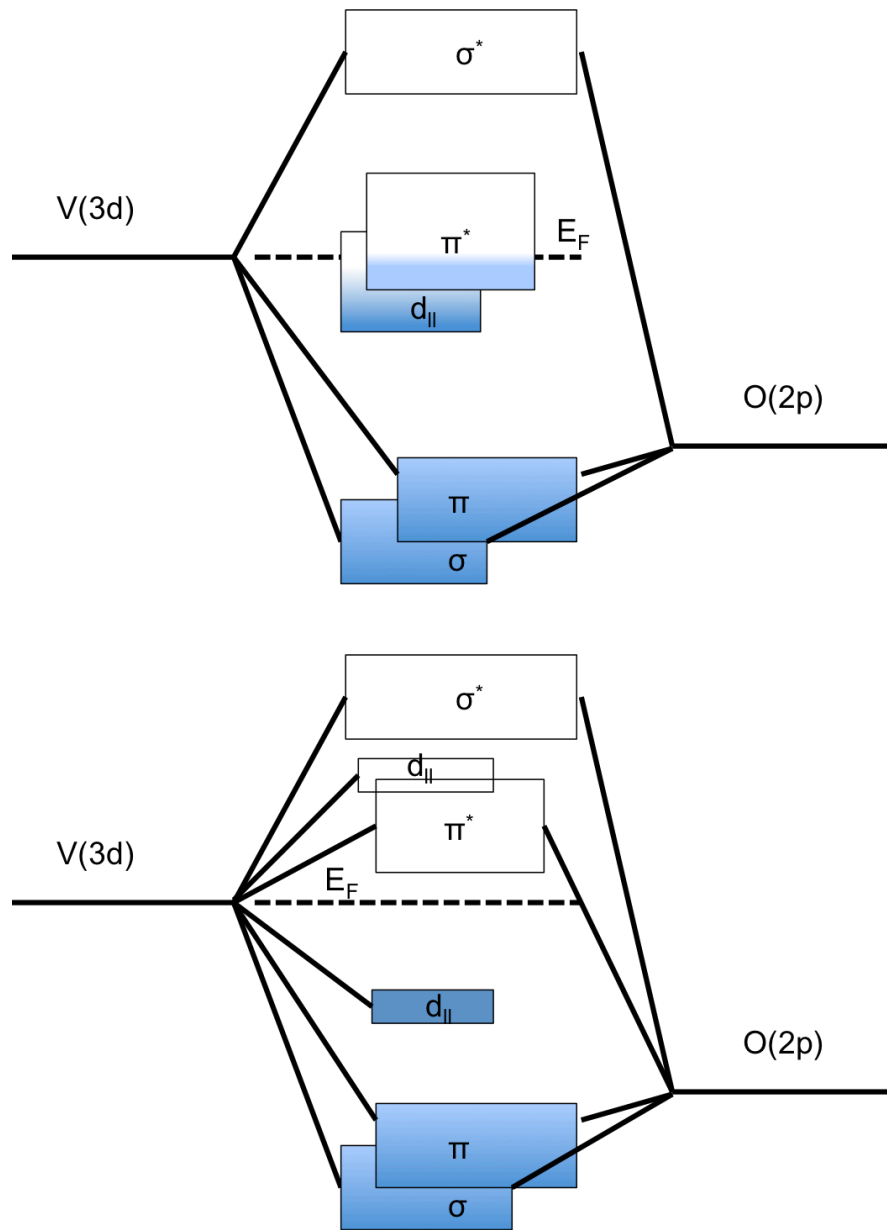


Figure 4.7. Band diagrams of V-O hybridization for the monoclinic (bottom) and tetragonal phases (top). The blue shading schematically represents the band occupancy.

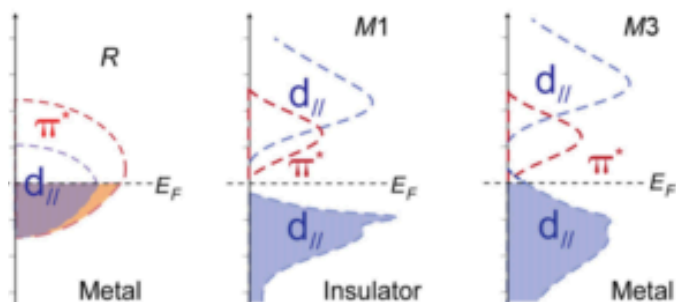


Figure 4.8. Density of states for monoclinic and tetragonal phases of VO_2 (adapted from Tao *et al.*).²³⁶

4.2 Methods

Chemicals. Vanadium oxychloride, tungsten chloride, molybdenum chloride, chromium chloride, cobalt chloride, nickel chloride, manganese chloride, iron chloride, niobium chloride, 1-octadecene, and oleic acid were purchased from Sigma Aldrich and used without additional purification.

Synthesis and Purification. The procedure for synthesis of VO_x used for generating VO_2 thin films was reported by Paik *et al.*²⁰⁹ The tungsten chloride precursor was substituted with molybdenum, chromium, cobalt, nickel manganese, iron, and niobium, and chloride. In brief, oleic acid, 1-octadecene, and dopant precursor(s) were evacuated at 100°C for 30 minutes using a Schlenk line technique for purging and refilling with nitrogen. After degassing, the solution was exposed to

air and the temperature was increased to 200°C. At this point, vanadium oxychloride precursor was injected and aged for 20 minutes. The VO_x nanocrystals were collected, washed with ethanol and centrifuged at 7000 RPM to remove the supernatant. After centrifugation, the nanoparticles were re-dispersed in hexane. ICP measurements were done using a Spectro Genesis spectrometer with a concentric nebulizer. The operating conditions are as follows: RF power: 1350 W; plasma Ar flow rate: 13.50 L/min; auxiliary Ar flow rate: 1.00 L/min; nebulizer flow rate: 0.9 L/min. For each metal, calibration standards were made ranging in concentration from 0.1-50 ppm. The dilutions were used to make a regression curve for intensity vs. concentration. The unknown sample concentrations were calculated using this regression.

Characterization. For electron microscopy, the nanoparticles were deposited on 300-mesh carbon-coated copper grids purchased from Electron Microscopy Sciences purchased from Ted Pella, Inc. TEM was done on a JEOL 1400 TEM with a LaB₆ filament, operating at 120 kV and equipped with an SC1000 ORIUS CCD camera and Digital Micrograph software.

High-resolution X-ray powder diffraction was done at Advanced Photon Source (APS) 17-BM-B at Argonne National Laboratory with 17.00524 keV beam corresponding to a wavelength of 0.72910 Å. Sample to detector distance was 30

cm. Background contributions from the Kapton capillary tube were subtracted from the data.

EXAFS was done at Advanced Photon Source 12-BM-B and 20-BMB. The same nanocrystal thin films used in diffraction measurements were used in X-ray absorption measurements in fluorescence mode. The incident X-ray beam was tuned using a Si (111) double crystal fixed exit monochromator, and higher-order harmonics rejection was achieved with a coated mirror. The absorption was measured in focused beam mode from the V K-edge and W L_{III}-edge and calibrated by normalization of the pre-edge and post-edge from vanadium and gallium foils, respectively. The ΔE_0 shift from V and Ga foil references, collected before each set of measurements, were used for all samples. The V absorption K-edge was calibrated to be 5.46376 keV as reported by Kraft *et al.*¹⁸⁶ EXAFS collection parameters at the V K-edge and W L_{III}-edge are summarized in Table 4.3 and Table 4.4, respectively. XANES scans at the V K-edge are summarized in Table 4.5. Photographs of the experimental setup, furnace cell dimensions, and cryostat are provided in Appendix F.

Table 4.3. EXAFS data collection k weighting and time at the V K-edge at 5463.76 eV for a total of 534 points.

Energy from Edge (eV)	Step Size (\AA^{-1})	Integration Time (s)	Weight
-150 to -10	5	1	1
-10 to 40	0.2	1	1
40 to 971.41	0.05	1	1

Table 4.4. EXAFS data collection k weighting and time at the W L_{III} -edge at 10207.00 eV for a total of 415 points.

Energy from Edge (eV)	Step Size (\AA^{-1})	Integration Time (s)	Weight
-150 to -20	5	2	1
-20 to 50	0.5	2	1
50 to 973.38	0.05	2	1.2

Table 4.5. XANES data collection k weighting and time at the V K-edge at 5463.76 eV for a total of 337 points.

Energy from Edge (eV)	Step Size (\AA^{-1})	Integration Time (s)	Weight
-150 to -10	5	1	1
-10 to 40	0.2	1	1
40 to 307.98	0.10	1	0

Six to sixteen fluorescence scans were averaged for the reported absorption intensity using ATHENA, an open source package for spectroscopy analysis.⁵¹ Analysis was done during the *ab-initio* package ARTEMIS⁵¹ and structure models were created using ATOMS⁵².

4.3 Results and Discussion

4.3.1 Bragg Diffraction and Optical Switching

The VO₂ films were first characterized with X-ray diffraction to confirm the transformation from amorphous VO_x to VO₂. In annealing the VO_x nanocrystals into VO₂ from 50 to 500°C (Figure 4.9) under reduced oxygen environment (1 mTorr), *in-situ* powder diffraction revealed there was a transformation and sintering at 435°C (Figure 4.9). The temperature ramp is shown in Figure 4.10. The phase transformation to VO₂ (ICDD PDF# 82-0661) is complete beginning at 500°C as shown in Figure 4.11. After annealing at this temperature for 20 minutes, the particles coarsen and line widths are significantly much more narrow than that of VO_x nanocrystals annealed as thin films on quartz substrates. Annealing the VO_x nanocrystals under ambient conditions; however, produced a sintered V₂O₃ phase, which is stable for 50 minutes at 500°C as shown in Figure 4.12. Subsequent annealing revealed a coexistence of the V₂O₃ and VO₂ phases as

the material transformed to pure VO₂ (Figure 4.13). To avoid the mixture of these two phases, it is advisable to anneal under reduced oxygen pressure to obtain VO₂.

The XRD patterns in Figure 4.14 tracks the shift in q of the M1 (011) peak as a function of dopant concentration. A shift of 0.011 Å⁻¹ is observed for the end members of the doping series (7.2×10^{-3} Å⁻¹ per atomic percent of W). The structural transformation of W on VO₂ is a dramatic change as the monoclinic M1 (011) peak shifts towards the tetragonal (110) peak. Ascertained from Table 4.6, there is slight variability in the full-width half-maximum values for the Voigt fits of the (011) peak. The Gaussian and Lorentzian components are summarized in Table 4.7. Despite the dispersion, the doping effect is linear with respect to atomic percent inclusion into the VO₂.

The hysteresis of the properties response is observed when comparing the direction of the change in temperature (heating or cooling) as shown in Figure 4.15. Transmittance in the infrared region is often tracked in optical spectroscopy. The observed transmittance at 2000 nm for the solution processable doped VO₂ thin films are shown in as a function of temperature. The thin films were deposited on a quartz substrate, which was background subtracted from the thin film signal. The hystereses were fit using a sigmoid function, and the first

derivative is shown in Figure 4.16 for the W-doped series. The inflection point in each sigmoid are plotted in Figure 4.17, which shows a transition temperature depression rate of 28.58 degrees (heating) or 13.62 degrees (cooling) per atomic W doping percent. This is in agreement with previous reports of W-doped VO₂ in which the transition temperature depression were approximately 20-28 degrees per atomic percent.^{196,235} The linear regressions are summarized in Table 4.8.

4.3.2 Local Structure of W-doped VO₂

The X-ray absorption spectra in Figure 4.18 are shown in greater detail in Figure 4.19a, which depicts the energy increase in the position of the pre-edge peak centroid. The k^3 -weighted $\chi(k)$ (Figure 4.19b) shows the differences not only in the intensity but also the phase signal of the samples below (solid lines) and above (dashed lines) their MIT temperatures. The Fourier transforms (Figure 4.19c) show the stark differences in which the higher symmetry tetragonal phase has fewer number of peaks in the 1-2.5 Å region, thus corresponding with fewer unique V-O distances in the local structure. For the trend is consistent for increasing amounts of tungsten from 0.2% to 0.7%. One would expect this to proceed increasing from 0.7% to 1.4%. However, the 1.4% W-doped samples were measured at -249 °C, which is well below the transition temperature of 6°C.

Select temperatures were chosen for the EXAFS to capture the phases below or above their transition temperatures. Temperature control available in the experimental hutch was a cryostat system (Pfeiffer vacuum and Neocera temperature controller) that allowed for easy and rapid access to -249°C with helium exchange gas. The existence of the M1 phase at low temperatures is in accordance with previous reports of doped VO_2 . As Marini *et al.* 2013 demonstrated for Cr-doped VO_2 system, at temperatures $< 223^{\circ}\text{C}$, the doped samples still exist as monoclinic M1 structure as opposed to the more frustrated M2 or M3 phases.²⁰⁸

A rough estimate of the density of states can be seen in the shaded region of Figure 4.19a. The shaded region can be treated as the difference in the occupancy of the hybridized bands between the monoclinic and tetragonal phases. Normalizing the difference to one for the controlled, undoped VO_2 sample, the integrated area differences are plotted in Figure 4.20 for the W-doped samples. While there is a linear dependence on atomic concentration for this set of samples in this doping range, previous reports by Whittaker *et al.* have claimed two fitting ranges in which there is a linear dependence up to a threshold of approximately 1% W doping. Beyond this amount, the transition temperature based on differential scanning calorimetry (DSC) reaches a plateau and there is

less significant depression of T_c .²³⁵ This could be reasoned with a “nano puddles” model in which the effects of W reaches a plateau at a certain percolation threshold.²³⁷ However, Tan *et al.*²³⁴ later reported a single linear relationship up to 2.38% of W doping. Both methods relied DSC measurements. However, the synthetic conditions for Whittaker *et al.* involved hydrothermal treatments for 12 hours to 7 days with V_2O_5 precursors while Tan *et al.* started with vanadyl acetylacetonate with subsequent calcination under an inert atmosphere. As reviewed by Gao *et al.*¹⁹⁶, transition temperature and hysteresis widths are highly sensitive to synthesis and processing conditions. Thus, it is advisable to compare each sample set internally due to the materials’ inherent stress and strain.

The Fourier transforms of the EXAFS were fitted with the M1, M2, or tetragonal phase of VO_2 as shown in Figure 4.21. The V-O and V-V bonds used in the fitting procedure are summarized in Table 4.9 and Table 4.10 with “goodness of fit” reported in Table 4.11. The V-O bonds in the monoclinic M1 phase were separated in two groups based on the bulk values of the half-path length. Due to limitations in the k -range and R -range, the Nyquist criterion for number of independent variables was met maintaining a constant reduction amplitude for all V-O and V-V bonds. Only ΔE_0 , ΔR , and σ^2 were input as fitting parameters.

The structural distortions from inducing tungsten substitutional dopants have been demonstrated from V K-edge EXAFS analysis. The W L_{III}-edge confirms the influence of W dopants on the VO₂ matrix towards a more tetragonal structure with increasing W concentration. For 0.2% W, $k^3\chi(R)$ shown in Figure 4.22 maintains the M1 structure. However, the 1.4% W-doped VO₂ sample has a tetragonal structure based on the collapse of the V-O peaks between 1 and 2 Å into one peak. As expected for a more symmetric environment, the $k^3\chi(R)$ at the L_{III}-edge was fitted to a tetragonal WO₂ model with the apical and equatorial W-O bonds represented as one distance and the W-W bonds as 2 distinct distances. Similar constraints were imposed on the fitting procedure for the W L_{III}-edge as the V K-edge. For the k range of 9 Å⁻¹ and R range of 1-3 Å, the reduction amplitude was restricted at a constant value of 0.67.

4.3.3 Structural Hysteresis of Doped VO₂

The 0.2% W-doped VO₂ sample was chosen for structural transition comparison against the control of the undoped sample. Starting at 79.4°C, XANES data was collected during slowly cooling undoped VO₂ powder (Figure 4.23a with spline background subtraction in Figure 4.23b and first derivative shown in Figure 4.23c). A list of the full temperature range for the VO₂ data set is provided in Table 4.12. EXAFS data for 0.2% W-doped VO₂ was collected for the sample at

25°C, 55°C, 62°C, 71°C, and 100°C. These temperatures are within the regions of interest: plateaus beyond the transition, near the inflection point, and at the inflection point. XANES scans collected at intermediate temperatures capture the pre-edge centroid shift towards higher energy as well as a decrease in overall intensity. For both undoped and doped VO₂ systems, the pre-edge peak also becomes more symmetric as the V(3d)/O(2p) bands become more filled due to the increase in temperature (Figure 4.24a). The centroid shifts are captured first zero-crossing first derivative of $\chi\mu(E)$ (Figure 4.24b). The XANES scans were aligned according to the E_0 shift from the vanadium reference foil. This reference foil data was collected simultaneously with the sample by the usage of a secondary detector, which was positioned in line behind the first detector. Calibration of the vanadium K-edge was first performed with the scan at 79.4°C and set to 5463.76 eV in accordance with Kraft *et al.*¹⁸⁶ Proper alignment in the ΔE_0 shifts was performed for all scans in the temperature series. The aligned series capture the isobestic points in the absorption spectra at 5466.9 eV and 5472.4 eV (Figure 4.23a). The pre-edge peaks can be deconvoluted into two peaks that correspond to the electron transitioning from V 1s to the hybridized t_{2g} (A1) and e_g (A2) orbitals to track the change in the density of states. For historic reasons, these peaks are labeled as A1 and A2.²³⁸ The Gaussian fits of the

deconvoluted peaks are shown in Figure 4.25. The fits for the starting and end temperatures are shown for clarity Figure 4.25a-b with more select set of temperatures shown in Figure 4.25c and fractional areas in Figure 4.25d. The first-order transition at 65°C is captured in the arctangent fit of the fractional areas of A1 and A2 of their sum. Similarly, $A1/(A1+A2)$ and $A2/(A1+A2)$ for the 0.2% W-doped VO₂ samples shown in Figure 4.26 show a transition at 66°C. It should be noted that the transition temperature for the bulk sample is similar to that of the W-doped VO₂ samples. However, the two samples were prepared under different conditions. The increase in transition temperature can be attributed to strain built into the sample during the thin film preparation for doped VO₂. While nanocrystalline VO₂ have been shown to have an effect on transition temperature depression, the annealed films have grain sizes on the order of hundreds of micrometers, thus ruling out a finite size effect. The grain sizes were calculated to be 171 +/- 24 nm, 320 +/- 84 nm, and 260 +/- 29 nm from the width broadening of the Voigt fits at (011), ($\bar{2}02$), and (200) peaks.

4.3.4 Oxidation States of W-doped VO₂

In the XANES region, the peaks of the V K-edge as highlighted in the magnified plot in Figure 4.18b track the dipole-allowed 1s to 4p transition. As previously reported by Wong *et al.*²³⁹ and Giuli *et al.*²⁴⁰ for vanadium-oxygen compounds

(VO, V₂O₃, V₂O₄, V₄O₇, V₂O₅), both the pre-edge and post-edge profiles and peak centroids are indicative of differences in the V oxidation states according to Kunz's Law. For pristine octahedral symmetry, the pre-edge peak in the XANES region is absent.^{239,241} In the W-doped VO₂ samples, the shift to higher energy in the pre-edge peak and concomitant shift to lower energy in the post-edge peaks correspond to a decrease in oxidation state of V due to W dopants further breaking of octahedral symmetry at V⁺⁴ sites. The deviation from octahedral symmetry is also seen as 0.2% W-doped VO₂ is cooled from the tetragonal phase to the monoclinic phase. The zero-crossing of the absorption first-derivative as shown in Figure 4.24b increases as a function of temperature. XANES at the W L_{III}-edge captures the 2p to 5d t_{2g} or e_g transition in the end members of this W-doped series (0.2% and 1.4%). The splitting of 3 eV (peak center-to-center) is consistent with previous reports of tungsten oxide standards with W⁺⁶ oxidation states in octahedral bonding configurations.²³⁵ The energy difference for W in tetrahedral sites in compounds such as Na₂WO₄ and Sc₃W₃O₁₂ has been reported by Yamazoe *et al.* to be lower.²⁴² The inclusion of W into octahedral sites destroys the pristine monoclinic zig-zag chains of V⁺⁴-V⁺⁴ dimers and depresses the phase transition temperature.

4.3.5 Mo-, Cr-, and Fe-doped VO₂

The 0.9%-molybdenum and 1.2% chromium-doped VO₂ samples were fitted with M1 and M2 models, respectively. The expected tetragonal phase was confirmed by EXAFS as shown in Figure 4.27. The d⁴ elements have different effects on VO₂ structure as distorted by dopant inclusions. While the 4d and 5d chemistry are similar due to their relatively orbital size as compared to V, the 3d orbitals of Cr are comparable to V, and thus do not behave similarly to Mo and W. EXAFS fitting was extremely difficult to perform given the large deviation from the monoclinic M1 structure as summarized in Table 4.13. The M1 V-O bonds at 1.7 and 2 Å were fitted for Mo, Cr and Fe; however, the splitting of the peak is less than that of pristine M1 VO₂. This is due to the transition to the tetragonal phase in which the 6 V-O bonds in M1 collapse into 2 sets of 4 equatorial and 2 apical V-O bonds.

While the W series clearly show a structurally driven phase transition consistent with the Peierls model, the existence of the M2 phase in Cr is more consistent with electron-electron repulsion model for inducing a Mott-type band gap. A recent 2014 study by Sun *et al.*¹⁹⁵ reported that the modulation of MIT temperature could be dependent on a number of variables such as stability of the doped cation in the VO₂, volume change of the unit cell, β angle change of the

unit cell, and formation enthalpy. By screening transition metal, alkali, alkaline earth, and main group dopants, Sun and co-workers elucidated that based on their supercell DFT+U calculations that large cation (4d, 5d elements) dopants that decrease the β angle are most effective at MIT depression. This is in agreement with experimental data thus far. Interestingly, 3d elements such as Cr, Mn, Fe, Co, Ni increase the MIT temperature. These 3d dopants also shift the center of the M1 (011) peak to higher q position (Figure 4.28). Optical hysteresis showed a significant increase in the MIT temperature during cooling but not during heating (Figure 4.29). Their *a priori* elucidation of the W and Mo effects are consistent with previous reports that +3 species increase the temperature and higher oxidation state species decrease the temperature, but the slight difference of 0.06 \AA^3 between is indiscernible. Furthermore, the volume and β angle differences do not explain fully why W is doubly more effective as a dopant in MIT depression as that of Mo species.

4.4 Conclusion

Doping VO_2 with W, Mo, and Cr via a colloidal synthetic technique has allowed for uniform formation of thin films with optical tunability. In particular, as W dopant concentration is increased, the local symmetry of V sites below the MIT temperature shifts towards tetragonal phase observed above the MIT

temperature. This suggests that the depression of the MIT temperature with increasing W concentration is structurally driven by symmetry tuning of the local V sites. Furthermore, tracking the contributions of the 1s to V(3d)/O(2p) t_{2g} (A1) and e_g orbitals (A2) from the pre-edge peaks of VO₂ and 0.2% W-doped VO₂ show the first-order transition from the tetragonal to monoclinic phase. Probing the XANES region showed a gradual decrease in oxidation state of V⁺⁴ with increase in W concentration. Comparing the d⁴ elements, the symmetry effects of W and Mo doping are different than that of Cr. For the fitting of EXAFS data of Cr-doped VO₂, the V-O bonds were fitted with an M2 model; however, there is a mixture of the tetragonal and M2 phases as seen in the decrease of the fitted V-V half-path lengths.

4.5 Future Directions

The study of the origins of the MIT has occupied scientific research for the past 56 years and will continue for at least another half century given the complexity, and thus fascination with unraveling the competing properties of the system. The tunability of solution processable techniques allow for manipulation of not only the modulation in MIT temperature but also the hysteresis width. Not only do different elements have variable hysteresis widths, but solution mixtures of

different doped VO₂ systems can lead to narrowing of the hysteresis. This is advantageous for fast switching applications.

In terms of materials selection for doping VO₂, the choice can be made to adjust the transmission color of the solution as well as temperature. Mg⁺² have been reported to blue shift the absorption wavelength resulting in a deviation from the typical orange/brown emission. This is advantageous for coating applications in which transparent and colorless windows are often preferred choices. Sun *et al.* have calculated Sc⁺³ experience similar electrostatic attraction to tetravalent vanadium cation to induce a blue shift similar to Mg⁺². The advantage would be color and more effective temperature modulation, which for Mg⁺² is only 2-3 degrees per atomic percent.

While most applications benefit from MIT depression towards room temperature or colder, it is still worthwhile to study the inclusion of Fe for its ability to be included at a higher concentration. Fe has similar effects on VO₂ to Cr in that it can increase the M1 (011) peak center by 0.07 Å⁻¹ (Figure 4.28). This is a significant increase as compared to its 3d neighbors such as Co, Ni, and Mn. Reports of the existence of M2 and M3 phases by Blauw *et al.* and Phillips *et al.* suggest that the transitions in Fe-doped VO₂ is rich for local structure investigation.^{243,244} Compounded with iron oxide's ferromagnetism and stability

in spinel phases, Fe-doped VO₂ would be a fascinating study for understanding solid-solid transformations between the monoclinic phases as well as through the MIT.

4.6 Figures

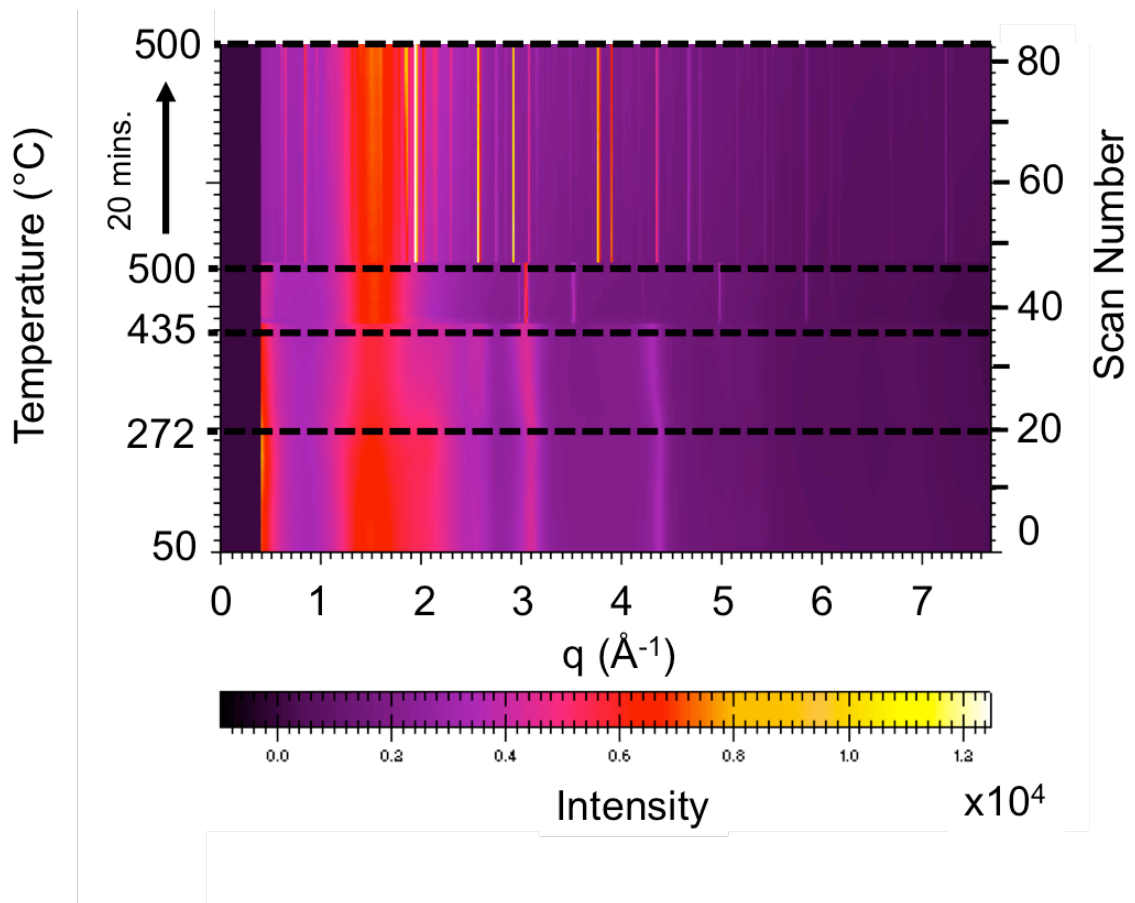


Figure 4.9. *In-situ* powder diffraction of VO_x nanocrystals during annealing under 1 mTorr oxygen atmosphere. There is significant line width narrowing as the particles sinter into VO₂ starting at 500°C.

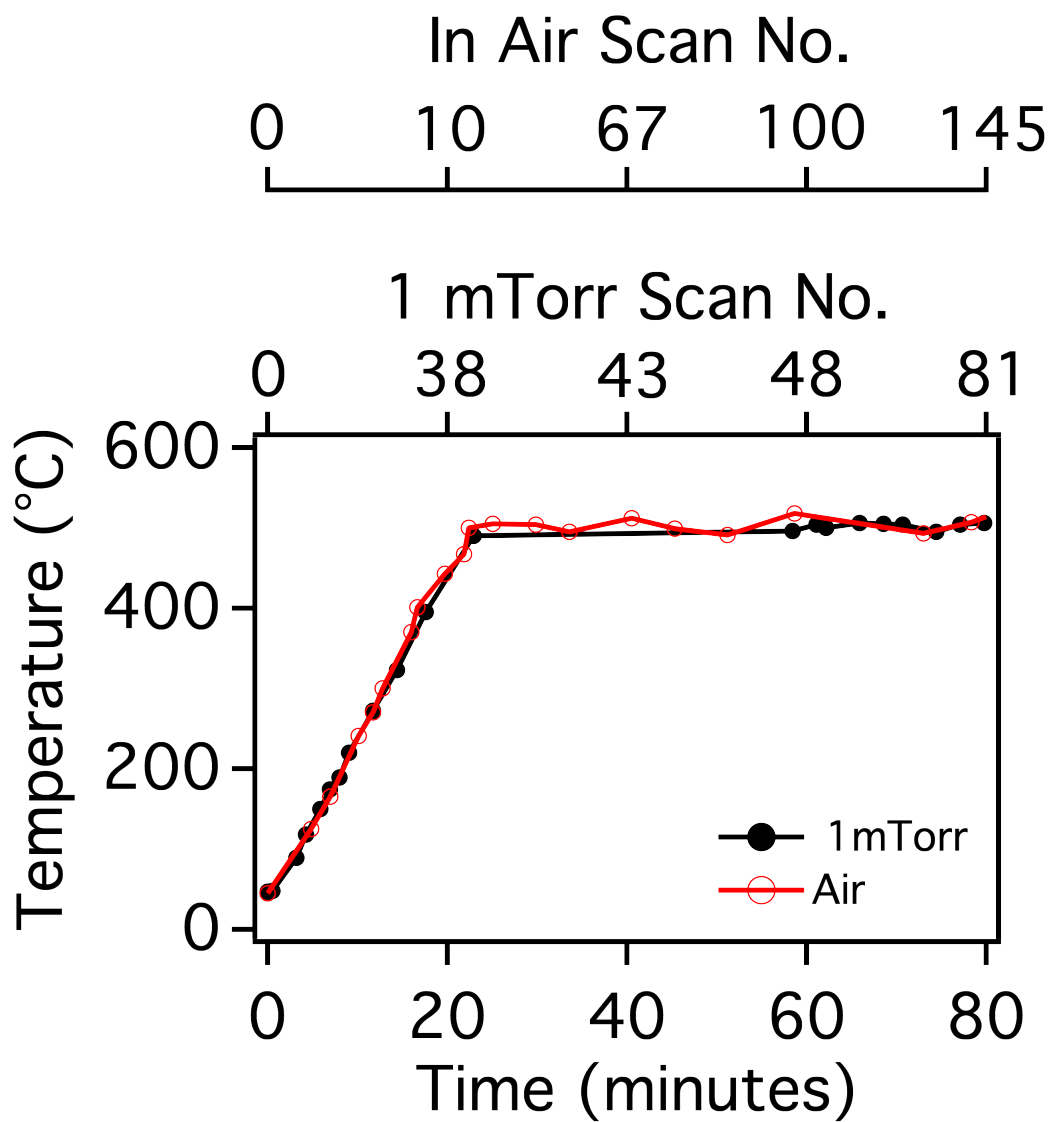


Figure 4.10. Temperature profile of VO_x annealing cycle under 1 mTorr (black) and under ambient pressure (red) over 80 minutes.

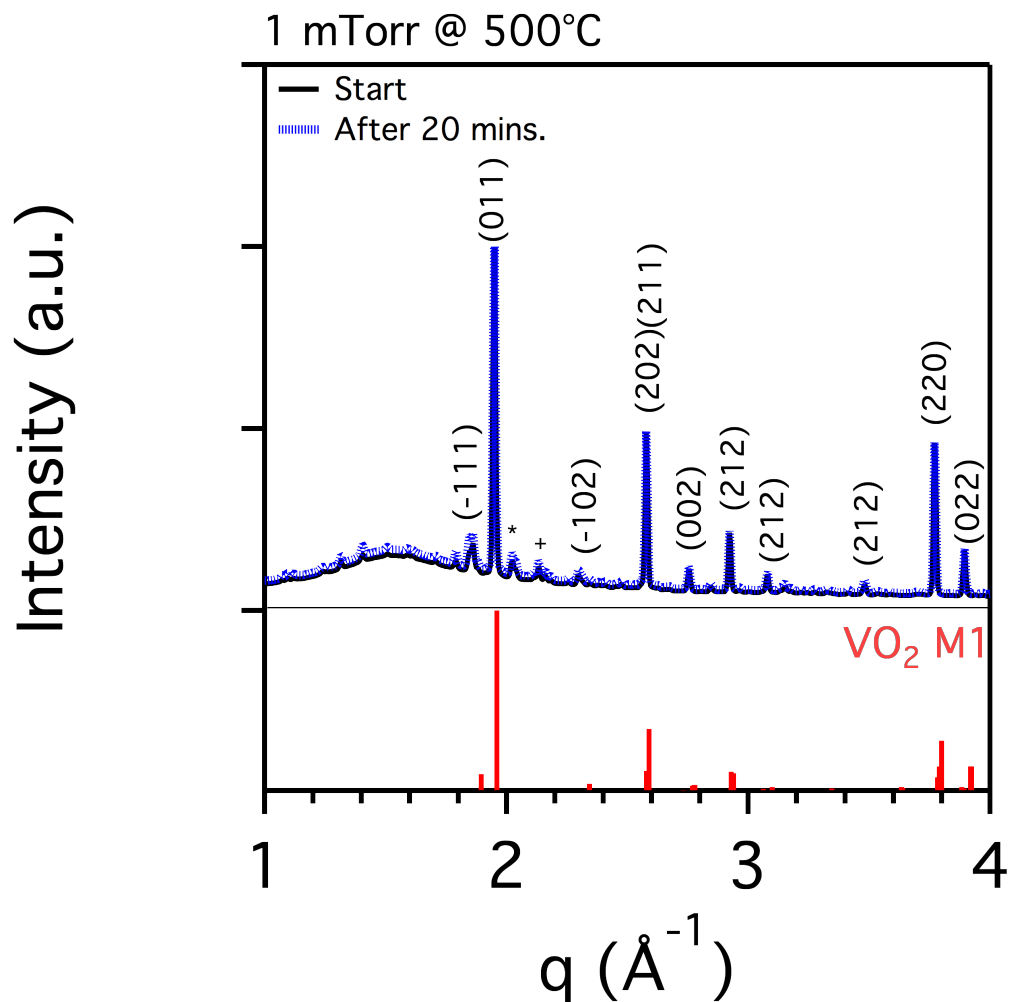


Figure 4.11. The powder diffraction patterns of VO_2 at 500°C (black) is maintained after 20 minutes (dashed blue line). There are minority peaks that may attributed to the V_2O_5 phase as denoted with an asterisk (*) and plus sign (+) corresponding to the (301) and (112) reflections. However, the dominant (002) peak at $q = 1.25 \text{ \AA}^{-1}$ for V_2O_5 is absent.

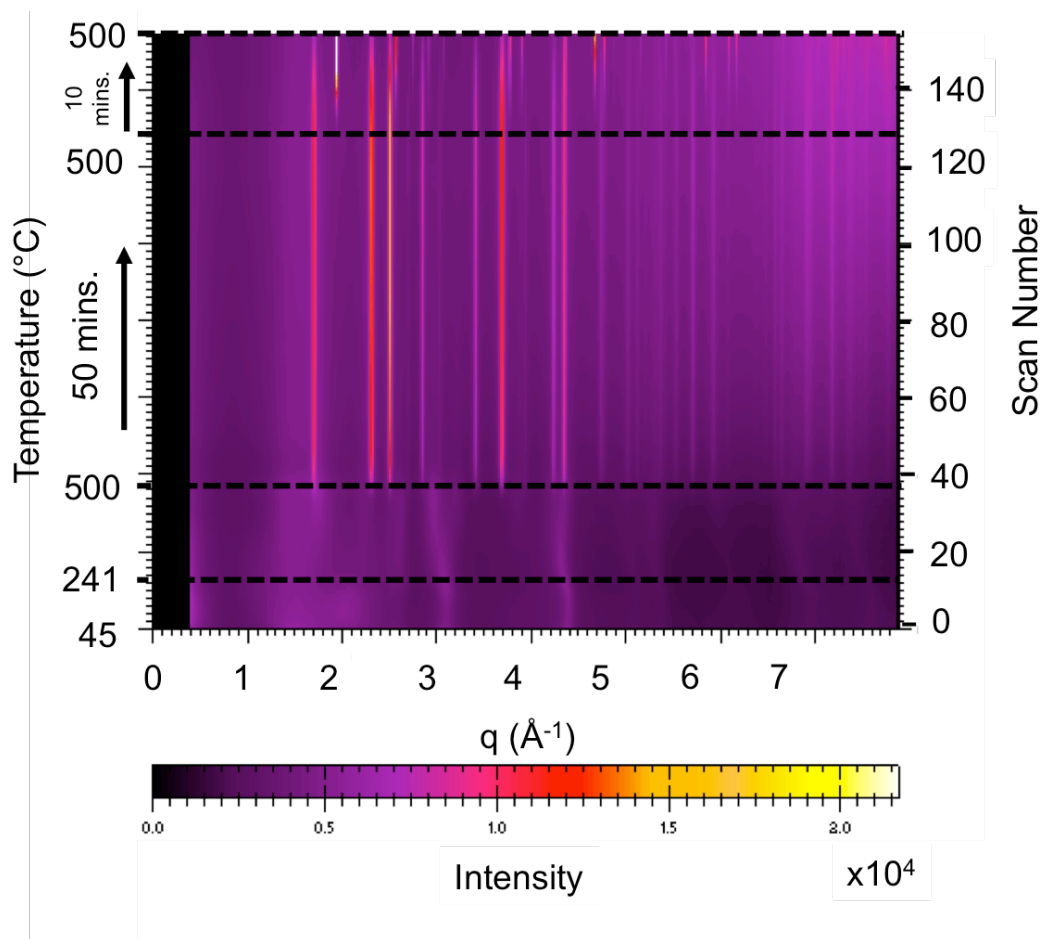


Figure 4.12. *In-situ* powder diffraction of VO_x nanocrystals during annealing under ambient pressure. There is significant line width narrowing as the particles sinter into VO_2 starting at 500°C as well formation of V_2O_5 species.

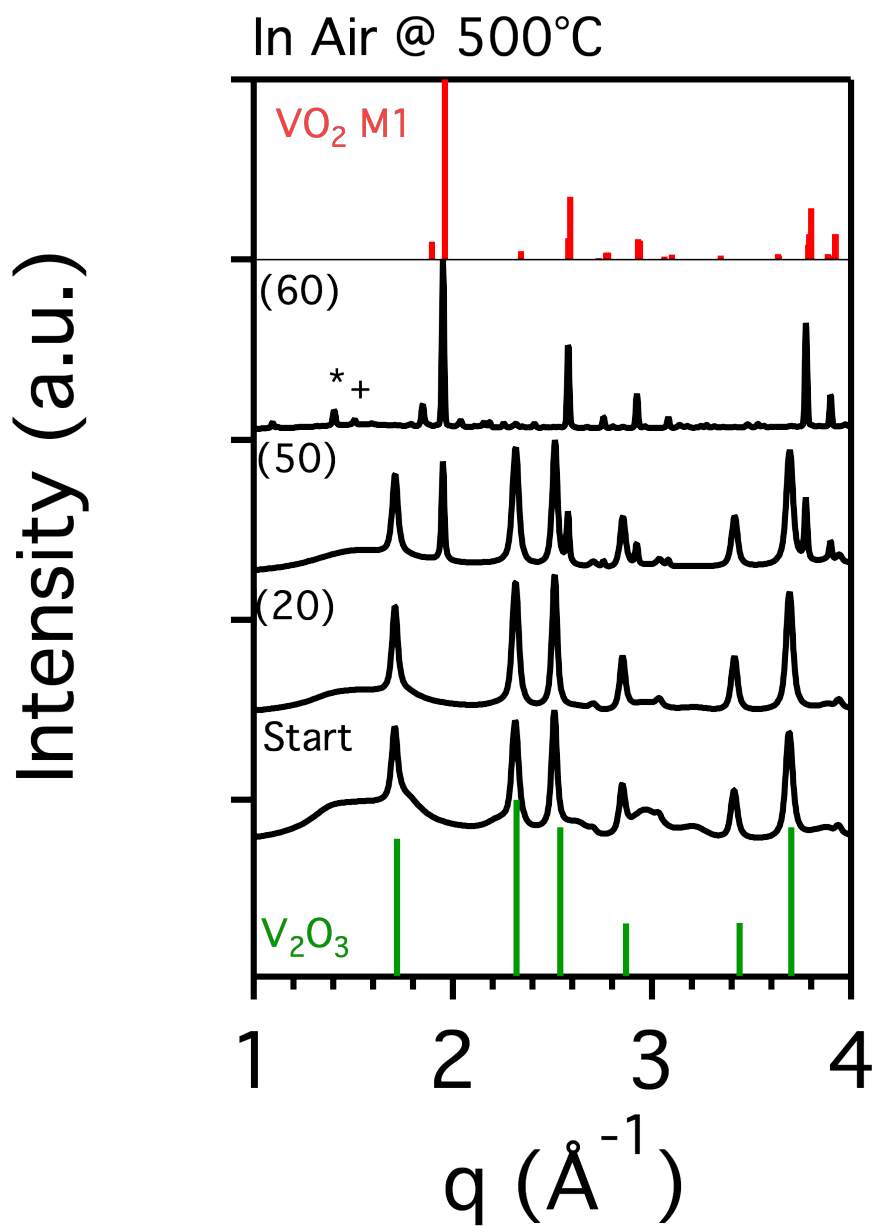


Figure 4.13. Annealing VO_x nanocrystals in an ambient environment reveals a transformation from V₂O₃ to VO₂ with a coexistence of the two phases 50 minutes at 500°C. The material subsequently transforms to VO₂ 10 minutes (60 minutes

total) still at 500°C. There are minority peaks that may be attributed to V_2O_5 as denoted with an asterisk (*) and plus sign (+).

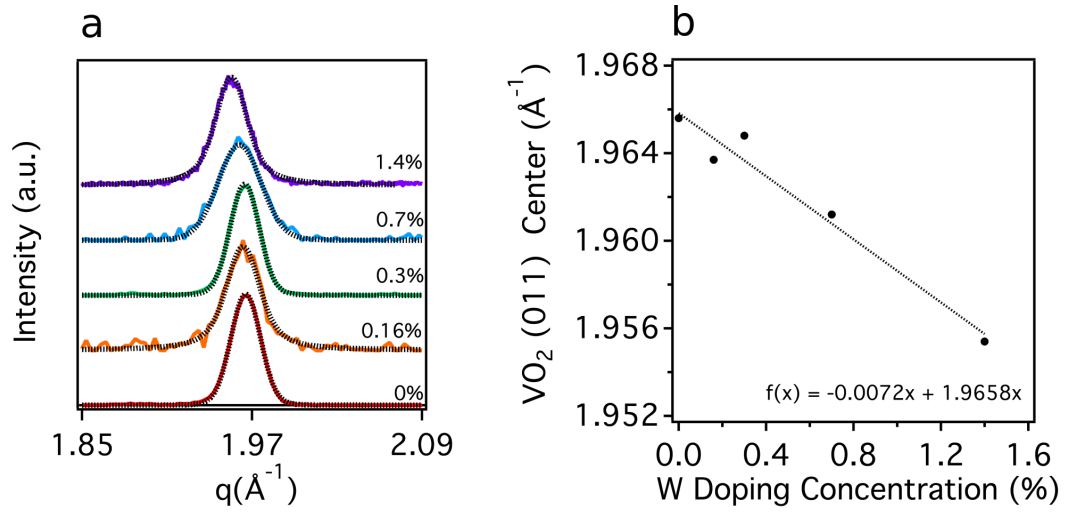


Figure 4.14. (a) X-ray diffraction patterns with Voigt peak fits and (b) the (011) peak centers as a function of doping concentration (0%, 0.2%, 0.3%, 0.7%, and 1.4%) in W-doped VO_2 thin films.

Table 4.6. Voigt fitting parameters for (011) peaks in Figure 4.14a.

W Doping %	Center (\AA^{-1})	FWHM	Area	Height
0	$1.9656 \pm 4.6470 \times 10^{-5}$	0.024564	$0.02755 \pm 1.3014 \times 10^{-4}$	$1.0141 \pm 3.5007 \times 10^{-4}$
0.2	$1.9637 \pm 3.3731 \times 10^{-4}$	0.028448	$0.03656 \pm 8.5375 \times 10^{-4}$	$0.9419 \pm 3.3731 \times 10^{-4}$
0.3	$1.9648 \pm 4.4618 \times 10^{-5}$	0.024325	$0.02776 \pm 1.8092 \times 10^{-4}$	$1.0167 \pm 3.2875 \times 10^{-4}$
0.7	$1.9612 \pm 2.2291 \times 10^{-4}$	0.035628	$0.03779 \pm 8.083 \times 10^{-4}$	$0.8900 \pm 3.3744 \times 10^{-4}$
1.4	$1.9554 \pm 6.4254 \times 10^{-5}$	0.027003	$0.03617 \pm 1.6956 \times 10^{-4}$	$0.9848 \pm 1.9223 \times 10^{-5}$

Table 4.7. Gaussian and Lorentzian fitting components for (011) peaks in Figure 4.14a.

W Doping %	Gauss FWHM	Lorentzian FWHM
0	0.023463 ± 0.00032058	0.0021524 ± 0.00043261
0.2	0.018087 ± 0.00042241	0.016949 ± 0.00078221
0.3	0.0228 ± 0.00030634	0.002956 ± 0.00040504
0.7	0.030596 ± 0.0016274	0.009354 ± 0.0019871
1.4	$0.017334 \pm 8.13 \times 10^{-5}$	0.015876 ± 0.0001486

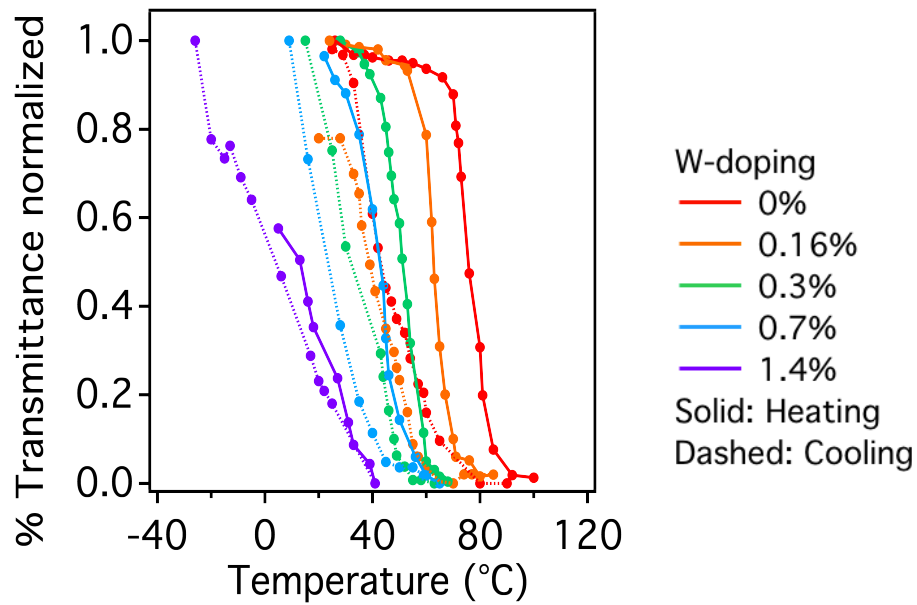


Figure 4.15. The percent transmittance in each VO₂ thin film on quartz substrate decreases upon heating (solid) and increases upon cooling (dashed).

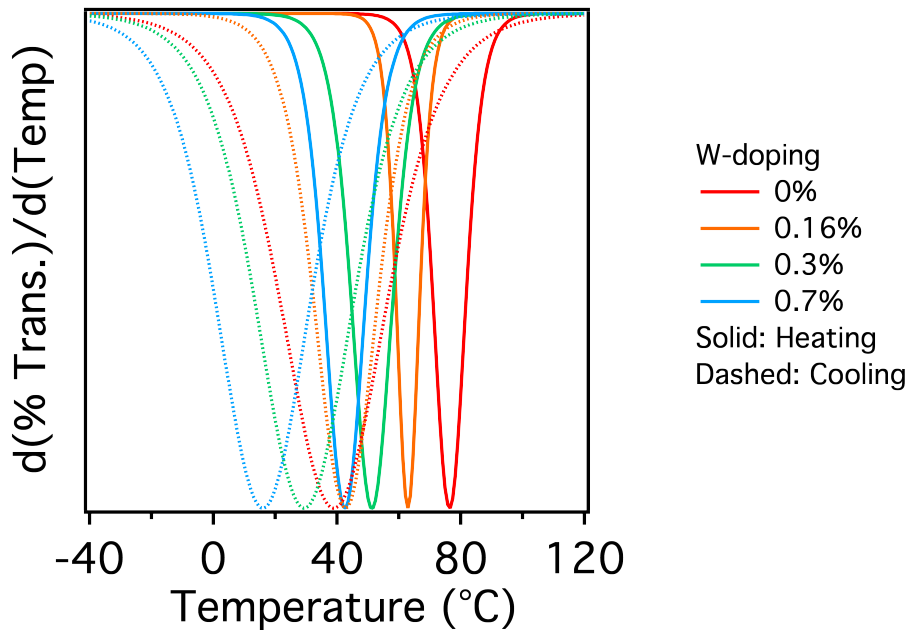


Figure 4.16. First derivative of sigmoid fit as a function of temperature.

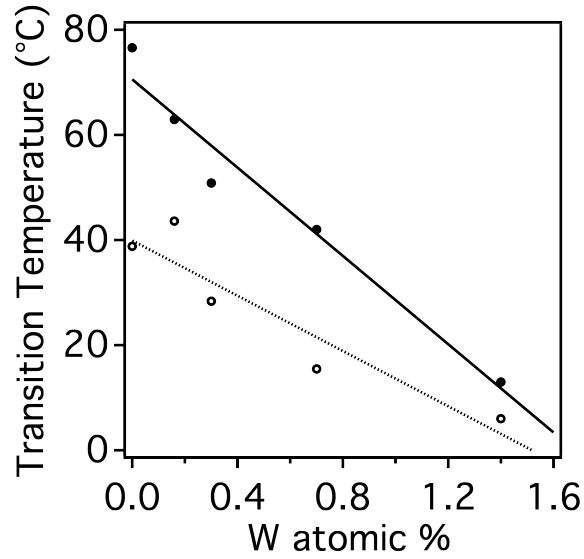


Figure 4.17. Optical transition temperature for W-doped VO₂ as a function of W atomic percent, which is dependent upon heating (solid) and cooling (dashed).

Table 4.8. Linear regression (($f(x) = a + bx$)) for optical transition temperature depression rate of W-doped VO₂ samples.

Direction	a	b
Heating	70.573 ± 3.5	-41.993 ± 4.89
Cooling	39.905 ± 4.08	-26.287 ± 5.7

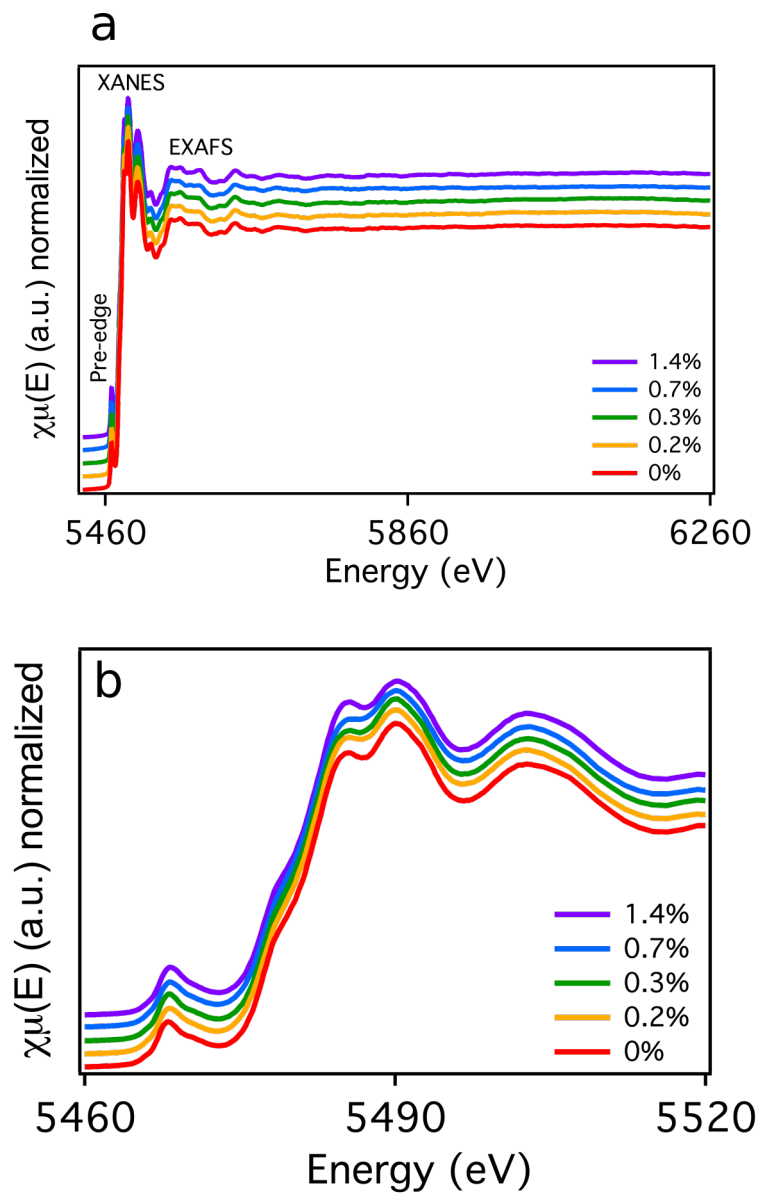


Figure 4.18. (a) Full absorption and (b) XANES spectra of undoped, 0.2%, 0.3%, 0.7%, and 1.4% W-doped VO₂ thin films.

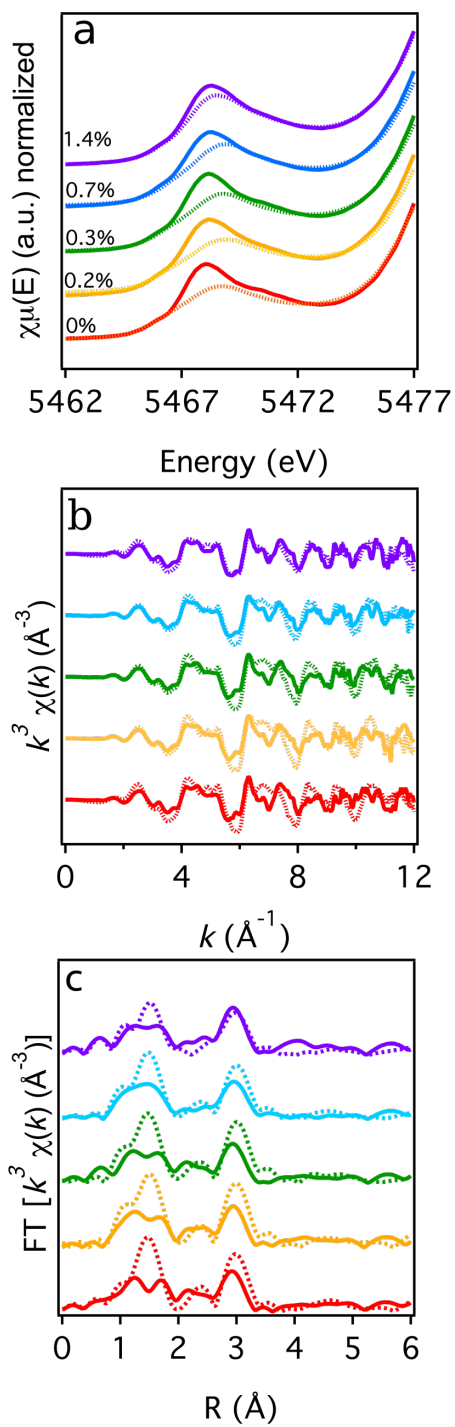


Figure 4.19. X-ray normalized absorption, k^3 -weighted $\chi(k)$ and its Fourier transforms for undoped, 0.2%, 0.3%, 0.7%, and 1.4% W-doped VO_2 thin films.

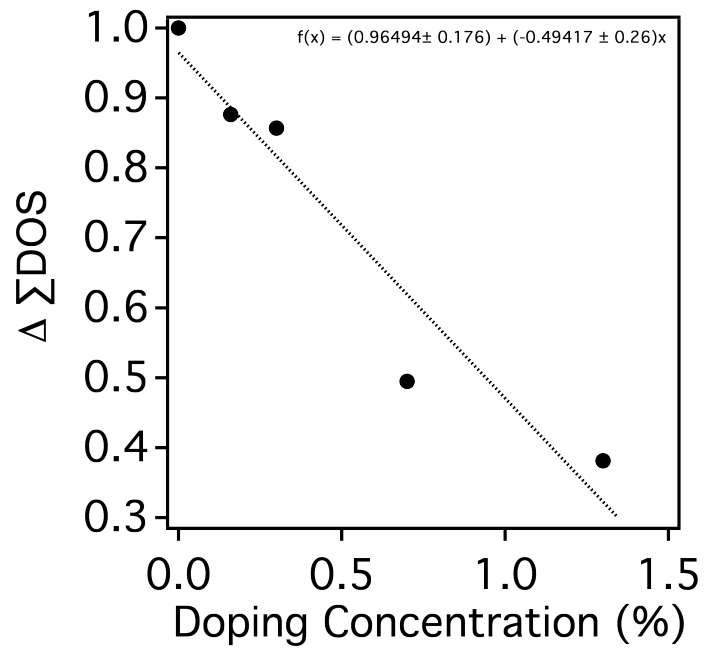


Figure 4.20. Differences in the integrated area in the pre-edge peak for the VO_2 samples below and above the MIT temperature.

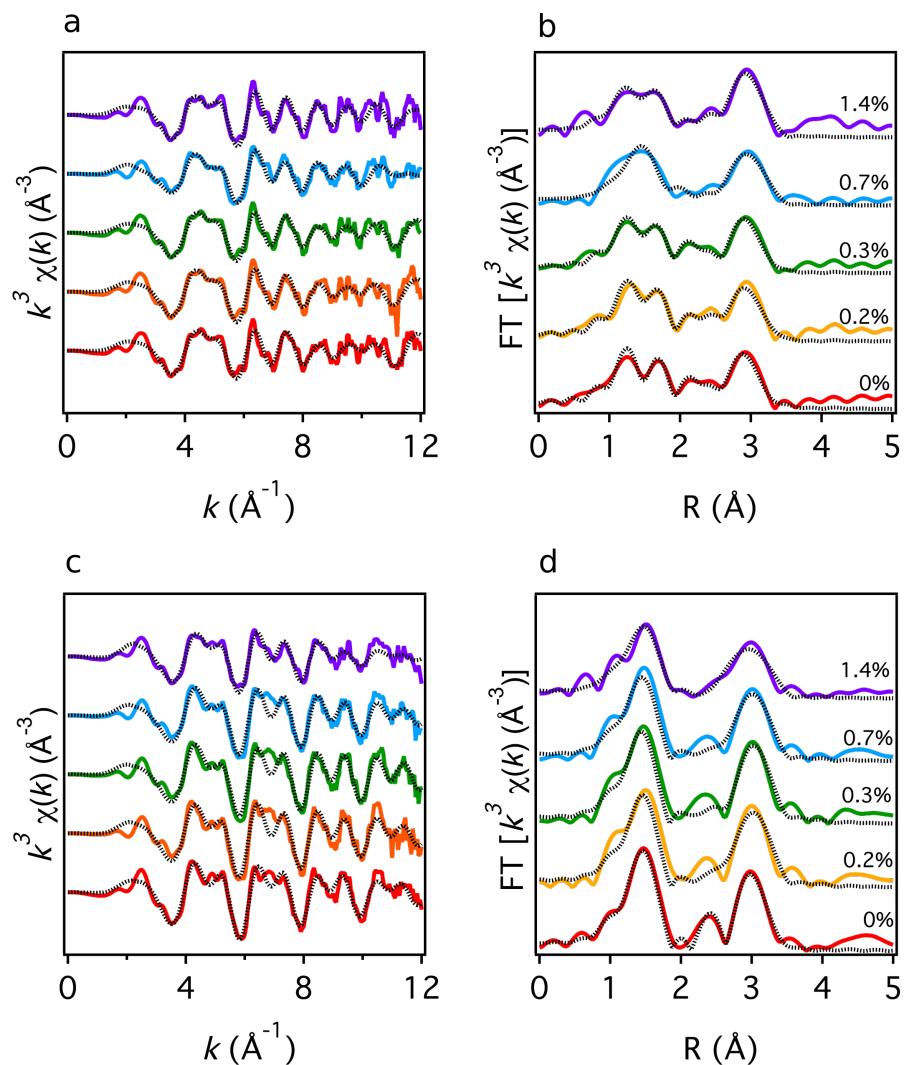


Figure 4.21 (a), (b) Fourier transform of the k^3 -weighted EXAFS equation shows threshold of W concentration in monoclinic phase at 0.7%. The splitting of the peak between 1 and 2 \AA is lost for the sample with 0.7% W. The collapse of this peak indicates a structural change towards a more symmetric phase. (c), (d) The k^3 -weighted EXAFS equation and its Fourier transform show a tetragonal phase with one V-O bond peak between 1 and 2 \AA as well as peaks at 2.36 and 2.98 \AA corresponding to V-V interactions.

Table 4.9. EXAFS fitting parameters for V-O and V-V distances below the transition temperature for W-doped VO₂.

W Doping %	N	R (Å)	σ^2 (Å ²)	ΔE_0 (eV)	ΔR (Å)	R_{eff} (Å)
V-O Bonds						
0%	3	1.8113	0.00391	-5.298	0.04960	1.7617
	3	1.99405	0.00244	-5.298	-0.02635	2.0204
0.2%	3	1.82383	0.00487	-8.082	0.06213	1.7617
	3	1.99108	0.00311	-8.082	-0.02932	2.0204
0.3%	3	1.81155	0.00483	-6.064	0.04985	1.7617
	3	1.98418	0.00300	-6.064	-0.03622	2.0204
0.7%	6	1.90508	0.01383	-9.562	-0.02072	1.9258
	8	3.74891	0.01240	-9.562	0.29041	3.4585
1.4%	3	1.80218	0.00564	-7.242	0.04048	1.7617
	3	1.97332	0.00335	-7.242	-0.04708	2.0204
V-V Bonds						
0%	1	2.60560	0.00476	-5.298	-0.04853	2.6541
0.2%	1	2.57430	0.00659	-8.082	-0.07977	2.6541
0.30%	1	2.5978	0.00488	-6.064	-0.05629	2.6541
0.70%	2	2.5583	0.01577	-9.562	-0.29671	2.8550
	8	3.4777	0.01158	-9.562	-0.04530	3.5230
1.40%	1	2.5755	0.01019	-7.242	-0.07861	2.6541

Table 4.10. EXAFS fitting parameters for V K-edge above the transition temperature.

W Doping %	N	R (Å)	σ^2 (Å ²)	ΔE_0 (eV)	ΔR (Å)	R_{eff} (Å)
V-O Bonds						
0%	6	1.91040	0.00622	-4.172	-0.01540	1.9258
0.2	6	1.90815	0.00714	-5.308	-0.01765	1.9258
0.3	6	1.91627	0.00728	-5.111	-0.00953	1.9258
0.7	6	1.92017	0.00827	-4.802	-0.00563	1.9258
1.4	6	1.90728	0.01060	-6.957	-0.01852	1.9258
V-V Bonds						
0%	2	2.909440	0.00683	-4.172	0.054440	2.855
	8	3.531570	0.00852	-4.172	0.008570	3.523
0.2%	2	3.169770	0.03113	-5.308	0.314770	2.855
	8	3.540608	0.00716	-5.308	-0.01892	3.523
0.30%	2	2.947670	0.01045	-5.111	0.092670	2.855
	8	3.510340	0.00910	-5.111	-0.012660	3.523
0.70%	2	2.971920	0.01083	-4.802	0.116920	2.855
	8	3.510050	0.01050	-4.802	-0.012950	3.523
1.40%	2	2.549070	0.02091	-6.957	-0.305940	2.855
	8	3.491900	0.00996	-6.957	-0.031100	3.523

Table 4.11. Reduced χ^2 and R-factor for EXAFS fitting below and above the transition temperature for k -range of 2.7 to 12 \AA^{-1} .

W Doping %	Temp ($^{\circ}\text{C}$)	Reduced χ^2	R-factor	R Range (\AA)	Phase
0	25	247.5063976	0.0240376	0.9-3.7	M1
0.2	25	158.9337068	0.0256982	0.9-3.7	M1
0.3	25	358.8155589	0.0151618	0.9-3.7	M1
0.7	25	331.7706310	0.0360680	1-3.7	M1
1.4	-249	202.5763446	0.0189563	1-3.7	M1
0	100	560.251353	0.0397981	1-3.4	Tet
0.2	100	249.4916052	0.0455174	1-3.4	Tet
0.3	100	615.5877592	0.0432276	1-3.4	Tet
0.7	100	348.4214155	0.041627	1-3.4	Tet
1.4	25	184.8078199	0.0212489	1-3.4	Tet

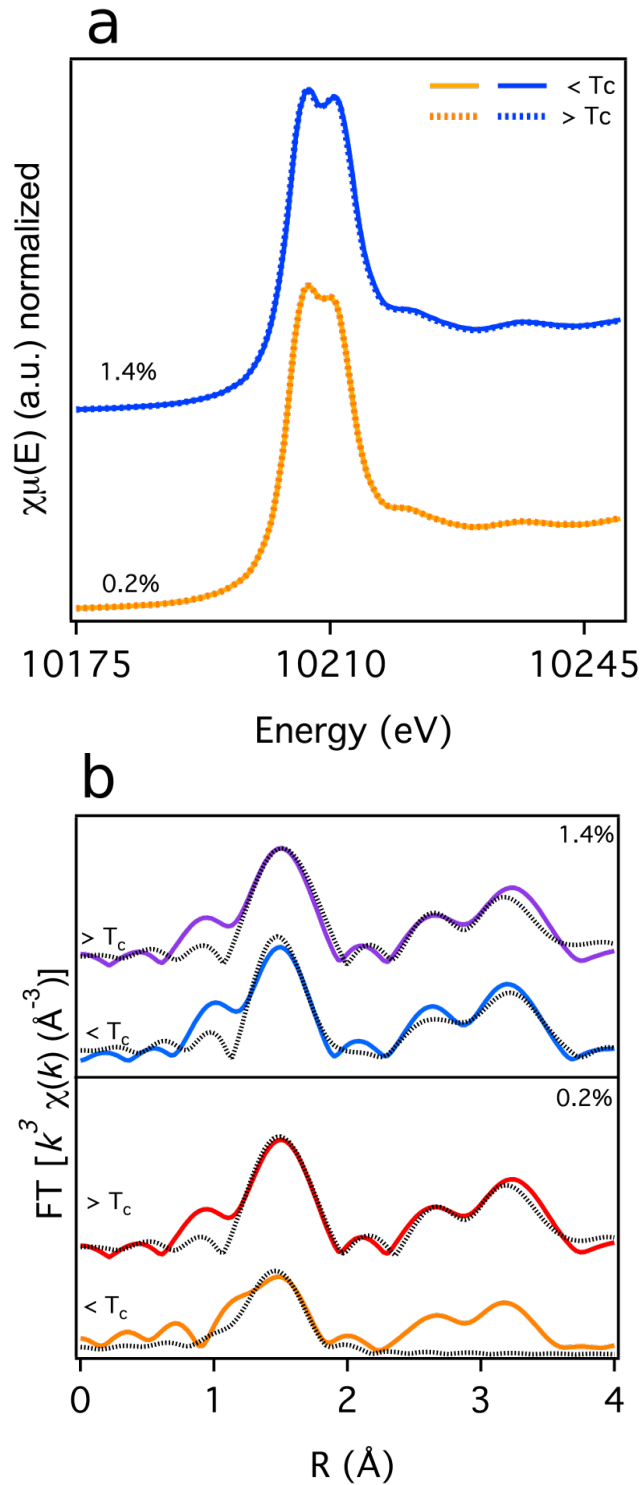


Figure 4.22. (a) W L_{III} -edge absorption peaks and (b) Fourier transforms of the EXAFS equation for 0.2% W and 1.4% W-doped VO_2 .

Table 4.12. Undoped VO₂ temperatures for each scan in transmission mode. The “Start” and “End” values are the temperature at the beginning and end of the XANES scan, respectively.

Scan No.	Start Temp. (°C)	End Temp. (°C)	Avg. Temp. (°C)	Scan No.	Start Temp. (°C)	End Temp. (°C)	Avg. Temp. (°C)
1	79.4	79.3	79.35	29	70.2	69.9	70.05
2	79.2	78.9	79.05	30	69.8	69.4	69.6
3	78.7	78.4	78.55	31	69.3	69.0	69.15
4	78.4	78.2	78.3	36	68.0	68.0	68.0
5	78.1	77.9	78.0	37	67.9	67.7	67.8
6	77.8	77.6	77.7	38	67.5	67.3	67.4
7	77.5	77.3	77.4	39	67.3	67.0	67.15
8	77.2	76.9	77.05	40	67.0	66.8	66.9
9	76.8	76.6	76.7	41	66.6	66.6	66.6
10	76.4	76.3	76.35	42	66.5	66.3	66.4
11	76.2	75.9	76.05	43	66.1	65.9	66.0
12	75.8	75.5	75.65	44	--	65.7	65.7
13	75.4	75.2	75.3	45	65.6	65.4	65.5
14	75.1	74.8	74.95	46	65.4	65.3	65.35
15	74.7	74.5	74.6	47	65.2	65.1	65.15
16	74.4	74.2	74.3	48	65.0	64.9	64.95
17	74.1	74	74.05	49	64.5	64.4	64.45
18	73.9	73.5	73.7	50	64.4	64.2	64.3
19	73.5	73.3	73.4	51	63.9	64.0	63.95
20	73.2	73	73.1	52	63.8	63.7	63.75
21	72.8	72.7	72.75	53	63.7	63.5	63.6
22	72.5	72.4	72.45	54	63.3	63.1	63.2
23	72.2	71	71.6	55	63	62.9	62.95
24	71.7	71.6	71.65	56	62.8	62.7	62.75
25	71.5	71.2	71.35	57	62.6	62.4	62.5
26	71.1	71	71.05	58	62.3	62.2	62.25
27	70.9	70.7	70.8	59	62.1	62.0	62.05
28	70.6	70.3	70.45	60	61.8	61.8	61.8

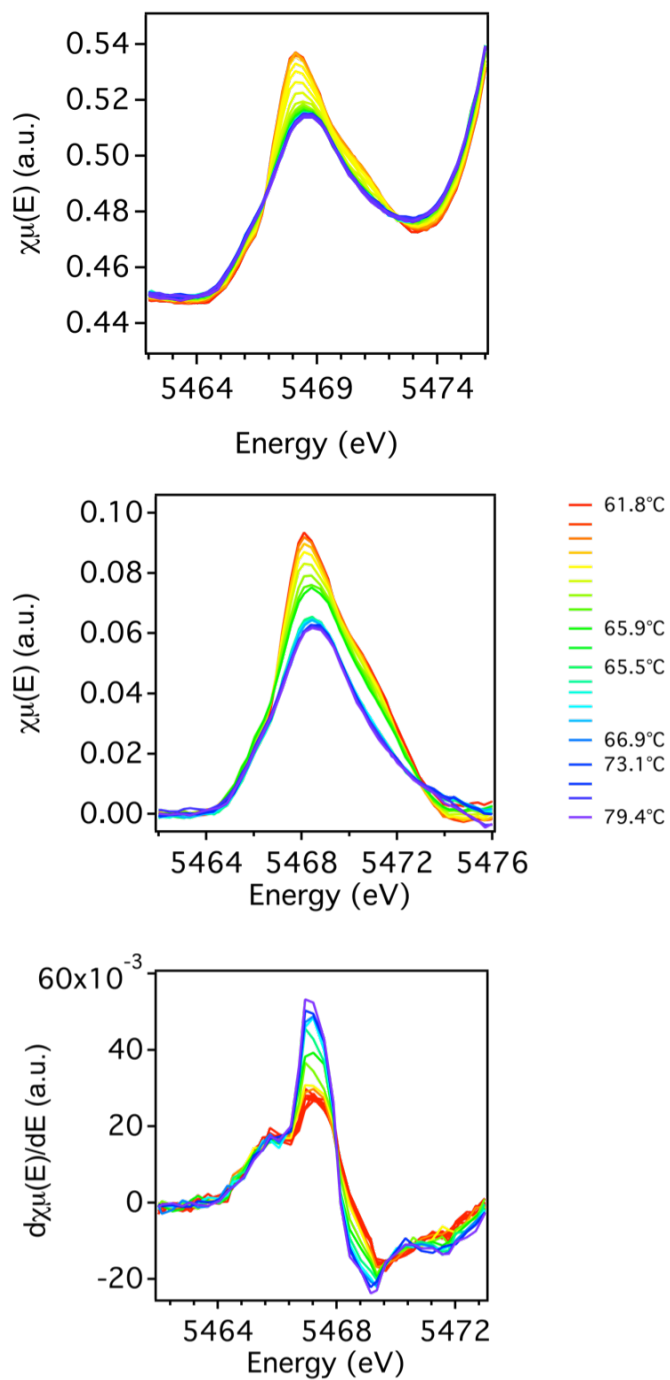


Figure 4.23. The VO_2 pre-edge peak collected at the vanadium K-edge (top) is background subtracted using a spline fitting between 5462 eV and 5472 eV (middle). (Bottom) The zero-crossing of the first derivative of the pre-edge peak shifts to a higher energy as the sample is cooled.

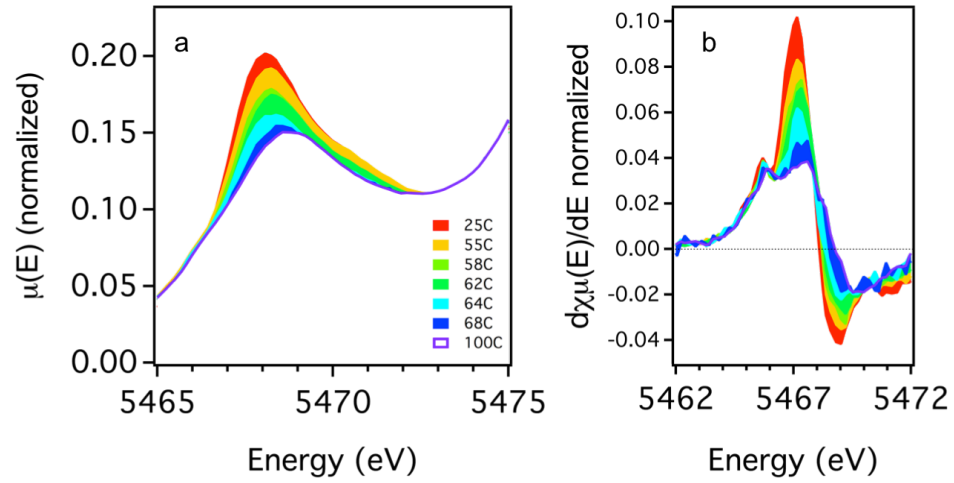


Figure 4.24. (a) The first centroid of 0.2% W-doped VO₂ absorption pre-edge peak as a function of temperature can be determined from (b) the zero-crossing of its first derivative as a function of energy.

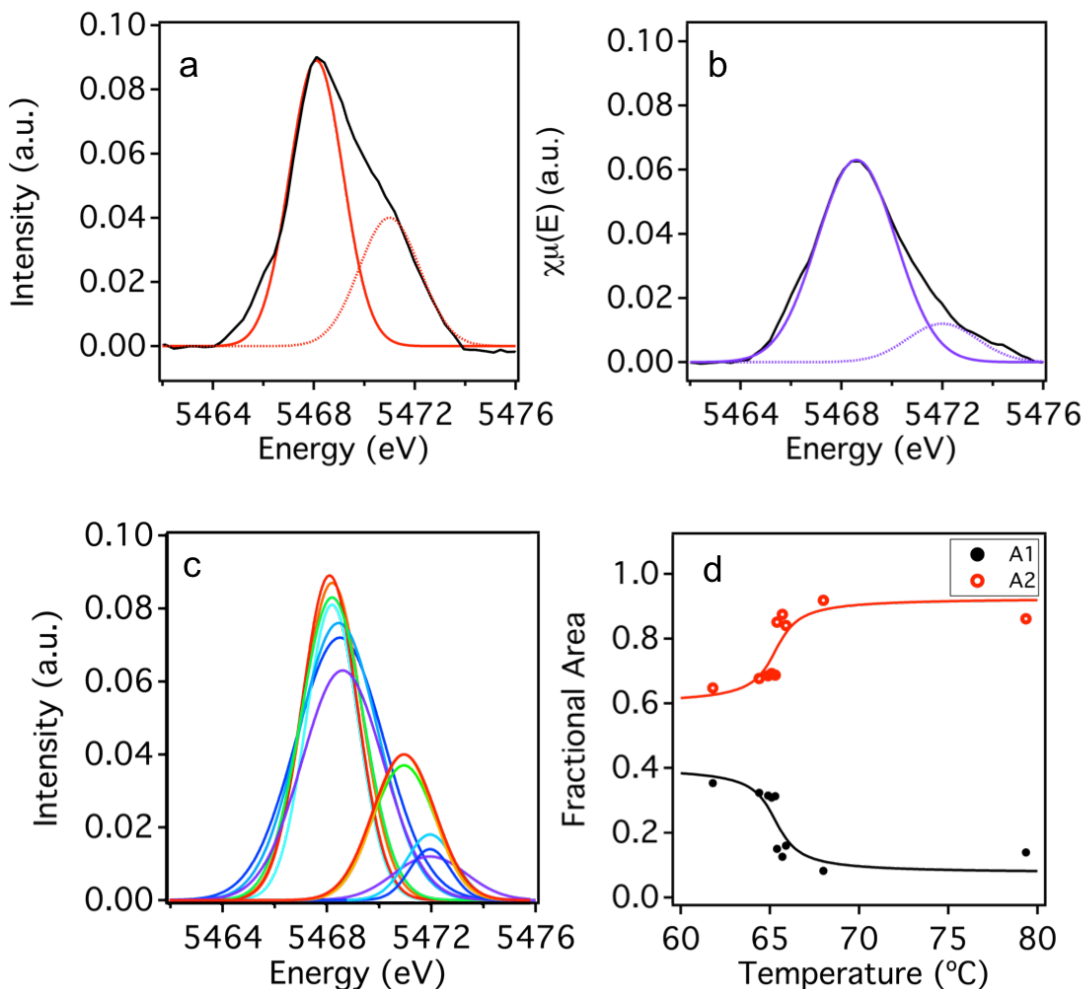


Figure 4.25. (a) and (b) Deconvolution of the pre-edge peak for undoped VO₂ at 79.4°C and 62.1°C. (c) The Gaussian fits are summarized with the ratios of the A1 and A2 areas showing a transition at 65°C. The data was collected by Dr. Mahalingam Balasubramanian in transmission mode as the sample cooled from 79.4 °C. The range of temperature for each scan is listed in Table 4.12.

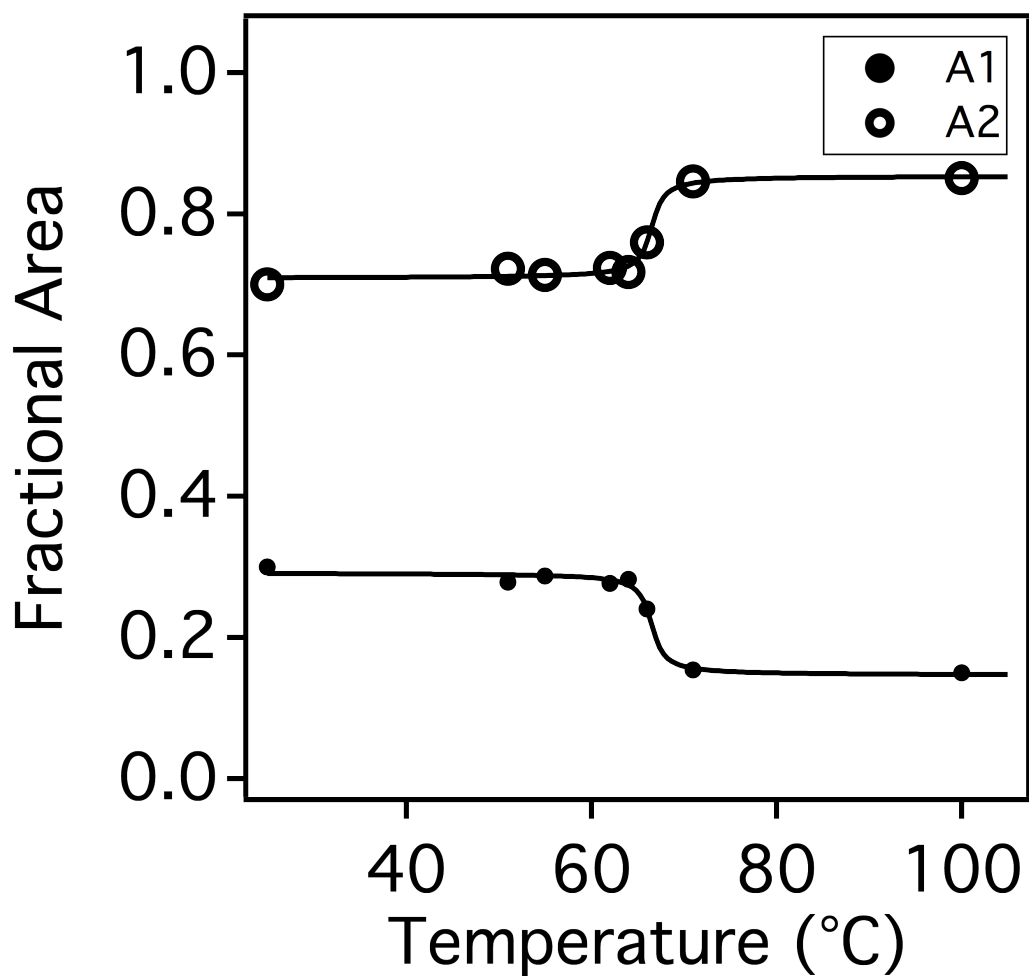


Figure 4.26. A1 and A2 fractional areas are plotted as a function of temperature for 0.2% W-doped VO₂. The inflection points of the arctangent fits are located at 65°C.

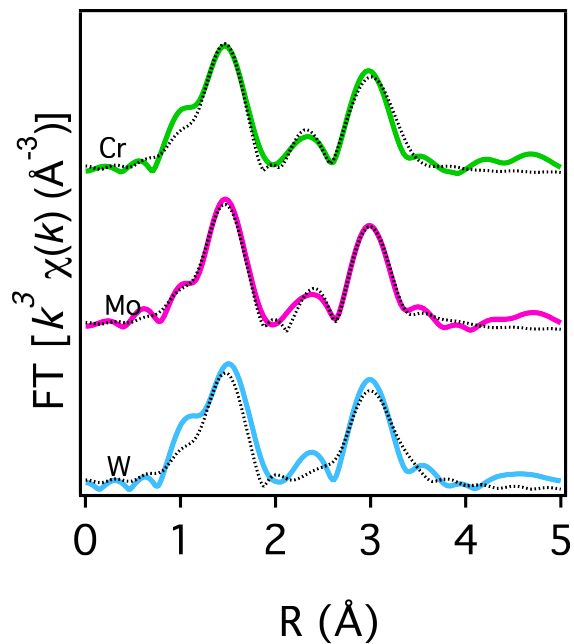
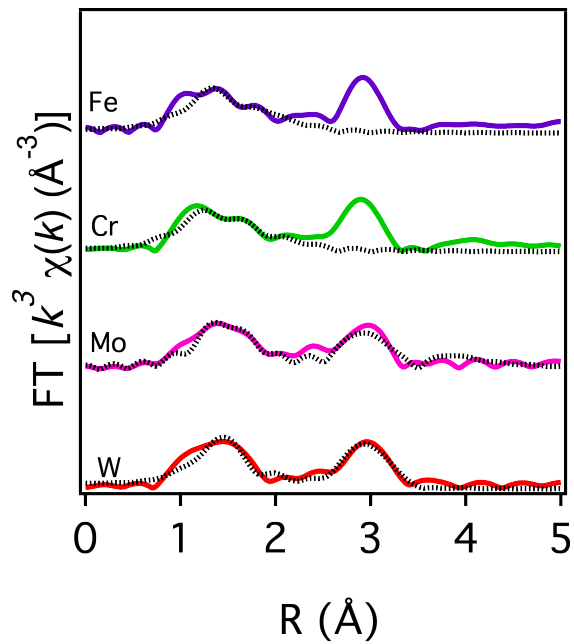


Figure 4.27. Fourier transforms and EXAFS fits of W-, Mo-, Cr-, and Fe-doped VO₂ k³-weighted $\chi(k)$ below the transition temperature (top) and above the transition temperature (bottom).

Table 4.13. EXAFS fitting parameters for V-O and V-V distances below the transition temperature for Mo-, Cr-, and Fe-doped VO₂.

M Doping %	N	R (Å)	σ^2 (Å ⁻²)	ΔE_0 (eV)	ΔR (Å)	R_{eff} (Å)
V-O Bonds						
Mo 0.9%	3	1.88855	0.0062	0.937	0.12685	1.7617
	3	2.05763	0.00556	0.937	0.03723	2.0204
Cr 1.2%	4	1.87762	0.00961	-6.292	0.01562	1.862
	2	2.03964	0.00705	-6.292	-0.04876	2.0884
Fe 9.3%	3	1.85830	0.00772	-5.319	0.09660	1.7617
	3	2.01218	0.00810	-5.319	-0.00822	2.0204
V-V Bonds						
Cr 1.2%	1	2.57371	0.00807	-6.292	0.03581	2.5379
	1	3.10377	0.00299	-6.292	-0.15533	3.2591
	8	3.46833	0.01306	-6.292	0.03673	3.4316
Fe 9.3%	1	2.60229	0.00924	-5.319	-0.05181	2.6541
	1	3.05895	0.00668	-5.319	-0.06565	3.1246
	2	3.47375	0.00119	-5.319	0.10415	3.3696

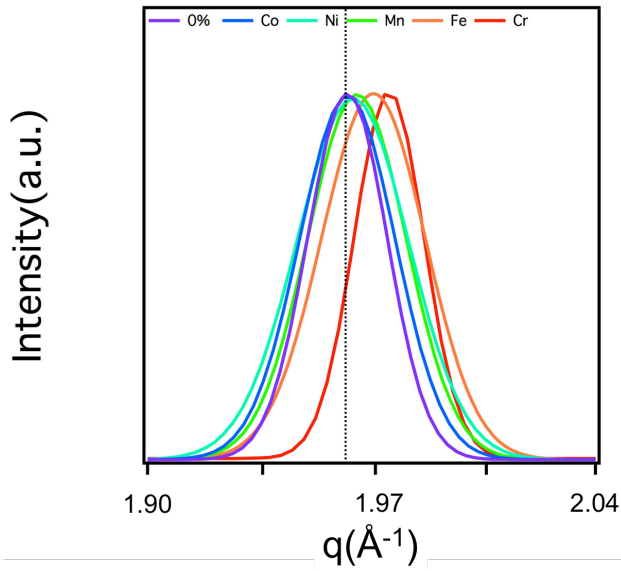


Figure 4.28. X-ray diffraction of first row transition metal-doped VO₂. While 4.1% Co-, 6.6% Ni-, and 5.2% Mn have negligible effects on (011) peak of VO₂, 1.2% Cr and 9.6% Fe increase the peak center by > 0.07 Å⁻¹.

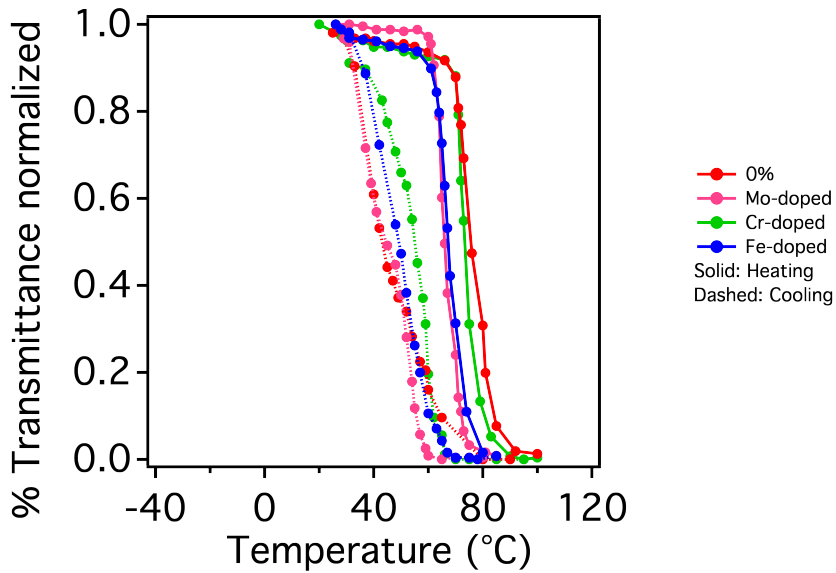


Figure 4.29. Optical response of Mo-, Cr-, Fe-doped VO₂.

5. Structure Determination and Modeling of Monoclinic Trioctylphosphine Oxide

Chapter 5—in part—was published in *Acta Crystallographica C*. V.V.T. Doan-Nguyen, P.J. Carroll, C.B. Murray. Structure Determination and Modeling of Monoclinic Trioctylphosphine Oxide. *Acta Crystallographica C* 71: 239-241 (2015).

5.1 Introduction

Trioctylphosphine oxide (TOPO) is a widely used chemical compound in nanocrystal synthesis, for the removal of heavy metals, and removal of toxins in waste water.²⁴⁵ TOPO is often used as a ligand stabilizer for colloids in traditional thermal decomposition synthetic techniques.^{246–249} The white crystalline material is also used as a phosphorus source as the compound decomposes in high-temperature ($> 300^{\circ}\text{C}$) reactions for colloidal synthesis¹⁶⁴ and has been characterized by nuclear magnetic resonance.^{250–253} In this report, we provide additional spectroscopic data beyond the single crystal diffraction, which was done using a Bruker APEXII with a Mo $K\alpha$ source ($\lambda=0.71073 \text{ \AA}$). Crystal structure refinement was performed using SHELXL97—a full-matrix least-squares algorithm.²⁵⁴

5.2 Methods

Synthesis and crystallization. Trioctylphosphine oxide (90%) was purchased from Sigma Aldrich and acetone (99.5% reagent grade) was purchased from Fisher Scientific. TOPO (0.5 g) was dissolved in 5 mL of acetone in a 25-mL scintillation vial, which was left uncapped for ambient evaporation at 20°C for 12 hours. The single crystals were collected and loaded onto a Kapton capillary tube for measurement.

Refinement. Refinement data is summarized in Table 5.1. Hydrogen atoms were refined using a riding model in which standard C–H bond distances were applied, and the H atom positions were adjusted during refinement. Isotropic thermal parameters of methylene hydrogens were assigned as 33% larger than the attached carbon; methyl hydrogens had thermal parameters 50% larger. In addition, the methyl torsion angle (for rotation about the C–Me bond) was optimized by the refinement program.

Trioctylphosphine oxide (0.05 g) was mixed with potassium bromide and pressed to form a pellet for FTIR, which was done using a Nicolet spectrometer and averaged for 16 scans in a nitrogen atmosphere to reduce molecular vibrations from ambient environment. Raman spectroscopy was performed using a B&W Tek iRaman spectrometer with a 532 nm excitation source.

Modeling of the X-ray scattering patterns were done using an in-house code²⁵⁵ calculating the Debye Equation. In computing the X-ray scattering intensities for the 2 to 8 nm crystallite sizes of trioctylphosphine oxide, the parameters f_i and f_j are the atomic scattering factors tabulated from Cromer-Mann coefficients, q is the wave vector in \AA^{-1} , r_{ij} is the pairwise distance in \AA .^{188,256,257} The bulk crystal simulation was performed using CrystalDiffract.²⁵⁸

5.3 Results and Discussion

Slow evaporation resulted in a mixture of single crystals—of which the highest quality single crystals were collected. The atomic coordinates and monoclinic structural parameters are summarized in Table 5.1, and the ORTEP (Johnson, 1976) representation is shown in Figure 5.1. Additional refined positional parameters are summarized in Appendix G. The unit cell is drawn more compactly in Figure 5.2. As shown in Figure 2, the phosphonyl group within each molecular unit is oriented so that the polar functional groups are 180° from each other. Each oxygen atom is 3.94\AA from the phosphorus atom on the nearest neighboring molecular unit. The 2D projection of the unit cell onto the (010) plane depicts the alternating directions of the dipole from the P=O bonds. The flexible hydrocarbon chains are aligned parallel to neighboring octyl chains, which allows for compact packing of the molecular units.

In processes that require careful removal excess TOPO from solution such as post-synthesis nanocrystal purification, total X-ray scattering provides high-resolution and rapid acquisition of data to track TOPO impurities that will crystallize with varying grain sizes. The X-ray scattering for the 77-atom unit cell was calculated as a function of crystallite size for comparison with the total X-ray scattering data obtained with a synchrotron light source ($\lambda = 0.2114 \text{ \AA}$). The simulations in Figure 5.3a track the peak width broadening as the crystal size decreased from an infinite crystal to a few unit cells. The decrease in the inverse of full-width half-maximum of the Gaussian fits is linearly correlated with the crystal size (Figure 5.3b) and matches well with the collected scattering data. The slope of the fit for crystal diameter as a function of the inverse of full-width half maximum was calculated to be 1.101 ± 0.323 for the dominant (11-4) set of planes, which corresponds with the $\kappa\lambda/\cos(\theta)$ in which κ is the shape factor of value 0.9, λ is the X-ray wavelength of value 0.2114 \AA , and θ is the peak center of value 1.40 \AA^{-1} . Spectroscopy from FTIR shows the $-\text{CH}_2$ stretching modes in the three alkyl chains at 2850 and 2919 cm^{-1} . The characteristic $\text{P}=\text{O}$ and $\text{P}-\text{C}$ stretching modes were observed at 1146 cm^{-1} and 1465 cm^{-1} , respectively (Figure 5.4). The complementary Raman spectroscopic data, which has previously been unreported, confirms the phosphonyl stretching mode in a trialkylphosphonyl

environment results in a much weaker peak at 1145 cm^{-1} than the dominant methylene stretching modes at 2847 and 2882 cm^{-1} (Figure 5.5).

5.4 Figures

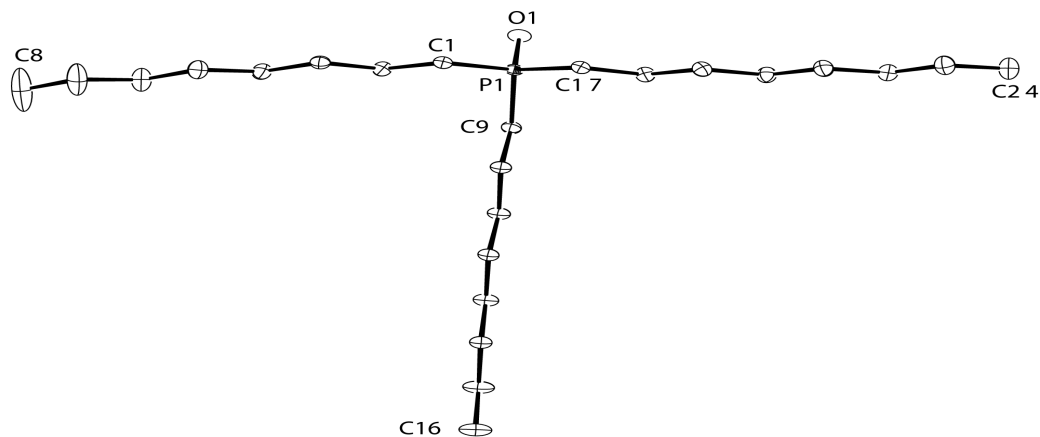


Figure 5.1. Refined ORTEP schematic for monoclinic trioctylphosphine oxide with 50% probability thermal ellipsoids.

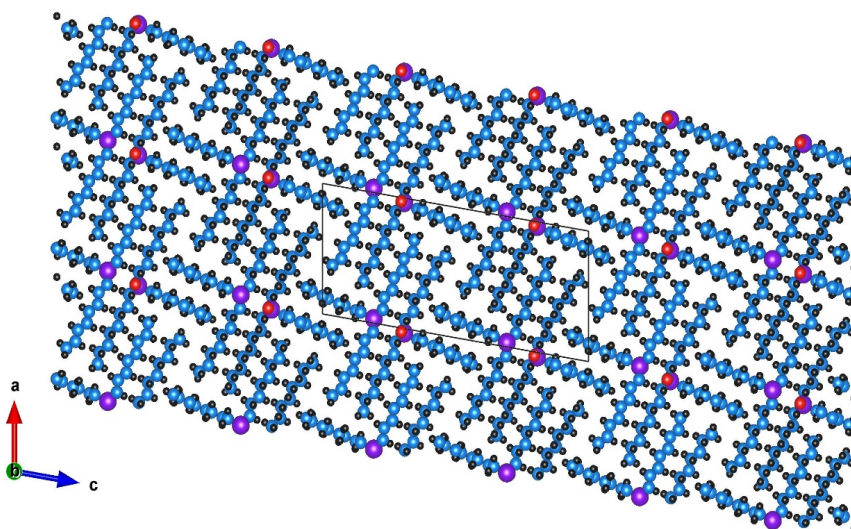


Figure 5.2. In the 2D projection of triethylphosphine oxide supercell, the carbon atoms are shown in blue, hydrogen atoms in gray, phosphorus atoms in purple, and oxygen atoms in red. The unit cell is outlined in black solid lines for clarity.

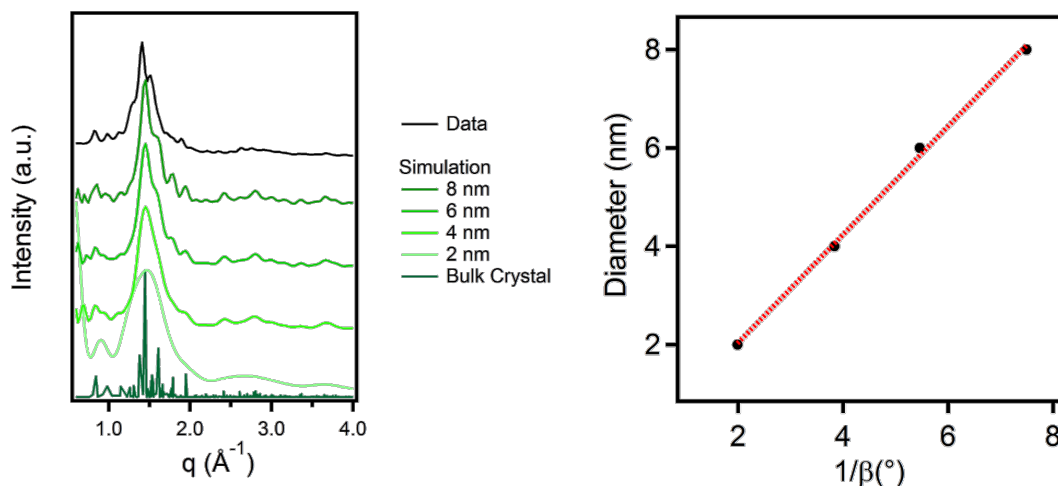


Figure 5.3. (a) Total X-ray scattering (black) is simulated as a function of crystallite size from 2 to 8 nm in diameter (green). The bulk crystal wide-angle diffraction calculation shows the most intense peak at 1.45 \AA^{-1} corresponding to the (1 1 -4) set of Miller planes followed by the characteristic peaks at $q = 0.84, 1.61, 1.79, 1.95 \text{ \AA}^{-1}$ corresponding to the set of (2 0 0), (2 0 8), (1 1 $\bar{7}$), (2 0 $\bar{10}$) planes, respectively. (b) The Gaussian fits of the peaks for the 2 to 8 nm calculated scattering data has a linear dependence with the inverse of the full-width half-maximum values.

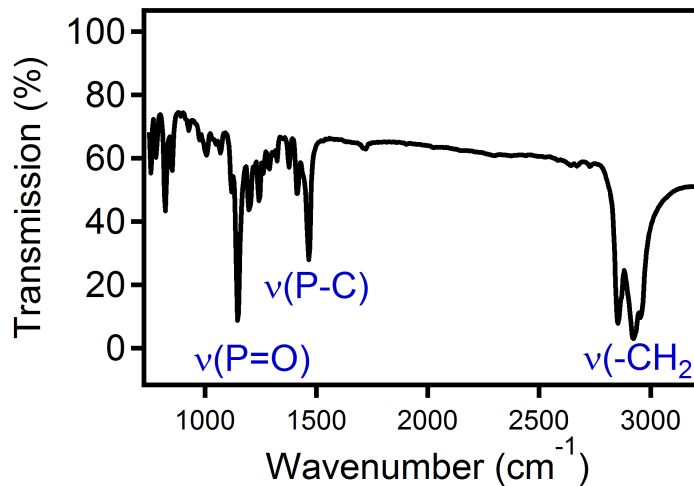


Figure 5.4. FTIR spectroscopy of trioctylphosphine oxide show the characteristic vibrational stretching of the P=O bond at 1146 cm^{-1} , P—C bond at 1465 cm^{-1} , and C—H bonds from the alkyl chains at 2850 and 2919 cm^{-1} .

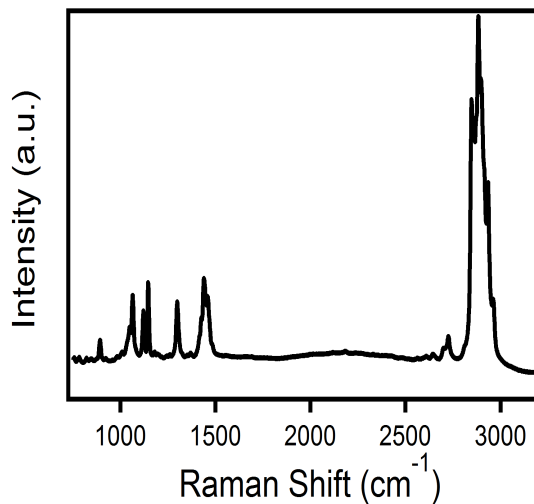


Figure 5.5. Raman spectroscopy of trioctylphosphine oxide captures the vibrational modes for P=O, P—C, and C—H stretching at 1145 , 1138 , and $2848/2882\text{ cm}^{-1}$, respectively.

Table 5.1. Refinement parameters for trioctylphosphine oxide.

Crystal data	
Chemical formula	C ₂₄ H ₅₁ OP
M _r	386.62
Crystal system, space group	Monoclinic, P2 ₁ /c
Temperature (K)	100
a, b, c (Å)	15.0889 (4), 5.2252 (1), 33.5535 (9)
β (°)	99.449 (1)
V (Å ³)	2609.55 (11)
Z	4
Radiation type	Mo Kα
μ (mm ⁻¹)	0.12
Crystal size (mm)	0.38 × 0.24 × 0.07
Data collection	
Diffractometer	Bruker APEXII diffractometer
Absorption correction	Multi-scan (SADABS; Sheldrick, 2007)
T _{min} , T _{max}	0.709, 0.746
No. of measured, independent and observed [I > 2σ(I)] reflections	43246, 5926, 5115
R _{int}	0.026
(sin θ/λ) _{max} (Å ⁻¹)	0.651
Refinement	
R[F ² > 2σ(F ²)], wR(F ²), S	0.039, 0.103, 1.10
No. of reflections	5926
No. of parameters	239
No. of restraints	0
H-atom treatment	H-atom parameters constrained
ΔQ _{max} , ΔQ _{min} (e Å ⁻³)	0.41, -0.35

6. Conclusions

This work has involved the combination of colloidal synthesis, structural characterization, and functional testing of metal, metal phosphide, and metal oxide NPs. The monodispersity of the materials have allowed for correlating their properties to their specific size and shape. For Ni and Pd NPs of less 5 nm in diameter, local atomic packing clearly deviates from the bulk *fcc* structure. From pair distribution function analysis in real space, their local structure can be reasoned to possess icosahedral symmetry despite their long-range disorder. Co₂P nanorods morphology was probed by high-resolution electron microscopy and a suite of X-ray-based techniques to elucidate their crystal structure and morphology. From modeling of total X-ray scattering data, it was demonstrated there was contraction along the *b* lattice parameter of the orthorhombic crystal structure. EXAFS and HAADF-STEM confirmed the existence of a shell of amorphous CoO around the NRs. The Co₂P NRs were shown to be a promising electrocatalyst for the oxygen reduction reaction in fuel cells. Their stability as a catalyst is enhanced by the 1-D structure interaction with the carbon support. This was similarly demonstrated for Pt-based 1-D structures relative to their 0-D counterparts. The structural complexity of doped VO₂ thin films was probed with X-ray absorption to reveal how substitutional dopants distorted the

monoclinic phase to increase or decrease the metal-to-insulator temperature. Finally, the first structural determination of crystalline trioctylphosphine oxide is reported here, obtained via single crystal diffraction.

Investigations of the aforementioned nanomaterials in reciprocal space and subsequent analysis in real space have demonstrated that the bridge to understanding structure-property relations may lie in their small crystallographic distortions. The ability to tune NP size, shape, and architecture can also provide for opportunities to introduce disorder in a controlled manner. The parameter space to do so is vast. Our continually advancing capabilities for determining and refining structure and disorder allow for an exciting future in the research on the structure of matter and design of their functional properties.

Appendix A. Bismuth Nanoparticles

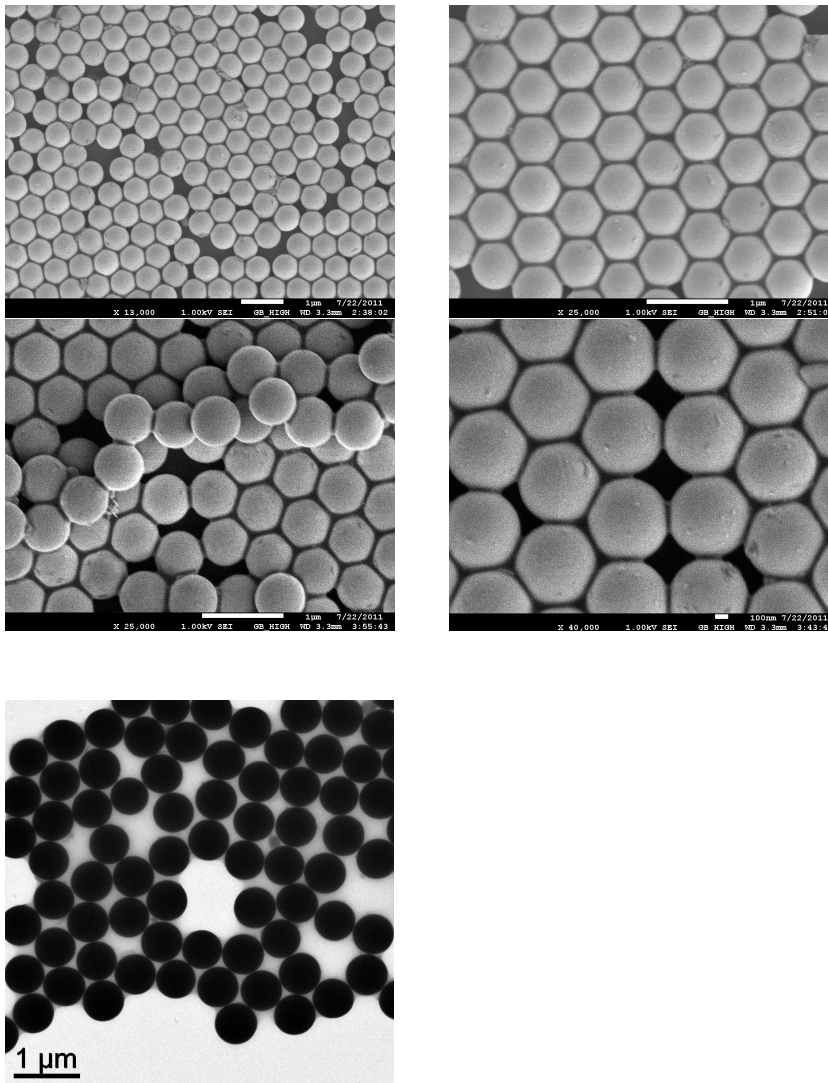


Figure A1. SEM (top) and TEM (bottom) image of bismuth nanoparticles closed-packed on a Cu TEM grid.

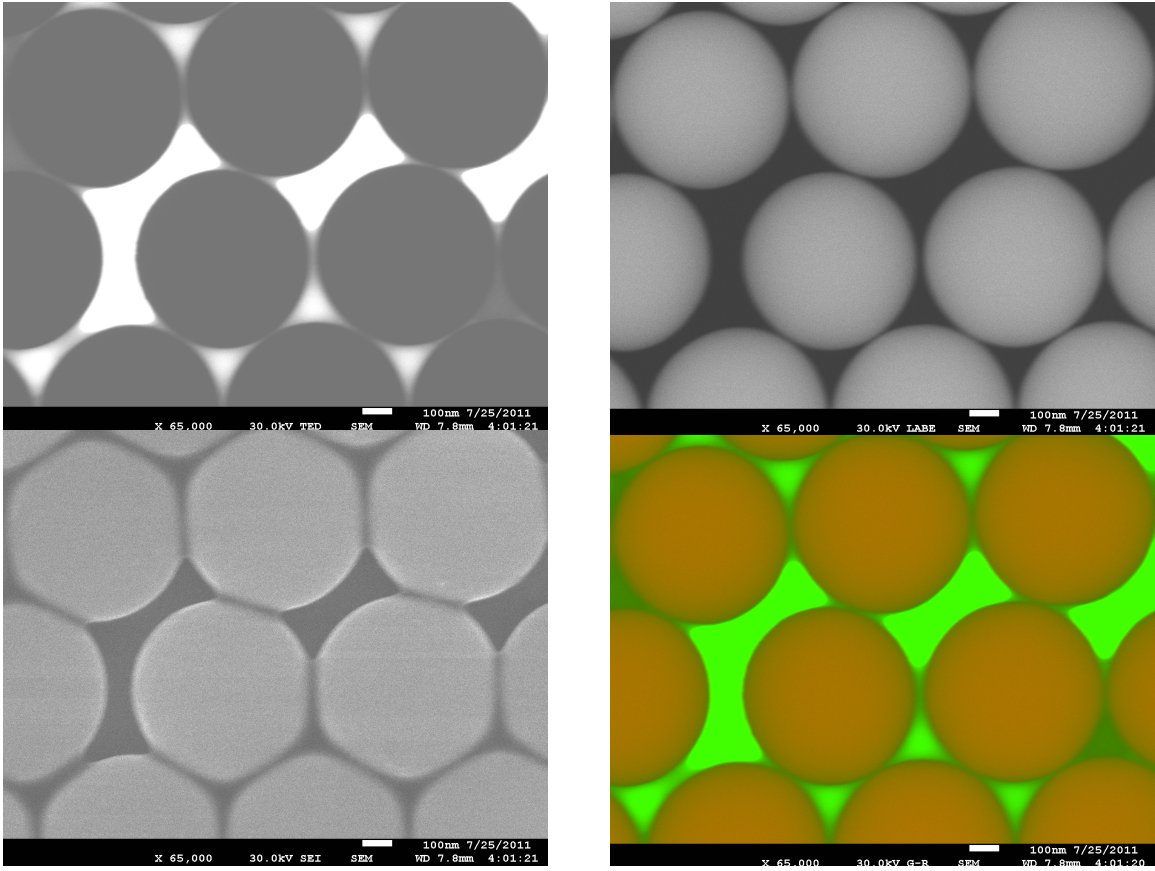


Figure A2. Backscattered electron imaging of bismuth particles.

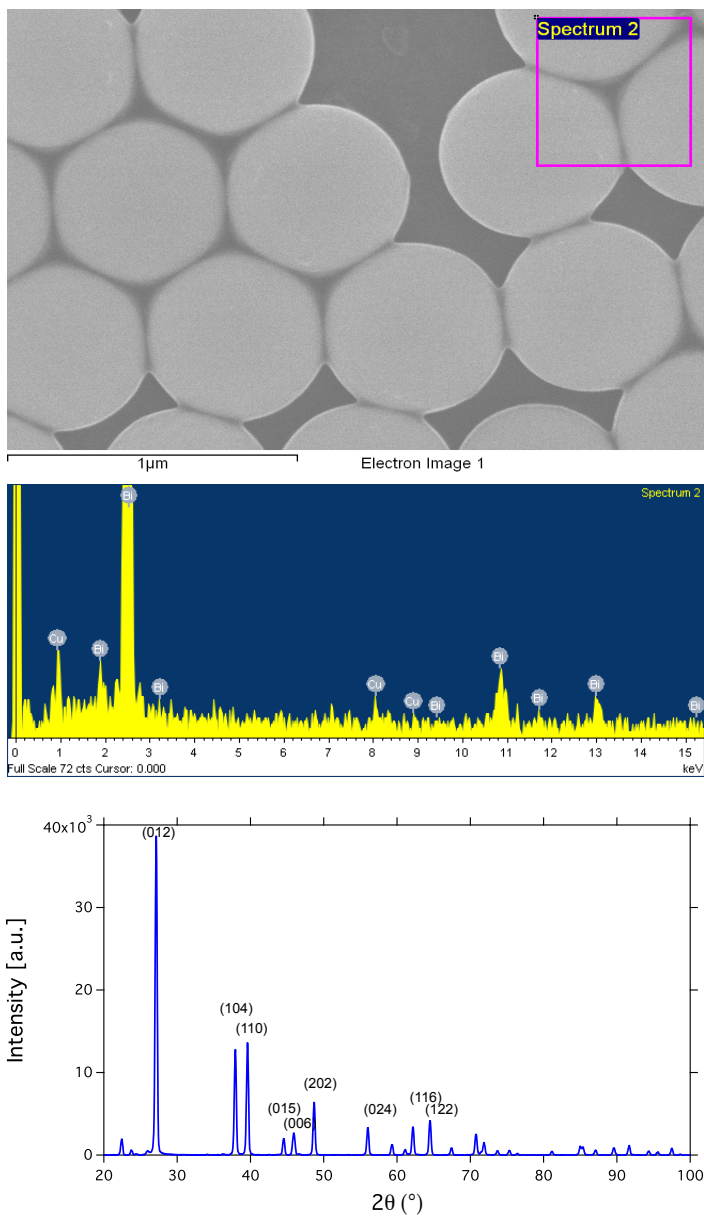


Figure A3. Elemental analysis of bismuth particles (top) and their X-ray diffraction pattern.

Appendix B. Microwave-Assisted Synthesis

Microwave-assisted synthesis (MAS) is a robust technique for facile synthesis of metallic, semiconductor and oxide nanoparticles^{259,26}. The synthetic technique has involved modifications of traditional aqueous, polyol and thermal decomposition methods to include microwave irradiation. From our previous chemical syntheses, we have been able to apply this to technique to the rare-earth metal sulfide system such as EuS. Ni(acac)₂ , Pd(acac)₂ , Pt(acac)₂, trioctylphosphine (TOP) (97%), oleylamine (OLAM) (90%) were purchased from Sigma Aldrich. The precursor for EuS (tetraphenylphosphonium tetrakis(diethyl-dithiocarbamate) europium (III) ((PPh₄) [Eu(S₂CNEt₂)₄])) was prepared as previously reported.²⁶⁰ For the metallic systems, 0.2 mmol of metal salt precursor, a range of molar equivalent of oleylamine and trioctylphosphine (x3, x6, x10) in dimethylformamide (DMF) were combined in a 75-mL Schlenk flask. The solution was maintained and vigorously stirred at 100°C for 15 minutes in an oil bath. The reaction solutions were evacuated to < 1 Torr and refilled with nitrogen. The reaction vessel was transferred to the microwave port and pulsed at constant power of 300 W for 30 s and cooled for 10 s. Magnetization measurements were performed on a Magnetic Property Measurement System from Quantum Design. The TEM images for EuS in Figure B1 show an evolution

towards increasing monodispersity of particle size and shape with increasing reaction time. The reaction time is decreased to 60 minutes with microwave-assisted synthesis as compared to five to six hours via traditional heat-up thermal decomposition methods in the absence of microwave irradiation. TEM images are provided in Figure B2 for the monodispersed EuS nanoparticles synthesized at 290°C for 60 minutes. The paramagnetic EuS (Figure B3) samples and metallic Ni and Pd systems were successfully synthesized by translating thermal decomposition conditions to MAS technique. For Pd, monodispersity is maintained via MAS as shown in Figure B4. For Ni, the rapid heat up of the reaction due to microwave irradiation has resulted in polyhedral nanoparticles resembling tetrahedral as shown in Figure B5. For future work, the Explorer robotic arm combined with the CEM Discovery microwave (Figure B6) can be a powerful tool for screening new synthetic conditions for control over size, shape, and architecture.

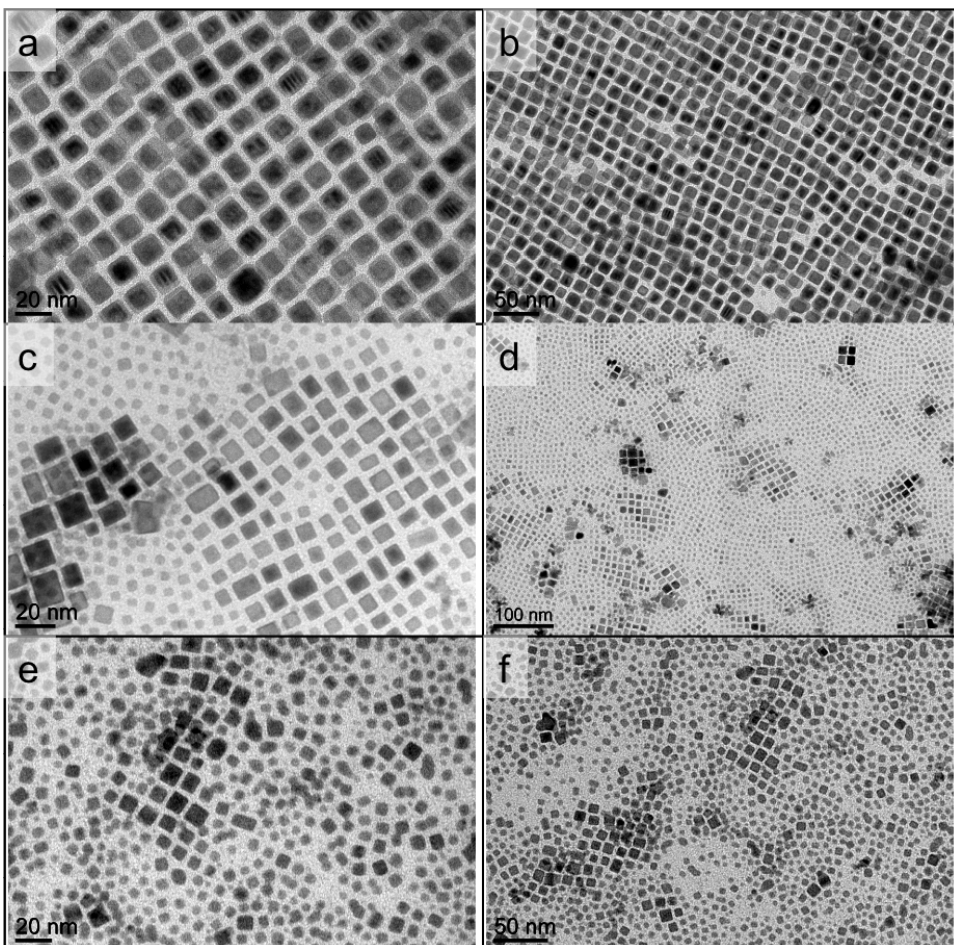


Figure B1. Transmission electron micrographs of EuS cubes. The reaction times were varied while the temperature was maintained at a constant 290°C. The reactions are as follows: (a), (b) 60 minutes, (c), (d) 30 minutes, and (e), (f) 15 minutes.

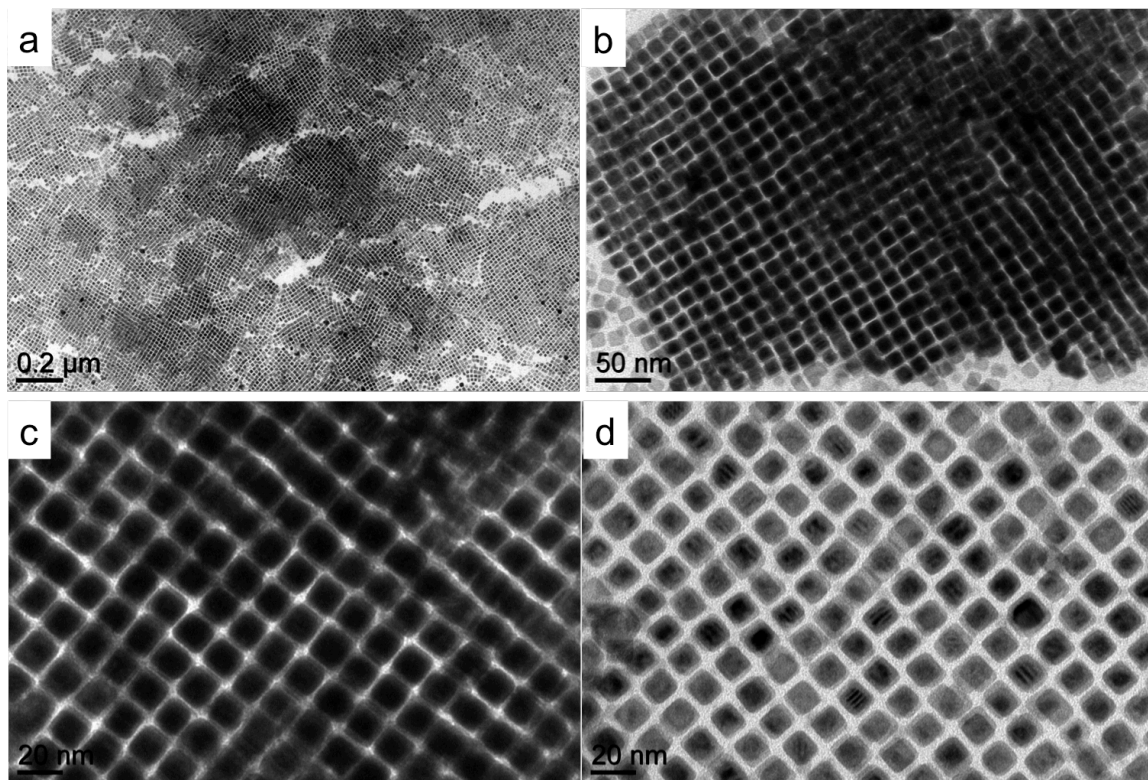


Figure B2. (a-d) TEM images at different magnifications for the EuS samples synthesized at 290°C for 60 minutes.

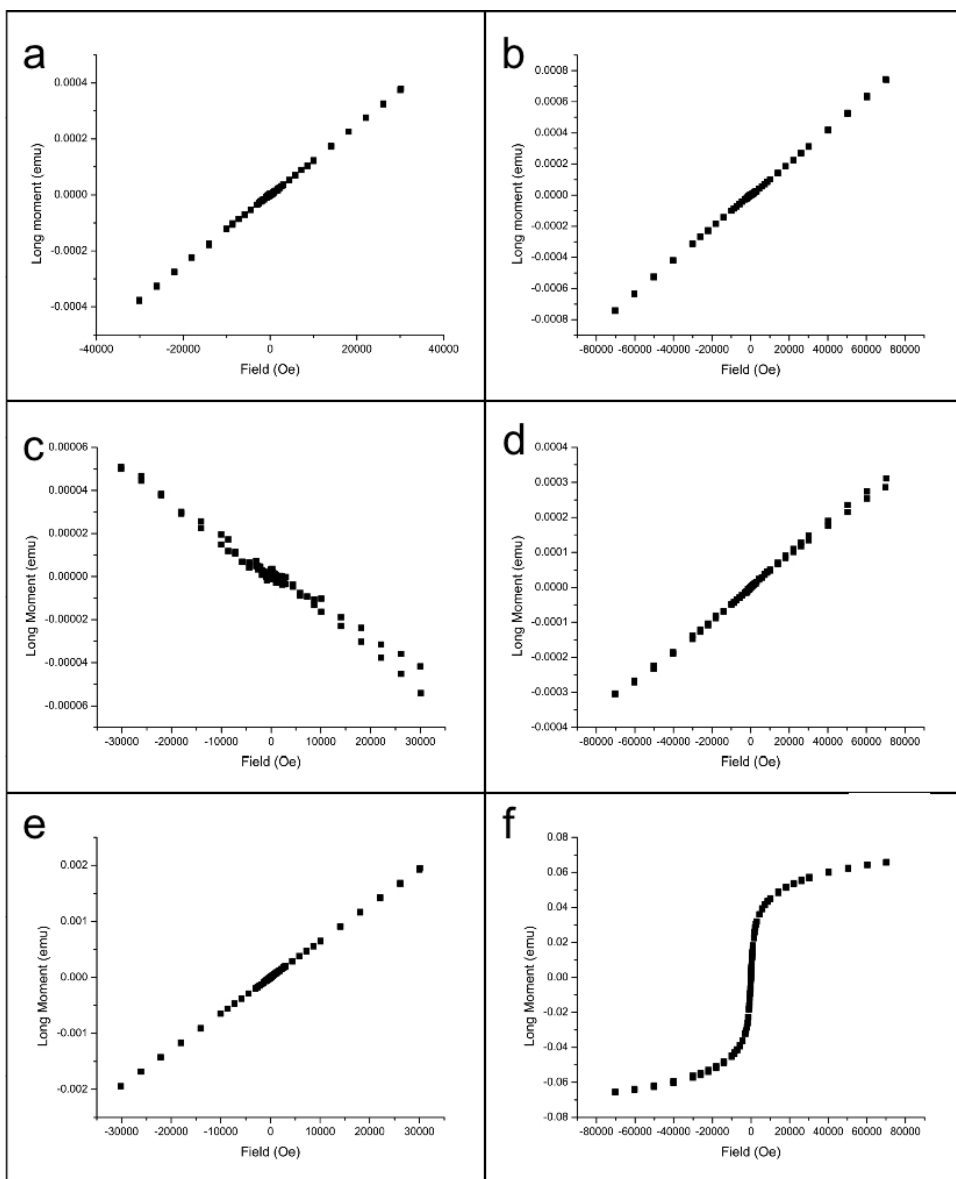


Figure B3. Magnetic measurements for 4 nm Pd at (a) 300 K and (b) 15 K, 2.5 nm Pt NPs at (c) 300 K and (d) 15 K, and EuS at (e) 300 K and (f) 15 K.

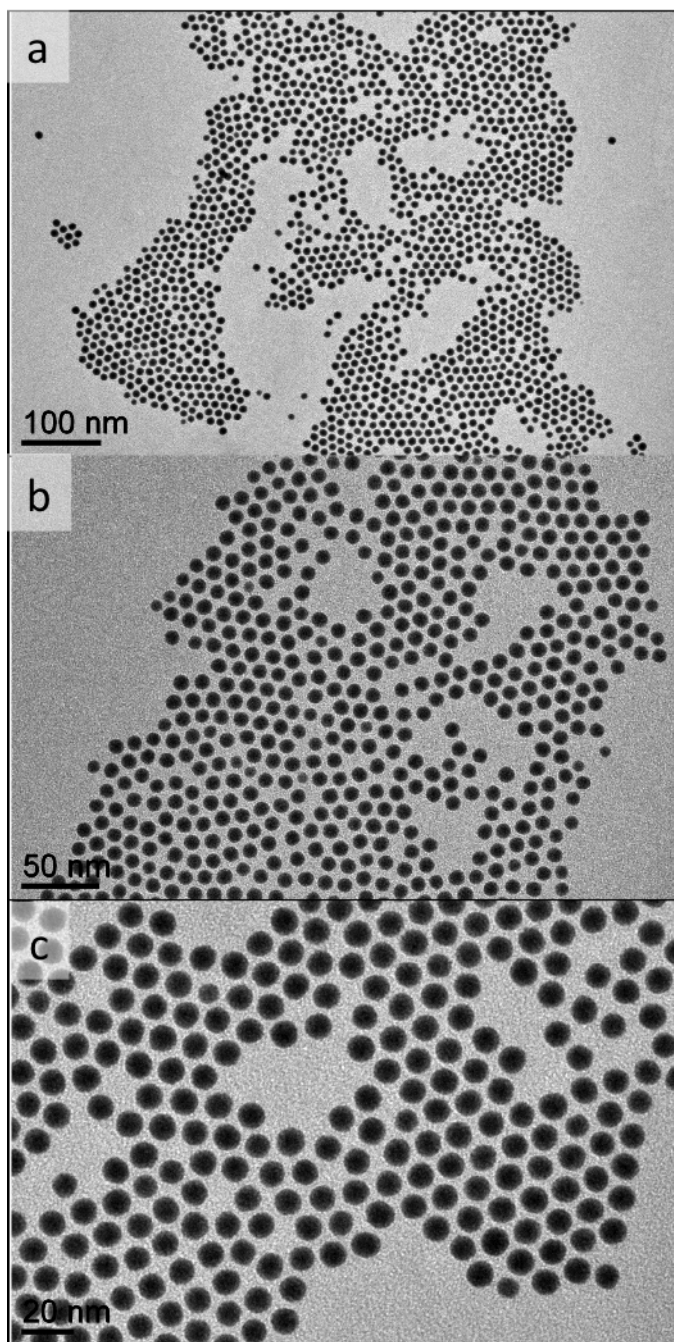


Figure B4. Transmission electron micrographs of 6 nm Pd synthesized via MAS.

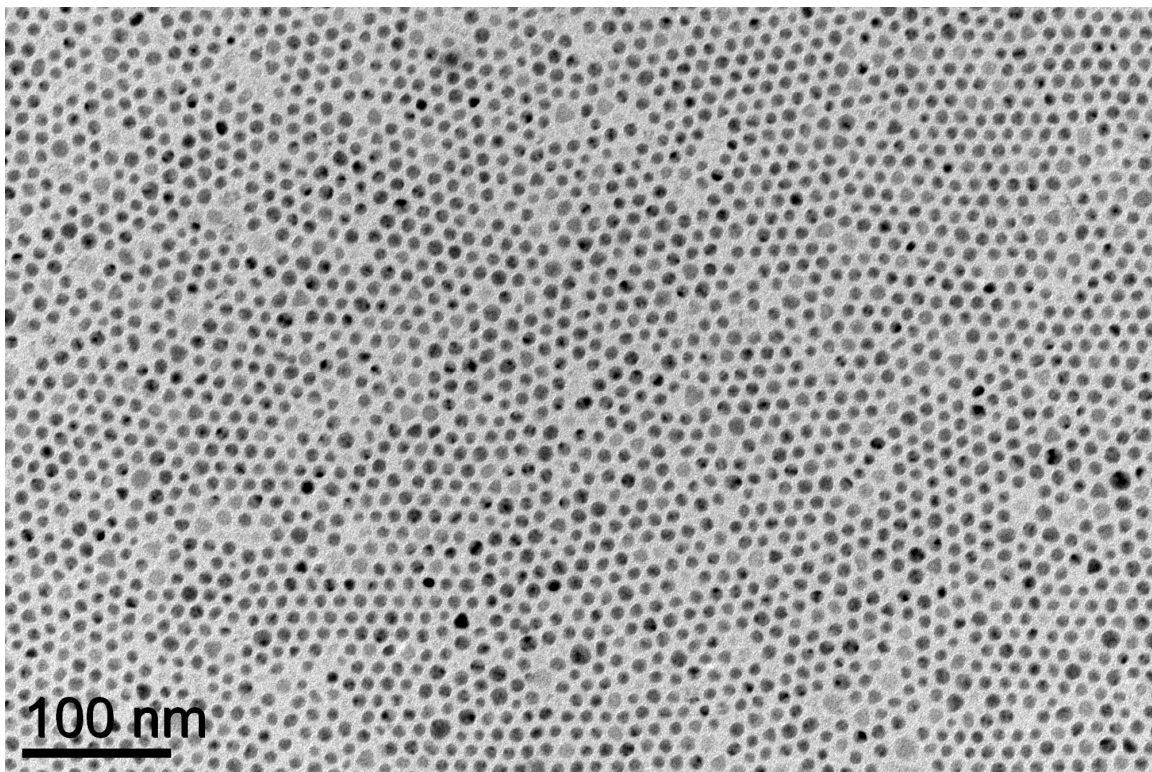


Figure B5. TEM image of dispersion in shape of Ni nanoparticles produced from MAS.

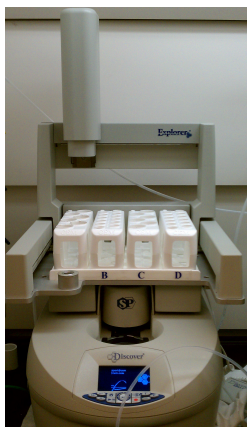


Figure B6. CEM Discovery microwave with Explorer robotic arm.

Appendix C. Cromer-Mann Coefficients

H	0	0.489918	20.6593	0.262003	7.74039	0.196767	49.5519			
		0.049879	2.20159	0.001305						
H	-1	0.897661	53.1368	0.565616	15.187	0.415815	186.576			
		0.116973	3.56709	0.002389						
He	0	0.8734	9.1037	0.6309	3.3568	0.3112	22.9276	0.178	0.9821	0.0064
Li	0	1.1282	3.9546	0.7508	1.0524	0.6175	85.3905	0.4653	168.261	0.0377
Li	1	0.6968	4.6237	0.7888	1.9557	0.3414	0.6316	0.1563	10.0953	0.0167
Be	0	1.5919	43.6427	1.1278	1.8623	0.5391	103.483	0.7029	0.542	0.0385
Be	2	6.2603	0.0027	0.8849	0.8313	0.7993	2.2758	0.1647	5.1146	-6.1092
B	0	2.0545	23.2185	1.3326	1.021	1.0979	60.3498	0.7068	0.1403	-0.1932
C	0	2.31	20.8439	1.02	10.2075	1.5886	0.5687	0.865	51.6512	0.2156
N	0	12.2126	0.0057	3.1322	9.8933	2.0125	28.9975	1.1663	0.5826	-11.529
O	0	3.0485	13.2771	2.2868	5.7011	1.5463	0.3239	0.867	32.9089	0.2508
O	-1	4.1916	12.8573	1.63969	4.17236	1.52673	47.0179	-20.307	-0.0140421	9.412
O	-2	3.75040	16.5151	2.84294	6.59203	1.54298	0.319201		1.62091	43.3486
		0.242060								
F	0	3.5392	10.2825	2.6412	4.2944	1.517	0.2615	1.0243	26.1476	0.2776
F	-1	3.6322	5.27756	3.51057	14.7353	1.26064	0.442258		0.940706	47.3437
		0.653396								
Ne	0	3.9553	8.4042	3.1125	3.4262	1.4546	0.2306	1.1251	21.7184	0.3515
Na	0	4.7626	3.285	3.1736	8.8422	1.2674	0.3136	1.1128	129.424	0.676
Na	1	3.2565	2.6671	3.9362	6.1153	1.3998	0.2001	1.0032	14.039	0.404
Mg	0	5.4204	2.8275	2.1735	79.2611	1.2269	0.3808	2.3073	7.1937	0.8584
Mg	2	3.4988	2.1676	3.8378	4.7542	1.3284	0.185	0.8497	10.1411	0.4853
Al	0	6.4202	3.0387	1.9002	0.7426	1.5936	31.5472	1.9646	85.0886	1.1151
Al	3	4.17448	1.93816	3.3876	4.14553	1.20296	0.228753		0.528137	8.28524
		0.706786								
Si	0	6.2915	2.4386	3.0353	32.3337	1.9891	0.6785	1.541	81.6937	1.1407
Si	4	4.43918	1.64167	3.20345	3.43757	1.19453	0.2149	0.41653	6.65365	0.746297
P	0	6.4345	1.9067	4.1791	27.157	1.78	0.526	1.4908	68.1645	1.1149
S	0	6.9053	1.4679	5.2034	22.2151	1.4379	0.2536	1.5863	56.172	0.8669
Cl	0	11.4604	0.0104	7.1964	1.1662	6.2556	18.5194	1.6455	47.7784	-9.5574
Cl	-1	18.2915	0.0066	7.2084	1.1717	6.5337	19.5424	2.3386	60.4486	-16.378
Ar	0	7.4845	0.9072	6.7723	14.8407	0.6539	43.8983	1.6442	33.3929	1.4445
K	0	8.2186	12.7949	7.4398	0.7748	1.0519	213.187	0.8659	41.6841	1.4228
K	1	7.9578	12.6331	7.4917	0.7674	6.359	-0.002	1.1915	31.9128	-4.9978
Ca	0	8.6266	10.4421	7.3873	0.6599	1.5899	85.7484	1.0211	178.437	1.3751
Ca	2	15.6348	-0.0074	7.9518	0.6089	8.4372	10.3116	0.8537	25.9905	-14.875
Sc	0	9.189	9.0213	7.3679	0.5729	1.6409	136.108	1.468	51.3531	1.3329
Sc	3	13.4008	0.29854	8.0273	7.9629	1.65943	-0.286041	5.7936	16.0662	-6.6667
Ti	0	9.7595	7.8508	7.3558	0.5	1.6991	35.6338	1.9021	116.105	1.2807
Ti	2	9.11423	7.5243	7.62174	0.457585		2.2793	19.5361	0.087899	61.6558
		0.897155								

Ti	3	17.7344	0.22061	8.73816	7.04716	5.25691	-0.157621	9.2134	15.9768	-14.652
Ti	4	19.5114	0.178847		8.23473	6.67018	2.01341	-0.292631	5.5208	12.9464 -13.28
V	0	10.2971	6.8657	7.3511	0.4385	2.0703	26.8938	2.0571	102.478	1.2199
V	2	10.106	6.8818	7.3541	0.4409	2.2884	20.3004	0.0223	115.122	1.2298
V	3	9.43141	6.39535	7.7419	0.383349		2.15343	15.1908	0.016865	63.969
		0.656565								
V	5	15.6887	0.679003		8.14208	5.40135	2.03081	9.97278	-9.576	0.940464
		1.7143								
Cr	0	10.6406	6.1038	7.3537	0.392	3.324	20.2626	1.4922	98.7399	1.1832
Cr	2	9.54034	5.66078	7.7509	0.344261		3.58274	13.3075	0.509107	32.4224
		0.616898								
Cr	3	9.6809	5.59463	7.81136	0.334393		2.87603	12.8288	0.113575	32.8761
		0.518275								
Mn	0	11.2819	5.3409	7.3573	0.3432	3.0193	17.8674	2.2441	83.7543	1.0896
Mn	2	10.8061	5.2796	7.362	0.3435	3.5268	14.343	0.2184	41.3235	1.0874
Mn	3	9.84521	4.91797	7.87194	0.294393		3.56531	10.8171	0.323613	24.1281
		0.393974								
Mn	4	9.96253	4.8485	7.97057	0.283303		2.76067	10.4852	0.054447	27.573
		0.251877								
Fe	0	11.7695	4.7611	7.3573	0.3072	3.5222	15.3535	2.3045	76.8805	1.0369
Fe	2	11.0424	4.6538	7.374	0.3053	4.1346	12.0546	0.4399	31.2809	1.0097
Fe	3	11.1764	4.6147	7.3863	0.3005	3.3948	11.6729	0.0724	38.5566	0.9707
Co	0	12.2841	4.2791	7.3409	0.2784	4.0034	13.5359	2.3488	71.1692	1.0118
Co	2	11.2296	4.1231	7.3883	0.2726	4.7393	10.2443	0.7108	25.6466	0.9324
Co	3	10.338	3.90969	7.88173	0.238668		4.76795	8.35583	0.725591	18.3491
		0.286667								
Ni	0	12.8376	3.8785	7.292	0.2565	4.4438	12.1763	2.38	66.3421	1.0341
Ni	2	11.4166	3.6766	7.4005	0.2449	5.3442	8.873	0.9773	22.1626	0.8614
Ni	3	10.7806	3.5477	7.75868	0.22314	5.22746	7.64468	0.847114		16.9673
		0.386044								
Cu	0	13.338	3.5828	7.1676	0.247	5.6158	11.3966	1.6735	64.8126	1.191
Cu	1	11.9475	3.3669	7.3573	0.2274	6.2455	8.6625	1.5578	25.8487	0.89
Cu	2	11.8168	3.37484	7.11181	0.244078		5.78135	7.9876	1.14523	19.897 1.14431
Zn	0	14.0743	3.2655	7.0318	0.2333	5.1652	10.3163	2.41	58.7097	1.3041
Zn	2	11.9719	2.9946	7.3862	0.2031	6.4668	7.0826	1.394	18.0995	0.7807
Ga	0	15.2354	3.0669	6.7006	0.2412	4.3591	10.7805	2.9623	61.4135	1.7189
Ga	3	12.692	2.81262	6.69883	0.22789	6.06692	6.36441	1.0066	14.4122	1.53545
Ge	0	16.0816	2.8509	6.3747	0.2516	3.7068	11.4468	3.683	54.7625	2.1313
Ge	4	12.9172	2.53718	6.70003	0.205855		6.06791	5.47913	0.859041	11.603
		1.45572								
As	0	16.6723	2.6345	6.0701	0.2647	3.4313	12.9479	4.2779	47.7972	2.531
Se	0	17.0006	2.4098	5.8196	0.2726	3.9731	15.2372	4.3543	43.8163	2.8409
Br	0	17.1789	2.1723	5.2358	16.5796	5.6377	0.2609	3.9851	41.4328	2.9557
Br	-1	17.1718	2.2059	6.3338	19.3345	5.5754	0.2871	3.7272	58.1535	3.1776
Kr	0	17.3555	1.9384	6.7286	16.5623	5.5493	0.2261	3.5375	39.3972	2.825
Rb	0	17.1784	1.7888	9.6435	17.3151	5.1399	0.2748	1.5292	164.934	3.4873

Rb	1	17.5816	1.7139	7.6598	14.7957	5.8981	0.1603	2.7817	31.2087	2.0782	
Sr	0	17.5663	1.5564	9.8184	14.0988	5.422	0.1664	2.6694	132.376	2.5064	
Sr	2	18.0874	1.4907	8.1373	12.6963	2.5654	24.5651	-34.193	-0.0138	41.4025	
Y	0	17.776	1.4029	10.2946	12.8006	5.72629	0.125599		3.26588	104.354	1.91213
Y	3	17.9268	1.35417	9.1531	11.2145	1.76795	22.6599	-33.108	-0.0131	1940.2602	
Zr	0	17.8765	1.27618	10.948	11.916	5.41732	0.117622		3.65721	87.6627	2.06929
Zr	4	18.1668	1.2148	10.0562	10.1483	1.01118	21.6054	-2.6479	-0.102769	41454	
Nb	0	17.6142	1.18865	12.0144	11.766	4.04183	0.204785		3.53346	69.7957	3.75591
Nb	3	19.8812	0.019175		18.0653	1.13305	11.0177	10.1621	1.94715	28.3389	-12.912
Nb	5	17.9163	1.12446	13.3417	0.028781		10.799	9.28206	0.337905		25.7228
											-6.3934
Mo	0	3.7025	0.2772	17.2356	1.0958	12.8876	11.004	3.7429	61.6584	4.3875	
Mo	3	21.1664	0.014734		18.2017	1.03031	11.7423	9.53659	2.30951	26.6307	-14.421
Mo	5	21.0149	0.014345		18.0992	1.02238	11.4632	8.78809	0.740625		23.3452
											-14.316
Mo	6	17.8871	1.03649	11.175	8.48061	6.57891	0.058881		0	0	
											0.344941
Tc	0	19.1301	0.864132		11.0948	8.14487	4.64901	21.5707	2.71263	86.8472	5.40428
Ru	0	19.2674	0.80852	12.9182	8.43467	4.86337	24.7997	1.56756	94.2928	5.37874	
Ru	3	18.5638	0.847329		13.2885	8.37164	9.32602	0.017662		3.00964	22.887
											-3.1892
Ru	4	18.5003	0.844582		13.1787	8.12534	4.71304	0.36495	2.18535	20.8504	1.42357
Rh	0	19.2957	0.751536		14.3501	8.21758	4.73425	25.8749	1.28918	98.6062	5.328
Rh	3	18.8785	0.764252		14.1259	7.84438	3.32515	21.2487	-6.1989	-0.0103611	18.678
Rh	4	18.8545	0.760825		13.9806	7.62436	2.53464	19.3317	-5.6526	-0.0102	11.2835
Pd	0	19.3319	0.698655		15.5017	7.98929	5.29537	25.2052	0.605844		76.8986
											5.26593
Pd	2	19.1701	0.696219		15.2096	7.55573	4.32234	22.5057	0	0	5.2916
Pd	4	19.2493	0.683839		14.79	7.14833	2.89289	17.9144	-7.9492	0.005127	
											13.0174
Ag	0	19.2808	0.6446	16.6885	7.4726	4.8045	24.6605	1.0463	99.8156	5.179	
Ag	1	19.1812	0.646179		15.9719	7.19123	5.27475	21.7326	0.357534		66.1147
											5.21572
Ag	2	19.1643	0.645643		16.2456	7.18544	4.3709	21.4072	0	0	5.21404
Cd	0	19.2214	0.5946	17.6444	6.9089	4.461	24.7008	1.6029	87.4825	5.0694	
Cd	2	19.1514	0.597922		17.2535	6.80639	4.47128	20.2521	0	0	5.11937
In	0	19.1624	0.5476	18.5596	6.3776	4.2948	25.8499	2.0396	92.8029	4.9391	
In	3	19.1045	0.551522		18.1108	6.3247	3.78897	17.3595	0	0	4.99635
Sn	0	19.1889	5.8303	19.1005	0.5031	4.4585	26.8909	2.4663	83.9571	4.7821	
Sn	2	19.1094	0.5036	19.0548	5.8378	4.5648	23.3752	0.487	62.2061	4.7861	
Sn	4	18.9333	5.764	19.7131	0.4655	3.4182	14.0049	0.0193	-0.7583	3.9182	
Sb	0	19.6418	5.3034	19.0455	0.4607	5.0371	27.9074	2.6827	75.2825	4.5909	
Sb	3	18.9755	0.467196		18.933	5.22126	5.10789	19.5902	0.288753		55.5113
											4.69626
Sb	5	19.8685	5.44853	19.0302	0.467973		2.41253	14.1259	0	0	4.69263
Te	0	19.9644	4.81742	19.0138	0.420885		6.14487	28.5284	2.5239	70.8403	4.352

I	0	20.1472	4.347	18.9949	0.3814	7.5138	27.766	2.2735	66.8776	4.0712	
I	-1	20.2332	4.3579	18.997	0.3815	7.8069	29.5259	2.8868	84.9304	4.0714	
Xe	0	20.2933	3.9282	19.0298	0.344	8.9767	26.4659	1.99	64.2658	3.7118	
Cs	0	20.3892	3.569	19.1062	0.3107	10.662	24.3879	1.4953	213.904	3.3352	
Cs	1	20.3524	3.552	19.1278	0.3086	10.2821	23.7128	0.9615	59.4565	3.2791	
Ba	0	20.3361	3.216	19.297	0.2756	10.888	20.2073	2.6959	167.202	2.7731	
Ba	2	20.1807	3.21367	19.1136	0.28331	10.9054	20.0558	0.77634	51.746	3.02902	
La	0	20.578	2.94817	19.599	0.244475		11.3727	18.7726	3.28719	133.124	2.14678
La	3	20.2489	2.9207	19.3763	0.250698		11.6323	17.8211	0.336048		54.9453
		2.4086									
Ce	0	21.1671	2.81219	19.7695	0.226836		11.8513	17.6083	3.33049	127.113	1.86264
Ce	3	20.8036	2.77691	19.559	0.23154	11.9369	16.5408	0.612376		43.1692	2.09013
Ce	4	20.3235	2.65941	19.8186	0.21885	12.1233	15.7992	0.144583		62.2355	1.5918
Pr	0	22.044	2.77393	19.6697	0.222087		12.3856	16.7669	2.82428	143.644	2.0583
Pr	3	21.3727	2.6452	19.7491	0.214299		12.1329	15.323	0.97518	36.4065	1.77132
Pr	4	20.9413	2.54467	20.0539	0.202481		12.4668	14.8137	0.296689		45.4643
		1.24285									
Nd	0	22.6845	2.66248	19.6847	0.210628		12.774	15.885	2.85137	137.903	1.98486
Nd	3	21.961	2.52722	19.9339	0.199237		12.12	14.1783	1.51031	30.8717	1.47588
Pm	0	23.3405	2.5627	19.6095	0.202088		13.1235	15.1009	2.87516	132.721	2.02876
Pm	3	22.5527	2.4174	20.1108	0.185769		12.0671	13.1275	2.07492	27.4491	1.19499
Sm	0	24.0042	2.47274	19.4258	0.196451		13.4396	14.3996	2.89604	128.007	2.20963
Sm	3	23.1504	2.31641	20.2599	0.174081		11.9202	12.1571	2.71488	24.8242	
		0.954586									
Eu	0	24.6274	2.3879	19.0886	0.1942	13.7603	13.7546	2.9227	123.174	2.5745	
Eu	2	24.0063	2.27783	19.9504	0.17353	11.8034	11.6096	3.87243	26.5156	1.36389	
Eu	3	23.7497	2.22258	20.3745	0.16394	11.8509	11.311	3.26503	22.9966	0.759344	
Gd	0	25.0709	2.25341	19.0798	0.181951		13.8518	12.9331	3.54545	101.398	2.4196
Gd	3	24.3466	2.13553	20.4208	0.155525		11.8708	10.5782	3.7149	21.7029	
		0.645089									
Tb	0	25.8976	2.24256	18.2185	0.196143		14.3167	12.6648	2.95354	115.362	3.58324
Tb	3	24.9559	2.05601	20.3271	0.149525		12.2471	10.0499	3.773	21.2773	
		0.691967									
Dy	0	26.507	2.1802	17.6383	0.202172		14.5596	12.1899	2.96577	111.874	4.29728
Dy	3	25.5395	1.9804	20.2861	0.143384		11.9812	9.34972	4.50073	19.581	0.68969
Ho	0	26.9049	2.07051	17.294	0.19794	14.5583	11.4407	3.63837	92.6566	4.56796	
Ho	3	26.1296	1.91072	20.0994	0.139358		11.9788	8.80018	4.93676	18.5908	
		0.852795									
Er	0	27.6563	2.07356	16.4285	0.223545		14.9779	11.3604	2.98233	105.703	5.92046
Er	3	26.722	1.84659	19.7748	0.13729	12.1506	8.36225	5.17379	17.8974	1.17613	
Tm	0	28.1819	2.02859	15.8851	0.238849		15.1542	10.9975	2.98706	102.961	6.75621
Tm	3	27.3083	1.78711	19.332	0.136974		12.3339	7.96778	5.38348	17.2922	1.63929
Yb	0	28.6641	1.9889	15.4345	0.257119		15.3087	10.6647	2.98963	100.417	7.56672
Yb	2	28.1209	1.78503	17.6817	0.15997	13.3335	8.18304	5.14657	20.39	3.70983	
Yb	3	27.8917	1.73272	18.7614	0.13879	12.6072	7.64412	5.47647	16.8153	2.26001	
Lu	0	28.9476	1.90182	15.2208	9.98519	15.1	0.261033		3.71601	84.3298	7.97628

Lu	3	28.4628	1.68216	18.121	0.142292	12.8429	7.33727	5.59415	16.3535	2.97573
Hf	0	29.144	1.83262	15.1726	9.5999	14.7586	0.275116	4.30013	72.029	8.58154
Hf	4	28.8131	1.59136	18.4601	0.128903	12.7285	6.76232	5.59927	14.0366	2.39699
Ta	0	29.2024	1.77333	15.2293	9.37046	14.5135	0.295977	4.76492	63.3644	9.24354
Ta	5	29.1587	1.50711	18.8407	0.116741	12.8268	6.31524	5.38695	12.4244	1.78555
W	0	29.0818	1.72029	15.43	9.2259	14.4327	0.321703	5.11982	57.056	9.8875
W	6	29.4936	1.42755	19.3763	0.104621	13.0544	5.93667	5.06412	11.1972	1.01074
Re	0	28.7621	1.67191	15.7189	9.09227	14.5564	0.3505	5.44174	52.0861	10.472
Os	0	28.1894	1.62903	16.155	8.97948	14.9305	0.382661	5.67589	48.1647	11.0005
Os	4	30.419	1.37113	15.2637	6.84706	14.7458	0.165191	5.06795	18.003	6.49804
Ir	0	27.3049	1.59279	16.7296	8.86553	15.6115	0.417916	5.83377	45.0011	11.4722
Ir	3	30.4156	1.34323	15.862	7.10909	13.6145	0.204633	5.82008	20.3254	8.27903
Ir	4	30.7058	1.30923	15.5512	6.71983	14.2326	0.167252	5.53672	17.4911	6.96824
Pt	0	27.0059	1.51293	17.7639	8.81174	15.7131	0.424593	5.7837	38.6103	11.6883
Pt	2	29.8429	1.32927	16.7224	7.38979	13.2153	0.263297	6.35234	22.9426	9.85329
Pt	4	30.9612	1.24813	15.9829	6.60834	13.7348	0.16864	5.92034	16.9392	7.39534
Au	0	16.8819	0.4611	18.5913	8.6216	25.5582	1.4826	5.86	36.3956	12.0658
Au	1	28.0109	1.35321	17.8204	7.7395	14.3359	0.356752	6.58077	26.4043	11.2299
Au	3	30.6886	1.2199	16.9029	6.82872	12.7801	0.212867	6.52354	18.659	9.0968
Hg	0	20.6809	0.545	19.0417	8.4484	21.6575	1.5729	5.9676	38.3246	12.6089
Hg	1	25.0853	1.39507	18.4973	7.65105	16.8883	0.443378	6.48216	28.2262	12.0205
Hg	2	29.5641	1.21152	18.06	7.05639	12.8374	0.284738	6.89912	20.7482	10.6268
Tl	0	27.5446	0.65515	19.1584	8.70751	15.538	1.96347	5.52593	45.8149	13.1746
Tl	1	21.3985	1.4711	20.4723	0.517394	18.7478	7.43463	6.82847	28.8482	12.5258
Tl	3	30.8695	1.1008	18.3481	6.53852	11.9328	0.219074	7.00574	17.2114	9.8027
Pb	0	31.0617	0.6902	13.0637	2.3576	18.442	8.618	5.9696	47.2579	13.4118
Pb	2	21.7886	1.3366	19.5682	0.488383	19.1406	6.7727	7.01107	23.8132	12.4734
Pb	4	32.1244	1.00566	18.8003	6.10926	12.0175	0.147041	6.96886	14.714	8.08428
Bi	0	33.3689	0.704	12.951	2.9238	16.5877	8.7937	6.4692	48.0093	13.5782
Bi	3	21.8053	1.2356	19.5026	6.24149	19.1053	0.469999	7.10295	20.3185	12.4711
Bi	5	33.5364	0.91654	25.0946	0.39042	19.2497	5.71414	6.91555	12.8285	-6.7994
Po	0	34.6726	0.700999	15.4733	3.55078	13.1138	9.55642	7.02588	47.0045	13.677
At	0	35.3163	0.68587	19.0211	3.97458	9.49887	11.3824	7.42518	45.4715	13.7108
Rn	0	35.5631	0.6631	21.2816	4.0691	8.0037	14.0422	7.4433	44.2473	13.6905
Fr	0	35.9299	0.646453	23.0547	4.17619	12.1439	23.1052	2.11253	150.645	13.7247
Ra	0	35.763	0.616341	22.9064	3.87135	12.4739	19.9887	3.21097	142.325	13.6211
Ra	2	35.215	0.604909	21.67	3.5767	7.91342	12.601	7.65078	29.8436	13.5431
Ac	0	35.6597	0.589092	23.1032	3.65155	12.5977	18.599	4.08655	117.02	13.5266
Ac	3	35.1736	0.579689	22.1112	3.41437	8.19216	12.9187	7.05545	25.9443	13.4637
Th	0	35.5645	0.563359	23.4219	3.46204	12.7473	17.8309	4.80703	99.1722	13.4314
Th	4	35.1007	0.555054	22.4418	3.24498	9.78554	13.4661	5.29444	23.9533	13.376
Pa	0	35.8847	0.547751	23.2948	3.41519	14.1891	16.9235	4.17287	105.251	13.4287
U	0	36.0228	0.5293	23.4128	3.3253	14.9491	16.0927	4.188	100.613	13.3966
U	3	35.5747	0.52048	22.5259	3.12293	12.2165	12.7148	5.37073	26.3394	13.3092
U	4	35.3715	0.516598	22.5326	3.05053	12.0291	12.5723	4.7984	23.4582	13.2671
U	6	34.8509	0.507079	22.7584	2.8903	14.0099	13.1767	1.21457	25.2017	13.1665

Np	0	36.1874	0.511929	23.5964	3.25396	15.6402	15.3622	4.1855	97.4908	13.3573
Np	3	35.7074	0.502322	22.613	3.03807	12.9898	12.1449	5.43227	25.4928	13.2544
Np	4	35.5103	0.498626	22.5787	2.96627	12.7766	11.9484	4.92159	22.7502	13.2116
Np	6	35.0136	0.48981	22.7286	2.81099	14.3884	12.33	1.75669	22.6581	13.113
Pu	0	36.5254	0.499384	23.8083	3.26371	16.7707	14.9455	3.47947	105.98	13.3812
Pu	3	35.84	0.484938	22.7169	2.96118	13.5807	11.5331	5.66016	24.3992	13.1991
Pu	4	35.6493	0.481422	22.646	2.8902	13.3595	11.316	5.18831	21.8301	13.1555
Pu	6	35.1736	0.473204	22.7181	2.73848	14.7635	11.553	2.28678	20.9303	13.0582
Am	0	36.6706	0.483629	24.0992	3.20647	17.3415	14.3136	3.49331	102.273	13.3592
Cm	0	36.6488	0.465154	24.4096	3.08997	17.399	13.4346	4.21665	88.4834	13.2887
Bk	0	36.7881	0.451018	24.7736	3.04619	17.8919	12.8946	4.23284	86.003	13.2754
Cf	0	36.9185	0.437533	25.1995	3.00775	18.3317	12.4044	4.24391	83.7881	13.2674

Appendix D. Total Scattering Experimental Set-Up

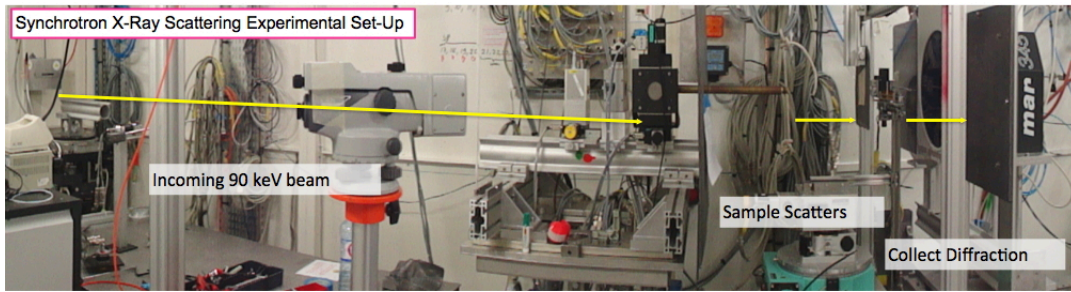
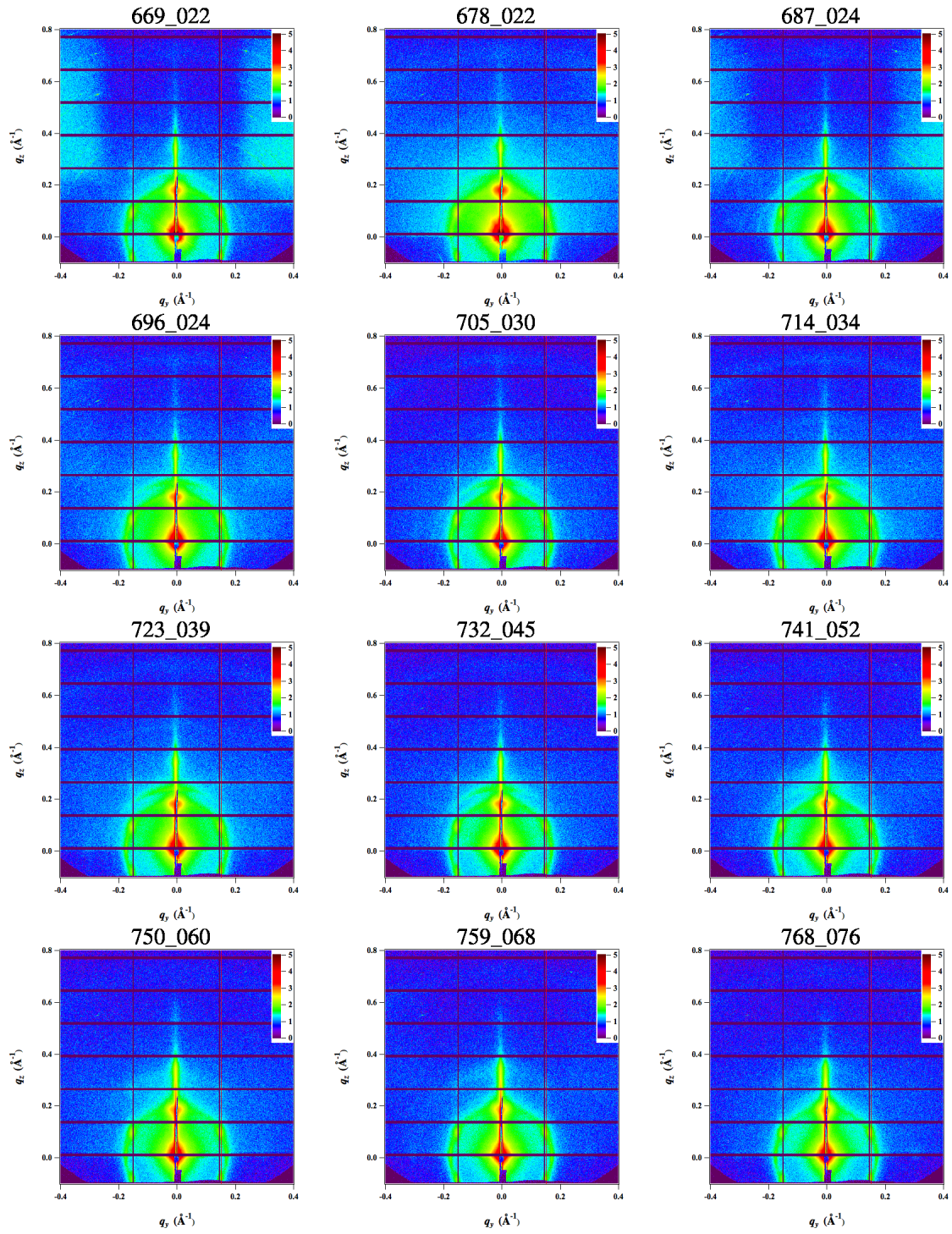


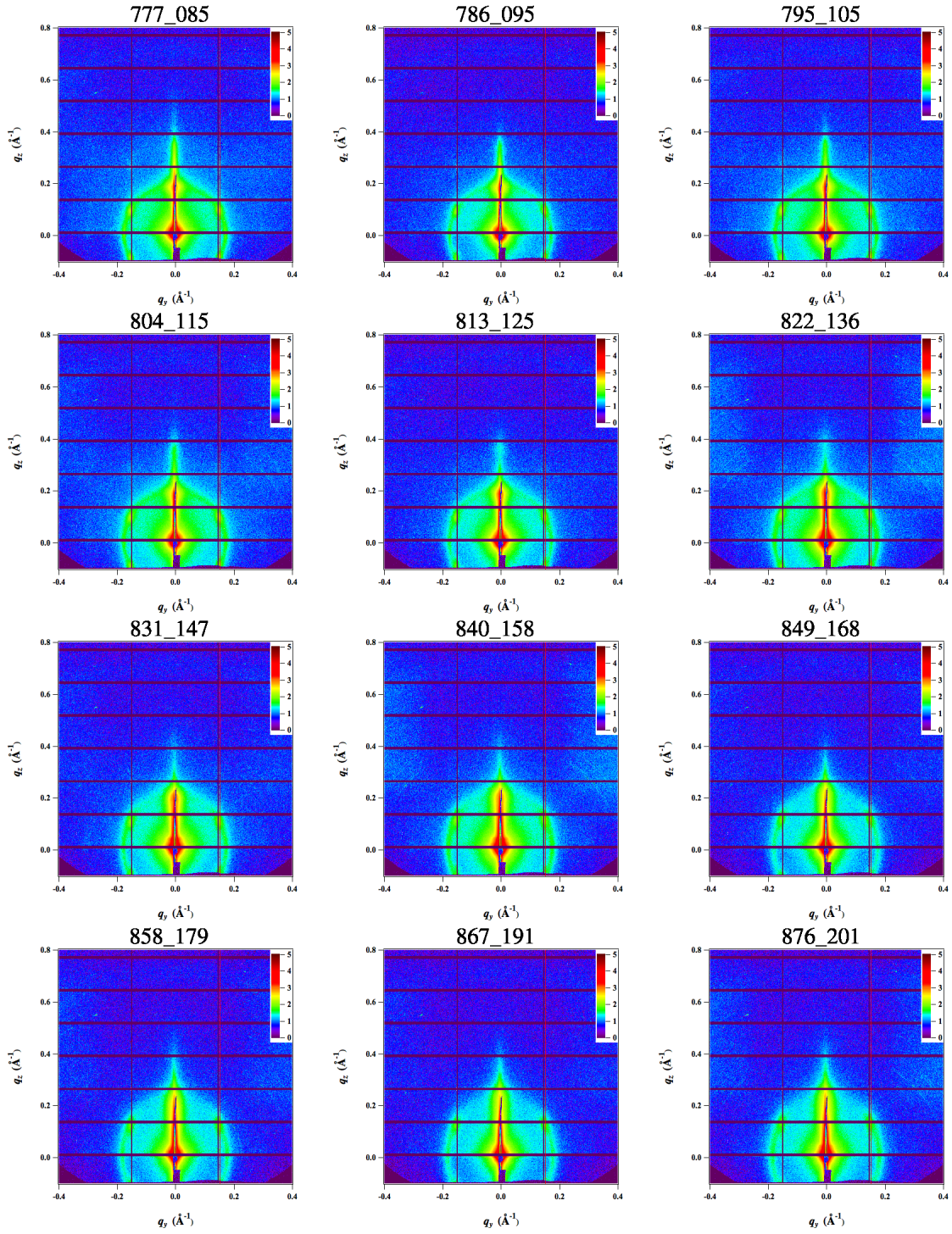
Figure D1. Photograph of a typical experimental set up for total X-ray scattering data acquisition with the sample, beam stop, and area detector in a line. This photograph was taken at ESRF ID-15-B.



Figure D2. Multi-sample holder designed for rapid acquisition at ESRF ID-15-B.

Appendix E. Co₂P Film Assembly GISAXS





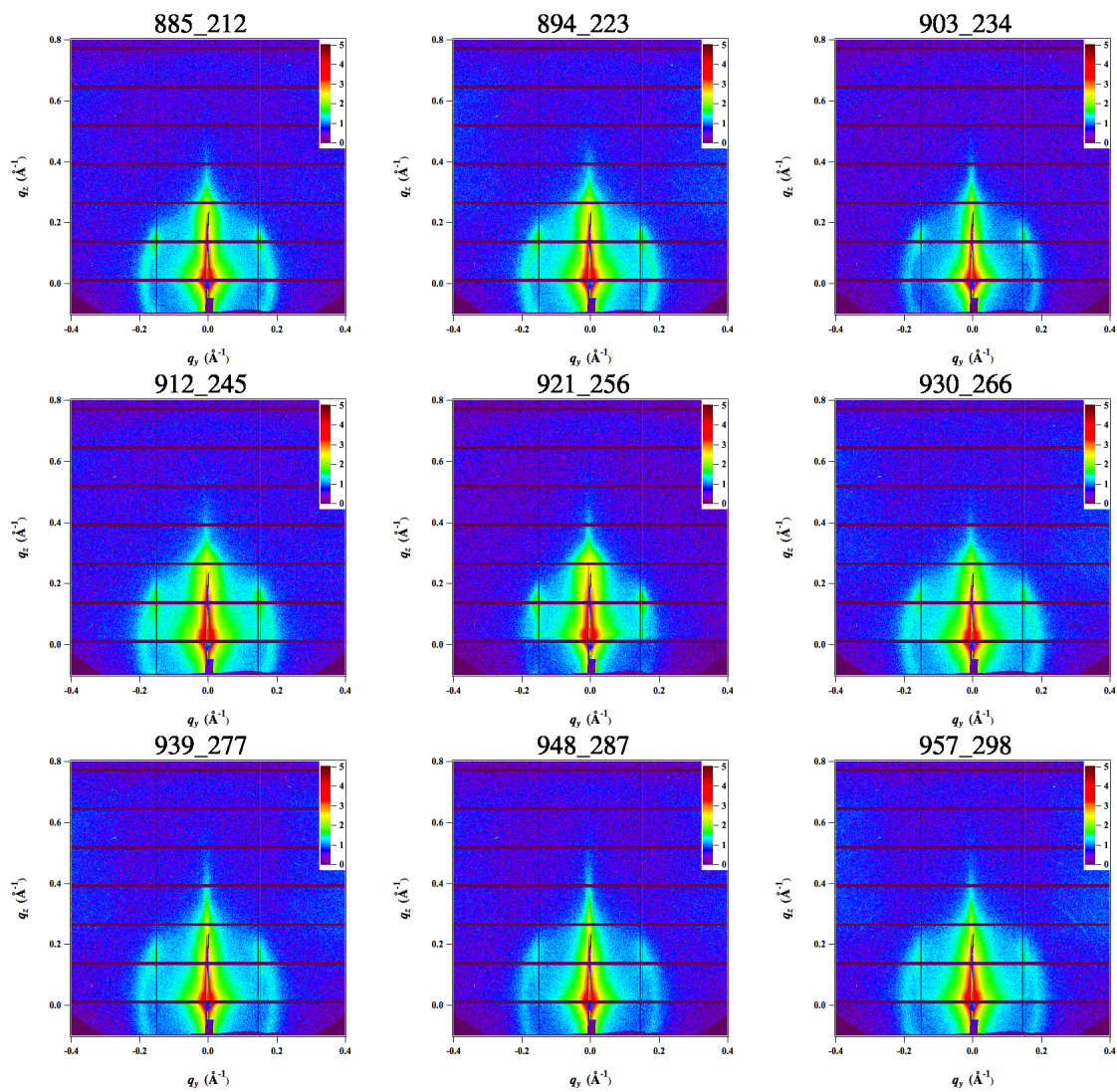


Figure D1. GISAXS of Co₂P films as a function of temperature (22-298°C).

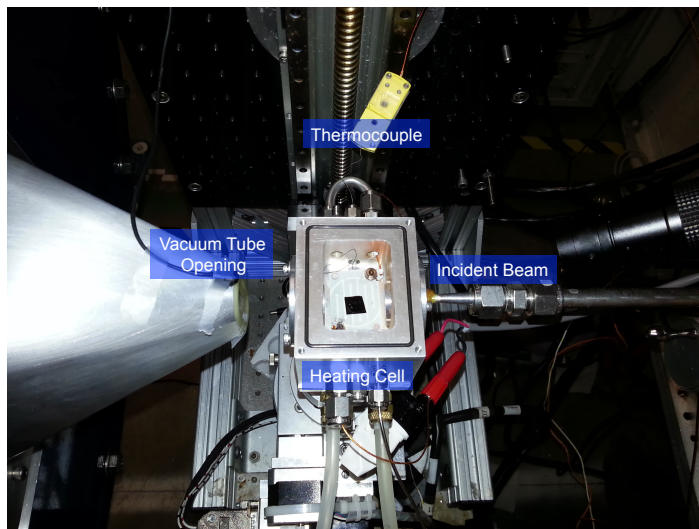


Figure E2. Set up for the variable temperature grazing incident small angle X-ray scattering experiments at the Advanced Photon Source 12-ID-B. The stage was resistively heated to the set temperature.

Appendix F. EXAFS Experimental Set Up

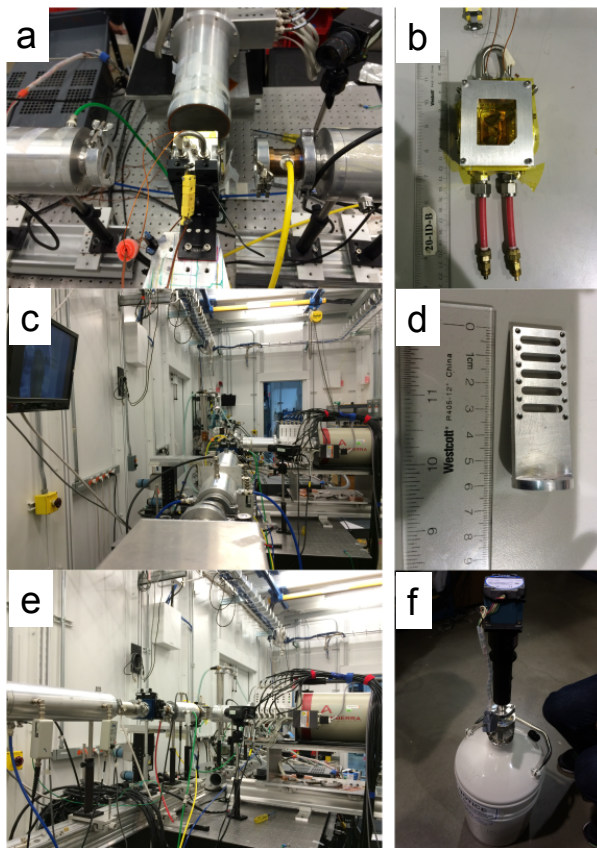


Figure F1. Photographic examples of EXAFS experimental set-up at the Advanced Photon Source 20-BM-B: (a) furnace cell in the beam path (direction left to right), (b) furnace cell dimensions, (c) beam path, (d), cryostat cell dimensions, (e), beam path with fluorescence detector, and (f) cryostat sample holder being cooled in liquid nitrogen dewar.

Appendix G. Trioctylphosphine Oxide Structural Parameters

Table G1. Summary of scan parameters for TOPO structure refinement.

Scan type	2 θ	ω	φ	χ	Frames
φ	-20.50	295.58	13.34	30.75	739
φ	-25.50	328.40	41.51	76.58	739
φ	24.50	78.84	344.38	-35.57	739

Table G2. Refined positional parameters P, O, and C atoms in TOPO.

Atom	x	y	z	$U_{eq}, \text{\AA}^2$
P1	0.964925(19)	0.28059(5)	0.807347(8)	0.01219(8)
O1	0.97088(6)	0.55665(15)	0.79639(2)	0.01736(18)
C1	1.06979(7)	0.1118(2)	0.80961(3)	0.0139(2)
C2	1.14331(8)	0.2257(2)	0.84150(3)	0.0168(2)
C3	1.23423(8)	0.0937(2)	0.84433(3)	0.0167(2)
C4	1.30304(8)	0.2070(2)	0.87799(4)	0.0199(2)
C5	1.39368(8)	0.0723(3)	0.88518(4)	0.0248(3)
C6	1.45903(9)	0.1911(3)	0.91950(5)	0.0340(3)
C7	1.54930(11)	0.0577(4)	0.92834(6)	0.0550(5)
C8	1.61270(15)	0.1832(6)	0.96298(9)	0.0929(10)
C9	0.93336(8)	0.2526(2)	0.85700(3)	0.0147(2)
C10	0.93063(8)	-0.0148(2)	0.87519(3)	0.0159(2)
C11	0.90403(8)	-0.0038(2)	0.91718(3)	0.0179(2)
C12	0.89991(8)	-0.2624(2)	0.93744(3)	0.0163(2)
C13	0.87432(9)	-0.2429(2)	0.97944(3)	0.0198(3)
C14	0.86248(8)	-0.5003(2)	0.99905(3)	0.0176(2)
C15	0.83663(10)	-0.4757(2)	1.04085(4)	0.0264(3)
C16	0.82193(11)	-0.7311(3)	1.06044(4)	0.0302(3)
C17	0.88283(7)	0.1070(2)	0.77284(3)	0.0141(2)
C18	0.78867(8)	0.2239(2)	0.76869(3)	0.0171(2)
C19	0.72044(8)	0.0881(2)	0.73714(3)	0.0178(2)
C20	0.62707(8)	0.2075(2)	0.73202(4)	0.0196(2)
C21	0.55913(8)	0.0772(2)	0.69986(4)	0.0210(3)
C22	0.46664(8)	0.2019(3)	0.69385(4)	0.0225(3)
C23	0.39931(9)	0.0748(3)	0.66114(4)	0.0294(3)
C24	0.30764(9)	0.2059(3)	0.65488(5)	0.0385(4)

$$U_{eq} = \frac{1}{3} [U_{11}(aa^*)^2 + U_{22}(bb^*)^2 + U_{33}(cc^*)^2 + 2U_{12}aa^*bb^*\cos\gamma + 2U_{13}aa^*cc^*\cos\beta + 2U_{23}bb^*cc^*\cos\alpha]$$

Table G3. Refined positional parameters hydrogen atoms in trioctylphosphine oxide.

Atom	x	y	z	$U_{iso}, \text{\AA}^2$
H1a	1.0611	-0.0667	0.8159	0.018
H1b	1.0888	0.1193	0.7834	0.018
H2a	1.1504	0.4052	0.8354	0.022
H2b	1.1240	0.2160	0.8676	0.022
H3a	1.2273	-0.0874	0.8493	0.022
H3b	1.2558	0.1115	0.8188	0.022
H4a	1.3125	0.3851	0.8717	0.026
H4b	1.2782	0.2030	0.9029	0.026
H5a	1.3848	-0.1063	0.8914	0.033
H5b	1.4197	0.0791	0.8606	0.033
H6a	1.4687	0.3686	0.9129	0.045
H6b	1.4319	0.1890	0.9438	0.045
H7a	1.5770	0.0601	0.9042	0.073
H7b	1.5401	-0.1197	0.9351	0.073
H8a	1.6269	0.3534	0.9553	0.139
H8b	1.6669	0.0845	0.9689	0.139
H8c	1.5842	0.1905	0.9865	0.139
H9a	0.9750	0.3552	0.8756	0.020
H9b	0.8743	0.3285	0.8558	0.020
H10a	0.8877	-0.1195	0.8576	0.021
H10b	0.9893	-0.0941	0.8770	0.021
H11a	0.9469	0.1032	0.9344	0.024
H11b	0.8456	0.0773	0.9150	0.024
H12a	0.9581	-0.3450	0.9395	0.022
H12b	0.8563	-0.3693	0.9206	0.022

Atom	x	y	z	$U_{iso}, \text{\AA}^2$
H13a	0.9205	-0.1471	0.9967	0.026
H13b	0.8187	-0.1474	0.9775	0.026
H14a	0.9182	-0.5959	1.0012	0.023
H14b	0.8163	-0.5967	0.9818	0.023
H15a	0.8837	-0.3832	1.0582	0.035
H15b	0.7820	-0.3755	1.0388	0.035
H16a	0.7737	-0.8211	1.0441	0.045
H16b	0.8070	-0.7022	1.0868	0.045
H16c	0.8759	-0.8313	1.0628	0.045
H17a	0.9013	0.1036	0.7465	0.019
H17b	0.8807	-0.0683	0.7821	0.019
H18a	0.7684	0.2158	0.7946	0.023
H18b	0.7917	0.4028	0.7613	0.023
H19a	0.7417	0.0921	0.7114	0.024
H19b	0.7164	-0.0898	0.7449	0.024
H20a	0.6053	0.1997	0.7576	0.026
H20b	0.6315	0.3866	0.7249	0.026
H21a	0.5533	-0.1005	0.7074	0.028
H21b	0.5817	0.0802	0.6744	0.028
H22a	0.4435	0.1958	0.7191	0.030
H22b	0.4726	0.3805	0.6869	0.030
H23a	0.3920	-0.1027	0.6684	0.039
H23b	0.4228	0.0776	0.6359	0.039
H24a	0.2837	0.2022	0.6797	0.058
H24b	0.2675	0.1176	0.6342	0.058
H24c	0.3141	0.3803	0.6468	0.058

Table G4. Refined thermal parameters for phosphorus, oxygen, and carbon atoms in trioctylphosphine oxide.

Atom	U ₁₁	U ₂₂	U ₃₃	U ₂₃	U ₁₃	U ₁₂
P1	0.01648(14)	0.00943(14)	0.01102(14)	0.00056(10)	0.00335(10)	0.00030(11)
O1	0.0257(4)	0.0109(4)	0.0163(4)	0.0012(3)	0.0058(3)	0.0000(3)
C1	0.0173(5)	0.0121(5)	0.0126(5)	-0.0004(4)	0.0034(4)	0.0005(4)
C2	0.0170(5)	0.0167(6)	0.0169(5)	-0.0026(4)	0.0033(4)	-0.0007(4)
C3	0.0188(6)	0.0167(6)	0.0151(5)	-0.0001(4)	0.0044(4)	0.0004(4)
C4	0.0170(6)	0.0221(6)	0.0206(6)	-0.0023(5)	0.0034(4)	-0.0002(5)
C5	0.0191(6)	0.0262(7)	0.0285(7)	-0.0007(5)	0.0022(5)	0.0026(5)
C6	0.0203(6)	0.0389(8)	0.0398(8)	-0.0038(7)	-0.0037(6)	0.0019(6)
C7	0.0250(8)	0.0568(12)	0.0756(13)	-0.0050(10)	-0.0143(8)	0.0091(8)
C8	0.0389(11)	0.100(2)	0.121(2)	-0.0212(17)	-0.0427(13)	0.0108(12)
C9	0.0186(5)	0.0132(5)	0.0128(5)	-0.0002(4)	0.0042(4)	0.0013(4)
C10	0.0209(6)	0.0147(5)	0.0130(5)	0.0005(4)	0.0050(4)	0.0001(4)
C11	0.0247(6)	0.0166(6)	0.0134(5)	0.0014(4)	0.0065(4)	0.0010(5)
C12	0.0208(6)	0.0158(6)	0.0131(5)	0.0009(4)	0.0049(4)	0.0003(4)
C13	0.0295(6)	0.0159(6)	0.0157(5)	0.0019(4)	0.0088(5)	0.0013(5)
C14	0.0230(6)	0.0164(6)	0.0143(5)	0.0008(4)	0.0059(4)	-0.0007(5)
C15	0.0447(8)	0.0195(6)	0.0187(6)	0.0021(5)	0.0158(6)	0.0017(6)
C16	0.0481(9)	0.0243(7)	0.0215(6)	0.0049(5)	0.0157(6)	-0.0031(6)
C17	0.0173(5)	0.0124(5)	0.0125(5)	-0.0004(4)	0.0027(4)	0.0011(4)
C18	0.0179(5)	0.0161(6)	0.0173(5)	-0.0023(4)	0.0029(4)	0.0019(4)
C19	0.0188(6)	0.0176(6)	0.0166(5)	-0.0012(4)	0.0021(4)	0.0016(5)
C20	0.0181(6)	0.0207(6)	0.0198(6)	-0.0018(5)	0.0029(4)	0.0009(5)
C21	0.0195(6)	0.0229(6)	0.0199(6)	-0.0013(5)	0.0011(5)	0.0011(5)
C22	0.0186(6)	0.0250(6)	0.0236(6)	0.0007(5)	0.0024(5)	0.0001(5)
C23	0.0219(6)	0.0379(8)	0.0266(7)	0.0006(6)	-0.0014(5)	-0.0015(6)
C24	0.0207(7)	0.0525(10)	0.0397(8)	0.0061(7)	-0.0034(6)	-0.0011(7)

The form of the anisotropic displacement parameter is:

$$\exp[-2\pi^2(a^2U_{11}h^2+b^2U_{22}k^2+c^2U_{33}l^2+2b^*c^*U_{23}kl+2a^*c^*U_{13}hl+2a^*b^*U_{12}hk)]$$

Table G5. Bond distances within trioctylphosphine oxide.

Bond Type	Bond Length (Å)
P1-O1	1.4949(8)
P1-C9	1.8123(11)
C3-C4	1.5229(16)
C6-C7	1.516(2)
C10-C11	1.5281(15)
C13-C14	1.5207(16)
C17-C18	1.5316(15)
C20-C21	1.5217(16)
C23-C24	1.527(2)
P1-C17	1.7962(11)
C1-C2	1.5300(15)
C4-C5	1.5217(17)
C7-C8	1.527(3)
C11-C12	1.5184(16)
C14-C15	1.5217(16)
C18-C19	1.5251(16)
C21-C22	1.5232(17)
P1-C1	1.8023(11)
C2-C3	1.5246(16)
C5-C6	1.5202(18)
C9-C10	1.5283(15)
C12-C13	1.5246(15)
C15-C16	1.5196(18)
C19-C20	1.5247(16)
C22-C23	1.5201(18)

Table G6. Bond angles within trioctylphosphine oxide.

Bonds	Bond Angle(°)
O1-P1-C17	113.05(5)
O1-P1-C9	109.84(5)
C2-C1-P1	111.70(8)
C5-C4-C3	115.04(10)
C6-C7-C8	112.46(17)
C12-C11-C10	114.54(10)
C13-C14-C15	112.97(10)
C19-C18-C17	112.84(9)
C20-C21-C22	113.48(10)
O1-P1-C1	113.26(5)
C17-P1-C9	107.12(5)
C3-C2-C1	114.16(9)
C6-C5-C4	112.68(11)
C10-C9-P1	117.98(8)
C11-C12-C13	112.92(9)
C16-C15-C14	113.71(11)
C20-C19-C18	113.19(10)
C23-C22-C21	113.46(11)
C17-P1-C1	106.72(5)
C1-P1-C9	106.46(5)
C4-C3-C2	111.54(9)
C7-C6-C5	114.25(14)
C11-C10-C9	111.23(9)
C14-C13-C12	113.99(10)
C18-C17-P1	112.87(8)
C21-C20-C19	113.53(10)
C22-C23-C24	112.74(12)

Appendix H. Photocatalysis of CoO Nanoparticles

Photocatalysis encompasses the production of chemical fuels using light-mediated catalysis, and it is an area of great research interest for alternative energy production. Platinum deposited on TiO_2 has been demonstrated to be an efficient catalyst, and has been the subject of thousands of published reports. Less expensive, earth abundant alternatives for platinum has been the target of some of these investigations. Recently, Liao *et al.* calculated the band gap for nanocrystalline CoO from a modified Kubelka-Munk function and demonstrated that nanocrystalline CoO has band structure suitable for efficient water-splitting as compared to micropowder CoO (Figure H1).²⁶¹ With control over size and shape of CoO nanoparticles, photocatalytic hydrogen production can be tuned as recently demonstrated with TiO_2 nanocrystals by Gordon *et al.*

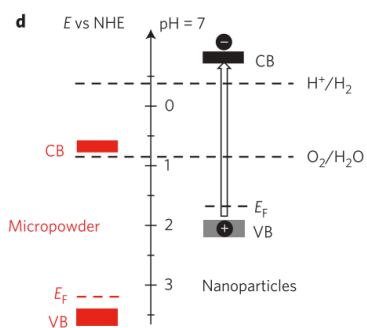


Figure H1. Band diagram of micropowder and nanocrystalline CoO (adapted from Liao *et al.*).²⁶¹

CoO nanocrystals have been synthesized from a thermal decomposition Schlenk line technique involving 2 mmol cobalt acetate tetrahydrate, 3 mmol oleic acid, 3 mmol 1-octadecanol, tributylphosphine, and 0.25 mmol trioctylphosphine oxide in 20 mL 1-octadecene. The resulting nanoparticles are shown in Figure H2 with a size distribution of $6.1 \text{ nm} \pm 1.1 \text{ nm}$ (Figure H3). The $Fm\bar{3}m$ crystal structure and dispersion is confirmed with X-ray scattering from APS 11-ID-B. A spherical model was used for the X-ray fitting shown in Figure H4. For photocatalytic testing, 1 wt% of CoO was deposited on Evonik TiO₂ P25. Yield of CoO from synthesis was determined by ICP using a Spectro Genesis spectrometer. The CoO/TiO₂ catalyst was sonicated and dispersed in a 1:1 40mL solution of ethanol to water. Ethanol was used as a hole scavenger in the reaction. Hydrogen production from CoO/TiO₂ was initially comparable to Pt photodeposited on TiO₂ nanocrystals²⁶² at nearly 2000 mmol H₂ per hour per gram as seen in Figure H5. After 8 hours, photocatalytic H₂ production stabilized to 1200 mmol h⁻¹ g⁻¹, comparable to CoCl₂ deposited on TiO₂. For the CoCl₂, activation occurs during the first three hours of the reaction in which CoCl₂ is reduced to zero-valent Co, which is responsible for hydrogen production. The photoreactor (coupled with a thermal gas reactor) with a Hg(Xe) 300W lamp is shown in Figure H6.

Better systematic control over CoO morphology and size can be pursued to investigate their effects on H₂ production. While the stabilization of the catalyst over a 24-hr period is promising, its overall activity could be improved to reduce the initial degradation.

Figures

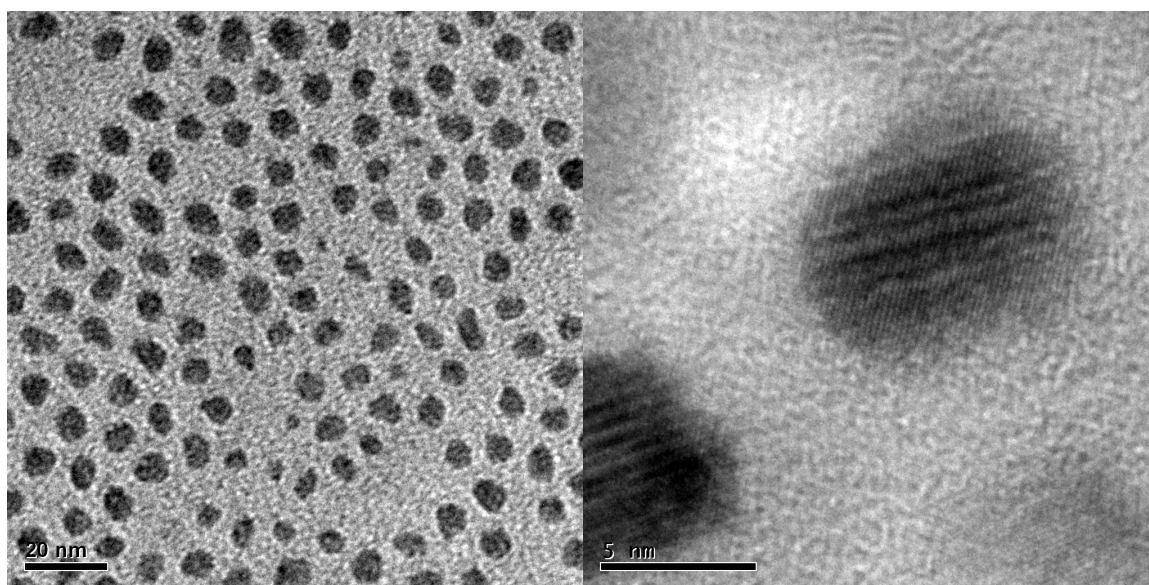


Figure H2. TEM images of CoO nanoparticles.

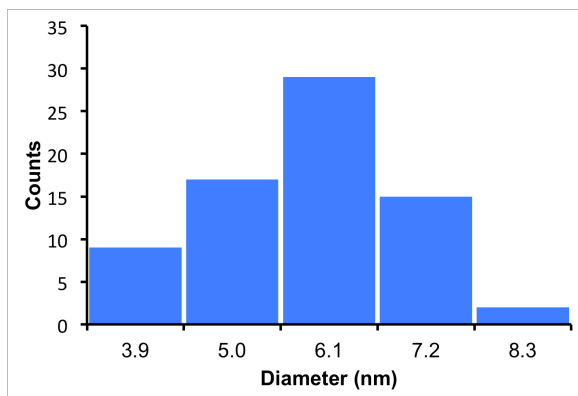


Figure H3. Histogram of CoO diameter sizes shows an average diameter of 6.1 nm \pm 1.1nm.

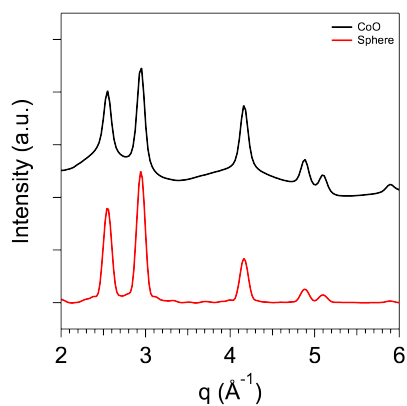


Figure H4. X-ray diffraction of CoO NPs as compared with a spherical model with diameter of 6.1 nm.

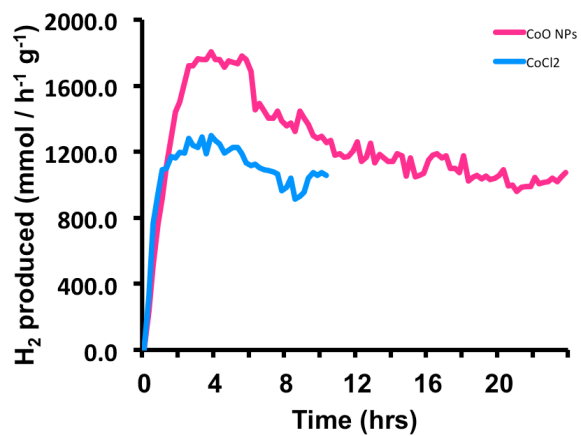


Figure H5. Hydrogen production from CoO NPs supported on TiO₂(P25).

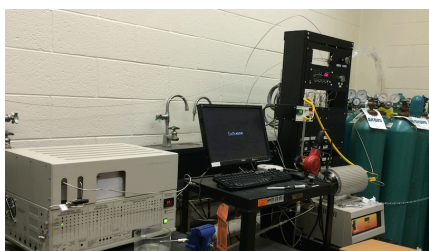


Figure H6. Experimental set-up for thermal gas reactor with photocatalysis module.

Appendix I. Publications

1. VVT Doan-Nguyen, S Najmr, M Balasubramanian, CB Murray. Structural Transition of Doped VO₂ Nanoparticles as Probed by Extended X-ray Absorption Fine Structure (working title). *In preparation*.
2. VVT Doan-Nguyen, D Diez, CD Barr, CB Murray. Quantification of Nanocrystal Superlattice Thin Film Quality Using Voronoi Tessellations (working title). *In preparation*.
3. VVT Doan-Nguyen, S Zheng, EB Trigg, R Agarwal, J Li, D Su, KI Winey, CB Murray. Synthesis and X-ray Characterization of Cobalt Phosphide (Co₂P) Nanorods for the Oxygen Reduction Reaction. *Submitted*.
4. M Cargnello, C Chen, BT Diroll, VVT Doan-Nguyen, RJ Gorte, CB Murray. Efficient Removal of Organic Ligands From Supported Nanocrystals by Fast Thermal Annealing Enables Catalytic Studies on Well Defined Active Phases. *Submitted*.
5. TR Gordon*, BT Diroll*, T Paik, VVT Doan-Nguyen, EA Gauding, CB Murray. Characterization of Shape and Monodispersity in Anisotropic Nanocrystals through Atomistic X-ray Scattering Simulation. *Chemistry of Materials* 27:2502-

- 2506 (2015). (*Equal contributions)
6. VVT Doan-Nguyen, PJ Carroll, CB Murray. Structure Determination and Modeling of Trioctylphosphine Oxide. *Acta Crystallographica C*. 71:239-241 (2015).
 7. BT Diroll, VVT Doan-Nguyen, M Cargnello, EA Gaubing, CB Murray. Mapping Nanoparticle Superlattices with X-rays. *ACS Nano* 8:12843-12850 (2014).
 8. S Zhang, Y Zhou, D Su, VVT Doan-Nguyen, Y Wu, CB Murray. Monodisperse Core/Shell Ni/FePt Nanoparticles for Efficient Electrocatalysis of Oxygen Reduction. *Journal of the American Chemical Society Communications*, 136:15921-15924 (2014).
 9. J Lynch, M Kotigua, VVT Doan-Nguyen, WL Queen, JD Forster, RA Schlitz, CB Murray, JB Neaton, ML Chabiny, JJ Urban. Ligand Symmetry Correlates with Thermopower Enhancement in Small-molecule/Quantum Dot Hybrid Materials. *ACS Nano* 8:10528-10536 (2014).
 10. VVT Doan-Nguyen*, SAJ Kimber*, D Pontoni, D Reifsnyder Hickey, BT Diroll, M Migliorini, CB Murray, SJL Billinge. Bulk Metallic Glass-like

- Scattering Signal in Small Metallic Nanoparticles. *ACS Nano* 8:6163-6170 (2014). (*Equal contributions)
11. M Araghchini, J Chen, V Doan-Nguyen, DV Harburg, D Jin, J Kim, MS Kim, S Lim, B Lu, D Piedra, J Qiu, J Ranson, M Sun, X Yu, H Yun, MG Allen, JA del Alamo, G DesGroseilliers, F Herrault, JH Lang, CG Levey, CB Murray, D Otten, T Palacios, DJ Perreault, CR Sullivan. A Technology Overview of the Powerchip Development Program. *IEEE Transactions on Power Electronics* 28: 4182-4201 (2013).
12. M Cargnello, VVT Doan-Nguyen, TR Gordon, K Bukhmutsky, P Fornasiero, RJ Gorte, CB Murray. Control of Metal Nanocrystal Size Reveals Metal-Support Interface Role for Ceria Catalysts. *Science* 341:771-773 (2013).
13. Y Kang, X Ye, J Chen, L Qi, R Rivas, V Doan-Nguyen, G Xing, CR Kagan, J Li, RJ Gorte, E Stach, and CB Murray. Engineering Catalytic Contacts and Thermal Stability: Gold-Iron-Oxide Binary Nanocrystal Superlattices for CO Oxidation. *Journal of the American Chemical Society* 153:1499-1505 (2013).
14. X Ye, L Jin, H Caglayan, J Chen, G Xing, C Zheng, V Doan-Nguyen, Y Kang, N Engheta, CR Kagan, CB Murray. Improved Size-Tunable Synthesis of Monodisperse Gold Nanorods through the Use of Aromatic Additives. *ACS*

- Nano* 6:2804-2817 (2012).
15. Y Liu, DK Ko, SJ Oh, TR Gordon, V Doan-Nguyen, T Paik, Y Kang, X Ye, L Jin, CR Kagan, and CB Murray. Near-Infrared Absorption of Monodisperse Silver Telluride (Ag_2Te) Nanocrystals and Photoconductive Response of Their Self-Assembled Superlattices. *Chemistry of Materials* 23:4657-4659 (2011).
 16. AT Fafarman, WK Koh, BT Diroll, DK Kim, DK Ko, SJ Oh, X Ye, V Doan-Nguyen, CR Crump, DC Reifsnyder, CB Murray, and CR Kagan. Thiocyanate-Capped Nanocrystal Colloids: Vibrational Reporter of Surface Chemistry and Solution-Based Route to Enhanced Coupling in Nanocrystal Solids. *Journal of the American Chemical Society* 133:15753-15761 (2011).
 17. T Paik, DK Ko, TR Gordon, V Doan-Nguyen, CB Murray. Studies of Liquid Crystalline Self-Assembly of GdF_3 Nanoplates by In-Plane, Out-of-Plane SAXS. *ACS Nano* 5:8322-8330 (2011).
 18. D Wang, Y Kang, V Doan-Nguyen, CB Murray. Synthesis and Oxygen Storage Capacity of Two-Dimensional Ceria Nanocrystals. *Angewandte Chemie International Ed. in English*. 50:4378-4381 (2010).
 19. V Doan-Nguyen and JP Loria. The Effects of Co-solutes on Protein Dynamics:

The Reversal of Denaturant-induced Protein Fluctuations by Trimethylamine
N-oxide. *Protein Science* 16:20-29 (2007).

Bibliography

- (1) Raney, M. Method of Producing Finely-Divided Nickel. 1,628,190, 1927.
- (2) Suzuki, A. Recent Advances in the Cross-Coupling Reactions of Organoboron Derivatives with Organic Electrophiles, 1995–1998. *Journal of Organometallic Chemistry* **1999**, 576, 147–168.
- (3) Cargnello, M.; Doan-Nguyen, V. V. T.; Gordon, T. R.; Paik, T.; Diaz, R. E.; Stach, E. A.; Gorte, R. J.; Fornasiero, P.; Murray, C. B. Control of Metal Nanocrystal Size Reveals Metal-Support Interface Role for Ceria Catalysts. *Science* **2013**, 341, 771–773.
- (4) Faraday, M. The Bakerian Lecture: Experimental Relations of Gold (and Other Metals) to Light. *Philosophical Transactions of the Royal Society of London* **1857**, 147, 145–181.
- (5) Murray, C. B.; Norris, D. J.; Bawendi, M. G. Synthesis and Characterization of Nearly Monodisperse CdE (E=S, Se,Te) Semiconductor Nanocrystals. *Journal of the American Chemical Society* **1993**, 115, 8706–8715.
- (6) Hyeon, T.; Lee, S. S.; Park, J.; Chung, Y.; Na, H. B. Synthesis of Highly Crystalline and Monodisperse Maghemite Nanocrystallites without a Size-Selection Process. *Journal of the American Chemical Society* **2001**, 123, 12798–12801.
- (7) Haruta, M.; Yamada, N.; Kobayashi, T.; Iijima, S. Gold Catalysts Prepared by Coprecipitation for Low-Temperature Oxidation of Hydrogen and of Carbon Monoxide. *Journal of Catalysis* **1989**, 115, 301–309.
- (8) Haruta, M.; Tsubota, S.; Kobayashi, T.; Kageyama, H.; G., M. J.; Delmon, B. Low-Temperature Oxidation of CO over Gold Supported TiO₂, Alpha-Fe₂O₃, and Co₃O₄. *Journal of Catalysis* **1993**, 144, 175–192.
- (9) Joo, J.; Yu, T.; Kim, Y. W.; Park, H. M.; Wu, F.; Zhang, J. Z.; Hyeon, T. Multigram Scale Synthesis and Characterization of Monodisperse Tetragonal Zirconia Nanocrystals. *Journal of the American Chemical Society* **2003**, 125, 6553–6557.

- (10) Masala, O.; Seshadri, R. Synthesis Routes for Large Volumes of Nanoparticles. *Annual Review of Materials Research* **2004**, *34*, 41–81.
- (11) Iravani, S. Green Synthesis of Metal Nanoparticles Using Plants. *Green Chemistry* **2011**, *13*, 2638.
- (12) LaMer, V. K.; Dinegar, R. H. Theory, Production and Mechanism of Formation of Monodispersed Hydrosols. *Journal of the American Chemical ...* **1950**, *72*, 4847–4854.
- (13) Murray, C. B.; Kagan, C. R.; Bawendi, M. G. Synthesis and Characterization of Monodisperse Nanocrystals and Close-Packed Nanocrystal Assemblies. *Annual Reviews of Science* **2000**, 545–610.
- (14) Yin, Y.; Rioux, R. M.; Erdonmez, C. K.; Hughes, S.; Somorjai, G. A.; Alivisatos, A. P. Formation of Hollow Nanocrystals through the Nanoscale Kirkendall Effect. *Science* **2004**, *304*, 711–714.
- (15) Porter, D. A.; Easterling, K. E. *Phase Transformations in Metals and Alloys*; 2nd ed.; Chapman & Hall: Cheltenham, U.K., 1992.
- (16) *Microwaves in Organic Synthesis*; de la Hoz, A.; Loupy, A., Eds.; 3rd ed.; Wiley-VCH: Weinheim, 2012.
- (17) Lidström, P.; Tierney, J.; Wathey, B.; Westman, J. Microwave Assisted Organic Synthesis—a Review. *Tetrahedron* **2001**, *57*, 9225–9283.
- (18) Kappe, C. O. Controlled Microwave Heating in Modern Organic Synthesis. *Angewandte Chemie* **2004**, *43*, 6250–6284.
- (19) Nguyen, H. L.; Howard, L. E. M.; Giblin, S. R.; Tanner, B. K.; Terry, I.; Hughes, A. K.; Ross, I. M.; Serres, A.; Bürckstümmer, H.; Evans, J. S. O. Synthesis of Monodispersed Fcc and Fct FePt/FePd Nanoparticles by Microwave Irradiation. *Journal of Materials Chemistry* **2005**, *15*, 5136–5143.
- (20) Donegan, K. P.; Godsell, J. F.; Tobin, J. M.; O’Byrne, J. P.; Otway, D. J.; Morris, M. A.; Roy, S.; Holmes, J. D. Microwave-Assisted Synthesis of Icosahedral Nickel Nanocrystals. *CrystEngComm* **2011**, *13*, 2023.

- (21) Mohamed, M. B.; AbouZeid, K. M.; Abdelsayed, V.; Aljarash, A. A.; El-Shall, M. S. Growth Mechanism of Anisotropic Gold Nanocrystals via Microwave Synthesis: Formation of Dioleamide by Gold Nanocatalysis. *ACS Nano* **2010**, *4*, 2766–2772.
- (22) Abdelsayed, V.; Aljarash, A.; El-Shall, M. S.; Al Othman, Z. A.; Alghamdi, A. H. Microwave Synthesis of Bimetallic Nanoalloys and CO Oxidation on Ceria-Supported Nanoalloys. *Chemistry of Materials* **2009**, *21*, 2825–2834.
- (23) Rao, K. J. K.; Mahesh, K.; Kumar, S. A Strategic Approach for Preparation of Oxide Nanomaterials. *Bulletin of Materials Science* **2005**, *28*, 19–24.
- (24) Hu, X.; Yu, J. C. High-Yield Synthesis of Nickel and Nickel Phosphide Nanowires via Microwave-Assisted Processes. *Chemistry of Materials* **2008**, *20*, 6743–6749.
- (25) Pein, A.; Baghbanzadeh, M.; Rath, T.; Haas, W.; Maier, E.; Amenitsch, H.; Hofer, F.; Kappe, C. O.; Trimmel, G. Investigation of the Formation of CuInS₂ Nanoparticles by the Oleylamine Route: Comparison of Microwave-Assisted and Conventional Syntheses. *Inorganic chemistry* **2011**, *50*, 193–200.
- (26) Song, Q.; Ai, X.; Topuria, T.; Rice, P. M.; Alharbi, F. H.; Bagabas, A.; Bahattab, M.; Bass, J. D.; Kim, H.-C.; Scott, J. C.; *et al.* Microwave-Assisted Synthesis of Monodispersed CdTe Nanocrystals. *Chemical Communications* **2010**, *46*, 4971–4973.
- (27) Roy, M. D.; Herzing, A. A.; De Paoli Lacerda, S. H.; Becker, M. L. Emission-Tunable Microwave Synthesis of Highly Luminescent Water Soluble CdSe/ZnS Quantum Dots. *Chemical Communications* **2008**, 2106–2108.
- (28) Baghbanzadeh, M.; Carbone, L.; Cozzoli, P. D.; Kappe, C. O. Microwave-Assisted Synthesis of Colloidal Inorganic Nanocrystals. *Angewandte Chemie (International Ed. in English)* **2011**, *50*, 11312–11359.
- (29) Williams, D. B.; Carter, C. B. *Diffraction from Crystals*; 2009.
- (30) Alexander, L.; Klug, H. P. Determination of Crystallite Size with the X-Ray Spectrometer. *Journal of Applied Physics* **1950**, *21*, 137–142.

- (31) Cullity, B. D.; Stock, S. R. *Elements of X-Ray Diffraction*; Prentice Hall: Upper Saddle River, NJ, 2001.
- (32) Vegard, L. Die Konstitution Der Mischkristalle Und Die Raumbfüllung Der Atome. *Zeitschrift für Physik* **1921**, *5*, 17–26.
- (33) Glatter, O.; Kratky, O. *Small Angle X-Ray Scattering*; Academic Press, Inc.: New York, 1982.
- (34) Guinier, A.; Fournet, G. *Small-Angle Scattering of X-Rays*; John Wiley & Sons, Inc.: London, England, 1955.
- (35) Corricelli, M.; Altamura, D.; Curri, M. L.; Sibillano, T.; Siliqi, D.; Mazzone, A.; Depalo, N.; Fanizza, E.; Zanchet, D.; Giannini, C.; *et al.* GISAXS and GIWAXS Study on Self-Assembling Processes of Nanoparticle Based Superlattices. *CrystEngComm* **2014**, *16*, 9482–9492.
- (36) Renaud, G.; Lazzari, R.; Leroy, F. Probing Surface and Interface Morphology with Grazing Incidence Small Angle X-Ray Scattering. *Surface Science Reports* **2009**, *64*, 255–380.
- (37) Jiang, Z. Theory of GISAXS. In *American Crystallographic Association Meeting*; 2014.
- (38) Lazzari, R. IsGISAXS : A Program for Grazing-Incidence Small-Angle X-Ray Scattering Analysis of Supported Islands. *Journal of Applied Crystallography* **2002**, *35*, 406–421.
- (39) Petkov, V.; Ohta, T.; Hou, Y.; Ren, Y. Atomic-Scale Structure of Nanocrystals by High-Energy X-Ray Diffraction and Atomic Pair Distribution Function Analysis: Study of Fe. *Journal of Physical Chemistry C* **2007**, *111*, 714–720.
- (40) Chupas, P. J.; Qiu, X.; Hanson, J. C.; Lee, P. L.; Grey, C. P.; Billinge, S. J. L. Rapid-Acquisition Pair Distribution Function (RA-PDF) Analysis. *Journal of Applied Crystallography* **2003**, *36*, 1342–1347.

- (41) Qiu, X.; Thompson, J. W.; Billinge, S. J. L. PDFgetX2: A GUI Driven Program to Obtain the Pair Distribution Function from X-Ray Powder Diffraction Data. *Journal of Applied Crystallography* **2004**, *37*, 678–678.
- (42) Juhás, P.; Davis, T.; Farrow, C. L.; Billinge, S. J. L. PDFgetX3: A Rapid and Highly Automatable Program for Processing Powder Diffraction Data into Total Scattering Pair Distribution Functions. *Journal of Applied Crystallography* **2013**, *46*, 560–566.
- (43) Farrow, C. L.; Juhas, P.; Liu, J. W.; Bryndin, D.; Bozin, E. S.; Bloch, J.; Proffen, T.; Bilinge, S. J. L. PDFfit2 and PDFgui: Computer Programs for Studying Nanostructure in Crystals. *Journal of Physics: Condensed Matter* **2007**, *19*, 335219.
- (44) Farrow, C.; Juhas, P.; Billinge, S. J. L. SrFit. <http://www.diffpy.org/>.
- (45) IUCr. *IUCr Dictionary Entries*; 2011.
- (46) Feldman, L.; Mayer, J. *Fundamentals of Surface and Thin Film Analysis*; Prentice Hall, 1986.
- (47) Newville, M. *Fundamentals of XAFS*; 2004.
- (48) Bouguer, P. *Essai D'optique Sur La Gradation de La Lumière*; Claude Jombert, 1729.
- (49) Lambert, J. H. Photometria Sive de Mensura et Gradibus Luminis, Colorum et Umbrae [Photometry, Or, On the Measure and Gradations of Light, Colors, and Shade]. In; Eberhardt Klett: Augsburg, Germany, 1760; p. 391.
- (50) Beer, A. Bestimmung Der Absorption Des Rothen Lichts in Farbigen Flüssigkeiten. *Annalen der Physik* **1852**, *162*, 78–88.
- (51) Ravel, B.; Newville, M. ATHENA, ARTEMIS, HEPHAESTUS: Data Analysis for X-Ray Absorption Spectroscopy Using IFEFFIT. *Journal of Synchrotron Radiation* **2005**, *12*, 537–541.

- (52) Ravel, B. ATOMS : Crystallography for the X-Ray Absorption Spectroscopist. *Journal of Synchrotron Radiation* **2001**, *8*, 314–316.
- (53) Ramirez, R. *The FFT: Fundamentals and Concepts*; Tektronix, Inc.: Beaverton, OR, 1975.
- (54) Hartmann, W. *Signals, Sound, and Sensation*; Springer-Verlag: New York, NY, 1998.
- (55) Calvin, S. *XAFS for Everyone*; CRC Press: Boca Raton, FL, 2013.
- (56) Hamilton, W. C. Significance Tests on the Crystallographics R Factor. *Acta Cryst.* **1965**, *18*, 502–510.
- (57) Russell, A. E.; Rose, A. X-Ray Absorption Spectroscopy of Low Temperature Fuel Cell Catalysts. *Chemical Reviews* **2004**, *104*, 4613–4635.
- (58) Bunker, G. *Introduction to XAFS*; 2010.
- (59) Kelly, S. *Basics of EXAFS Data Analysis X-Ray-Absorption Fine Structure*.
- (60) Ravel, B. A Practical Introduction to Multiple Scattering Theory. *Journal of Alloys and Compounds* **2005**, *401*, 118–126.
- (61) Rehr, J. J.; Albers, R. C. Theoretical Approaches to X-Ray Absorption Fine Structure. *Reviews of Modern Physics* **2000**, *72*, 621–654.
- (62) Pröfrock, D.; Prange, A. Inductively Coupled Plasma-Mass Spectrometry (ICP-MS) for Quantitative Analysis in Environmental and Life Sciences: A Review of Challenges, Solutions, and Trends. *Applied Spectroscopy* **2012**, *66*, 843–868.
- (63) Beauchemin, D. Inductively Coupled Plasma Mass Spectrometry. *Analytical Chemistry* **2006**, *78*, 4111–4136.
- (64) Boss, C. B.; Fredeen, K. J. *Concepts, Instrumentation and Techniques in Inductively Coupled Plasma Optical Emission Spectrometry*; 3rd ed.; PerkinElmer, Inc.: Shelton, CT, 2004.

- (65) Daniel, M.-C.; Astruc, D. Gold Nanoparticles: Assembly, Supramolecular Chemistry, Quantum-Size-Related Properties, and Applications toward Biology, Catalysis, and Nanotechnology. *Chemical Reviews* **2004**, *104*, 293–346.
- (66) Murray, C. B.; Sun, S. H.; Doyle, H.; Betley, T. Monodisperse 3d Transition-Metal (Co, Ni, Fe) Nanoparticles and Their Assembly into Nanoparticle Superlattices. *MRS Bulletin* **2001**, *26*, 985–991.
- (67) Sun, Y.; Xia, Y. Shape-Controlled Synthesis of Gold and Silver Nanoparticles. *Science* **2002**, *298*, 2176–2179.
- (68) Nikoobakht, B.; El-sayed, M. A. Preparation and Growth Mechanism of Gold Nanorods (NRs) Using Seed-Mediated Growth Method. *Chemistry of Materials* **2003**, *15*, 1957–1962.
- (69) Wang, X.; Zhuang, J.; Peng, Q.; Li, Y. A General Strategy for Nanocrystal Synthesis. *Nature* **2005**, *437*, 121–124.
- (70) Longo, E.; Cavalcante, L. S.; Volanti, D. P.; Gouveia, A. F.; Longo, V. M.; Varela, J. A.; Orlandi, M. O.; Andres, J. Direct in-Situ Observation of the Electron-Driven Synthesis of Ag Filaments on Alpha-Ag₂WO₄ Crystals. *Scientif Reports* **2013**, *3*, 1676.
- (71) Simonsen, S. B.; Chorkendorff, I.; Dahl, S.; Skoglundh, M.; Sehested, J.; Helveg, S. Direct Observations of Oxygen-Induced Platinum Nanoparticle Ripening Studied by in-Situ TEM. *Journal of the American Chemical Society* **2010**, *132*, 7968–7975.
- (72) Murray, C. B.; Sun, S.; Gaschler, W.; Doyle, H.; Betley, T. A.; Kagan, C. R. Colloidal Synthesis of Nanocrystals and Nanocrystal Superlattices. *IBM Journal of Research and Development* **2001**, *45*, 47–56.
- (73) Kang, Y.; Murray, C. B. Synthesis and Electrocatalytic Properties of Cubic Mn-Pt Nanocrystals (Nanocubes). *Journal of the American Chemical Society* **2010**, *132*, 7568–7569.
- (74) Zhou, W.; Wu, J.; Yang, H. Highly Uniform Platinum Icosahedra Made by Hot Injection-Assisted GRAILS Method. *Nano Letters* **2013**, *13*, 2870–2874.

- (75) Marks, L. D.; Howie, A. Multiply-Twinned Particles in Silver Catalysts. *Nature* **1981**, *282*, 196–198.
- (76) Marks, L. D. Experimental Studies of Small Particle Structures. *Reports on Progress in Physics* **1994**, *603*, 603–649.
- (77) Velazquez-Salazar, J. J.; Esparza, R.; Mejia-Rosales, S. J.; Estrada-Salas, R.; Ponce, A.; Deepak, F. L.; Castro-Guerrero, C.; Jose-Yacaman, M. Experimental Evidence of Icosahedral and Decahedral Packing in One-Dimensional Nanostructures. *ACS Nano* **2011**, *5*, 6272–6278.
- (78) Zhang, Q.; Xie, J.; Yang, J.; Lee, J. Y. Monodisperse Icosahedral Ag, Au, and Pd Nanoparticles: Size Control Strategy and Superlattice Formation. *ACS Nano* **2009**, *3*, 139–148.
- (79) Lim, B.; Xiong, Y.; Xia, Y. A Water-Based Synthesis of Octahedral, Decahedral, and Icosahedral Pd Nanocrystals Supporting Information. *Angewandte Chemie (International ed. in English)* **2007**, *46*, 9279–9282.
- (80) Seo, D.; Yoo, C. I.; Chung, I. S.; Park, S. M.; Ryu, S.; Song, H. Shape Adjustment between Multiply Twinned and Single-Crystalline Polyhedral Gold Nanocrystals: Decahedra, Icosahedra, and Truncated Tetrahedra. *Journal of Physical Chemistry C* **2008**, *112*, 2469–2475.
- (81) Habas, S. E.; Lee, H.; Radmilovic, V.; Somorjai, G. A.; Yang, P. Shaping Binary Metal Nanocrystals through Epitaxial Seeded Growth. *Nature Materials* **2007**, *6*, 692–697.
- (82) Wiley, B.; Sun, Y.; Mayers, B.; Xia, Y. Shape-Controlled Synthesis of Metal Nanostructures: The Case of Silver. *Chemistry European Journal* **2005**, *11*, 454–463.
- (83) Tao, A. R.; Habas, S.; Yang, P. Shape Control of Colloidal Metal Nanocrystals. *Small* **2008**, *4*, 310–325.
- (84) Tian, N.; Zhou, Z.-Y.; Sun, S.-G.; Ding, Y.; Wang, Z. L. Synthesis of Tetrahedral Platinum Nanocrystals with High-Index Facets and High Electro-Oxidation Activity. *Science* **2007**, *316*, 732–735.

- (85) Sau, T. K.; Rogach, A. L. Nonspherical Noble Metal Nanoparticles: Colloid-Chemical Synthesis and Morphology Control. *Advanced Materials* **2010**, *22*, 1781–1804.
- (86) Kim, F.; Connor, S.; Song, H.; Kuykendall, T.; Yang, P. Platonic Gold Nanocrystals. *Angewandte Chemie (International Ed. in English)* **2004**, *43*, 3673–3677.
- (87) Urban, J. J.; Talapin, D. V.; Shevchenko, E. V.; Murray, C. B. Self-Assembly of PbTe Quantum Dots into Nanocrystal Superlattices and Glassy Films. *Journal of the American Chemical Society* **2006**, *128*, 3248–3255.
- (88) Liu, Y.; Ko, D.; Oh, S. J.; Gordon, T. R.; Doan-Nguyen, V.; Paik, T.; Kang, Y.; Ye, X.; Jin, L.; Kagan, C. R.; *et al.* Near-Infrared Absorption of Monodisperse Silver Telluride (Ag₂Te) Nanocrystals and Photoconductive Response of Their Self-Assembled Superlattices. *Chemistry of Materials* **2011**, *23*, 4657–4659.
- (89) Black, C. T.; Murray, C. B.; Sandstrom, R. L.; Sun, S. Spin-Dependent Tunneling in Self-Assembled Cobalt-Nanocrystal Superlattices. *Science* **2000**, *290*, 1131–1134.
- (90) Macfarlane, R. J.; Lee, B.; Jones, M. R.; Harris, N.; Schatz, G. C.; Mirkin, C. A. Nanoparticle Superlattice Engineering with DNA. *Science* **2011**, *334*, 204–208.
- (91) Chen, C.; Kang, Y.; Huo, Z.; Zhu, Z.; Huang, W.; Xin, H. L.; Snyder, J. D.; Li, D.; Herron, J. A.; Mavrikakis, M.; *et al.* Highly Crystalline Multimetallic Nanoframes with Three-Dimensional Electrocatalytic Surfaces. *Science* **2014**, *343*, 1339–1343.
- (92) Wu, J.; Qi, L.; You, H.; Gross, A.; Li, J.; Yang, H. Icosahedral Platinum Alloy Nanocrystals with Enhanced Electrocatalytic Activities. *Journal of the American Chemical Society* **2012**, *134*, 11880–11883.
- (93) Neder, R. B.; Korsunskiy, V. I.; Chory, C.; Müller, G.; Hofmann, A.; Dembski, S.; Graf, C.; Rühl, E. Structural Characterization of II-VI Semiconductor Nanoparticles. *Physica Status Solidi (C)* **2007**, *4*, 3221–3233.

- (94) Masadeh, A. S.; Božin, E. S.; Farrow, C. L.; Paglia, G.; Juhas, P.; Billinge, S.; Karkamkar, A.; Kanatzidis, M. Quantitative Size-Dependent Structure and Strain Determination of CdSe Nanoparticles Using Atomic Pair Distribution Function Analysis. *Physical Review B* **2007**, *76*, 115413.
- (95) Huang, W. J.; Sun, R.; Tao, J.; Menard, L. D.; Nuzzo, R. G.; Zuo, J. M. Coordination-Dependent Surface Atomic Contraction in Nanocrystals Revealed by Coherent Diffraction. *Nature Materials* **2008**, *7*, 308–313.
- (96) Page, K.; Hood, T. C.; Proffen, T.; Neder, R. B. Building and Refining Complete Nanoparticle Structures with Total Scattering Data. *Journal of Applied Crystallography* **2011**, *44*, 327–336.
- (97) Rosenthal, S. J.; McBride, J. R.; Pennycook, S. J.; Feldman, L. C. Synthesis, Surface Studies, Composition and Structural Characterization of CdSe, Core/shell and Biologically Active Nanocrystals. *Surface Science Reports* **2007**, *62*, 111–157.
- (98) Yang, X.; Masadeh, A. S.; McBride, J. R.; Božin, E. S.; Rosenthal, S. J.; Billinge, S. J. L.; Bozin, E. S.; Rosenthal, S. J.; Billinge, S. J. L. Confirmation of Disordered Structure of Ultrasmall CdSe Nanoparticles from X-Ray Atomic Pair Distribution Function Analysis. *Physical Chemistry Chemical Physics* **2013**, *15*, 8480–8486.
- (99) Jadzinsky, P. D.; Calero, G.; Ackerson, C. J.; Bushnell, D. A.; Kornberg, R. D. Structure of a Thiol Monolayer-Protected Gold Nanoparticle at 1.1 Å Resolution Supporting Information. *Science* **2007**, *318*, 430–433.
- (100) Zeng, C.; Li, T.; Das, A.; Rosi, N. L.; Jin, R. Chiral Structure of Thiolate-Protected 28-Gold-Atom Nanocluster Determined by X-Ray Crystallography. *Journal of the American Chemical Society* **2013**, *135*, 10011–10013.
- (101) Frenkel, A. Solving the 3D Structure of Metal Nanoparticles. *Zeitschrift für Kristallographie* **2007**, *222*, 605–611.
- (102) Gafner, Y. Y.; Gafner, S. L.; Entel, P. Formation of an Icosahedral Structure during Crystallization of Nickel Nanoclusters. *Physics of the Solid State* **2004**, *46*, 1327–1330.

- (103) Yi, X.; Liu, R.; Tian, Z.; Hou, Z.; Li, X.; Zhou, Q. Formation and Evolution Properties of Clusters in Liquid Metal Copper during Rapid Cooling Processes. *Trans. Nonferrous Met. Soc. China* **2008**, *18*, 33–39.
- (104) Barry, J. C.; Bursilla, A.; Sanders, J. V. Electron Microscope Images of Icosahedral and Cuboctahedral (f.c.c. Packing) Clusters of Atoms. *Australian Journal of Physics* **1985**, *38*, 437–448.
- (105) Chen, C.-C.; Zhu, C.; White, E. R.; Chiu, C.-Y.; Scott, M. C.; Regan, B. C.; Marks, L. D.; Huang, Y.; Miao, J. Three-Dimensional Imaging of Dislocations in a Nanoparticle at Atomic Resolution. *Nature* **2013**, *496*, 74–79.
- (106) Egami, T.; Billinge, S. J. L. *Underneath the Bragg Peaks: Structural Analysis of Complex Materials*; 2nd ed.; Elsevier: Amsterdam, 2013.
- (107) Peker, A.; Johnson, W. L. A Highly Processable Metallic Glass: $Zr_{41.2}Ti_{13.8}Cu_{12.5}Ni_{10.0}Be_{22.5}$. *Applied Physics Letters* **1993**, *63*, 2342–2344.
- (108) Busch, R.; Kim, Y. J.; Johnson, W. L. Thermodynamics and Kinetics of the Undercooled Liquid and the Glass Transition of the $Zr_{41.2}Ti_{13.8}Cu_{12.5}Ni_{10.0}Be_{22.5}$ Alloy. *Journal of Applied Physics* **1995**, *77*, 4039–4043.
- (109) Voloshin, V. P.; Beaufils, S.; Medvedev, N. N. Void Space Analysis of the Structure of Liquids. *Journal of Molecular Liquids* **2002**, *96-97*, 101–112.
- (110) Voloshin, V. P.; Naberukhin, Y. I. On the Origin of the Splitting of the Second Maximum in the Radial Distribution Function of Amorphous Solids. *Journal of Structural Chemistry* **1997**, *38*, 62–70.
- (111) Chirawatkul, P.; Zeidler, A.; Salmon, P. S.; Takeda, S.; Kawakita, Y.; Usuki, T.; Fischer, H. E. Structure of Eutectic Liquids in the Au-Si, Au-Ge, and Ag-Ge Binary Systems by Neutron Diffraction. *Physical Review B* **2011**, *83*, 014203–014210.
- (112) Salmon, P. S.; Petri, I. Structure of Glassy and Liquid $GeSe_2$. *Journal of Physics: Condensed Matter* **2003**, *15*, S1509–S1528.

- (113) Petkov, V.; Billinge, S.; Shastri, S.; Himmel, B. Polyhedral Units and Network Connectivity in Calcium Aluminosilicate Glasses from High-Energy X-Ray Diffraction. *Physical Review Letters* **2000**, *85*, 3436–3439.
- (114) Hirata, A.; Kang, L. J.; Fujita, T.; Klumov, B.; Matsue, K.; Kotani, M.; Yavari, A. R.; Chen, M. W. Supporting Information: Geometric Frustration of Icosahedron in Metallic Glasses. *Science* **2013**, *341*, 376–379.
- (115) Di Cicco, A.; Trapananti, A.; Faggioni, S.; Filipponi, A. Is There Icosahedral Ordering in Liquid and Undercooled Metals? *Physical Review Letters* **2003**, *91*, 135505–4.
- (116) Billinge, S. J. L.; Levin, I. The Problem with Determining Atomic Structure at the Nanoscale. *Science* **2007**, *316*, 561–565.
- (117) Tyrsted, C.; Jensen, K. M. Ø.; Bøjesen, E. D.; Lock, N.; Christensen, M.; Billinge, S. J. L.; Brummerstedt Iversen, B. Understanding the Formation and Evolution of Ceria Nanoparticles under Hydrothermal Conditions. *Angewandte Chemie (International Ed. in English)* **2012**, *51*, 9030–9033.
- (118) Murray, C. B.; Sun, S. H.; Doyle, H.; Betley, T. Monodisperse 3d Transition-Metal (Co, Ni, Fe) Nanoparticles and Their Assembly into Nanoparticle Superlattices. *Materials Research Bulletin* **2010**, *33*, 985–991.
- (119) Hammersley, A. P. P.; Svensson, S. O. O.; Hanfland, M.; Fitch, A. N. N.; Hausermann, D. Two-Dimensional Detector Software: From Real Detector to Idealised Image or Two-Theta Scan. *High Pressure Research* **1996**, *14*, 235–248.
- (120) Hwang, J.; Melgarejo, Z.; Kalay, Y.; Kalay, I.; Kramer, M.; Stone, D.; Voyles, P. Nanoscale Structure and Structural Relaxation in Zr₅₀Cu₄₅Al₅ Bulk Metallic Glass. *Physical Review Letters* **2012**, *108*, 195505.
- (121) Miracle, D. B. A Structural Model for Metallic Glasses. *Nature Materials* **2004**, *3*, 697–702.
- (122) Hirata, A.; Guan, P.; Fujita, T.; Hirotsu, Y.; Inoue, A.; Yavari, A. R.; Sakurai, T.; Chen, M. Direct Observation of Local Atomic Order in a Metallic Glass. *Nature materials* **2011**, *10*, 28–33.

- (123) Wang, W. H.; Dong, C.; Shek, C. H. Bulk Metallic Glasses. *Materials Science and Engineering: R* **2004**, *44*, 45–89.
- (124) Liu, Y. H.; Wang, G.; Wang, R. J.; Zhao, D. Q.; Pan, M. X.; Wang, W. H. Super Plastic Bulk Metallic Glasses at Room Temperature. *Science (New York, N.Y.)* **2007**, *315*, 1385–1388.
- (125) Liu, X. J.; Xu, Y.; Lu, Z. P.; Hui, X.; Chen, G. L.; Zheng, G. P.; Liu, C. T. Atomic Packing Symmetry in the Metallic Liquid and Glass States. *Acta Materialia* **2011**, *59*, 6480–6488.
- (126) Basu, J.; Ranganathan, S. Bulk Metallic Glasses : A New Class of Engineering Materials. **2003**, *28*, 783–798.
- (127) Hofmann, D. C.; Suh, J.-Y.; Wiest, A.; Duan, G.; Lind, M.-L.; Demetriou, M. D.; Johnson, W. L. Designing Metallic Glass Matrix Composites with High Toughness and Tensile Ductility. *Nature* **2008**, *451*, 1085–1089.
- (128) Klement, W.; Willens, R. H.; Duwez, P. Non-Crystalline Structure in Solidified Gold-Silicon Alloys. *Nature* **1960**, *187*, 869–870.
- (129) Duwez, P. Structure and Properties of Glassy Metals. *Annual Reviews* **1976**, 83–117.
- (130) Schroers, J. Bulk Metallic Glasses. *Physics Today* **2013**, *66*, 32.
- (131) Ma, D.; Stoica, A. D.; Wang, X. L. Power-Law Scaling and Fractal Nature of Medium-Range Order in Metallic Glasses. *Nature Materials* **2009**, *8*, 30–34.
- (132) Robinson, K.; Tweet, D. J. Surface X-Ray Diffraction. *Reports on Progress in Physics* **1992**, *55*, 599–651.
- (133) Nam, H.-S.; Hwang, N.; Yu, B.; Yoon, J.-K. Formation of an Icosahedral Structure during the Freezing of Gold Nanoclusters: Surface-Induced Mechanism. *Physical Review Letters* **2002**, *89*, 275502.
- (134) Cheng, Y. Q.; Ma, E. Atomic-Level Structure and Structure–property Relationship in Metallic Glasses. *Progress in Materials Science* **2011**, *56*, 379–473.

- (135) Haruta, M. Size- and Support-Dependency in the Catalysis of Gold. *Catalysis Today* **1997**, *36*, 153–166.
- (136) Ilavsky, J.; Jemian, P. R. Irena: Tool Suite for Modeling and Analysis of Small-Angle Scattering. *Journal of Applied Crystallography* **2009**, *42*, 347–353.
- (137) *Basic Research Needs for the Hydrogen Economy*; 2003.
- (138) Energy, D. of. *Hydrogen and Fuel Cells Program Plan*; 2011.
- (139) EG&G Technical Services, I. *Fuel Cell Handbook*; 2004.
- (140) Markovic, N. M.; Ross, P. N. Surface Science Studies of Model Fuel Cell Electrocatalysts. *Surface Science Reports* **2002**, *45*, 117–229.
- (141) Jaouen, F.; Proietti, E.; Lefèvre, M.; Chenitz, R.; Dodelet, J.-P.; Wu, G.; Chung, H. T.; Johnston, C. M.; Zelenay, P. Recent Advances in Non-Precious Metal Catalysis for Oxygen-Reduction Reaction in Polymer Electrolyte Fuel Cells. *Energy & Environmental Science* **2011**, *4*, 114.
- (142) Markovic, N. M.; Schmidt, T. J.; Stamenkovic, V.; Ross, P. N. Oxygen Reduction Reaction on Pt and Pt Bimetallic Surfaces: A Selective Review. *Fuel Cells* **2001**, *1*, 105–116.
- (143) Guo, S.; Zhang, S.; Sun, S. Tuning Nanoparticle Catalysis for the Oxygen Reduction Reaction. *Angewandte Chemie (International Ed. in English)* **2013**, *52*, 8526–8544.
- (144) Stamenkovic, V. R.; Fowler, B.; Mun, B. S.; Wang, G.; Ross, P. N.; Lucas, C. A.; Marković, N. M. Improved Oxygen Reduction Activity on Pt₃Ni(111) via Increased Surface Site Availability. *Science* **2007**, *315*, 493–497.
- (145) Lim, B.; Jiang, M.; Camargo, P. H. C.; Cho, E. C.; Tao, J.; Lu, X.; Zhu, Y.; Xia, Y. Pd-Pt Bimetallic Nanodendrites with. *Science* **2009**, *324*, 1301–1305.
- (146) Toda, T.; Igarashi, H.; Uchida, H.; Watanabe, M. Enhancement of the Electroreduction of Oxygen on Pt Alloys with Fe, Ni, and Co. *Journal of The Electrochemical Society* **1999**, *146*, 3750–3756.

- (147) Mukerjee, S.; Srinivasan, S.; Soriaga, M. P.; McBreen, J. Role of Structural and Electronic Properties of Pt and Pt Alloys on Electrocatalysis of Oxygen Reduction. *Journal of The Electrochemical Society* **1995**, *142*, 1409–1422.
- (148) Paulus, U. A.; Wokaun, A.; Scherer, G. G. Oxygen Reduction on Carbon-Supported Pt - Ni and Pt - Co Alloy Catalysts. *Journal of Physical Chemistry B* **2002**, *106*, 4181–4191.
- (149) Chen, Z.; Higgins, D.; Yu, A.; Zhang, L.; Zhang, J. A Review on Non-Precious Metal Electrocatalysts for PEM Fuel Cells. *Energy & Environmental Science* **2011**, *4*, 3167.
- (150) Bashyam, R.; Zelenay, P. A Class of Non-Precious Metal Composite Catalysts for Fuel Cells. *Nature* **2006**, *443*, 63–66.
- (151) Nallathambi, V.; Lee, J.-W.; Kumaraguru, S. P.; Wu, G.; Popov, B. N. Development of High Performance Carbon Composite Catalyst for Oxygen Reduction Reaction in PEM Proton Exchange Membrane Fuel Cells. *Journal of Power Sources* **2008**, *183*, 34–42.
- (152) Qu, L.; Liu, Y.; Baek, J. B.; Dai, L. Nitrogen-Doped Graphene as Efficient Metal-Free Electrocatalyst for Oxygen Reduction in Fuel Cells. *ACS Nano* **2010**, *4*, 1321–1326.
- (153) Yang, S.; Feng, X.; Wang, X.; Müllen, K. Graphene-Based Carbon Nitride Nanosheets as Efficient Metal-Free Electrocatalysts for Oxygen Reduction Reactions. *Angewandte Chemie (International Ed. in English)* **2011**, *50*, 5339–5343.
- (154) Geng, D.; Chen, Y.; Chen, Y.; Li, Y.; Li, R.; Sun, X.; Ye, S.; Knights, S. High Oxygen-Reduction Activity and Durability of Nitrogen-Doped Graphene. *Energy & Environmental Science* **2011**, *4*, 760.
- (155) Ye, X.; Jin, L.; Caglayan, H.; Chen, J.; Xing, G.; Zheng, C.; Doan-Nguyen, V.; Kang, Y.; Engheta, N.; Kagan, C. R.; *et al.* Improved Size-Tunable Synthesis of Monodisperse Gold Nanorods through the Use of Aromatic Additives. *ACS Nano* **2012**, *6*, 2804–2817.

- (156) Spurgeon, J. M.; Atwater, H. A.; Lewis, N. S. A Comparison Between the Behavior of Nanorod Array and Planar Cd(Se, Te). *Journal of Physical Chemistry C* **2008**, *112*, 6186–6193.
- (157) Cordente, N.; Respaud, M.; Senocq, F.; Casanove, M.-J.; Amiens, C.; Chaudret, B. Synthesis and Magnetic Properties of Nickel Nanorods. *Nano Letters* **2001**, *1*, 565–568.
- (158) Park, J.; Koo, B.; Hwang, Y.; Bae, C.; An, K.; Park, J.-G.; Park, H. M.; Hyeon, T. Novel Synthesis of Magnetic Fe₂P Nanorods from Thermal Decomposition of Continuously Delivered Precursors Using a Syringe Pump. *Angewandte Chemie (International Ed. in English)* **2004**, *43*, 2282–2285.
- (159) Xie, X.; Li, Y.; Liu, Z.; Haruta, M.; Shen, W. Low-Temperature Oxidation of CO Catalysed by Co₃M₂O₄ Nanorods. *Nature* **2009**, *458*, 746–749.
- (160) Zhang, S.; Shan, J.; Zhu, Y.; Frenkel, A. I.; Patlolla, A.; Huang, W.; Yoon, S. J.; Wang, L.; Yoshida, H.; Takeda, S.; *et al.* WGS Catalysis and in Situ Studies of CoO_{1-x}, PtCo_n/Co₃O₄, and Pt_mCo_m/CoO_{1-x} Nanorod Catalysts. *Journal of the American Chemical Society* **2013**, *135*, 8283–8293.
- (161) Qian, X. F.; Xie, Y.; Qian, Y. T.; Zhang, X. M.; Wang, W. Z.; Yang, L. Organo-Thermal Preparation of Nanocrystalline Cobalt Phosphides. *Materials Science and Engineering: B* **1997**, *49*, 135–137.
- (162) Park, J. J.; Koo, B.; Yoon, K. Y.; Hwang, Y.; Kang, M.; Hyeon, T.; Park, J. J.; Hyeon, T. Generalized Synthesis of Metal Phosphide Nanorods via Thermal Decomposition of Continuously Delivered Metal-Phosphine Complexes Using a Syringe Pump. *Journal of the American Chemical Society* **2005**, *127*, 8433–8440.
- (163) Ryu, J.; Jung, N.; Lim, D.-H.; Shin, D. Y.; Park, S. H.; Ham, H. C.; Jang, J. H.; Kim, H.-J.; Yoo, S. J. P-Modified and Carbon Shell Coated Co Nanoparticles for Efficient Alkaline Oxygen Reduction Catalysis. *Chemical Communications* **2014**, *50*, 15940–15943.
- (164) Ha, D.-H.; Moreau, L. M.; Bealing, C. R.; Zhang, H.; Hennig, R. G.; Robinson, R. D. The Structural Evolution and Diffusion during the

Chemical Transformation from Cobalt to Cobalt Phosphide Nanoparticles. *Journal of Materials Chemistry* **2011**, *21*, 11498–11510.

- (165) Lukehart, C. M.; Milne, S. B.; Stock, S. R. Formation of Crystalline Nanoclusters of Fe₂P, RuP, Co₂P, Rh₂P, Ni₂P, Pd₅P₂, or PtP₂ in a Silica Xerogel Matrix from Single-Source Molecular Precursors. *Chemistry of Materials* **1998**, *10*, 903–908.
- (166) Wang, J.; Yang, Q.; Zhang, Z.; Sun, S. Phase-Controlled Synthesis of Transition-Metal Phosphide Nanowires by Ullmann-Type Reactions. *Chemistry (Weinheim an der Bergstrasse, Germany)* **2010**, *16*, 7916–7924.
- (167) Henkes, A. E.; Vasquez, Y.; Schaak, R. E. Converting Metals into Phosphides: A General Strategy for the Synthesis of Metal Phosphide Nanocrystals. *Journal of the American Chemical Society Communications* **2007**, *129*, 1–5.
- (168) Brock, S. L.; Perera, S. C.; Stamm, K. L. Chemical Routes for Production of Transition-Metal Phosphides on the Nanoscale: Implications for Advanced Magnetic and Catalytic Materials. *Chemistry (Weinheim an der Bergstrasse, Germany)* **2004**, *10*, 3364–3371.
- (169) Lo, C.-T.; Kuo, P.-Y. Synthesis and Magnetic Properties of Iron Phosphide Nanorods. *The Journal of Physical Chemistry C* **2010**, *114*, 4808–4815.
- (170) Perera, S. C.; Tsoi, G.; Wenger, L. E.; Brock, S. L. Synthesis of MnP Nanocrystals by Treatment of Metal Carbonyl Complexes with Phosphines: A New, Versatile Route to Nanoscale Transition Metal Phosphides. *Journal of the American Chemical Society* **2003**, *125*, 13960–13961.
- (171) Zhang, J.; Yan, Y.; Chen, J.; Chance, W. M.; Hayat, J.; Gai, Z.; Tang, C. Nanostructured Metal/Carbon Composites from Heterobimetallic Block Copolymers with Controlled Magnetic Properties. *Chemistry of Materials* **2014**, *26*, 3185–3190.
- (172) Lu, A.; Chen, Y.; Li, H.; Dowd, A.; Cortie, M. B.; Xie, Q.; Guo, H.; Qi, Q.; Peng, D.-L. Supplementary Information Magnetic Metal Phosphide Nanorods as Effective Hydrogen-Evolution Electrocatalysts. *International Journal of Hydrogen Energy* **2014**, *39*, 18919–18928.

- (173) Ni, Y.; Li, J.; Zhang, L.; Yang, S.; Wei, X. Urchin-like Co₂P Nanocrystals: Synthesis, Characterization, Influencing Factors and Photocatalytic Degradation Property. *Materials Research Bulletin* **2009**, *44*, 1166–1172.
- (174) Tian, J.; Liu, Q.; Asiri, A. M.; Sun, X. Self-Supported Nanoporous Cobalt Phosphide Nanowire Arrays: An Efficient 3D Hydrogen-Evolving Cathode over the Wide Range of pH 0-14. *Journal of the American Chemical Society Communications* **2014**, *136*, 7587–7590.
- (175) Pralong, V.; Souza, D. C. S.; Leung, K. T.; Nazar, L. F. Reversible Lithium Uptake by CoP₃ at Low Potential : Role of the Anion. *Electrochemistry Communications* **2002**, *4*, 516–520.
- (176) Peng, W.; Jiao, L.; Huan, Q.; Li, L.; Yang, J.; Zhao, Q.; Wang, Q.; Du, H.; Liu, G.; Si, Y.; *et al.* Co₂P: A Facile Solid State Synthesis and Its Applications in Alkaline Rechargeable Batteries. *Journal of Alloys and Compounds* **2012**, *511*, 198–201.
- (177) Yuan, F.; Ni, Y.; Zhang, L.; Ma, X.; Hong, J. Rod-Like Co₂P Nanostructures: Improved Synthesis, Catalytic Property and Application in the Removal of Heavy Metal. *Journal of Cluster Science* **2013**, *24*, 1067–1080.
- (178) Popczun, E. J.; Read, C. G.; Roske, C. W.; Lewis, N. S.; Schaak, R. E. Highly Active Electrocatalysis of the Hydrogen Evolution Reaction by Cobalt Phosphide Nanoparticles. *Angewandte Chemie (International Ed. in English)* **2014**, *53*, 5427–5430.
- (179) Popczun, E. J.; McKone, J. R.; Read, C. G.; Biacchi, A. J.; Wiltrout, A. M.; Lewis, N. S.; Schaak, R. E. Nanostructured Nickel Phosphide as an Electrocatalyst for the Hydrogen Evolution Reaction. *Journal of the American Chemical Society* **2013**, *135*, 9267–9270.
- (180) Alayoglu, S.; Zavalij, P.; Eichhorn, B.; Wang, Q.; Frenkel, A. I.; Chupas, P. Structural and Architectural Evaluation of Bimetallic Nanoparticles: A Case Study of Pt-Ru Core-Shell and Alloy Nanoparticles. *ACS Nano* **2009**, *3*, 3127–3137.
- (181) Sasaki, K.; Wang, J. X.; Naohara, H.; Marinkovic, N.; More, K.; Inada, H.; Adzic, R. R. Recent Advances in Platinum Monolayer Electrocatalysts for

- Oxygen Reduction Reaction: Scale-up Synthesis, Structure and Activity of Pt Shells on Pd Cores. *Electrochimica Acta* **2010**, *55*, 2645–2652.
- (182) Principi, E.; Witkowska, A.; Dsoke, S.; Marassi, R.; Di Cicco, A. An XAS Experimental Approach to Study Low Pt Content Electrocatalysts Operating in PEM Fuel Cells. *Physical Chemistry Chemical Physics* **2009**, *11*, 9987–9995.
- (183) Alayoglu, S.; Nilekar, A. U.; Mavrikakis, M.; Eichhorn, B. Ru-Pt Core-Shell Nanoparticles for Preferential Oxidation of Carbon Monoxide in Hydrogen. *Nature Materials* **2008**, *7*, 333–338.
- (184) Rundqvist, S. The Structures of Co_2P , Ru_2P and Related Phases. *Acta Chemica Scandinavica* **1960**, *14*, 1961–1979.
- (185) Trigg, E. B. DebyeByPy Github Repository
<https://github.com/etrigg/DebyeByPy>.
- (186) Kraft, S.; Stümpel, J.; Becker, P.; Kuetgens, U. High Resolution X-Ray Absorption Spectroscopy with Absolute Energy Calibration for the Determination of Absorption Edge Energies. *Review of Scientific Instruments* **1996**, *67*, 681–687.
- (187) Puentes, V. F.; Krishnan, K. M.; Alivisatos, A. P. Colloidal Nanocrystal Shape and Size Control: The Case of Cobalt. *Science* **2001**, *291*, 2115–2117.
- (188) Debye, P. Zerstreuung von Röntgenstrahlen. *Annalen der Physik* **1915**, *351*, 809–823.
- (189) Xia, W.; Zou, R.; An, L.; Xia, D.; Guo, S. A Metal–organic Framework Route to in Situ Encapsulation of $\text{Co@Co}_3\text{O}_4\text{@C}$ Core@shell Nanoparticles into a Highly Ordered Porous Carbon Matrix for Oxygen Reduction. *Energy & Environmental Science* **2015**, *8*, 568–576.
- (190) Liang, Y.; Li, Y.; Wang, H.; Zhou, J.; Wang, J.; Regier, T.; Dai, H. Co_3O_4 Nanocrystals on Graphene as a Synergistic Catalyst for Oxygen Reduction Reaction. *Nature Materials* **2011**, *10*, 780–786.

- (191) Guo, S.; Zhang, S.; Wu, L.; Sun, S. Co/CoO Nanoparticles Assembled on Graphene for Electrochemical Reduction of Oxygen. *Angewandte Chemie* **2012**, *51*, 11770–11773.
- (192) Zhu, H.; Zhang, S.; Guo, S.; Su, D.; Sun, S. Synthetic Control of FePtM Nanorods (M = Cu, Ni) to Enhance the Oxygen Reduction Reaction. *Journal of the American Chemical Society* **2013**, *135*, 7130–7133.
- (193) Guo, S.; Zhang, S.; Su, D.; Sun, S. Seed-Mediated Synthesis of Core/shell FePtM/FePt (M = Pd, Au) Nanowires and Their Electrocatalysis for Oxygen Reduction Reaction. *Journal of the American Chemical Society* **2013**, *135*, 13879–13884.
- (194) Yang, Z.; Ko, C.; Ramanathan, S. Oxide Electronics Utilizing Ultrafast Metal-Insulator Transitions. *Annual Review of Materials Research* **2011**, *41*, 337–367.
- (195) Sun, C.; Yan, L.; Yue, B.; Liu, H.; Gao, Y. The Modulation of Metal–insulator Transition Temperature of Vanadium Dioxide: A Density Functional Theory Study. *Journal of Materials Chemistry C* **2014**, *2*, 9283–9293.
- (196) Gao, Y.; Luo, H.; Zhang, Z.; Kang, L.; Chen, Z.; Du, J.; Kanehira, M.; Cao, C. Nanoceramic VO₂ Thermochromic Smart Glass: A Review on Progress in Solution Processing. *Nano Energy* **2012**, *1*, 221–246.
- (197) Andersson, G. Studies on Vanadium Oxides. II. The Crystal Structure of Vanadium Dioxide. *Acta Chemica Scandinavica* **1956**, *10*, 623–628.
- (198) Goodenough, J. B. The Two Components of the Crystallographic Transition in VO₂. *Journal of Solid State Chemistry* **1971**, *3*, 490–500.
- (199) Ji, Y.; Zhang, Y.; Gao, M.; Yuan, Z.; Xia, Y.; Jin, C.; Tao, B.; Chen, C.; Jia, Q.; Lin, Y. Role of Microstructures on the M1-M2 Phase Transition in Epitaxial VO₂ Thin Films. *Scientific Reports* **2014**, *4*, 4854.
- (200) Pouget, J. P.; Launois, H.; D’Haenens, J. P.; Merenda, P.; Rice, T. M. Electron Localization Induced by Uniaxial Stress in Pure VO₂. *Physical Review Letters* **1975**, *35*, 873–875.

- (201) Aetukuri, N. B.; Gray, A. X.; Drouard, M.; Cossale, M.; Gao, L.; Reid, A. H.; Kukreja, R.; Ohldag, H.; Jenkins, C. a; Arenholz, E.; *et al.* Control of the Metal-Insulator Transition in Vanadium Dioxide by Modifying Orbital Occupancy. *Nat Phys* **2013**, *9*, 661–666.
- (202) Nag, J.; Haglund Jr, R. F. Synthesis of Vanadium Dioxide Thin Films and Nanoparticles. *Journal of Physics: Condensed Matter* **2008**, *20*, 264016.
- (203) Liu, S.; Fang, H.; Su, Y.; Hsieh, J. Metal–insulator Transition Characteristics of Mo- and Mn-Doped VO₂ Films Fabricated by Magnetron Cosputtering Technique. *Japanese Journal of Applied Physics* **2014**, *53*, 063201–063205.
- (204) Beteille, F.; Morineau, R.; Livage, J. Switching Properties of V_{1-x}Ti_xO₂ Thin Films Deposited from Alkoxides. *Materials Research Bulletin* **1997**, *32*, 1109–1117.
- (205) Gao, Y.; Cao, C.; Dai, L.; Luo, H.; Kanehira, M.; Ding, Y.; Wang, Z. L. Phase and Shape Controlled VO₂ Nanostructures by Antimony Doping. *Energy & Environmental Science* **2012**, *5*, 8708.
- (206) Marezio, M.; McWhan, D. B.; Remeika, J. P.; Dernier, P. D. Structural Aspects of the Metal-Insulator Transitions in Cr-Doped VO₂. *Physical Review B* **1971**, *91*, 2541.
- (207) Pouget, J. P.; Launois, H.; Rice, T. M.; Dernier, P.; Gossard, A.; Villeneuve, G.; Hagenmuller, P. Dimerization of a Linear Heisenberg Chain in the Insulating Phase of V_{1-x}Cr_xO₂. *Physical Review B* **1974**, *10*, 1801–1815.
- (208) Marini, C.; Pascarelli, S.; Mathon, O.; Joseph, B.; Malavasi, L.; Postorino, P. Tracking Competitive Lattice Distortions in Strongly Correlated VO₂-Based Systems: A Temperature-Dependent EXAFS Study. *EPL (Europhysics Letters)* **2013**, *102*, 66004.
- (209) Paik, T.; Hong, S.; Gaulding, E. A.; Caglayan, H.; Gordon, T. R.; Engheta, N.; Kagan, C. R.; Murray, C. B. Solution-Processed Phase-Change Vanadium Oxide (VO_x) Nanocrystals. *ACS Nano* **2014**, *8*, 797–806.
- (210) Morin, F. J. Oxides Which Show a Metal-to-Insulator Transition at the Neel Temperature. *Physical Review Letters* **1959**, *3*, 34–36.

- (211) Zylbersztein, A.; Mott, N. F. Metal-Insulator Transition in Vanadium Dioxide. *Physical Review B* **1975**, *11*, 4383–4395.
- (212) Eyert, V. The Metal-Insulator Transitions of VO₂: A Band Theoretical Approach. *Annalen der Physik* **2002**, *11*, 650–702.
- (213) Budai, J. D.; Hong, J.; Manley, M. E.; Specht, E. D.; Li, C. W.; Tischler, J. Z.; Abernathy, D. L.; Said, A. H.; Leu, B. M.; Boatner, L. A.; *et al.* Metallization of Vanadium Dioxide Driven by Large Phonon Entropy. *Nature* **2014**, *515*, 535–539.
- (214) Oka, Y.; Yao, T.; Yamamoto, N.; Ueda, Y.; Hayashi, A. Phase Transition and V⁴⁺-V⁴⁺ Pairing in VO₂(B). *Journal of Solid State Chemistry* **1993**, *105*, 271–278.
- (215) Yao, T.; Oka, Y.; Yamamoto, N. A Structural Study of the High-Temperature Phase of VO₂(A). *Journal of Solid State Chemistr* **1994**, *112*, 196–198.
- (216) Corr, S. A.; Grossman, M.; Shi, Y.; Heier, K. R.; Stucky, G. D.; Seshadri, R. VO₂(B) Nanorods: Solvothermal Preparation, Electrical Properties, and Conversion to Rutile VO₂ and V₂O₃. *Journal of Materials Chemistry* **2009**, *19*, 4362.
- (217) Theobald, F. Hydrothermal Study of VO₂-VO_{2.5}-H₂O System. *Journal of the Less-Common Metals* **1977**, *53*, 55–71.
- (218) Booth, J. M.; Casey, P. S. Anisotropic Structure Deformation in the VO₂ Metal-Insulator Transition. *Physical Review Letters* **2009**, *103*, 086402–086404.
- (219) Suh, J. Y.; Lopez, R.; Feldman, L. C.; Haglund, R. F. Semiconductor to Metal Phase Transition in the Nucleation and Growth of VO₂ Nanoparticles and Thin Films. *Journal of Applied Physics* **2004**, *96*, 1209–1213.
- (220) Wriedt, H. A. The O-V (Oxygen-Vanadium) System. *Bulletin of Alloy Compounds* **1989**, *10*, 271–277.

- (221) Cavalleri, A.; Dekorsy, T.; Chong, H. H. W.; Kieffer, J. C.; Schoenlein, R. W. Evidence for a Structurally-Driven Insulator-to-Metal Transition in VO₂: A View from the Ultrafast Timescale. *Physical Review B* **2004**, *70*, 161102R – 4.
- (222) Baum, P.; Yang, D.-S.; Zewail, A. H. 4D Visualization of Transitional Structures in Phase Transformations by Electron Diffraction. *Science* **2007**, *318*, 788–792.
- (223) Lysenko, S.; Rúa, A.; Vikhnin, V.; Fernández, F.; Liu, H. Insulator-to-Metal Phase Transition and Recovery Processes in VO₂ Thin Films after Femtosecond Laser Excitation. *Physical Review B* **2007**, *76*, 035104–035106.
- (224) Jin, S.; Tiefel, T. H.; McCormack, M.; Fastnacht, R. A.; Ramesh, R.; Chen, L. H. Thousandfold Change in Resistivity in Magnetoresistive La-Ca-Mn-O Films. *Science* **1994**, *264*, 413–415.
- (225) Mott, N. F. S. *Metal-Insulator Transition*; 2nd ed.; Taylor & Francis: London, 1990; Vol. 40.
- (226) Marini, C.; Bendele, M.; Joseph, B.; Kantor, I.; Mitrano, M.; Mathon, O.; Baldini, M.; Malavasi, L.; Pascarelli, S.; Postorino, P. Probing the Electronic and Local Structural Changes across the Pressure-Induced Insulator-to-Metal Transition in VO₂. *Europhysics Letters* **2014**, *108*, 36003–36005.
- (227) Adler, D. Mechanisms for Metal-Nonmetal Transitions in Transition-Metal Oxides and Sulfides. *Reviews of Modern Physics* **1968**, *40*, 714–736.
- (228) Imada, M.; Fujimori, A.; Tokura, Y. Metal-Insulator Transitions. *Reviews of Modern Physics* **1998**, *70*, 1039–1263.
- (229) Granqvist, C. G. Transparent Conductors as Solar Energy Materials: A Panoramic Review. *Solar Energy Materials and Solar Cells* **2007**, *91*, 1529–1598.
- (230) Chettiar, U. K.; Engheta, N. Modeling Vanadium Dioxide Phase Transition due to Continuous-Wave Optical Signals. **2015**, *23*, 272–274.

- (231) Donev, E. U.; Lopez, R.; Feldman, L. C.; Haglund, R. F. Confocal Raman Microscopy across the Metal-Insulator Transition of Single Vanadium Dioxide Nanoparticles. *Nano Letters* **2009**, *9*, 702–706.
- (232) Petrov, G. I.; Yakovlev, V. V.; Squier, J. Raman Microscopy Analysis of Phase Transformation Mechanisms in Vanadium Dioxide. *Applied Physics Letters* **2002**, *81*, 1023.
- (233) Whittaker, L.; Patridge, C. J.; Banerjee, S. Microscopic and Nanoscale Perspective of the Metal \rightarrow Insulator Phase Transitions of VO₂: Some New Twists to an Old Tale. *Journal of Physical Chemistry Letters* **2011**, *2*, 745–758.
- (234) Tan, X.; Yao, T.; Long, R.; Sun, Z.; Feng, Y.; Cheng, H.; Yuan, X.; Zhang, W.; Liu, Q.; Wu, C.; *et al.* Unraveling Metal-Insulator Transition Mechanism of VO₂ Triggered by Tungsten Doping. *Scientific Reports* **2012**, *2*, 466.
- (235) Whittaker, L.; Wu, T.-L.; Patridge, C. J.; Sambandamurthy, G.; Banerjee, S. Distinctive Finite Size Effects on the Phase Diagram and Metal–insulator Transitions of Tungsten-Doped Vanadium(IV) Oxide. *Journal of Materials Chemistry* **2011**, *21*, 5580–5592.
- (236) Tao, Z.; Han, T.-R.; Mahanti, S.; Duxbury, P.; Yuan, F.; Ruan, C.-Y.; Wang, K.; Wu, J. Decoupling of Structural and Electronic Phase Transitions in VO₂. *Physical Review Letters* **2012**, *109*, 1–5.
- (237) Qazilbash, M. M.; Brehm, M.; Chae, B.-G.; Ho, P.-C.; Andreev, G. O.; Kim, B.-J.; Yun, S. J.; Balatsky, A. V.; Maple, M. B.; Keilmann, F.; *et al.* Mott Transition in VO₂ Revealed by Infrared Spectroscopy and Nano-Imaging. *Science* **2007**, *318*, 1750–1753.
- (238) Bianconi, A. Multiplet Splitting of Final-State Configurations in X-Ray Absorption Spectrum of Metal VO₂: Effect of Core-Hole Screening, Electron Correlation, and Metal-Insulator Transition. *Physical Review B* **1982**, *26*, 2741–2747.
- (239) Wong, J.; Lytle, F. W.; Messmer, R. P.; Maylotte, D. H. K-Edge Absorption Spectra of Selected Vanadium Compounds. *Physical Review B* **1984**, *30*, 5596–5610.

- (240) Giuli, G.; Paris, E.; Mungall, J.; Romano, C.; Dingwell, D. V Oxidation State and Coordination Number in Silicate Glasses by XAS. *American Mineralogist* **2004**, *89*, 1640–1646.
- (241) Chaurand, P.; Rose, J.; Briois, V.; Salome, M.; Proux, O.; Nassif, V.; Olivi, L.; Susini, J.; Hazemann, J.-L.; Bottero, J.-Y. New Methodological Approach for the Vanadium K-Edge X-Ray Absorption Near-Edge Structure Interpretation: Application to the Speciation of Vanadium in Oxide Phases from Steel Slag. *Journal of Physical Chemistry B* **2007**, *111*, 5101–5110.
- (242) Yamazoe, S.; Hitomi, Y.; Shishido, T.; Tanaka, T. XAFS Study of Tungsten L1- and L3 -Edges : Structural Analysis of WO₃ Species Loaded on TiO₂ as a Catalyst for Photo-Oxidation of NH₃. *Society* **2008**, 6869–6879.
- (243) Blaauw, C.; Leenhouts, F.; Woude, van der. Phase Transitions in Fe Doped VO₂. *Solid State Communications* **1975**, *17*, 559–563.
- (244) Phillips, T. E.; Murphy, R. A.; Poehler, T. O. Electrical Studies of Reactively Sputtered Fe-Doped VO₂ Thin Films. *Materials Research Bulletin* **1987**, *22*, 1113–1123.
- (245) Praveen, P.; Loh, K.-C. Trioctylphosphine Oxide-Impregnated Hollow Fiber Membranes for Removal of Phenol from Wastewater. *Journal of Membrane Science* **2013**, *437*, 1–6.
- (246) Manna, L.; Scher, E. C.; Alivisatos, A. P.; August, R. V. Synthesis of Soluble and Processable Rod-, Arrow-, Teardrop-, and Tetrapod-Shaped CdSe Nanocrystals. *Journal of the American Chemical Society* **2000**, *122*, 12700–12706.
- (247) Murray, C. B.; Norris, D. J.; Bawendi, M. G. Synthesis and Characterization of Nearly Monodisperse CdE (E = Sulfur, Selenium, Tellurium) Semiconductor Nanocrystallites. *Journal of the American Chemical Society* **1993**, *115*, 8706–8715.
- (248) Rockenberger, J.; Tröger, L.; Rogach, A. L.; Tischer, M.; Grundmann, M.; Eychmüller, A.; Weller, H. The Contribution of Particle Core and Surface to Strain, Disorder and Vibrations in Thiolcapped CdTe Nanocrystals. *The Journal of Chemical Physics* **1998**, *108*, 7807.

- (249) Talapin, D. V.; Rogach, A. L.; Kornowski, A.; Haase, M.; Weller, H. Highly Luminescent Monodisperse CdSe and CdSe/ZnS Nanocrystals Synthesized in a Hexadecylamine–Trioctylphosphine Oxide–Trioctylphosphine Mixture. *Nano Letters* **2001**, *1*, 207–211.
- (250) Hens, Z.; Moreels, I.; Martins, J. C. In-Situ ¹H NMR Study on the Trioctylphosphine Oxide Capping of Colloidal InP Nanocrystals. *ChemPhysChem* **2005**, *6*, 2578–2584.
- (251) Hilliard, C. R.; Bhuvanesh, N.; Gladysz, J. A.; Blümel, J. Synthesis, Purification, and Characterization of Phosphine Oxides and Their Hydrogen Peroxide Adducts. *Dalton Transactions (Cambridge, England : 2003)* **2012**, *41*, 1742–1754.
- (252) Kriz, J.; Dybal, J.; Makrlik, E.; Budka, J.; Vanura, P. Interaction of Hydrated Protons with Trioctylphosphine Oxide : NMR and Theoretical. *Journal of Physical Chemistry A* **2009**, *113*, 5896–5905.
- (253) Liu, H.; Owen, J. S.; Alivisatos, A. P.; Information, S. Mechanistic Study of Precursor Evolution in Colloidal Group II-VI Semiconductor Nanocrystal Synthesis. *Materials Science* **2007**, *129*, 305–312.
- (254) Sheldrick, G. M. A Short History of SHELX. *Acta crystallographica. Section A, Foundations of crystallography* **2008**, *A64*, 112–122.
- (255) Gordon, T. G.; Diroll, B. T.; Paik, T.; Doan-Nguyen, V. V. T.; Gaulding, E. A.; Murray, C. B. Characterization of Shape and Monodispersity of Anisotropic Nanocrystals through Atomistic X-Ray Scattering Simulation. *Chemistry of Materials* **2015**, *27*, 2502–2506.
- (256) Hovestreydt, E. International Union of Crystallography. *Acta Crystallographica* **1983**, *A39*, 268–269.
- (257) Brown, P. J.; Fox, A. G.; Maslen, E. N.; O’Keefe, M. A.; Willis, B. T. M. *International Tables for Crystallography*; Prince, E., Ed.; 3rd ed.; Kluwer Academic Publishers: Dordrecht, 2003; Vol. C.
- (258) CrystalMaker Software Ltd. CrystalMaker (2015). CrystalDiffract.

- (259) Abdelsayed, V.; Aljarash, A.; El-Shall, M. S.; Al Othman, Z. a.; Alghamdi, A. H. Microwave Synthesis of Bimetallic Nanoalloys and CO Oxidation on Ceria-Supported Nanoalloys. *Chemistry of Materials* **2009**, *21*, 2825–2834.
- (260) Tanaka, A.; Kamikubo, H.; Doi, Y.; Hinatsu, Y.; Kataoka, M.; Kawai, T.; Hasegawa, Y. Self-Assembly and Enhanced Magnetic Properties of Three-Dimensional Superlattice Structures Composed of Cube-Shaped EuS Nanocrystals. *Chemistry of Materials* **2010**, *22*, 1776–1781.
- (261) Liao, L.; Zhang, Q.; Su, Z.; Zhao, Z.; Wang, Y.; Li, Y.; Lu, X.; Wei, D. D.; Feng, G.; Yu, Q.; *et al.* Efficient Solar Water-Splitting Using a Nanocrystalline CoO Photocatalyst. *Nature Nanotechnology* **2014**, *9*, 69–73.
- (262) Gordon, T. R.; Cargnello, M.; Paik, T.; Mangolini, F.; Weber, R. T.; Murray, C. B.; Fornasiero, P.; Murray, C. B. Nonaqueous Synthesis of TiO₂ Nanocrystals Using TiF₄ to Engineer Morphology, Oxygen Vacancy Concentration, and Photocatalytic Activity. *Journal of the American Chemical Society* **2012**, *134*, 6751–6761.